Metal Extrusion Assays as a Tool for Sulfate Recognition

Thesis by

Gabrielle Shiels

A Thesis Submitted

To Fulfil the Requirements

Of the Degree of

Doctor of Philosophy

School of Chemistry

University of Sydney

Sydney, Australia

2025

DECLARATION

This thesis is a summary of work carried out in the School of Chemistry at the University of Sydney under the supervision of Professor Katrina A. Jolliffe between March 2021 and July 2025. Except where referenced, this thesis contains no material previously published or extracted in whole or in part from a thesis presented by me for any other degree or diploma and the work of other people has not been used without due acknowledgement. This thesis contains less than 80,000 words. This work was supported by the L E R Tonnet and Family Scholarship in Chemistry and the Agnes Campbell Honours Prize and Australian Government Research Training Program (RTP) offset. No generative AI was used in the preparation of this thesis.

Contents

ABSTRACT

Sulfate is a biologically relevant anion found in an array of aqueous media including biological and environmental fluids, including blood plasma and seawater. While sulfate is highly prevalent in these media, selective detection of sulfate poses a challenge due to its similarities with other relevant anions. While receptors specifically designed for sulfate have often been used, assay based approaches can also be used for sulfate recognition. In this study, Metal Extrusion Assays (MEAs) are used as a new approach for sulfate recognition. While this approach has been used for recognition of other relevant anions, this study presents one of the first MEAs for sulfate in a range of aqueous media.

To determine if this approach can be used for sulfate recognition in aqueous complex media, a range of synthetic and analytical techniques were employed, with fluorescence and UV-vis spectroscopy used as the main tools to detect binding. The photophysical characteristics of a range of receptors was determined in conjunction with studying these receptors as tools for cation binding. This then informed the creation of the MEAs, which were employed to detect sulfate. Variation of the receptor-ligand combination allowed for sulfate detection through MEAs in biological fluid mimics and sea-water mimics, indicating the potential of MEAs for use in complex media.

ACKNOWLEDGEMENTS

Firstly, I would like to thank my supervisor Kate Jolliffe for providing me guidance throughout my PhD journey as it would not have been possible without her knowledge and insight. A special thankyou to all members of the Jolliffe group who have helped me throughout the years. I would like to pay special thanks to Stephen Butler II and Nian Kee Tan for helping me with my lab work as well as proofreading this thesis, as well as postdocs past and present. I would also like to acknowledge the L E R Tonnet and Family Scholarship in Chemistry and the Agnes Campbell Honours Prize.

I am also grateful for the technical staff who kept the instruments running to produce this thesis, including Dr Ian Luck (NMR) and Dr Nick Proschogo (Mass Spectrometry Facility), as well as Dr Cody Szcepina (Separations Facility).

Finally, a thankyou to my friends and family for their support. A very special thankyou to my partner Georgio, who has kept me going and motivated me when I needed it the most.

ABBREVIATIONS

ppm	parts per million
δ	chemical shift
λ	wavelength
NMR	Nuclear Magnetic Resonance
DMF	Dimethylformamide
eq	equivalents
ESI	Electrospray Ionisation
EtOH	Ethanol
MeOH	Methanol
MeCN	Acetonitrile
IR	Infrared Resonance
K_a	Equilibrium Constant
M	Molar
m.p	Melting Point
TBA	*Tert*-butyl ammonium
THF	Tetrahydrofuran
TLC	Thin Layer chromatography
Et_3N	Triethylamine
TFA	Trifluoroacetic acid
EtOAc	Ethyl acetate
R.T	Room Temperature
TICT	Twisted Intramolecular Charge Transfer
ICT	Intramolecular Charge Transfer
PET	Photoinduced Electron Transfer
FRET	Forster Resonance Energy Transfer

CHEF/CHEQ	Chelation Enhanced Fluorescence/Quenching
BG	Bromocresol Green
CR	Cresol Red
HG	Host-Guest
SBP	Sulfate Binding Protein
HB	Hydrogen Bonds
XB	Halogen Bonds
DFT	Density Functional Theory
IDA	Indicator Displacement Assay
MEA	Metal Extrusion Assay
ML	Metal-Ligand
HEPES	(4-(2-hydroxyethyl)-1-piperazineethanesulfonic acid
Aza-CE	1-aza-18-crown-6-ether
di-Aza-CE	1,10-diaza-18-crown-6-ether
BODIPY	Boron dipyrromethene
Tris	Trisaminomethane

Chapter 1

Introduction

1.1 Sulfate Recognition

In the developing field of anion recognition chemistry, the selective detection and quantification of sulfate (SO_4^{2-}) in aqueous systems remains a challenge. Sulfate plays a critical role in a range of physiological and environmental processes, necessitating the development of selective receptors with high binding affinities that can function in effectively complex competitive media. Furthermore, contemporaneous extraction and removal of SO_4^{2-} is a highly attractive option, as it broadens the scope of recognition pathways and potential applications. While the development of receptors for SO_4^{2-} has been explored in depth, the development of assays for SO_4^{2-} detection and quantification remains relatively under-explored. The integration of these assay-based approaches allows for the growth of the field of anion recognition, and builds upon approaches targeted at detection, quantification, and removal of SO_4^{2-} from aqueous systems.

To begin, the literature targeted at SO_4^{2-} recognition will be explored and alternative methods for monitoring SO_4^{2-} concentration will also be reviewed. Finally, a new method of SO_4^{2-} recognition, quantification and removal will be proposed. This new assay mechanism has seldom been used, providing an optimal pathway into new methods of SO_4^{2-} detection. This assay mechanism relies heavily on cation recognition, so the underlying principles surrounding this mechanism will also be discussed.

Figure 1.1: Overview of the applications of sulfate recognition, including in biological systems, nuclear waste remediation and aqueous environments such as seawater.

1.1.1 Importance of Sulfate

Sulfate (SO_4^{2-}) is the fourth most abundant anion in blood with concentrations up to 500 μM.[1] Physiologically, SO_4^{2-} can be obtained through the metabolism of cysteine and methionine in protein rich foods, with blood plasma SO_4^{2-} levels undergoing drastic fluctuations during this process.[2] Sulfate is also an essential source of sulfur, which is the third most abundant mineral in the human body and is essential for bodily functions.[2] While highly abundant in biological fluids, SO_4^{2-} has a high hydrophilicity,[3] preventing it from passing through lipid bilayers. External transporters can allow SO_4^{2-} to cross cellular membranes,[4] but the total cellular concentration remains low. Therefore, the recognition of SO_4^{2-} is focused on biological fluids.

In biological systems, SO_4^{2-} deficiencies can lead to severe defects and diseases, and has been linked to rheumatoid arthritis[5] and dehydration.[6] Sulfate plays a vital role in the detoxification of drugs such as steroids and acetomeniphen.[1] Additionally, sulfonation of glycosaminoglycans (a form of polysaccharides) such as heparan sulfate ensures tissue structure and function is maintained.[1] Heparan sulfate proteoglycans embedded in the cellular membrane play a role in endocytosis of cellular receptors, so are essential in the functioning of cells and the immune response.[7]

While less influential in environmental contexts, SO_4^{2-} is still somewhat prevalent. In sea water, the concentration of SO_4^{2-} is $\simeq$ 2.5 mg/L, making it the second most abundant anion behind Cl^-. In industrial applications, SO_4^{2-} is often known to interfere in nuclear waste processing, where high SO_4^{2-} concentrations interfere with vitrification. Therefore, the development of selective probes for SO_4^{2-} detection in the environment is of importance.

It is obvious that SO_4^{2-} is an incredibly crucial anion, more-so in biological specimens. The link between SO_4^{2-} fluctuations and health impacts is actively being explored, however better tools are needed to provide an accurate measurement of concentration variations. The marriage between selective SO_4^{2-} sensors and high quantification accuracy is an ever present goal. This thesis aims to bridge the gap between current methods of SO_4^{2-} recognition with concentration quantification.

1.2 Challenges in Sulfate Binding

While being a seemingly simple anion, the selective recognition of SO_4^{2-} has presented a myriad of difficulties. The challenges encompass intrinsic properties of this anion, as well as extrinsic factors such as the environment in which sensing is occurring. The following section explores these challenges, as well as the range of interactions and mechanisms in which SO_4^{2-} can be bound.

The first factor to be considered is the intrinsic hydrophilicity of SO_4^{2-}. As mentioned prior, SO_4^{2-} is very hydrophilic, and this can be related using the Hofmeister series (Figure 1.2), which shows the relative hydrophilicity of common anions. Anions towards the hydrophilic end of the scale have very large standard enthalpy of hydration ($\Delta H°_{hyd}$), with SO_4^{2-} having a high $\Delta H°_{hyd}$ of -1035 kJ/-mol. In comparison to a hydrophobic anion such as I^- ($\Delta H°_{hyd}$ of -291 kJ/mol), the energy required to desolvate SO_4^{2-} is substantially harder to achieve,[3] resulting in a number of receptors being unable to effectively out-compete water. This

results in most receptors for SO_4^{2-} only functioning in organic media, which obviously limits their use in biological samples, which is also contributed to by the low solubility of receptors. Due to the inherent hydrophilicity , selective SO_4^{2-} recognition is difficult to achieve in water.

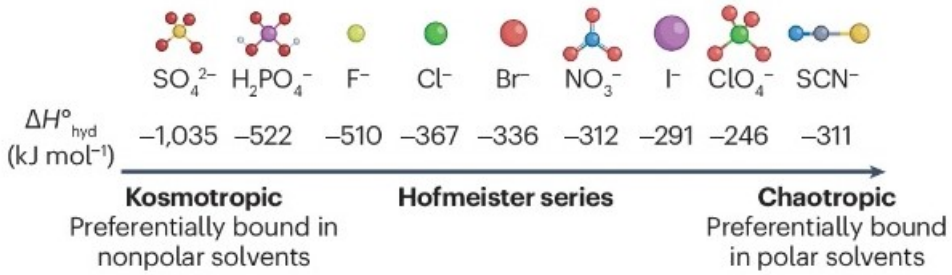

Figure 1.2: Hofmeister series in relation to a range of anions as well as the corresponding anionic geometries. Reprinted with permission from Nature Reviews Chemistry.[3]

The strength of the resultant binding interactions is also an intrinsic difficulty in SO_4^{2-} detection. Anions are more charge diffuse compared to their cationic counterparts, owing to their larger hydrodynamic radius. This results in weaker electrostatic interactions between the anion and a charged receptor motif. For instance, comparing Cl^- and K(I), the larger radius of Cl^- (0.18 nm) results in a more diffuse negative charge spread across a large molecule.[8] K(I) on the other hand, has a hydrodynamic radius of 0.14 nm and is substantially more charge dense,[8] resulting in significantly stronger binding interactions. This trend extends to SO_4^{2-} recognition, where the large hydrodynamic radius of 0.24 nm (Table 1.1) weakens the overall electrostatic interactions. In the same vein, anions of similar size (e.g SO_4^{2-} and I^-), often present a challenge in selective recognition.[8] The same size means that selective receptors cannot simply rely on a size complementarity due to interference from other similar anions. When combining charge diffusion and the strong hydrophilicity of SO_4^{2-}, the difficulties in developing a selective receptor become more pronounced.

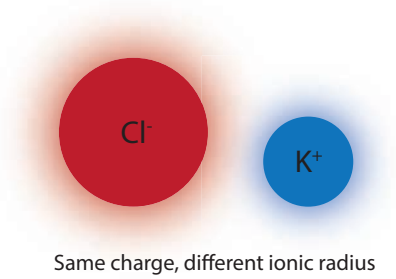

Figure 1.3: Visual comparison on the relative size differences between two ions, showing the difference in size and charge diffusion. Radii are not drawn to scale.

Table 1.1: Hydrodynamic radius of various hydrated anions.[8]

Anion	Ionic radius (nm)
F^-	0.12
CO_3^{2-}	0.16
Cl^-	0.18
I^-	0.23
SO_4^{2-}	0.24
$H_2PO_4^-$	0.24

When considering the development of chemo-selective receptors for SO_4^{2-}, one must also take into consideration the geometry of competing anions. In order to design a selective receptor, difficulty exists in out-competing binding to other similarly sized shape and charged anions. Sulfate exists in a tetrahedral geometry similar to phosphate and perchlorate as shown in Figure 1.2.[3] This suggests that attempting to design receptors based on a size match may be even more challenging when it comes to discriminating between these anions. Similarly, SO_4^{2-} exists in a resonance form with an overall 2- charge, similar to selenate and hydrogen phosphate. The similarity in charge causes difficulties when designing receptors relying on electrostatic interactions, often resulting in a lack of selectivity. The combination of these factors severely limits the ability to design selective SO_4^{2-} receptors.

Additionally, pH plays a significant role in developing selective receptors. The protonation states of many oxoanions changes based on pH, which may influence the size-to-charge ratio or the overall shape of the molecule. For instance, HSO_4^- has a pK_a of 2 (resulting in HSO_4^- as the dominant species at pH $< pK_a$),[9] while

the commonly competitive PO_4^{3-} has pK_a values of 2.2, 7.2 and 12.4, resulting in different phosphate species being present in solution depending on pH.[10] At neutral pH, the states of either anion are different compared to at higher or lower pH. Consequently, their shape, size and charge will also vary at differing pH values. Due to this, the pH of the desired application environment should also be considered in the design of selective receptors.

Due to the myriad of difficulties which arise in selective SO_4^{2-} recognition, a large number of interactions have been utilised to approach this challenge. In order to understand these interactions, a range of analytical and mathematical procedures have been developed.

1.2.1 Determining Binding Constants

Host-Guest (HG) chemistry plays a large role in the field of supramolecular chemistry. One component of HG chemistry aims to determine the binding interactions of receptors with a guest of choice and allows for the determination of the strength of this interaction, with this interaction referred to as the association constant (also known as the binding affinity or K_a)[11] as mathematically defined later in this introduction. This is vital in a range of applications, such as utilising curcurbiturils to encapsulate drugs for release in the body[12] or understanding how small molecules can bind to anions and cations. This can then allow for receptors to be chemically modified to change K_a or to alter the selectivity of the receptor.

Selectivity in HG chemistry is often thought of as the binding of only one target to a receptor, with this target out-competing all other analytes present. Selectivity is important to achieve, as it ensures that the receptor binds only to the target of choice, which is essential for maintaining analytical accuracy in analyte quantification or drug release. In instances where receptors exhibit non-selective binding, interference can arise from other guests during HG studies, which may lead to inaccurate results. Selectivity can be introduced in a number

of ways, including tailoring the receptor size and shape to ensure a good match to the guest,[13] or changing the interactions involved in binding (e.g changing from aromatic interactions to hydrogen bond interactions). While selectivity does not determine the strength of the binding interaction, it must always be considered when designing receptors for guest targeting.

Selectivity is typically determined by screening the receptor and its response to a wide variety of analytes. These analytes should be common interferants and should also include a range of structurally similar targets. The ideal receptor will only exhibit a response (e.g change in absorbance or emission) to one analyte, and ideally maintain this response in a mixture of interferants. Practically, this high level of selectivity for anions is difficult to achieve due to the aforementioned problems. The selectivity can also be tuned by altering pH (which will change charge and conformation), or by introducing higher polarity solvents to induce solvation of some guests (which will require desolvation to occur first before binding). These tools can be used to influence the overall selectivity profile.

Receptors and analytes can bind in a range of stoichiometries which are expressed as a ratio of host:guest (H:G). In a simple 1:1 system, one host molecule binds to one analyte, with no co-operativity present. In more complex 1:2 and 2:1 systems, there are multiple molecules binding, and co-operativity can also change the binding response. Co-operativity is the phenomenon in a 1:2 system where binding of the first analyte alters the receptor structurally or electronically, impacting the binding of the second guest molecule. Co-operativity can be positive, indicating preferential formation of the 1:2 or 2:1 complex over the 1:1 complex, or negative. Determination of the binding ratios comes from global fitting of titration data using mathematical software such as BindFit (http://supramolecular.org).[11] The data is commonly fit using the Nelder-Mead method and aim to solve for [HG] in the quadratic equation A.11 (for a 1:1 system) and K_1 and K_2 in the cubic equation A.12 (for more complex 1:2 and 2:1

systems).

Non-linear regression analysis is used to determine these binding stoichiometries, with Nelder-Mead optimisation used to minimise either the standard error (SE) or the χ^2 statistic presented in equation A.13. Goodness of fit can also be estimated by visual inspection of the binding isotherm.

The binding affinity K_a (commonly reported as $LogK_a$), is a measure of the strength of HG interactions. Host:Guest complexes with large K_a (generally in the order to $> 10^5$ M^{-1}) are often desirable, as this minimises the likelihood of unwanted analytes displacing the guest. However, a highly selective receptor with a lower K_a can also be desirable, as this still provides a selective response to allow for quantification purposes. The ideal selective receptor should either have a high K_a or high selectivity, as these are desirable characteristics. To determine these values, the binding equilibrium is examined. Often the aforementioned software are capable of determining these values, however there may be variations between programs. In the simplest form, the binding equilibrium for a 1:1 complex can be written according to 1.1:

$$H + G \rightleftharpoons HG \tag{1.1}$$

For the determination of K_a for a 1:1 system, equation 1.2 can be used:

$$K_a = \frac{[HG]}{[H][G]} \tag{1.2}$$

Where

[HG] = Host-guest concentration at equilibrium determined using equation A.11

[H] = Concentration of the Host molecule

[G] = Concentration of the Guest molecule

While for the determination of K_a for a 1:2 system, equation 1.3 can be used:

$$K_1 = \frac{[HG]}{[H][G]}, \quad K_2 = \frac{[HG_2]}{[H][HG]} \tag{1.3}$$

Where

[HG] = Host-guest concentration at equilibrium determined using equation A.12

[H] = Concentration of the Host molecule

[G] = Concentration of the Guest molecule

The equilibrium concentrations of each species is not simple to determine without analytical techniques. To determine these, titrations are the best suited and most common technique. An analytical titration can be performed spectrophotometrically (UV-vis or fluorescence) or through NMR or calorimetry, with each method having advantages and disadvantages. UV and fluorescence titrations are preferred when a chromophore is present, and that chromophore must exhibit a change upon binding, while NMR is a better methods where a chromophore is not present. In addition to this, spectrophotometric titrations are useful when the binding affinity of the HG complex is up to 10^6 M^{-1} as the concentration of receptor molecule can be in the nanomolar range,[11] thereby reducing the effects of excimer formation and allowing for analyte detection with higher sensitivity. If the anticipated binding strength is outside of this range, spectrophotometric titrations do not provide an accurate measure of K_a. The standard procedure involves dissolving the target analyte in a solution of the receptor to minimise effects from dilution. Increasing aliquots of this guest solution are subsequently added to a known volume of the receptor solution. From this, the change in response can be related to the K_a.

For titrations utilising UV-vis spectroscopy, equation A.14 (see Appendix) can be used to determine [HG]. UV-vis spectroscopic titrations require the known absorption coefficient ε of the fluorophore/host molecule. While for fluorescence spectroscopic titrations, the equation is slightly modified in the form shown in equation A.15. Fluorescence titrations can be influenced by quenching (whereby the host molecules' fluorescence in quenched upon analyte addition) or may not experience quenching. For cases in which quenching does not occur, equation A.15 (see Appendix) holds. In cases where fluorescence quenching occurs, equation A.16 (see Appendix) can be used.

Mass balance equations are used to derive these formulas. Effects such as dynamic quenching are not accounted for, and often displacement processes complicate the mathematics. Additionally, as the binding mode complexity increases (e.g from 1:1 to 1:2), the mathematical derivations increase in complexity substantially, and even more complex binding relationships (e.g 3:1) are unable to be accurately determined. Both equation A.14 and A.15 represent the simplest 1:1 binding model, and must be modified for more complex stoichiometries.

K_a determination also allows for a comparison of the Gibbs free energy (ΔG) to determine which complex is more likely to form. By knowing this, the position of the binding equilibrium can be assumed. The relationship between K_a and ΔG can be written according to equation 1.4. This relationship shows at 25 °C that as K_a increases by a factor of 2, the overall ΔG will increase by roughly -1.7 kJ/mol. This indicates that a comparison of the system energetics can provide information as to the possible binding fashion.

$$\Delta G = -RTlnK_a \tag{1.4}$$

G = Gibbs' free energy

R = Universal gas constant

T = Temperature in Kelvin

K_a = Binding affinity

1.3 Anion Binding Interactions

1.3.1 Hydrogen Bond Interactions

Nature provides a remarkable solution to binding to SO_4^{2-} with a high K_a. The Sulfate Binding Protein (SBP) isolated from *Salmonella typhimurium* is responsible for SO_4^{2-} membrane transport, and has provided a great deal of insight into the optimal interactions for SO_4^{2-} binding (Figure 1.4). This shows a range of amino acids within the protein binding pocket which contribute to SO_4^{2-} binding.

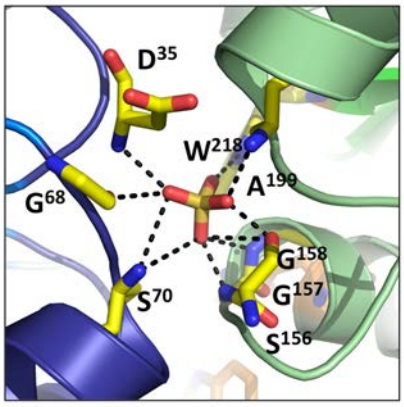

Figure 1.4: Crystal structure of the Sulfate Binding Protein.[14]

From solving the crystal structure, it was found that 7 Hydrogen Bonds (HB) form between these amino acids and SO_4^{2-}. These HBs are as a result of peptide backbone amides from glycine, aspartic acid and alanine, as well as a hydroxyl attributed to serine and the NH indole from tryptophan.[15] The binding pocket of the SBP lacks cationic residues,[16] suggesting that the strong binding ($LogK_a$ = 5.8) is afforded by these multiple HB as opposed to charge based interactions. Additional Van der Waals' forces also contribute to strong binding, however this contribution is lower in comparison to the contribution by HB.[14] Additionally, the

specificity for SO_4^{2-} arises from the specific set of amino acids, which allows for SO_4^{2-} to fit perfectly into the pocket, thus inducing size complementarity.[14] To translate this binding into a synthetically accessible receptor, a suitable receptor can utilise a high number of HB (or fewer HB in conjunction with other intermolecular interactions), as well as size complementarity to SO_4^{2-}. Practically, this can often be very difficult to achieve.

A high degree of HB donating sites can be synthetically accessed through a number of amide and urea based derivatives. A range of binding motifs including ureas,[17] imidazoliums[18] and guanidiniums[19] have been previously used for this application (Figure 1.5). Additionally, squaramides have also been used for SO_4^{2-} recognition, such as in peptides[20] and polymers.[21] In all cases, these binding motifs allow for selective functionalisation of either one or both arms to develop either symmetrical or asymmetrical receptors, allowing for the introduction of multiple binding motifs, fluorophores or water solubilising groups.

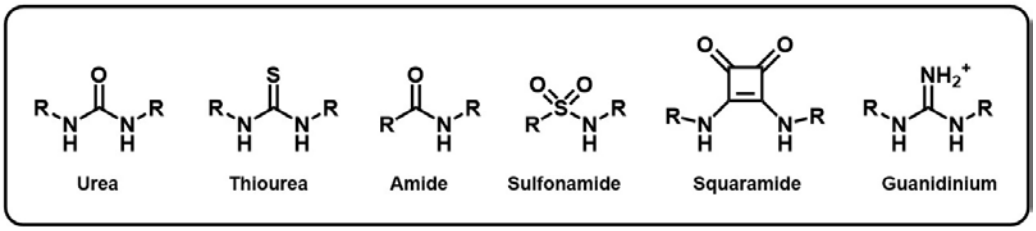

Figure 1.5: Chemical structures of various anion binding motifs.

Pre-organisation is a technique which involves intentionally developing a receptor with size complementarity (where the size cavity of the host matches that of the size of the desired guest) to a guest, to allow for the formation of a binding pocket with appropriately positioned binding sites to ensure guest binding. To provide a high degree of pre-organisation, a range of HB donors can be incorporated into macrocyclic backbones. As HB are highly directional,[22] positioning these groups so the N-H protons point into the binding pocket, (which can be introduced using the binding motifs presented in Figure 1.5), enhances encapsulation of SO_4^{2-}. Incorporation into a macrocycle allows for the tuning of the

number of HB sites for SO_4^{2-} binding,[23] influencing the selectivity and LogK_a. Additionally, the size of the macrocycle can be tuned to induce size complementarity with SO_4^{2-}. Through this, receptor design can be modified and tuned to impart size selectivity and increase K_a.

Hydrogen bond based receptors tend to exhibit varied responses with pH. Motifs such as squaramides were shown to have a pK_a at least 8.4,[24] altering the protonation state of te motif, however this value varies depending on substitution patterns. In conjunction with the various protonation states of anions, this can provide difficulties in receptor design for applications at particular pH ranges, as anion charge and shape may vary depending on solution pH.

While macrocyclic receptors are promising, synthesis of these receptors may involve high dilution conditions (particularly for motifs suffering from low solubility such as squaramides), which may present difficulties when synthesising these receptors on larger scales. While water soluble macrocycles are available (such as cyclodextrins and calixarenes), structurally simpler macrocycles may present lower water solubility, severely limiting their applications to organic solvents only. Additionally, most receptors exhibit lower K_a as water content increases, which is not ideal for SO_4^{2-} recognition in biological or waste water applications. However, there are a range of simple and complex structures which have been utilised for sulfate recognition.

This section explores a few examples of receptors for anion binding to highlight the key features and limitations of these receptors. The first example examined highlights the applicability of colorimetric receptors for anion recognition, while also highlighting the limitations in selectivity. The anion binding properties of a 4-nitrophenyl functionalised thiourea (**1**) and urea (**2**) molecular clefts utilising directional HB were explored by Manna *et al.* (Figure 1.6).[25] In studies performed in DMSO using UV-vis spectroscopy, the addition of either F^- or $H_2PO_4^-$ to a solution of **1** or **2** resulted in a colorimetric response, with a visible colour change

from yellow to red. It was observed that these receptors had a non-selective response, with an overall binding trend of LogK_a of $F^- > H_2PO_4^- > Cl^- > HSO_4^- > Br^- > I^- > ClO_4^- > NO_3^-$. It was noted that **1** exhibited stronger interactions overall (LogK_a for F^- of 3.70 and $H_2PO_4^-$ of 2.82) compared to **2** (LogK_a for F^- of 2.84 and $H_2PO_4^-$ of 2.07), attributed to the higher acidity of the thiourea motif. Although these receptors produce a colorimetric response, the LogK_a values amongst the anions tested were not substantially different, highlighting the difficulty in designing a selective anion receptor.

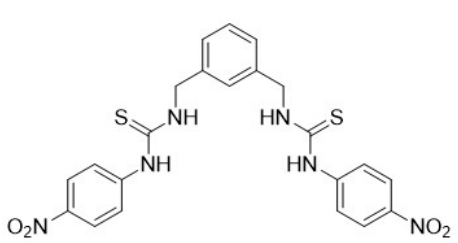

1

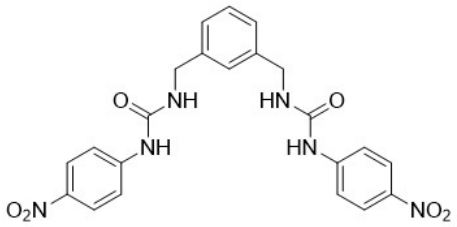

2

Receptor	Anion	LogK_a
1	F^-	3.70
	$H_2PO_4^-$	2.80
2	F^-	2.84
	$H_2PO_4^-$	2.07

Figure 1.6: 4-nitrophenyl functionalised molecular clefts for anion binding and corresponding LogK_a values obtained in DMSO.

While HB recognition motifs are utilised in SO_4^{2-} sensing, a simple acyclic symmetric squaramide (Figure 1.7) synthesised by Picci *et al.*[26] indicates that simple small molecule HB systems are not satisfactory to achieve selective SO_4^{2-} sensing. Compound **3** demonstrated binding of anions to the squaramide and indole NH protons through NMR titrations in 0.5 % H_2O:DMSO-d_6 upon guest addition to **3**, with a LogK_a for $AcO^- > 4$, $H_2PO_4^- > 4$ and Cl^- of 3.08. LogK_a values could not be obtained for F^- and CN^- due to receptor deprotonation, and for BzO^-, as the titration isotherm could not be fit to a model. Upon increasing the water content to 25 % H_2O:DMSO-d_6, the LogK_a values were lower as expected, with $H_2PO_4^-$ of 3.23, AcO^- of 2.34, BzO^- of 2.08 and Cl^- of 1.30.

This receptor was found to exhibit a cooperative binding mode, as the squaramide NH protons and the NH-indole stabilised the resultant anion complex.

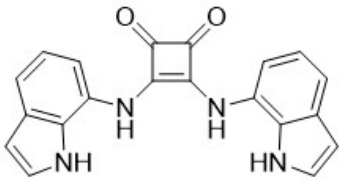

3

Figure 1.7: Acyclic squaramide for anion recognition.

Tripodal anion receptors have been extensively used for oxoanion recognition (Figure 1.8), highlighting the ability to increase selectivity for SO_4^{2-} over competing anions using higher numbers of HB sites. The hexaurea receptor **4** was designed to achieve conformational complementarity to SO_4^{2-} and PO_4^{3-} while providing the necessary 12 hydrogen bonds for strong binding.[27] It was observed that SO_4^{2-} binding in 0.5 % D_2O:DMSO-d_6 occurred with slow exchange and gave complexes with both 1:1 and 1:2 stoichiometries. In comparison, binding in 25 % D_2O only occurred in a 1:1 stoichiometry, and **4** was found to have an affinity for SO_4^{2-} of at least LogK_a of 4. While there was shape complementarity for PO_4^{3-}, the affinity was not determined, but competition studies indicated that that PO_4^{3-} could not displace SO_4^{2-}, suggesting higher affinity for SO_4^{2-}. This receptor was successfully used to extract SO_4^{2-} from an aqueous phase, providing an interesting application of this class of receptors for uses in extraction applications.

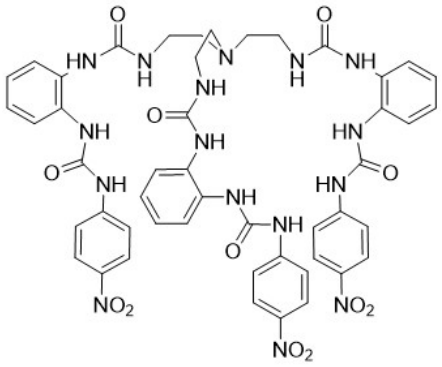

4

Figure 1.8: Tripodal receptor for SO_4^{2-} binding.

The next example demonstrates that high SO_4^{2-} binding can be achieved with the previously mentioned macrocyclic structures due to their size and charge complementarity to anions, such as the urea based macrocycle **5** developed by Kaur *et al.* (Figure 1.9) for SO_4^{2-} recognition.[28] The macrocycle contains an *N*,*N*-diethylmethylamine linker between two phenylene diurea motifs to provide the required HBs. Analysis of the crystal structure indicated that **5** binds to SO_4^{2-} through 9 HB interactions, with the ninth HB donor coming from protonation of the amine, where this charge assisted HB led to high K_a. In a 0.5% D_2O:DMSO-d_6 mixture, the macrocycle binds to SO_4^{2-} with a $LogK_a$ of 4.96, slightly higher compared to $H_2PO_4^-$ with a $LogK_a$ of 4.70. As water concentration was increased to 10%, the binding mode changed from 1:1 to 2:1 with $LogK_{a1}$ and $LogK_{a2}$ of 4.59 and 5 respectively for the SO_4^{2-} complex. While this macrocycle does exhibit strong affinity for SO_4^{2-} in partially aqueous media, it was not shown to be selective. Additionally, accurate binding constants could not be measured in higher water concentrations, suggesting limitations with this receptor. This system indicates that modifying the receptor to introduce higher degrees of interactions improves affinity, however is limited in application scope due to solubility and difficulty of synthesis.

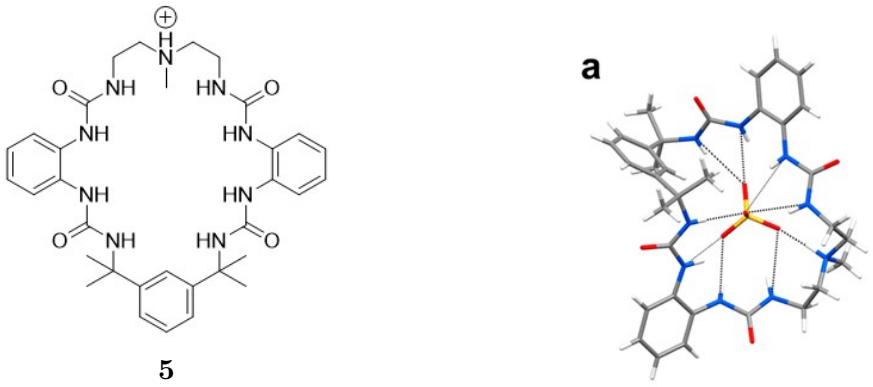

5

Figure 1.9: Urea macrocyclic probe for SO_4^{2-} recognition and crystal structure of **5**:SO_4^{2-}. Reprinted with permission from American Chemical Society.[28]

The properties of these macrocycles can be modified to allow for use in water, however these receptors still exhibit synthetic difficulties to introduce the required number of HB for SO_4^{2-} binding. Squaramide macrocycles have also been used for SO_4^{2-} recognition, as their highly directional nature allows for HB to form in the inner cavity of the macrocycle. In particular, a set of macrocyclic squaramides reported by Qin *et al.*[29] (**6** and **7**) were found to bind to SO_4^{2-} in aqueous mixtures up to 1:1 H_2O:DMSO-d_6. The macrocycle cavity size was increased from receptor **6** to **7**, and the introduction of water solubilising triethylene glycol groups increased the solubility and provided selectivity for SO_4^{2-} (3x greater compared to $H_2PO_4^-$) for receptor **7**. The LogK_a for both macrocycles was found to be 4, however receptor **6** was studied in 0.5 % H_2O:DMSO-d_6 and receptor **7** was studied in 1:2 H_2O:DMSO-d_6, meaning that **6** and **7** cannot be directly compared due to solvent system differences. This indicates that high SO_4^{2-} selectivity and high affinity in aqueous solvent mixtures can be achieved. However, the lack of fluorescent or colorimetric properties limits these receptors to NMR analysis only as opposed to a visual method of detection.

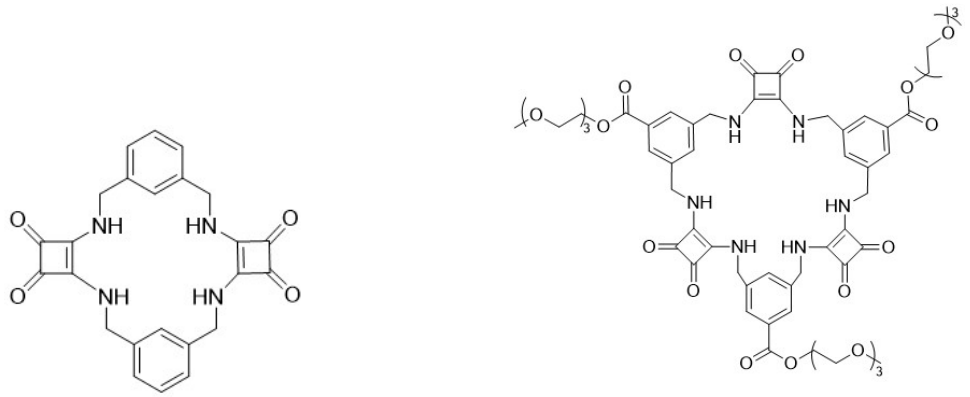

6 **7**

Figure 1.10: [2+2] macrocycle and the water solubilised [3+3] macrocycle.

While HB are often used for SO_4^{2-} sensing, these interactions can occur with metal centres to provide an indirect pathway for SO_4^{2-} recognition as presented in the next example. In another study, *de-novo* design was used to develop a nickel-coordinated cage **8** for SO_4^{2-} recognition, with a K_a similar to that of the SBP.[30] This was achieved using urea as the HB donors to form a resultant cage with an appropriate symmetry to match the SO_4^{2-}-urea complex. The Ni-cage (Figure 1.11a) had one SO_4^{2-} bound in the cage, with the optimal 12 HB to SO_4^{2-}. Barium addition led to $BaSO_4$ formation, allowing for removal of SO_4^{2-} as an indirect method utilising HB binding motifs. This formation was determined gravimetrically and allowed for the determination of $LogK_a$ which was 6.8 in water, higher than that of the SBP.

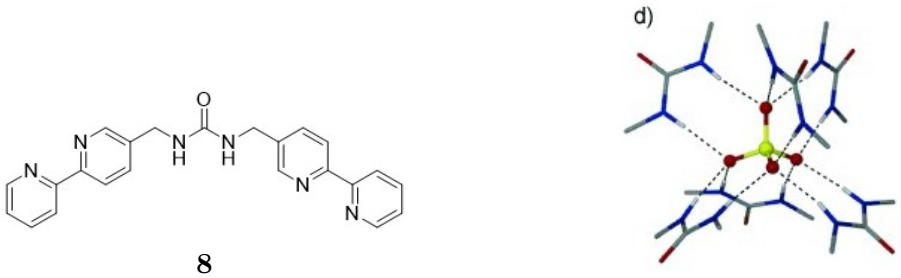

8

Figure 1.11: Ligand and sulfate binding site (C gray, H white, N blue, O red, S yellow) of **8**-Ni cage structure reprinted with permission from Angewandte Chemie.[30]

The next example demonstrates more complex binding systems can allow for both anion and cation recognition, opening a door to new sensing pathways. Cooperative binding using a ditopic receptor that recognises both SO_4^{2-} and a counter ion has also been explored in a study by Zaleskaya *et al.* Squaramide receptors **9** and **10** appended with a benzocrown motif (Figure 1.12)[31] were used, with the squaramide containing a pentafluoroaniline group was bound to SO_4^{2-}, while the benzocrown bound to alkali metals. Binding of the benzocrown portion was size dependent, leading to higher affinities for K(I) over Na(I). Through DOSY and crystal structure analysis, **10** was found to bind to SO_4^{2-} in a 4:1 model, with the crystal structure of **10**-K_2SO_4 indicating interactions of the crown ether cavity with K(I) and squaramide N-H interactions to SO_4^{2-}. Extraction of SO_4^{2-} using **10** was performed from aqueous solutions and confirmed using ion chromatography. It was found that the **10** was able to selectively remove K_2SO_4 in the presence of other potassium salts, while Na(I) exhibited slight interference. By using these ditopic receptors, this opens the door to selective extraction of SO_4^{2-}, however interference from other cations must be avoided.

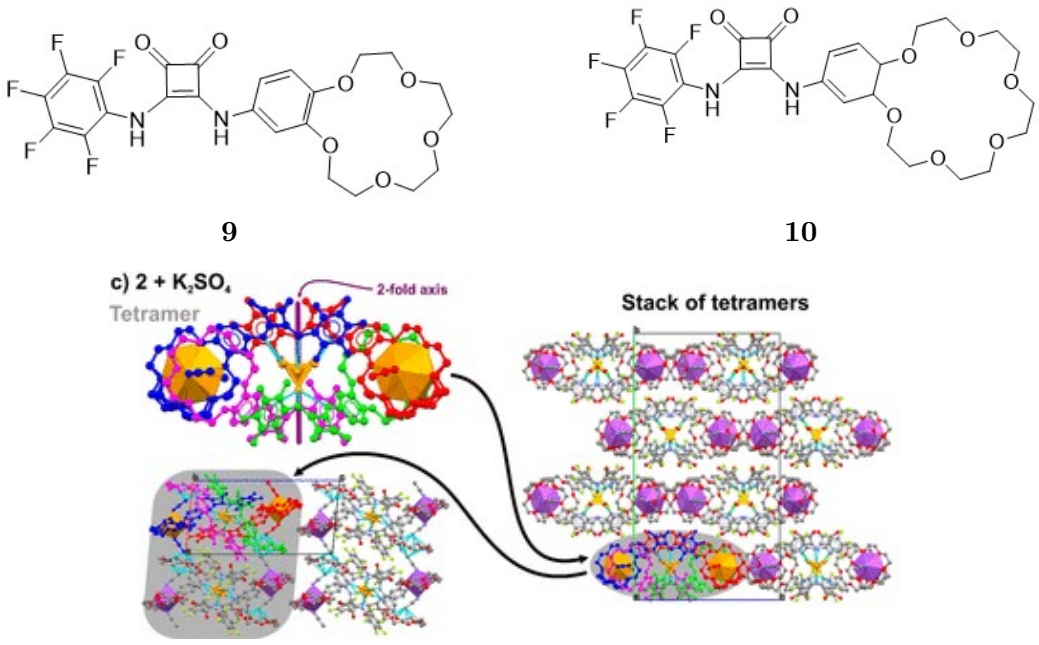

Figure 1.12: Squaramide ion pairs for SO_4^{2-} detection and extraction and 4:1 crystal structure of **10**.

The final example indicates that a high affinity for SO_4^{2-} can be achieved in a highly aqueous system, however severe synthetic limitations are observed through the formation of a complex interlocked receptor. In a recent study from the Chmielewski group, a fluorescent [2]catenane **11** (Figure 1.13) was developed for selective SO_4^{2-} binding.[32] The [2]catenane was based on the diamidocarbazole motif, which has been shown to bind to anions through hydrogen bonds. The intrinsic fluorescence of the motif allowed for easy analysis of anion recognition through fluorescence spectroscopy. The [2]catenane was formed *via* SO_4^{2-} templation and a subsequent ruthenium-catalysed ring closing metathesis, with **11** found to have varying conformations based on the binding model. A fluorescent turn on response was observed upon SO_4^{2-} addition, with a remarkably high $LogK_a = 5.9$ in a 1:9 H_2O:DMSO mixture. While this [2]catenane exhibited strong binding to SO_4^{2-} over $H_2PO_4^-$ ($LogK_a1$ 3.91 and $LogK_a2$ 3.51) and $PhCOO^-$ ($LogK_a$ 2.36), the synthetic difficulties limit applications for these systems.

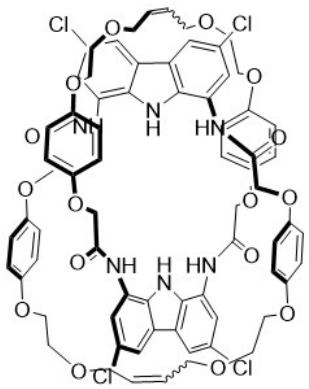

11

Figure 1.13: Fluorescent [2]catenane.

It was observed that through this small sampling of literature, a range of HB-based receptors have been developed for SO_4^{2-} recognition. These range from simple small-molecule based receptors, to structures of increased complexity ranging from tripodal sensors to interlocked macromolecules. As the complexity of the receptor increases, so too does the synthetic effort, providing a severe

limitation in the development of sulfate sensors. While these complex molecules may result in improved selectivity or increased K_a for SO_4^{2-}, this must be weighed against synthetic time and cost, as well as the overall properties of the receptors (e.g water solubility).

1.3.2 Halogen Interactions

Another form of electrostatic interactions used for anion binding are Halogen Bonds (XB). Halogen bonds can be thought of as complementary to HB due to the ability to provide directional interactions to guests. Halogen bonds arise as a result of the electronegativity of halogen atoms, creating a positively charged region (Figure 1.14) in the receptor which is amenable to electrostatic interactions to an anion. This receptor is primed for guest binding and may result in strong interactions to the guest, with the strength of these interactions similar to those observed for HB systems.[33] The electronegativity difference between a halogen and the adjacent atoms gives rise to the dipole that results in a sigma hole providing this interaction.[33] While these XB can be thought of as similar to HB, only a few examples have been reported for XB binding to SO_4^{2-} and these suffer from low binding affinities and selectivity issues.

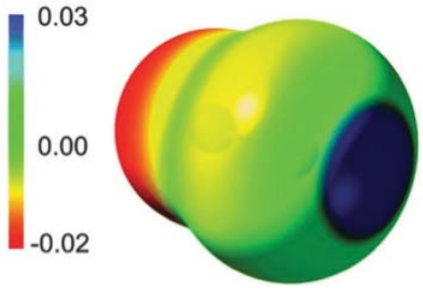

Figure 1.14: Electrostatic potential calculated for BrF showing the σ-hole and demonstrating the inherent polarisability. Reprinted with permission from Chemical Communications.[33]

The first example of XB receptors highlights that structurally complex receptors may result in high SO_4^{2-} affinities. A set of bis-iodotriazole-pyridinium receptors were recently developed by the Beer group, exploiting convergent XB interactions.[34] The linear receptor **12** was synthesised through CuAAC click

chemistry followed by methylation using iodomethane to yield **12**. Through NMR titrations, it was found that in a competitive solvent (DMSO-d_6), a strong affinity for SO_4^{2-} ($K_a > 10^4$) compared to Br^-, Cl^-, I^-, OAc^-, $H_2PO_4^-$ and NO_3^-, was observed for **12**, with X-ray analysis demonstrating a convergent binding nature between the bis-iodo groups and the respective anions. To increase the binding strength, the binding motif was incorporated in the [2]catenane **13**, however this resulted in a 25-fold increase in binding affinity for Br^- compared to **12**, suggesting that [2]catenane incorporation did not improve SO_4^{2-} selectivity. While chloride templation was used to synthesise **13**, it has been shown in other work using [2]catenanes that SO_4^{2-} templation may increase affinity or binding character to SO_4^{2-}, as shown in the HB-based receptor **11**, suggesting that this approach may be used to impart selectivity.[32]

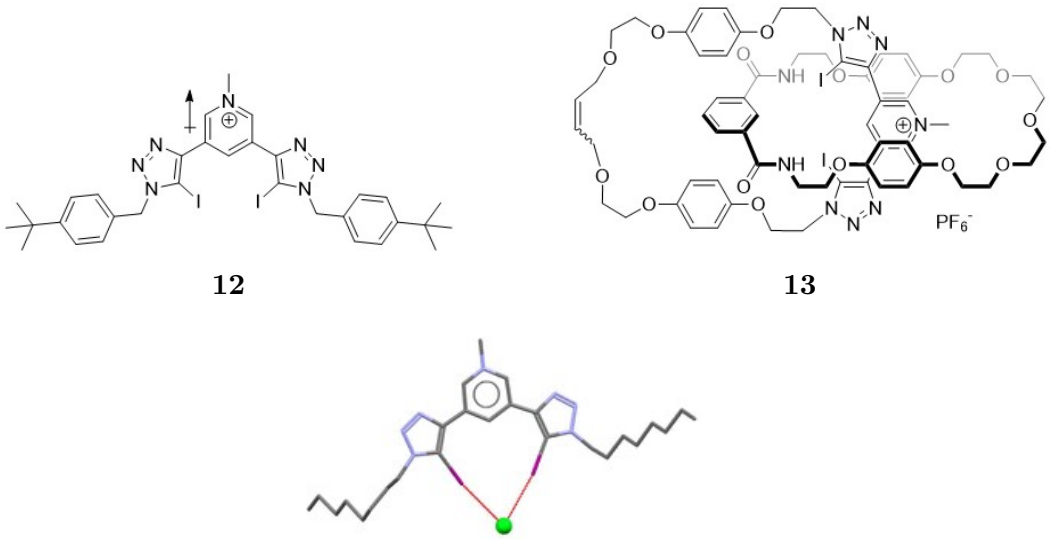

12 **13**

Figure 1.15: Linear bis-iodotriazol-pyridinium receptor and the corresponding [2]catenane. Crystal structure of **12**:SO_4^{2-} displayed.

Another example highlights a linear XB receptor can be developed which exhibits a higher affinity for SO_4^{2-} over other anions, however has poor selectivity as found in work by Tepper *et al.*[35] In this work, a series of receptors were designed, with the most promising being the iodo-1,2,3-triazolium **14** (Figure 1.16). Compound **14** was found to exhibit a higher affinity for SO_4^{2-} over other anions

tested, with the binding order of $I^- < Br^- < Cl^- < AcO^- < H_2PO_4^- < SO_4^{2-}$, with SO_4^{2-} found to have a K_a of 3400 M^{-1} in DMSO-d_6 as determined through NMR titrations. This response was attributed to the greater charge density of SO_4^{2-} causing stronger interactions with the σ hole. Additional DFT calculations indicated this this may also be caused by a greater σ-hole electrostatic potential imparted by the bulky iodine atoms, which increase the size and overall positive charge.

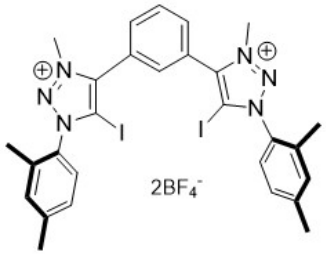

14

Figure 1.16: Iodo-1,2,3-triazolium receptor for SO_4^{2-} binding.

The next examples highlights the effect of XB incorporation on the selectivity profile of a set of receptors, providing insight into if XB incorporation is beneficial. A comparison was performed with a set of XB and HB receptors **15** − **17** (Figure 1.17) for SO_4^{2-} recognition, with a di-iodotriazolium carbazole linear receptor developed.[36] Comparing substituents, it was found that receptor **16** (aryl substituted) exhibited higher K_a values overall compared to the alkyl substituted receptor **15** attributed to higher pre-organisation and the presence of C-H—anion interactions. The binding profile and K_a for **16** was SO_4^{2-} (1450 M^{-1}) > Cl^- (430 M^{-1}) > Br^- > NO_3^- > I^- in comparison to **15** (SO_4^{2-} (341 M^{-1}) > Br^- (200 M^{-1}) > I^- > Cl^- > NO_3^-), with titrations performed in 10% D_2O:DMSO-d_6 for SO_4^{2-} and CD_3CN for the remaining guests. Receptor **17**, which replaces HB donors with XB donors, exhibited overall lower affinities compared to **15** (Br^- (893 M^{-1}) > SO_4^{2-} (493 M^{-1}) > Cl^- > I^-) and a change in binding profile, suggesting halide incorporation altered selectivity and reduced guest affinity.

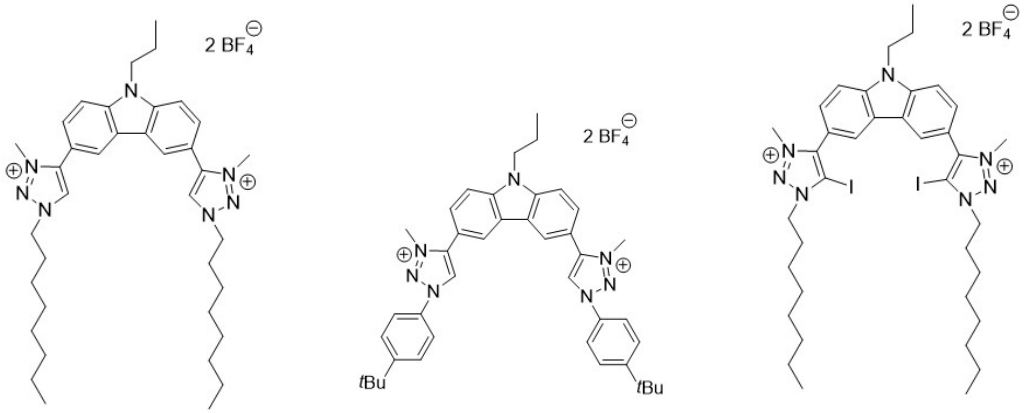

15 **16** **17**

Receptor	Anion	LogK$_a$
15	SO_4^{2-}	2.53
	Br^-	2.30
16	SO_4^{2-}	3.16
	Cl^-	2.63
17	SO_4^{2-}	2.69
	Br^-	2.95

Figure 1.17: Linear carbazole receptors for non-selective SO_4^{2-} binding and corresponding LogK$_a$ values obtained in 10% D_2O:DMSO-d_6 for SO_4^{2-} and CD_3CN for Br^- and Cl^-.

This effect of exchanging HB donors for XB donors was further explored in this next study, in which receptors **18** – **20**, based on 1,1'-bi-2-naphthol (BINOL), were developed.[37] A comparison was performed between ferrocenyl and phenyl substitution at the triazole (Figure 1.18) and it was found that the greater electron withdrawing nature of phenyl led to higher K$_a$ values when comparing **18** and **19**. In all cases while there was a response to SO_4^{2-}, it was not selective, with an overall binding trend of $HP_2O_7^{3-} > SO_4^{2-} > H_2PO_4^-$. The affinity for SO_4^{2-} was higher with HB donors compared to XB substitution when comparing **18** and **20**, suggesting that the XB is actually detrimental to selective SO_4^{2-} binding. The highest K$_a$ for SO_4^{2-} was 5.5 x 10^{-3} M^{-1} for **18** in 9:1 CD_3CN:CD_3OD, however this was orders of magnitude lower than the K$_a$ for $HP_2O_7^{3-}$. Competition due to $H_2PO_4^-$ could not be avoided, as the receptors produced a naked eye change in emission with phosphate, but no other anion. Ultimately, while there was a response to SO_4^{2-}, it could not out-compete the phosphate species, limiting

utility of the receptors for SO_4^{2-} recognition.

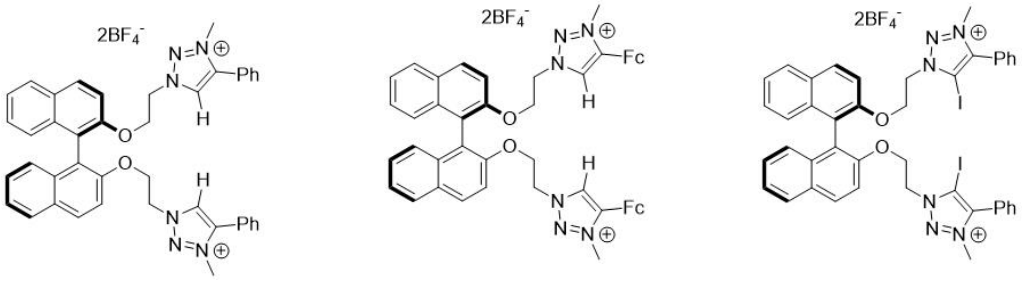

18 **19** **20**

Figure 1.18: Ferrocenyl and phenyl BINOL receptors for anion binding.

The final example demonstrates further the limited capability of XB receptors for SO_4^{2-} recognition, indicating that selectivity for SO_4^{2-} over halides is difficult to achieve. An imidazolium flanked by two iodotriazole groups was incorporated into a [2]rotaxane which was synthesised *via* chloride templation to form **21** (Figure 1.19).[38] Rotaxane **21** was found to bind to halides, presumably arising from the size match arising from the use of halide templation. The presence of the internal phenyl proton of the macrocycle pointing into the cavity through a C-H-anion interaction, as well as a conformational change of the methylene axle proton contributed to anion binding interactions. Preference of **21** was in the order $Cl^- >/= Br^- > SO_4^{2-} > I^-$. While this rotaxane did have some affinity for SO_4^{2-}, the preferential halide binding negates its effectiveness as a SO_4^{2-} sensor.

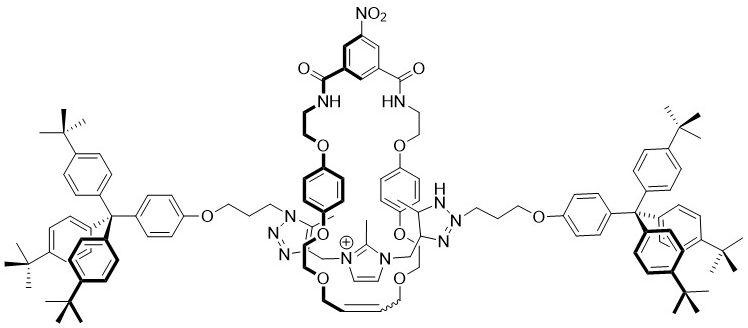

21

Figure 1.19: Halogen bonding based rotaxane.

From this, it can be seen that a range of different binding interactions are available. However, they all suffer from limitations, such as low oxoanion binding affinity in the case of XB, or selectivity issues in the case of HB. There are a substantial lack of XB receptors for SO_4^{2-}, and the selectivity issues which arise cannot be understated. Hydrogen bond receptors work well, but their lower affinities in water make them difficult for use in biological or environmental applications.

1.3.3 Metal-Anion Interactions

Another class of interactions available for SO_4^{2-} recognition consists of metal-anion (MA) interactions. A positively charged metal centre in a pre-formed complex allows for electrostatic interactions to the anion, and this complex may be pre-organised to enhance anion binding. The interaction between the metal and anion can be used to modulate properties such as the emission spectrum to serve as an indicator of anion binding. Common metal binding ligands contain oxygen, nitrogen or sulfur heteroatoms, allowing for a range of covalent and ionic interactions to the metal centre. A combination of these atoms can also be included to allow for more fine tuning of the metal-ligand binding character.

Different interactions are responsible for ligand binding to the metals. According to HSAB theory, a harder base such as oxygen will form stronger interactions with harder acids including alkali and alkaline earth metals, making them more suited for binding to these metals. Conversely, softer bases such as sulfur or phosphorus will form stronger interactions with softer acids, which are generally heavier transition metals. Intermediate bases including nitrogen will form stronger interactions with intermediate metals such as Zn(II) or Pb(II).[39] Additionally, the strength of a Lewis acid or base will increase as the radius decreases and the charge increases, suggesting that smaller ions with greater charges will act as stronger Lewis acids and bases. The stability of the eventual metal complex formed cannot be determined by simply looking at the strength of these

interactions.

These MA interactions have played a large role in advancing sensing of larger anions such as citrates and phosphates,[40,41] with limited research into using these interactions for SO_4^{2-} sensing. A variety of different sensing mechanisms have been used, including the use of indicator displacement approaches (explored in further detail in Section 1.5), e.g iron-based sensors for phosphate,[42] or changes in absorption or emission upon binding e.g copper-based sensors for citrate.[43] These often exploit the heavy atom effect leading to fluorescence quenching or excitation to a triplet state, allowing them to be monitored by changes in fluorescence or fluorescence lifetime. However, these can suffer interference from other heavy atoms commonly found in the body, such as I^-.

In order to showcase the applicability of these interactions, the first example is highlighted to show how these interactions can be used for biological applications. In a recent study by Rhaman *et al.*, a copper-based thiophene macrocycle (Figure 1.20) was employed for the sensing of citrate through an indicator displacement assay, demonstrating how metal based interactions can be employed for anion recognition.[43] By complexing the pre-organised copper containing probe **22** with the indicator Eosin-Y, an visual enhancement in emission intensity upon the addition of citrate in water at pH 7 was observed upon Eosin-Y displacement, providing a more selective response over other tested guests (oxalate, glutamate, phosphate, adipate, tartrate, AcO^-, BzO^-, F^-, Cl^-, Br^-, I^-, ClO_4^-, NO_3^- and SO_4^{2-}). Cytotoxicity studies in human fibroblast cells indicated that the **22**-Eosin-Y complex has low cytotoxicity indicating potential biological applications. Additionally, this provided the opportunity for the construction of a calibration curve to determine citrate concentration in water. By employing this strategy, it is clear that using a metal-indicator displacement probe is a viable route for anion detection, suggesting that this route may also be used for the detection of other anions.

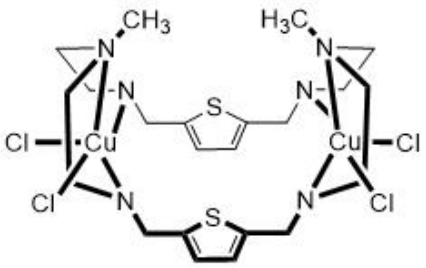

22

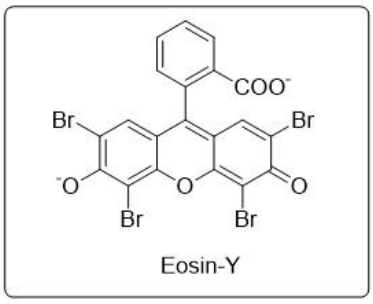

Figure 1.20: Copper(II) based probe for citrate detection and indicator structure.

The next example shows that these metal based interactions can be applied to species (such as phosphates) which compete with SO_4^{2-}, providing a potential pathway for SO_4^{2-} recognition.[44] A squaramide was asymmetrically substituted with a dipicolylamine (DPA) group and an ethylpiperazine (Figure 1.21) and complexed with Cu(II) to form **23**, with coordination conformation determined through DFT calculations. Receptor **23** exhibited different pH dependent Cu(II) species in aqueous solutions, with different Cu(II) complexes binding to different phosphate species, including AMP, ATP and ADP. To confirm Cu(II) complexation, NMR studies were performed in both DMSO and H_2O:D_2O (9:1 v/v) to elucidate the portions of the ligand involved in Cu(II) complexation, confirming coordination by both the DPA and ethylpiperazine motifs. This was further confirmed using UV-vis spectroscopic studies performed in 3-(*N*-morpholino)propanesulfonic acid (MOPS) buffer, with a change in absorbance upon Cu(II) addition to **23**. Potentiometric studies performed in aqueous KNO_3 yielded non-selective binding, with a profile of $PhP^{2-} < AMP < Haep^{-} < ADP^{3-} < HPPi^{3-} < ATP^{4-}$. While the receptor was water soluble, the minimal change observed through optical methods makes this less effective for applications, as potentiometric studies are more time consuming in comparison to absorption or emission based studies.

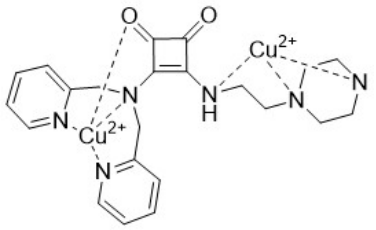

23

Figure 1.21: Asymmetric squaramide Cu(II) complex for phosphate recognition.

A zinc complex (**24**) has been used for Cl^- recognition,[45] with receptor design including a macrocyclic tetra-amine attached to a fluorescent pyridyl-oxadiazole-phenyl (PyPD) group *via* a short linker as depicted in Figure 1.22. Upon forming the $[ZnL]^{2+}$ complex **24**, photoinduced electron transfer (PET) is inhibited leading to fluorescence turn on. The receptor binds to zinc through interactions with both pyridine groups and the amine pendant arm, and the Zn-PyPD pyridine bond broken upon Cl^- introduction resulting in turn-off of fluorescence, with the system being selective to Cl^- over other tested anions (F^-, Br^-, I^-, OAc^-, HSO_4^-, $H_2PO_4^-$ and NO_3^-) in MeCN. Cl^- did not fully quench the fluorescence of **24**, but there was a hypsochromic shift to a longer wavelength in emission which could be used for the ratiometric sensing of Cl^-. The receptor could be regenerated and reused by addition of Ag(I) ions leading precipitation of AgCl. This study was performed in MeCN, meaning steps would need to be taken to use this in aqueous systems such as further functionalisation with water-solubilising groups. This example shows that metal based sensors can be used for selective anion sensing, and the sensor can be regenerated for re-use.

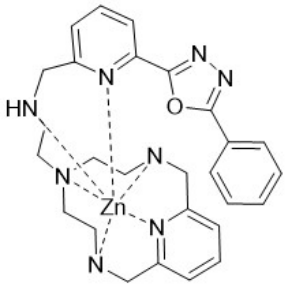

24

Figure 1.22: Zn(II) complex for subsequent chloride detection.

The selected examples above illustrate that MA interactions can provide an effective methods for anion recognition. However, no such examples currently exist for SO_4^{2-} sensing. Metals can be added to a system to modulate a property, such as changing fluorescence emission or changing NMR chemical shifts. These metal sensors can then bind to a desired anion, with a resultant change in the desired property acting as a marker for guest binding. Commonly used metals include Cu(II) and Zn(II), and these metals remain bound to the receptor upon anion addition, which may result in a selective sensor. Due to the changes in optical properties upon metal binding, there is basis for exploiting these MA interactions for other anions such as SO_4^{2-}.

1.4 Sulfate specific probes in complex aqueous mixtures

As can be seen *vide supra*, the task of developing selective receptors is a difficult one and is plagued by many challenges. This section will focus on receptors for binding to anions, with a narrow focus on binding in aqueous media and preferably complex aqueous mixtures. Aqueous media typically includes a mixture of an organic solvent, typically MeCN or DMSO, as these solvents help to minimise water out-competing the receptor by binding to the anion. This also ensures that the host molecules remain in solution and allow for accurate determination of concentration as many receptors are not completely soluble in water. The ideal receptor will have size and shape complementarity for the desired anion, be

water soluble, and be able to form a large number of binding interactions with anions. However, synthetically this is often not achievable. This portion focuses on receptors for SO_4^{2-} which specifically function in these aqueous systems.

The first example shows that while SO_4^{2-} recognition in water is possible, a synthetically complex macrocycle may be needed to achieve strong binding. The tetrakisimidazolium macrocycle **25** was developed which had remarkably high affinity and selectivity for SO_4^{2-} in 10 mM HEPES at pH 7.4 (Figure 1.23).[46] This was due to C-H hydrogen bond donors pointing into the macrocycle with the diglyme arms contributing to the overall number of interactions by folding over the anion, and the positively charged imidazoliums resulted in charge assisted interactions to SO_4^{2-}. The inner cavity of the macrocycle also had good size complementarity to SO_4^{2-} and π-π stacking stabilised the resultant complex. Compound **25** was selective to SO_4^{2-} even in the presence of other anions (ClO_4^-, NO_3^-, HCO_3^-, $H_2PO_4^-$, SCN^-, Br^-, Cl^- and I^-) and was found to have a K_a 8.6 x 10^9 M^{-2} in a 2:1 stoichiometry in water. Binding of SO_4^{2-} was determined by fluorescence but the change in emission was not very large, which is not beneficial for anion detection as there is less ability to distinguish between background signals.

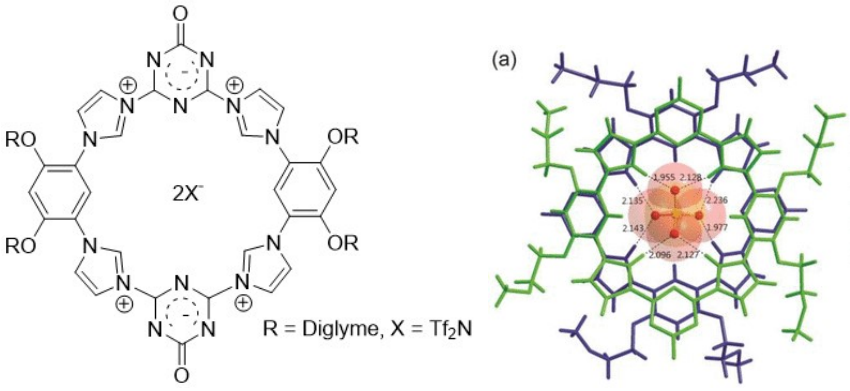

25

Figure 1.23: Tetrakisimidazolium macrocycle for SO_4^{2-} recognition in 100% water and **25**:SO_4^{2-} crystal structure. Reprinted with permission from Journal of American Chemical Society.[46]

The next example shows that size complementarity for a guest can also be induced using strapped systems to encapsulate a guest, providing a different structural pathway for guest recognition. The benzenebistriazole-strapped calix[4]pyrrole **26** was designed to bind to anions using both C-H HB donors from the triazoles and N-H donors from the pyrrole as confirmed through NMR studies (Figure 1.24).[47] This increases the number of potential electrostatic interactions, leading to higher affinities for tested anions. The calix[4]pyrrole was designed with a "strap", with size complementarity to a guest tuned by varying the "strap" length. With this design, SO_4^{2-} can be encapsulated in a hydrophobic pocket, limiting solvation effects and avoiding the effects of increasing water content. Through UV-vis spectroscopy titrations with **26** performed in 1% H_2O:DMSO, the binding trend and $LogK_a$ values were found to be SO_4^{2-} (6.50) > $H_2PO_4^-$ (6.00) > AcO^- (5.81) > Cl^- (5.60) > Br^- (3.80) » I^- > NO_3^- > ClO_4^-. While the affinity for SO_4^{2-} was high, the receptor also exhibited low overall selectivity, suggesting that the use of this "strap" can increase the strength of the binding interaction, but does not modify selectivity.

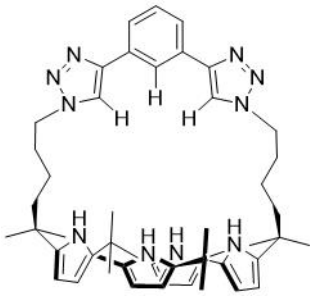

26

Figure 1.24: Strapped calix[4]pyrrole for non-selective SO_4^{2-} detection.

Building upon previous work shown by Jia *et al.*,[27] tripodal hexaurea receptors with varying substitution patterns (**27a-c**) were developed to extract SO_4^{2-} from water using liquid-liquid extraction (LLE).[48] These tripodal ligands (Figure 1.25) can fold in and encompass SO_4^{2-} through 12 HB. A combination of size complementarity of the inner cavity, and contributions of C-H—π interactions resulted in

strong binding to SO_4^{2-} (10^5 M^{-1}). Receptor **27a** bearing electron withdrawing *p*-nitrophenyl substituents extracted 95% SO_4^{2-} from water, but when electron donating groups are used, as in **27b** and **27c**, the amount of SO_4^{2-} extracted decreased (86% and 78% respectively) as confirmed through ion chromatography. This variation in extraction was attributed to enhanced acidity of the urea N-H proton of **27a**, priming the urea motif for anion binding, suggesting that the nature of the substituent plays a role in extraction and binding applications.

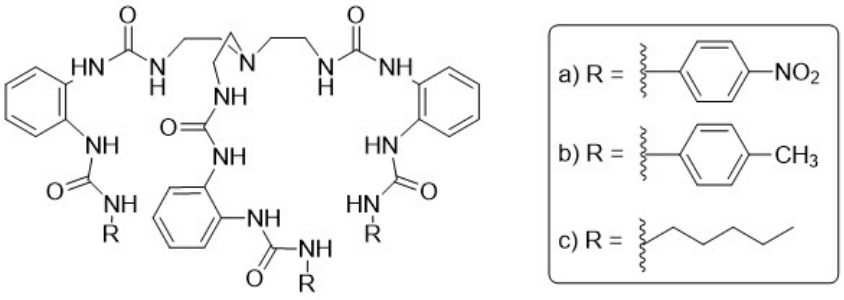

27

Figure 1.25: Tripodal hexaurea receptors for SO_4^{2-} extraction.

As can be seen, the recognition of SO_4^{2-} in complex mixtures is a difficult challenge to overcome. Most receptors are functional only in a small percentage of water and suffer lower affinities as the water content increases. There have been minimal studies on recognition of SO_4^{2-} in complex mixtures, such as biological samples or sea water, severely limiting the application scope of these sensors.

1.5 Assays for SO_4^{2-} Recognition

In addition to receptors that directly bind to anions, a number of alternative approaches to anion sensing have been developed. These include Indicator displacement assays (IDA), in which an indicator is bound to the receptor and can be displaced by the anion, leading to a colorimetric or fluorescent change. Indicator displacement assays still require that the receptor provides suitable binding interactions with the anion of interest to ensure complex formation of the receptor and anion. Another approach is Metal extrusion assays (MEAs), which work on

the principle of chelation of a ligand to a metal, with the metal displaced upon anion binding. By appending a chromophore, these system can be monitored by UV-vis or fluorescence spectroscopy. One benefit of MEAs is that direct binding of the anion is to a metal cation, rather than a tailored receptor. This may lessen synthetic complexity, as the required number of interactions for strong receptor-anion binding do not need to be introduced into the receptor structure. Both IDAs and MEAs can be utilised in the recognition and quantification of guests, as the change in response can be correlated to the guest concentration *via* a calibration curve. This is useful as often only one analyte may induce a response.

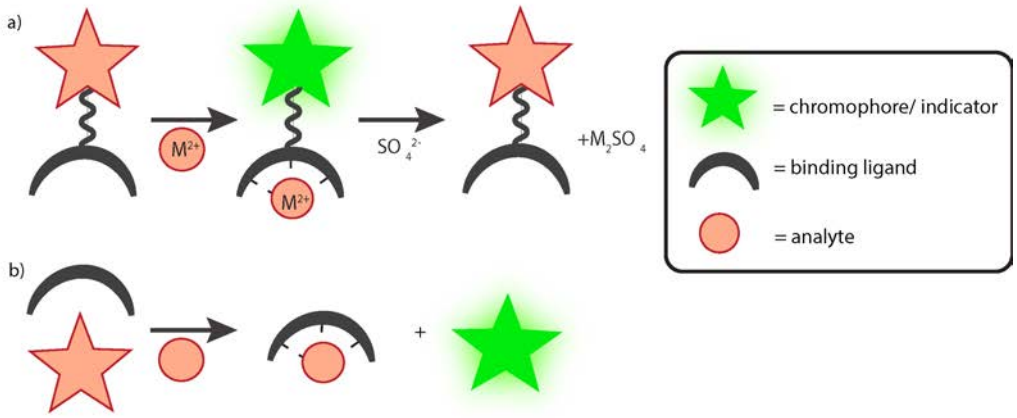

Figure 1.26: Generalised scheme showing some main assays for anion recognition. a) Metal Extrusion Assay (MEA), b) Indicator Displacement Assay (IDA). Red star indicates a quenched chromophore or fluorophore, while the green star indicates a fluorophore which has had a change in it's optical property.

Two IDA systems for SO_4^{2-} sensing which have been reported previously rely on squaramide hosts and show that this approach can be used for analyte quantification.[49] The first example uses a linear squaramide which was methylated to form the iodide salt **28** to improve solubility when compared to the non-alkylated product, while also providing a source of charged-based interactions between the charged host and the charged indicators and SO_4^{2-}. Two indicators, Cresol Red (CR) and Bromocresol Green (BG) were used in IDAs with **28** in 96% EtOH:H_2O. These indicators exist in different protonation states based on pH, so the relevant studies are performed below the pKa at apparent pH values. The

28-BG complex was found to be more selective but less sensitive for SO_4^{2-} over HPO_4^{2-} with binding resulting in both a visible colour change and a change in the UV-vis spectrum. By utilising the **28**:CR complex, linear calibration curves were constructed to quantify SO_4^{2-} concentrations from 0 − 120 ppm, and a combination of the **28**:CR and **28**:BG complex were used to quantify both SO_4^{2-} and HPO_4^{2-} in water samples with reasonable agreement compared to IC.

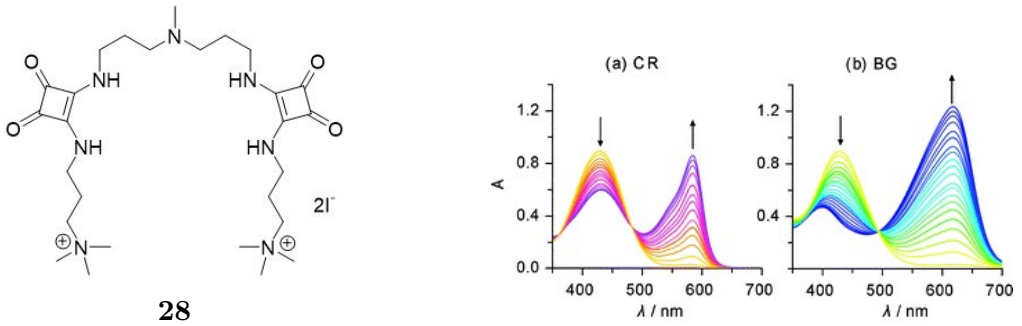

28

Figure 1.27: Linear TMA squaramide iodide salt and responses to CR and BG in 96% EtOH:H_2O. Reprinted with permission from New Journal of Chemistry.[49]

Additionally, the next example indicates that these can be performed using fluorescence spectroscopy to provide an alternative mode of sensing. Fluorescein disodium salt (FNa_2) was used as the indicator, with complexation to the macrocyclic host **29**, resulting in quenched fluorescence attributed to PET from the squaramide donor to FNa_2. The receptor is designed with the squaramides imparting rigidity in the macrocycle, and charge repulsion provided by the quaternary ammoniums yields a rigid, bow shaped receptor containing four directional hydrogen bond donors. The addition of SO_4^{2-} to the **29**:FNa_2 complex resulted in a turn on in emission in 9:1 MeOH:H_2O. This system was then used for the recognition of SO_4^{2-} from 0 − 200 ppm upon mixing with an incoming water stream.[50]

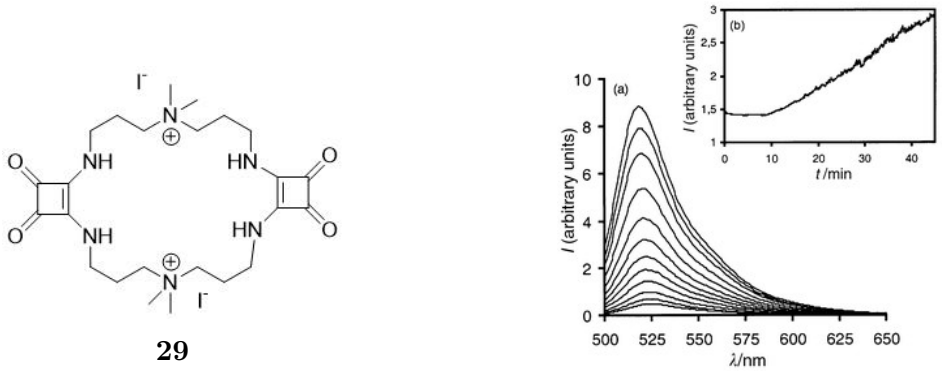

Figure 1.28: Cyclic TMA squaramide iodide salt and response to FNa_2 in water. Reprinted with permission from Chemical Communications.[50]

As observed in these examples, IDAs can be used as an effective tool for $SO_4{}^{2-}$ recognition. The IDAs used can be UV-vis spectroscopy based, in which there can be selective recognition in the presence of competing guests, or through Fluorescence spectroscopy. The responses generated from these assays can be used to generate statistical calibration curves, and be used as a tool to quantify levels of $SO_4{}^{2-}$ in systems.

While IDAs[51–53] and intramolecular indicator displacement assays (IIDAs which are a variation of IDA)[54,55] have been used for guest recognition, MEAs have been developed for anions such as phosphates. The majority of examples involve the use of transition metals, commonly Zn(II), Cu(II) or lanthanides as the metal centre.

The first example of an MEA for guest recognition shows that MEAs can be employed for colorimetric sensing, showcasing their utility. The dinuclear Zn(II)-azophenine **30** was used in a MEA for $H_2PO_4{}^-$ detection through visible colour change.[56] In 9:1 MeCN:H_2O, complex **30** (Figure 1.29) only exhibited a colour change from red to yellow upon $H_2PO_4{}^-$ addition, with this colour change not observed for CN^-, Br^-, F^-, I^-, $HSO_4{}^-$, OAc^-, $BF_4{}^-$, $NO_3{}^-$ and $N_3{}^-$. Upon phosphate introduction, the Zn(II) is released to form a zinc salt and the free ligand (metal free receptor) is released, as demonstrated *via* mass spectrometry

studies and NMR studies. This was applied to $H_2PO_4^-$ detection in bovine serum as well as binding to DNA phosphates, demonstrating that this method could be applicable in biological settings.

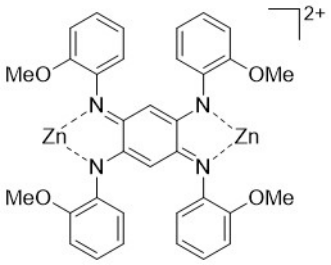

30

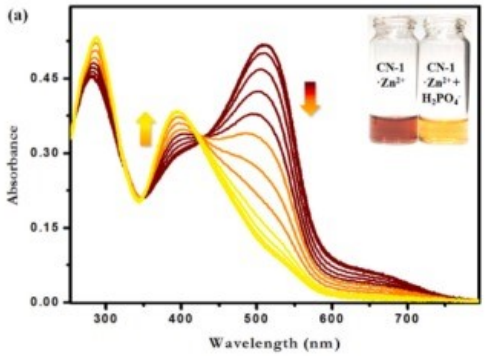

Figure 1.29: Azophenine Zn(II) complex for naked eye phosphate detection and resultant colour change upon $H_2PO_4^-$ addition to the Zn(II) complex. Reproduced with permission from Inorganic Chimica Acta.[56]

This potential to use MEA for colorimetric sensing is also explored in this next example, in which a mononuclear Zn(II) complex **31** with 2,2'-dihydroxyazobenzene was also used for $H_2PO_4^-$ detection.[57] The molecule has two forms (azo and hydrazone as presented in Figure 1.30), with π-π^* transitions observed in the UV-vis spectrum. Upon Zn(II) addition to **31** in 1:1 MeOH:H_2O (aq. 10 mM pH 7.5 HEPES), there was a decrease in the π-π^* band correlating to both forms with concomitant colour change from yellow to orange together with the appearance of a new longer wavelength peak ascribed to chelation enhanced fluorescence (CHEF). This was reversed upon $H_2PO_4^-$ addition, due to the formation of a zinc-phosphate species with release of the ligand as confirmed by UV-vis spectroscopy. Using fluorescence detection, the anion binding profile varied, with a turn-off response in fluorescence observed for $H_2PO_4^-$ and a weaker turn-off response observed for SO_4^{2-}, while CN^- induced a turn on fluorescence response, suggesting less selectivity through fluorescence spectroscopy. The colorimetric response is desirable for applications such as biological recognition as it allows for 'naked eye' determination of a binding event. While the receptor is not selective,

the significant variation in fluorescence turn-off could be used to identify $H_2PO_4^-$ and SO_4^{2-}.

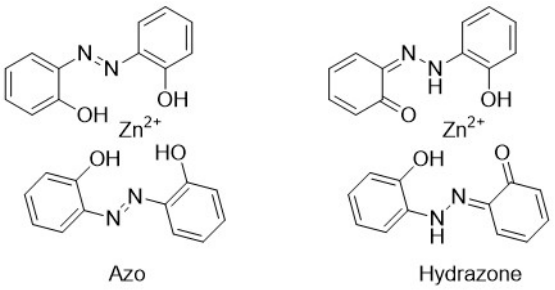

31

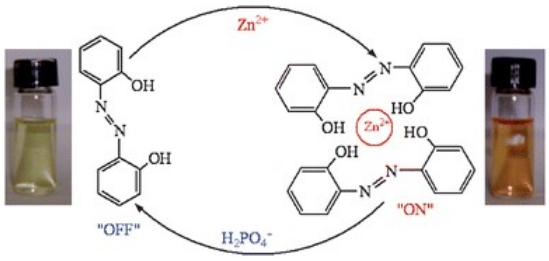

Figure 1.30: 2,2'-dihydroxyazobenzene Zn(II) complexes for phosphate recognition as presented in both forms and colour change upon $H_2PO_4^-$ addition. Reprinted with permission from Royal Society of Chemistry.[57]

The next example shows that this technique can be used for selective anion recognition in a competitive solvent system. A benzimidazole-Cu(II) complex **32** has been used for $H_2PO_4^-$ detection (Figure 1.31).[58] Due to its paramagnetic properties, Cu(II) complexation to **32** induces a turn-off fluorescence response which can be reversed upon anion introduction. Other transition metals (Zn(II), Co(II), Fe(III), Ni(II) and Hg(II)) induced quenching of **32**, however the change was greatest with Cu(II). Other metals, which were Ba(II), Ca(II), Cd(II), Ag(I), Mg(II), Na(I) and K(I) did not induce a change in emission. The addition of $H_2PO_4^-$ to the Cu(II) complex induced an enhancement in emission, as a result of the generation of the free ligand as confirmed through fluorescence spectroscopy. This displacement was selective for $H_2PO_4^-$, as no response was observed for F^-, Cl^-, Br^-, I^-, CN^-, HSO_4^-, NO_3^-, $HClO_4^-$, AcO^- and $P_2O_7^{4-}$, with these experiments performed in DMSO:10 mM aq. HEPES (7:3).

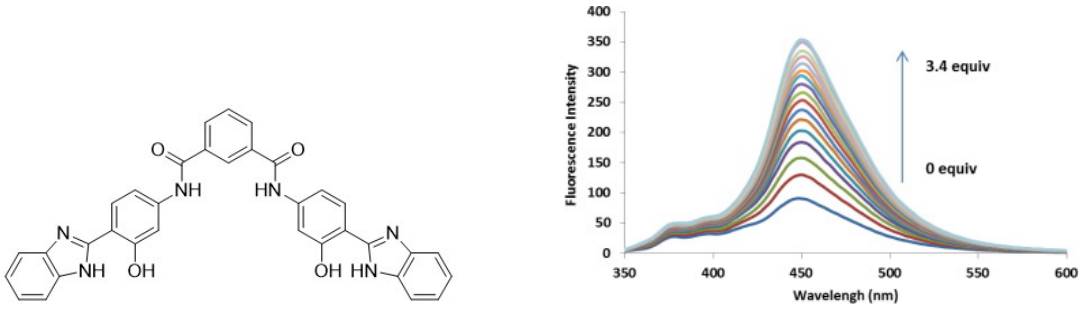

32

Figure 1.31: Benzimidazole receptor for Cu(II) complexation and fluorescence response upon phosphate addition to Cu(II) complex. Reprinted with permission from Tetrahedron Letters.[58]

The next example shows that this technique can be applied for anion quantification in biological fluids. A Cu(II)-based sensor (Figure 1.32), in which a dansyl fluorophore was attached to a geminal *N*,*N*-(ethoxy carbonyl methyl)-ethylenediamine to act as the Cu(II) binding site, was used for selective phosphate recognition.[59] Studies were performed in 5:1 MeOH:1 mM aq HEPES (pH 7.4), with Cu(II) addition to the free ligand resulting in visible quenching of emission, which did not occur with the other transition metals tested (Zn(II), Ag(I), Cr(III), Mn(II), Fe(II), Ni(II), Co(II)) and common metals (K(I), Na(I)). Phosphate addition caused extrusion of the Cu(II) to form $Cu_3(PO_4)_2$ and led to an increase in emission intensity, similar to that of the free ligand. ^{1}H NMR studies also showed that phosphate addition to the Cu(II) complex resulted in an identical spectrum to the free ligand. This was applied to phosphate quantification in human saliva, urine and chicken serum.

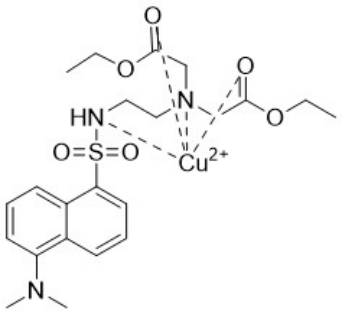

33

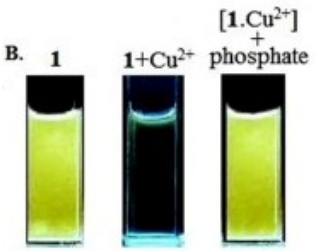

Figure 1.32: Dansyl ethylenediamine receptor for Cu(II) complexation and inorganic phosphate detection and observed responses. Reprinted with permission from Tetrahedron Letters.[59]

This technique can be employed using metals containing unique emission profiles to expand the range of applicable metal sensors as shown in the final example by utilising lanthanide complexes. Eu(III) was complexed with three tetradentate β-diketone ligands (**34** – **36**) with varying substituents (Figure 1.33).[60] The R_1 substituents were fluorinated to different degrees (comparing **34** to **36**) while the R_2 substituents varied in electron withdrawing power (**34** vs **35**). The studies were performed in a cetylpyridinium bromide (CPB) micellar solution at pH 7.2 using both UV-vis spectroscopy and luminescence. Selectivity and sensitivity varied depending on the substitution, with **34** displaying no discrimination between ATP, PPi, ADP and citrate. Receptor **36** was selective to PPi, while **35** exhibited discrimination between citrate and multi-phosphate species. While not selective, it can still be used to identify similarly sized phosphates and carboxylates. Receptor **36** was used to detect PPi in water containing 100 mM of NaCl and KCl, 10 mM of $CaCl_2$ and $MgSO_4$, 0.1 mM of $Fe(NO_3)_3$ and $ZnCl_2$, 1.0 mM of $NaHCO_3$ and NaH_2PO_4, 0.1 mM L-glutamine, and 1.0 mg/mL BSA, while **35** was used to monitor the Mg(II) dependent assay of PPi hydrolysis by pyrophosphatase.

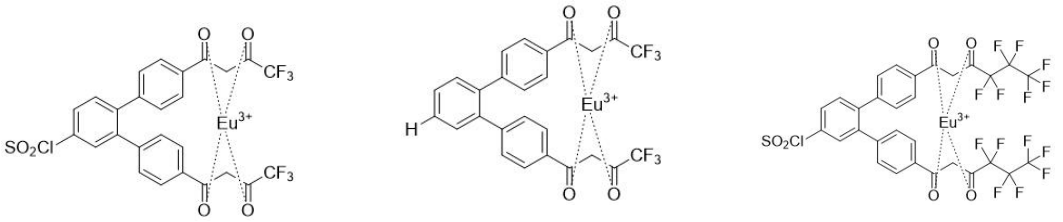

34 **35** **36**

Figure 1.33: Diketone Eu(III) complexes with varying R groups for phosphate detection.

There are relatively few studies of MEAs for anion sensing. Most contain Cu(II) or Zn(II) as the metal, and so far applications have been limited to phosphate and carboxylate sensing, while there are currently no MEA for SO_4^{2-}. The detection of SO_4^{2-} in complex aqueous systems is an ever present challenge that needs to be overcome to realise applications, such as quantification in biological or environmentally relevant samples. While assay based mechanisms are a valuable tool, MEA have not been previously used for SO_4^{2-} detection, severely limiting the current library of SO_4^{2-} recognition mechanisms.

To address this issue, MEAs can be developed for SO_4^{2-}. To induce precipitation of SO_4^{2-} from solution, a metal which forms an insoluble salt can be utilised. Additionally, for MEA use in biological samples, the metal should be present in low concentrations in the body, with a suitable option being Ba(II). To develop the MEA, the metal needs a suitable ligand, and the ligand should be directly attached to a fluorophore to allow for spectroscopic monitoring of metal extrusion. In order to determine a suitable ligand for metal binding, the following section focuses on metal recognition to inform assay design.

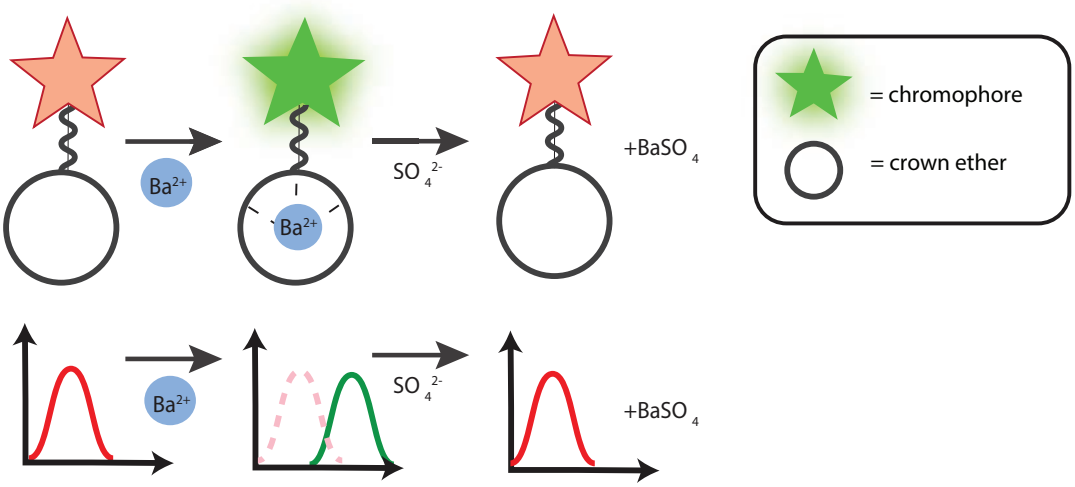

Figure 1.34: Proposed MEA set-up.

1.6 Group 1 and Group 2 Metal Recognition Using Crown Ethers

Numerous recognition motifs have been designed for selective detection of cations. Cations are easier to sense than anions, due to their highly charge dense nature, increasing the strength of electrostatic interactions. While there have been studies aimed at achieving selective recognition of transition metals and lanthanides, the recognition of alkali and alkali earth metals should also be explored. Ca(II) is one of the most important targets, as it plays a role in neurotransmission and is essential to bone health. Sr(II) and Ba(II) are similar to Ca(II), and can act as a bone strengthener and muscle relaxant respectively.[61] Some metals can also act as surrogates for radioisotopes, such as Ba-133 acting as a surrogate for Ra-223.[62] Li(I) is often used in batteries,[63] and K(I) is essential for cell signalling and nutrient transportation.[64]

Crown ethers (Figure 1.35) are a unique class of receptors which are capable of metal binding. They were first discovered by Charles Pedersen in the 1960's and contain repeating units $(CH_2CH_2O)_n$, where n is the number of units. Crown ethers are named using the convention: number of atoms in the macrocycle-crown-number of heteroatoms (e.g 12-crown-4). These crown ethers (CE) were found to

have exceptional metal binding properties, such as high affinities for K(I), Na(I) or Li(I).[65] Crown ethers can be modified by introducing other heteroatoms into the repeating units, creating classes of receptors such as triazacyclononane (TACN) and cyclen. A mixture of heteroatoms can be incorporated, such as in the case of aza-crown-ethers (Aza-CE), and/or the macrocycle can be functionalised such as in the case of benzocrown ethers. Crown ethers have uses in phase transfer catalysis, ion selective electrodes and aiding in metal salt dissolution.[66] Their unique solubility properties arise from the ability to expose either the hydrophilic oxygen atoms or the lipophilic ethylene atoms, allowing them to be soluble in both organic and aqueous solvents.[67]

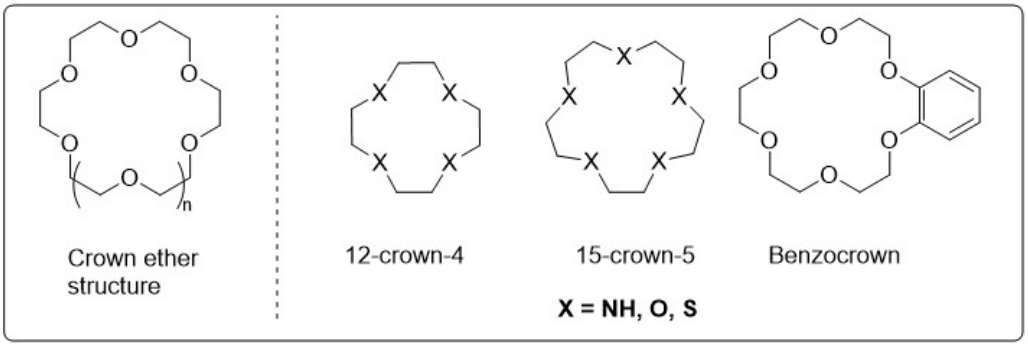

Figure 1.35: General structures of various crown ethers.

Aza-CE and their derivatives can be synthesised (Figure 1.36) in a range of ways, with the most common approach involving macrocyclisation *via* reaction of the desired tosyl-protected diethanolamine with an oligoethylene glycol ditosylate using a strong non-nucleophilic base, typically NaH. This yields the protected macrocycle, which can be deprotected using acid cleavage or reduction. The ring size can be modified by using different starting material lengths. The synthesis can also be modified to introduce a range of heteroatoms. Additionally, the diethanolamine can be modified with a range of groups, such as desired functional groups to modify the properties of the resultant macrocycle.[68] While there is a robust breadth of information on the synthesis of Aza-CE, the parent Aza-CE are readily commercially available, allowing for ease of receptor synthesis through further modification.

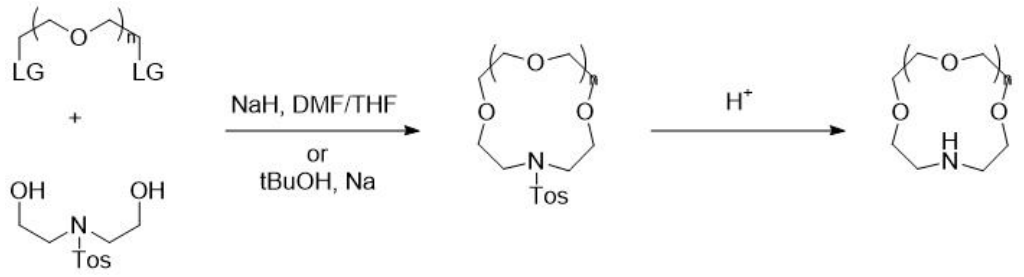

Figure 1.36: General synthetic scheme to access Aza-CE (LG represents leaving group).

There are many factors which can affect the binding properties of CE and Aza-CE to metals. The heteroatoms comprising the ligand play a role in binding, as Aza-CE containing mostly oxygen atoms are known to bind stronger to alkali metals, while Aza-CE containing all nitrogen atoms are known to bind strongly to heavy/transition metals, which correlates with HSAB theory.[68] Additionally, conformational changes, such as those seen in substituted di-aza-CE (Figure 1.37) may also influence the binding properties to metals, which may be further influenced by amine substitution.[69] While these factors play a role in metal binding, the cavity-size relationship, the macrocyclic effect, and the thermodynamic effect, play a more important role in metal binding by CE and Aza-CE.

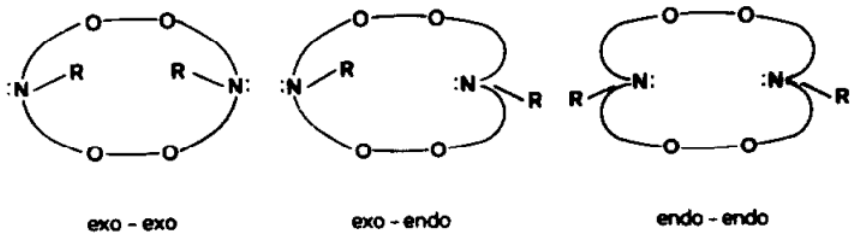

Figure 1.37: Different conformations of di-Aza-CE as determined by Buschmann. Reproduced with permission from ScienceDirect.[69]

To selectively bind to a cation, the size of the macrocycle cavity should complement that of the target cation. In terms of intrinsic preference, M(I) or M(II)-crown interactions are favoured for cations with a close match to cavity size. As the cavity of the macrocycle increases, larger cations can fit better in the cavity. The cavity size of mono-aza-18-crown-6 is $\simeq$ 0.27 nm, priming it for strong binding to larger cations like K(I), which has a hydrodynamic radius of 0.14 nm. The

relative inner radii of the common Aza-CE macrocycles are shown in Table 1.2. Notably, incorporation of additional nitrogen atoms results in a slight increase in cavity size. If a cation is very large relative to the macrocycle (cation radii presented in Table 1.3), multiplex formation (2:1 complex) can occur, and if a cation is smaller than the macrocycle, there are distortions in the shape which make binding energetically unfavourable,[70] with these distortions increasing as the metal size decreases.[71]

Table 1.2: Cavity sizes of Aza-CE.[70]

Aza-CE	**Cavity size (nm)**
Mono-aza-18C6 ether	0.268
Di-aza-18C6 ether	0.278

Table 1.3: Ionic radii of various cations.[8]

Cation	**Ionic radius (nm)**
Li(I)	0.071
Mg(II)	0.070
Na(I)	0.097
Ca(II)	0.103
Sr(II)	0.125
K(I)	0.141
Ba(II)	0.149
Cs(I)	0.173

For Aza-CE, binding to different metals has been analysed using theoretical calculations with the size-hole relationship explored.[70] B3LYP was exploited to investigate 1:1 binding with Ca(II), Sr(II) and Ba(II) to aza-crown ethers ranging from no nitrogen atoms up to hexaaza-18-crown-6 ether. For cations in which the ionic radius was too small for the cavity, the crown ether adopted a distorted conformation, where it was "cupping" the metal which was presented for hexaaza-18-crown-6 ether. For Ba(II) with hexaaza-18-crown-6 ether, the crown was completely planar, indicating a good size match between the metal and ligand showing the conformation upon binding to a suitably sized cation. Ba(II) also had the lowest change in energy between the 1:1 complex and the free aza-CE. It was noted that the stability of the resultant metal complexes increases as the number of nitrogen atoms in the ligand increases, which was attributed to greater

degrees of charge transfer between metal and ligand, however this was not further explored.

Computational studies of di-Aza-CE were used to explore selectivity for a range of group(I) metals.[72] Di-aza-18-crown-6 ether was computed to have several stable, low energy conformations were determined through computational calculations. The neutral ligand has C_{2h} symmetry, with the oxygen and nitrogen atoms alternating pointing up and down, with the N-H protons pointed in to the cavity in different conformations, consistent with [69]. It was determined that the depending on the cation size, di-aza-18-crown-6 presents different conformations, with cations larger than the inner cavity distorting the ligand and the cations are coordinated above the plane, as opposed to being coordinated in the centre of the ligand (Figure 1.38). The strength of this ML interaction decreases as cation size increases due to the poor size match to the metal. This shows a cation-size dependence of binding to di-aza-18-crown-6, with larger cations resulting in lower stability complexes.

Figure 1.38: Calculated conformations of di-aza-18-crown-6 upon formation of a complex with K(I) (yellow ball) and the larger Cs(I) (green ball). Reproduced with permission from ScienceDirect.[72]

Aside from size complementarity between the crown ether and the cation, another factor to consider is the macrocyclic effect, which describes the increase in stability constant of cyclic ligands compared to linear analogues. When comparing the relative stability constants of linear vs cyclic chains, the macrocycle will have a larger stability constant. The exact cause of the macrocyclic effect is contested,[66] but it is clear that both enthalpy and entropy contribute to this effect.

A study using isothermal titration calorimetry suggests that the macrocyclic effect is enthalpically driven.[73] In MeOH, the $LogK_a$ for K(I) for 18-crown-6 was 6.06, compared to the linear pentaglyme ($LogK_a$ 2.1) while the $LogK_a$ for Ba(II) for 18-crown-6 was 6.70, compared to $LogK_a$ 2.3 for the linear pentaglyme, showing an increase in stability between linear and macrocyclic analogues. The affinity of both the linear pentaglyme and 18-crown-6-ether for metals can be decreased by increasing the percentage of water in the solvent system, leading to an entropically favoured response upon metal desolvation. Complexation of Ba(II) to 18-crown-6-ether exhibited a greater macrocyclic effect, as the higher solvation energy of Ba(II) made complexation more entropically favoured.

The stability of the metal complex can also be altered by modifying the macrocycle, as shown by the higher affinity of thio-crown-ethers for transitions metal compared to the oxygen containing counterparts.[74] Additionally, stability of group (II) metal complexes can be tuned *via* substitution of both nitrogen atoms in 1,10-diaza-18-crown-6-ether. In this case, the functionalisation of the nitrogen atoms with oxygen containing substituents at both the 1- and 10-position was shown to increase affinity for Ba(II), Sr(II) and Ca(II) when compared to the un-substituted 1,10-diaza-18-crown-6-ether. This could reasonably arise from a greater number of interactions to the metal centre as a result of these substitutents. Conversely, bulky substituents resulted in lower $LogK_a$ values for Ba(II) and Sr(II) when compared to the un-substituted 1,10-diaza-18-crown-6-ether, suggesting that substituent can impact the overall metal complex stability..

Ultimately, crown ethers and their analogues provide a suitable option for selective binding of alkali and alkaline earth metals. These binding processes have been shown to induce conformational changes, which may may contribute to selectivity. This can also be affected by the size of the cation relative to the macrocycle cavity size,[67] solvent polarity, and the charge of the cation itself.

1.6.1 Receptors For Metal Recognition

Attachment of a crown ether or aza-crown ether to a fluorophore or chromophore can provide sensors for metal ions as a donor-acceptor system. In a recent example, naphthalimide aza-crown ether receptors (Figure 1.39) were developed for alkali metal binding.[75] Naphthalimide was employed as the fluorophore due to it's relatively high quantum yield (dependent on substituent)[76] and large Stokes' shift.[77] PET was determined to act as the primary sensing mechanism, and the receptors **37**, **38** and **39** all had selective responses to Ba(II) through fluorescence spectroscopy. Receptor **37** exhibited a turn-on response to Ca(II), Cu(II), Cd(II), Hg(II), while **38** exhibited a turn-on response for Ag(I), Cu(II) and Cd(II). Additionally **39** showed a turn-on response for Ag(I), Ca(II), Zn(II)and Cd(II). In all cases, the largest degree of turn-on was observed for Ba(II). Fluorescence spectroscopy studies performed in MeCN with Ba(II) yielded LogK_a of 6.14, 6.23 and 6.12 for **37**, **38** and **39** respectively. NMR studies indicated that the α-protons of the nitrogen atoms in the ligand did not interact with Ba(II) for **38** and **39**, while the same study indicated minimal interaction of the metal with the naphthalimide fluorophore. This shows that using substituted Aza-CE can provide higher selectivity for one metal (Ba(II)) over others with a high binding affinity.

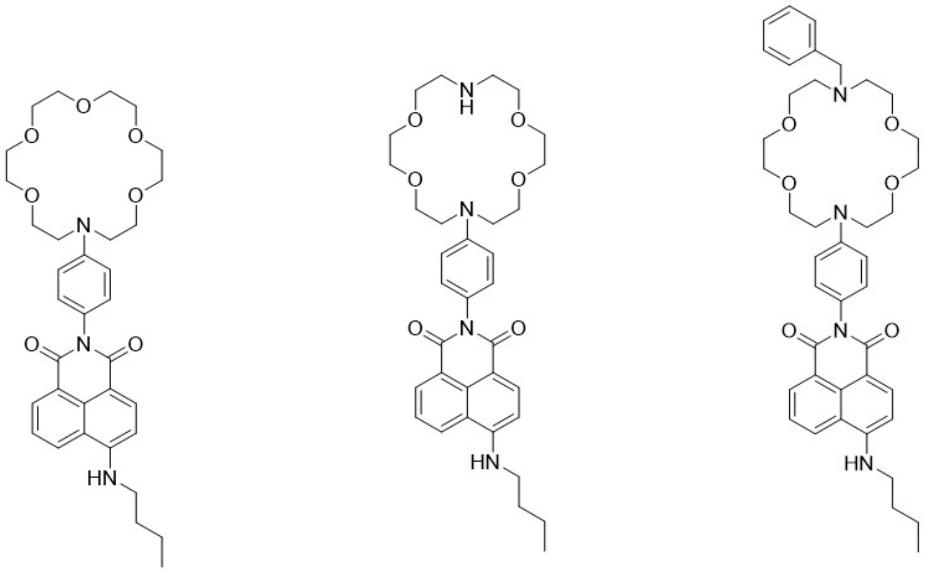

37 **38** **39**

Cation	Receptor	LogK$_a$
Ba(II)	**37**	6.14
	38	6.23
	39	6.12

Figure 1.39: Aza-18-crown-6-ether naphthalimide receptors for Ba(II) and corresponding LogK$_a$ values in MeCN (λ_{ex} = 430 nm, λ_{ex} = 530 nm.)

The next example shows that metal binding can occur in water, however selectivity limitations arise. A nitrobenzofurazan (NBD)-TEMPO-di-aza-18-crown-6-ether receptor **40** was developed (Figure 1.40) for non selective group(I) metal binding, with the aim to examine the properties of this pro-fluorescent free radical.[78] Using a combination of MS, EPR, NMR and luminescence in water, the response of **40** to group (I) metals (Na(I), K(I), Li(I) and Cs(I)) was found to be non-selective with a turn-off in fluorescence, however no K$_a$ values were reported. It was determined *via* NMR in DMSO-d_6 and $CDCl_3$ that the receptor underwent slight solvent dependent conformational changes. TEMPO addition did not alter the photophysical properties, as expected due to the lack of conjugation to the fluorophore, suggesting that it may not be a viable route for fluorescent radical sensing due to no electronic communication between the sensing ligand and the fluorophore.

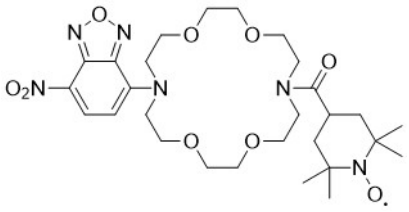

40

λ_{abs} **(nm)**	λ_{ex} **(nm)**	λ_{em} **(nm)**	$\Delta\lambda$ **(nm)**
344, 492	350, 500	548	48

Figure 1.40: TEMPO functionalised NBD di-aza-18-crown-6-ether and photophysical properties determined in DMSO.

It has been suggested that Ba(II) may act as a secretagogue (an agent which promotes secretion) of Ca(II) in cell studies, so a redox active water soluble di-aza-18-crown-6-ether receptor **41** was developed.[79] This sensor (Figure 1.41) was found to have a non-selective response to Ba(II), Mg(II), Ca(II) and K(I), binding all four cations in a 1:1 binding stoichiometry. This was confirmed through UV-vis spectroscopy in water (with a decrease in absorbance) with a binding profile and LogK_a of Ca(II) > Ba(II) (4.9) > Mg(II) (4.5) > K(I) (3.9), showing no clear correlation between cation size and affinity. NMR and electrochemical studies were used to confirm conformational rearrangement of **41** upon Ba(II) complex formation. This suggests that there may be some conformational variation as a result of Ba(II) binding in this di-aza-18-crown-6-ether receptor.

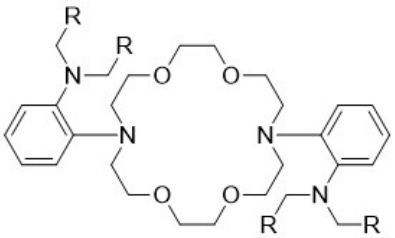

R = $CO_2^-Na^+$

41

Figure 1.41: Acetate functionalised di-aza-18-crown-6-ether (λ_{abs} = 263 nm).

The next example indicates that strong binding for metals can be achieved

through formation of more complex binding stoichiometries. Compound **42** exploited E/Z C=N isomerism as the mechanism for the recognition of Ba(II).[80] While **42** (Figure 1.42) was not selective for Ba(II), the probe exhibited higher sensitivity to Ba(II) through fluorescence spectroscopy when compared to other metals. This was confirmed using competition studies of **42**-**M** complexes (where **M** = Sr(II), Ca(II), Mg(II), Li(I), Na(I), Mn(II), Fe(II), Co(II), Ni(II), Cu(II), Zn(II), Cd(II), Hg(II) or Pb(II)), in which the addition of Ba(II) resulted in a turn-on response after Ba(II) addition. Titrations of **42** with Ba(II) in MeCN indicated formation of a 1:2 ligand:metal complex with a Logβ 7.04. Monitoring the increase in emission upon metal addition in a competition study indicated a seven fold turn on for Ba(II), which was the largest turn on for all complexes studied. No rationale was provided for the observed Ba(II) sensitivity, however this binding could be attributed to potential receptor conformations leading to sandwich formation.

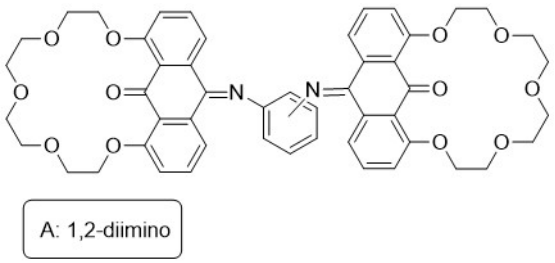

42

Figure 1.42: Anthracenone imine receptor for Ba(II) (λ_{ex} = 356 nm, λ_{em} = 520 nm).

This complex formation can be modified by changing the ligand size, as shown in the next example. Receptor **43** was developed containing two aza-15-crown-5 ethers binding sites bearing a thieno[2,3-*b*]thiophene to form a sandwich complex with Ba(II).[81] By using the smaller aza-15-crown-5 ether (Figure 1.43), Ba(II) was forced to bind in a sandwich complex, as it could not fit within the cavity. This receptor functions by inhibition of PET quenching to detect Ba(II) resulting in a turn on in fluorescence. A LogK_a of 5.3 for Ba(II) in MeCN was determined in 1:1

binding, with the largest CHEF turn-on emission response observed for Ba(II) in comparison to the response of **43** with K(I), Na(I), Li(I), Mg(II), Ca(II), Sr(II), Ni(II), Mn(II), Co(II), Cd(II) and Hg(II). This suggests that strong selective binding can arise from a poor size match to the cation in a sandwich structure.

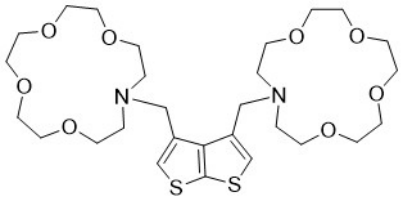

43

Figure 1.43: Thieno[2,3-*b*]thiophene receptor for Ba(II) (λ_{ex} = 300 nm, λ_{em} = 370 nm).

Selective water soluble sensors for metals can be developed, however require greater synthetic difficulties to access these as shown in the next example, such as cryptands and lariat ethers. In an example from Nakahara *et al.* (Figure 1.44),[82] an aza-cryptand bearing a pyrene signalling unit was synthesised to generate a PET-based sensor. While the ligand did not provide a response upon addition of Ba(II) in water, upon incorporation of **44** into micelles, a selective response to Ba(II) was observed, with no turn-on response for Mg(II), Ca(II), K(I), Na(I), Li(I) and Rb(I). This suggests that the binding profile of similar receptors could be modified by micelle incorporation while maintaining water solubility.

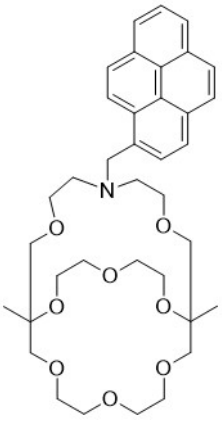

44

Figure 1.44: Pyrene functionalised monoaza-cryptand for selective Ba(II) recognition (λ_{ex} = 342 nm).

The next example was selected showing the difficulties in selective recognition of Ba(II) over K(I) due to cation size similarities. Coumarin receptor **45** bearing a hydrazone moiety appended to a 15-aza-crown-5 ether (Figure 1.45) was used for non-selective recognition of K(I) and Ba(II).[83] This receptor was hypothesised to work *via* inhibition of PET, however there is little conjugation between the fluorophore and the binding site, potentially leading to a different mechanism, with a limited response through UV-vis spectroscopy. In EtOH, the LogK_a values for K(I) and Ba(II) of 4.11 and 3.61 respectively. Although the smaller 15-aza-crown-5 was used, there was no evidence of a 2:1 complex formation in contrast to Wu *et al.* (receptor **43**).[81] However, this binding relationship was determined through Benesi-Hildebrand methods, which are considered to be outdated.[11] While this is a interesting step forward, having one smaller binding site clearly does not lead to selectivity, and intramolecular sandwich formation is better.[81]

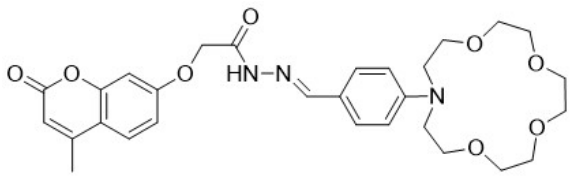

45

Figure 1.45: Coumarin functionalised monoaza-15-crown-5 for non-selective K(I) and Ba(II) recognition (λ_{ex} = 343 nm, λ_{em} = 406 nm).

The next example further highlights the effects of binding ligand cavity size and the effect this has on selectivity. A systematic study was performed on metal recognition by boron dipyrromethene (BODIPY)-benzo crown ethers (Figure 1.46) by varying the size of the crown ether.[84] No response was observed to metal ions in the excited state through UV-vis spectroscopy, while metals which did not have a suitable radius compared to the cavity radius induced a bimolecular fluorescence quenching. As expected, in MeOH the benzo-15-crown-5 **46** had a selective response only to Na(I) with LogK_a of 4.91 due to the cavity size match to the metal, while benzo-18-crown-6 **47** bound less selectively but most strongly to K(I) (LogK_a 5.99), Ba(II) (4.96) and Rb(I) (4.70), as determined by an increase in fluorescence intensity. The change in fluorescence enhancement was not directly correlated to affinity, and this work was applied to 'naked-eye' detection of K(I) showing the effect of crown ether size on selectivity.

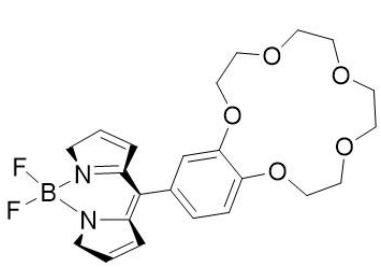

46

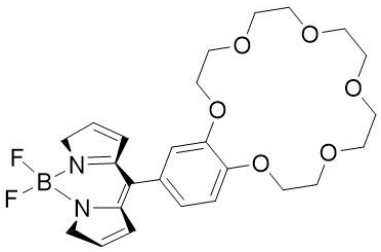

47

Receptor	Cation	LogK$_a$
46	Na(I)	4.91
47	K(I)	5.99
	Ba(II)	4.96
	Rb(I)	4.70

Figure 1.46: BODIPY functionalised benzocrowns for alkali metal recognition and corresponding LogK$_a$ values in MeOH (λ_{ex} = 475 nm, λ_{em} = 514 nm).

The next examples shows that cation recognition can occur using colorimetric methods. Naked eye detection of Ba(II) was performed using a 2,2'-bianthracene-15-aza-crown-5 receptor **48** (Figure 1.47).[85] By forming a sandwich complex, internal PET was inhibited leading to a turn on of fluorescence. The response was greatest for Ba(II), with other alkali metals producing only a slight response compared to Ba(II), with the Ba(II) complex having the greatest LogK$_a$of 5.83, orders of magnitude greater than the other metals. Receptor **48** was then used for naked eye detection under UV light, where only Ba(II) was visible. No group (I) metals were tested, so it is unclear if this selective response is maintained in the presence of other metals. This is an interesting step forward in developing receptors for visible metal detection, suggesting that sandwich complex formation may be a viable route.

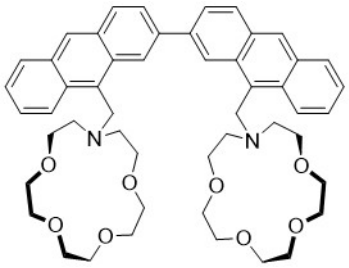

48

Figure 1.47: Bianthracene sandwich receptor for Ba(II) (λ_{ex} = 365 nm, λ_{em} = 462 nm).

Further naked eye detection has also been performed using a tris(bipyridinium crown ether) **49** as a donor-acceptor system in Figure 1.48.[86] Upon addition of Ba(II) to **49**, the solution changed from yellow to colourless, which was attributed to intramolecular charge transfer. The response was stronger for group (II) metals compared to group (I) metals, presumably due to the divalent charge, creating stronger electrostatic interactions. NMR titrations showed peak broadening only in the case of Ba(II) addition, attributed to stronger interactions of **49** to Ba(II) compared to Li(I) and K(I). While NMR titrations were only performed with these three metals, emission studies indicated that **49** was more sensitive to Ba(II) when compared to Li(I), Na(I), K(I), Rb(I), Cs(I), Mg(II) and Ca(II). This again opens the door for uses of colorimetric sensors. Given the incorporation of benzo-15-crown-5 rather than a larger crown that is better size matched to Ba(II), it is likely that the tripodal sensor forms a sandwich like structure upon Ba(II) addition, similar to those above.

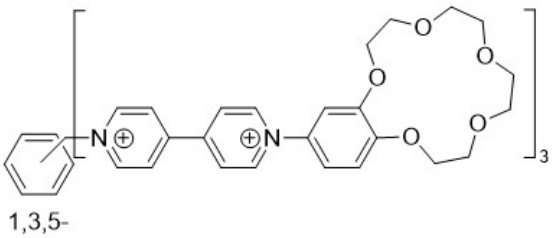

49

Figure 1.48: Tripodal colorimetric sensor for visible detection of Ba(II) (λ_{abs} = 450 nm).

This visual response is further explored in the next example. **50** and **51** have been developed containing an aza-crown ether functionalised naphthalene diimide (NDI) (Figure 1.49) for the visible discrimination of K(I) and Na(I) with varying crown cavity sizes.[87] Compound **50** displayed a visible response to Ca(II) (K_a 3750 M^{-1} in EtOH), however a large excess (> 2000 eq) of Ca(II) was required to detect a visible response, while **50** was more sensitive through fluorescence spectroscopy, requiring 75 eq Ca(II) to completely inhibit PET quenching. Receptor **51** was more sensitive, only requiring 50 eq of either K(I) and Na(I) to induce a response, with LogK_a values of 5.14 and 4.78 in EtOH respectively. DFT modelling was performed, and determined that **50**-Ca(II) complex formation resulted in cation interactions with both the Aza-CE and the NDI carbonyl groups. In comparison, **51**-K(I) was found to undergo a distortion of the binding ligand, preventing this interaction between the guest and the NDI core. Ultimately, **51** is desirable as a colorimetric sensor. Given the ability to functionalise the NDI core, it would be valuable to expand this space and generate more visible sensors for alkali metals.

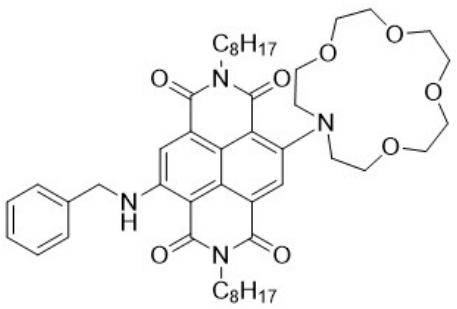

50

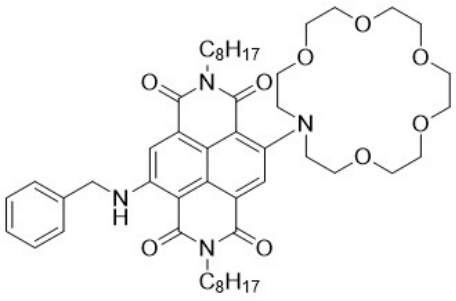

51

	λ_{abs} **(nm)**	ϵ	λ_{em} **(nm)**	ϕ_y
50	595	12500	639	0.01
50-Ca(II)	550	-	639	0.09
51	597	13900	643	0.01
51-K(I)	522	-	643	0.01

Figure 1.49: Aza-crown ether functionalised NDI receptors and respective photophysical properties in EtOH.

There is growing interest in the development of selective Ba(II) sensors due to their potential application in neutrino decay detection *via* decay of xenon to

Ba(II). Receptor **52** (Figure 1.50) was developed[88] containing *N*-anthryl-1-aza-18-crown-6-ether for dry phase sensing of Ba(II). NMR titrations with **52** and Ba(II) indicated that all heteroatoms in the ligand participated in binding to the metal. Similar studies with a pyrene fluorophore were unsuccessful due to excimer formation at the required concentrations. Addition of Ba(II) to a solution of **52** in 10:1 aq Tris (20 mM):MeCN resulted in a K_d of 16 mM.

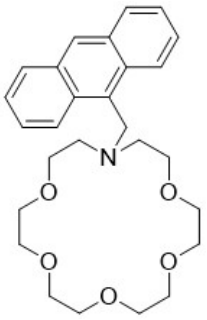

52

Figure 1.50: Anthracene receptor for dry-phase Ba(II) sensing (λ_{ex} = 367 nm, λ_{em} = 417 nm).

The next study was examined as information regarding conformational changes upon M(I) addition was explored. Similar anthracene based molecules were explored by Witulski *et al.*,[89] where the 10-cyano-9-*N*-anthryl-aza receptors **53** and **54** were explored (Figure 1.51). Upon addition of metals to a solution of **53**, a turn-on response due to ICT inhibition was observed, with K_a for Li(I) (1000 M^{-1}), Na(I) (110 M^{-1}) and K(I) (16 M^{-1}) in MeCN. Upon addition of metal to a solution of **54**, a turn-on response was observed, with with K_a for Li(I) (190 M^{-1}), Na(I) (9500 M^{-1}) and K(I) (710 M^{-1}) in MeCN. Crystal structures of both receptors (**53**-Na(I) and **54**-K(I)) indicated a conformational change upon complexation, with interactions occurring between the cation and the oxygenated portion of the macrocycle, providing an insight into the binding mechanism of aza-crown-ether receptors with metals.

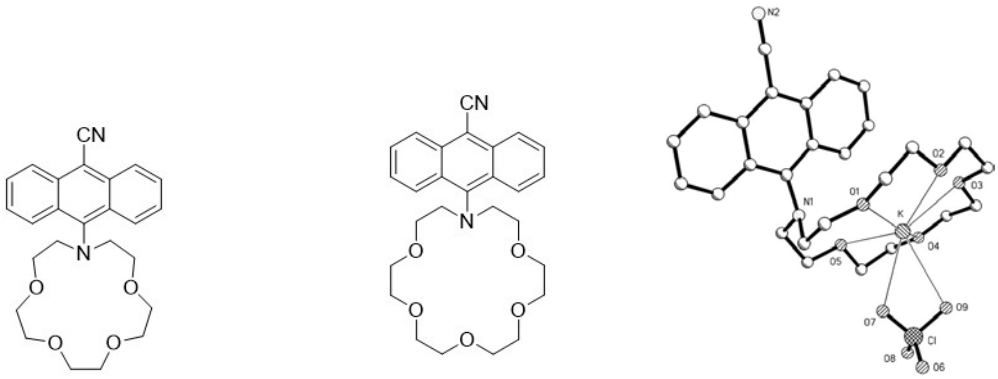

53 **54**

	λ_{em} **(nm)**	ϕ_y	τ **(ns)**
53	585	0.03	2.2
53-Li(I)	545	0.03	1.8
53-Na(I)	580	0.03	2.8
53-K(I)	585	0.03	2.5
54	570	0.09	2.9
54-Li(I)	555	0.05	3.1
54-Na(I)	540	0.12	3.7
54-K(I)	548	0.08	3.2

Figure 1.51: Cyano-anthracene receptors for alkali metal sensing and crystal structure of **54**:K(I) and respective photophysical properties. Reprinted with permission from Organic Letters.[89]

Another example showcases potential impacts of pH on metal binding. The anthracene receptor **55** containing two binding sites was developed[90] with a benzocrown and an aza-crown binding site (Figure 1.52). It was observed that the general emission profile of the receptor and the quantum yield varied based on pH. Titrations of **55** with a range of metals in MeOH yielded LogK_a for Li(I) (1.18), Na(I) (2.87), K(I) (4.80), Rb(I) (4.10) and Cs(I) (3.45). It was observed that the fluorescence intensity of **55** was higher in acidic conditions, with greater degrees of quenching in basic conditions ascribed to greater degrees of PET. Under basic conditions, the largest degree of turn-on emission was observed upon formation of the **55**-K(I) complex, while in acidic conditions this was observed upon formation of the **55**-Na(I) complex, indicating a change in binding profile with pH.

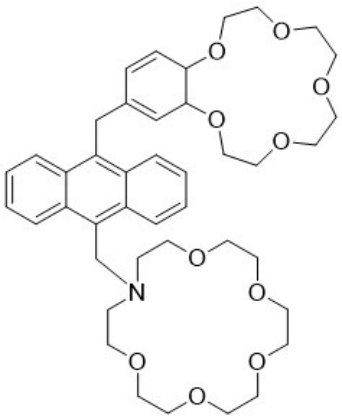

55

	Free	**Li(I)**	**Na(I)**	**K(I)**	**Rb(I)**	**Cs(I)**
55	0.048	0.060	0.053	0.39	0.31	0.12
55+$\mathbf{H}^+$	0.060	0.098	0.55	0.26	0.22	0.15

Figure 1.52: Dual motif anthracene receptor for non-selective metal recognition and respective ϕ in basic and acidic MeOH (λ_{ex} = 376 nm).

The next example shows that the sandwich structure can be formed, with a receptor utilising a styryl-benzocrown (Figure 1.53) used to detect metals.[91] A sandwich complex formed upon the addition of Ba(II) to **56**, with the cation complexed with the benzocrown portion. This binding mode was different when compared to that formed with either Hg(II) or Cd(II), in which the cation was complexed with the pyridine portion, with Ba(II) and Mg(II) inducing a modulation in both the UV-vis spectrum and the fluorescence spectrum upon 2:1 complex formation. In MeCN, the LogK_a values were 5.98 for the **56**-Mg(II) complex and 10.62 for the **56**-Ba(II) complex, with these complexes having a reduced fluorescence lifetime compared to the free ligand. Given the difference in binding mechanism between the transition metals and group (II) metals tested, this showcases a unique receptor design for metal recognition.

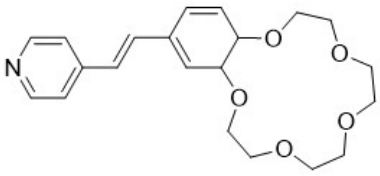

56

Compound	λ_{abs} (nm)	λ_{em} (nm)	ϕ_y	τ (ps)
56	330	408	0.01	49
56-Mg(II)	317	384	0.0073	17
56-Ba(II)	319	407	0.0094	24

Figure 1.53: Styryl-benzocrown for non-selective metal recognition and corresponding photophysical properties.

There are a range of other receptors which have also been used for metal recognition, including a receptor based on heteroleptic iridium cores,[92] as in the case of a remarkably selective receptor for Mg(II). K(I) can be discriminated over Na(I) by using an anthryl azacrowncalix[4]arene in CH_2Cl_2,[93] while a ruthenium based 1-methoxyanthraquinone receptor was developed using 18-crown-6-ether as the ligand for recognition of Ba(II), Sr(II) and Ca(II), with a binding order of Ba(II) » Sr(II) » Ca(II) confirmed through spectroscopic studies and NMR analysis.[61] Calixcrowns were also used for Ba(II) recognition and radionuclide Ba-133 extraction, however selectivity was not tested and the lack of a substantial chromophore limited the applications to higher energy UV-vis spectroscopy.[62] Additionally, a coumarin 1-aza-18-crown-6-ether was found to exhibit selectivity to Ca(II) over other group (I)/group (II)/transition metals in a non polar solvent (MeCN).[94] It has also been shown that a 1-benzo-15-crown-5-ether appended with 1-naphthaleneacetamide can detect Mg(II) with higher sensitivity than other alkaline earth metals, despite having a lower binding affinity for Mg(II) compared to Ca(II), Sr(II) and Ba(II) as a result of conformation rearrangements.[95]

Sensors developed for metals utilising crown ethers are often not selective, with interference from other metals. However, these examples above highlight multiple parameters that can be modified to modulate metal binding selectivity for crown ethers and aza-crown ethers, including the cavity size, heteroatom variation and

the further functionalisation of the aza-crown-ether core. While these factors can be altered to introduce some degree of control of the selectivity of these receptors. There are additional complications which arise during binding events, in which the observed response (emission profile, UV-vis absorbance profile or NMR response) does not always correspond to the binding affinity of the receptor. While these issues are present, there still exist receptors containing these crown ether ligands which provide a selective response to alkali or alkaline earth metals, and these responses may be colorimetric or fluorimetric.[75,82,84,85,88]

Throughout the examples above, the focus has been predominantly on the selective recognition of Ba(II). This is because it is envisaged that Ba(II) complexes may be useful in further applications, such as metal extrusion assays for SO_4^{2-} recognition. This is due to the low solubility of the resultant barium salt, and to address the need of assay development for SO_4^{2-} detection.

1.7 Thesis Overview and Aims

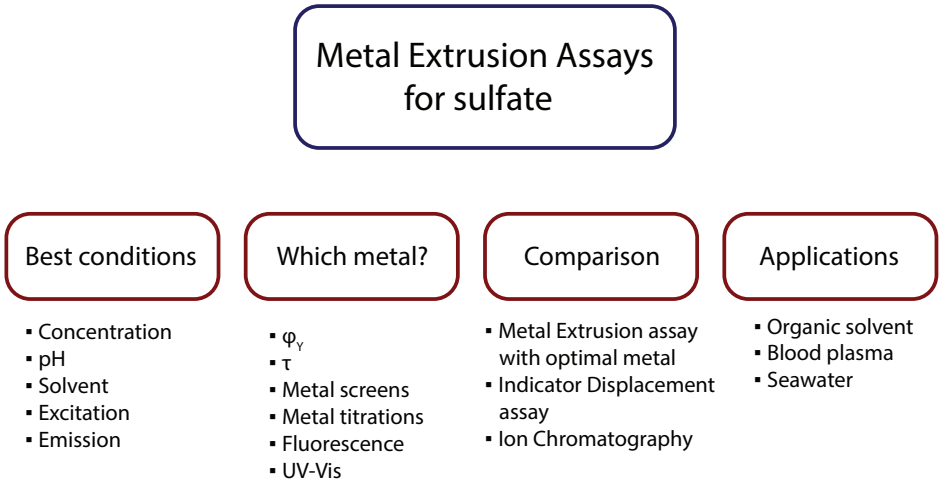

Figure 1.54: Overall aim of the thesis and sub-aims.

The overarching aim of this thesis is to develop systems which are able to quantify SO_4^{2-} concentrations in complex/aqueous solutions. This has been investigated using several approaches. These approaches include the use of HB receptors containing squaramides as SO_4^{2-} receptors in IDAs, and the use of MEAs using Ba(II) complexes containing 1-aza-18-crown-6-ether. These MEA

systems first required an understanding of Ba(II) complexation processes using a variety of sensing techniques. In order to achieve this aim, the thesis comprises of sub-aims as represented in Figure 1.54. The first aim is to determine optimal conditions for studying the MEA, including determining ideal concentrations, pH, solvent and excitation and emission. The next aim is to determine a suitable metal for the MEA, comprising of photophysical studies through UV-vis and fluorescence spectroscopy. The thesis then aims to compare the MEA to existing assays as well as Ion chromatography to evaluate the effectiveness of the newly developed MEA, while the final aim is to apply the MEA in a range of conditions.

To answer these aims, the synthesis of the studied receptors will be explored in Chapter 2, as well as the photophysical characterisation of these receptors prior to metal addition, in order to better understand metal complexation mechanisms. Chapter 3 explores this metal binding behaviour in more detail using photophysical studies to determine optimal metals for the MEA, while Chapter 4 provides a comparison between existing SO_4^{2-} detection methods to the MEA developed.

Chapter 2

Synthesis and Photophysical characterisation of receptors

2.1 Fluorescence Mechanisms

A number of photophysical techniques can be used for HG recognition, typically relying on fluorescence or UV-vis spectroscopy. Upon guest binding to a host molecule, the optical properties of probes can be modulated in a range of ways. Typically, a hypsochromic or bathochromic shift is observed, the intensity or absorbance may be modulated, while fluorescence responses can additionally be modulated through quenching or inhibition of quenching. Additionally, ratiometric responses may also be observed, or there may be a combination of changes such as concomitant intensity modulation and wavelength shifting. In the ideal host-guest system, this change is only observed for a single analyte, however often this is not the case.

There are additional mechanisms through which fluorescent systems may operate. Decay pathways can be influenced to increase or decrease the rate of exponential decay (termed fluorescent lifetime and denoted with τ). This value measures the time take for a photon to decay from $S_1 \rightarrow S_0$ (excited $\rightarrow$ ground state) through bond rotation or energy transfer, which can be affected upon guest complexation. There are also systems in which there is a change in the quantum yield (ϕ_y), which alters the brightness of the fluorophore either through a "turn-on" or a "turn-off" mechanism.

However, designing a probe suitable for guest recognition requires careful con-

sideration of the sensing environment. Sensors designed for guest recognition in biological media must have a suitable emission range, as many biological components including DNA and proteins absorb in the UV range (around 280 nm)[96] while haemoglobin absorbs from roughly 400 – 700 nm,[97] meaning an ideal sensor will have a $\lambda_{max} > 400$ nm in order to be distinguishable from biological components. Applying this to a fluorescent sensor, the ideal receptor should not have an excitation wavelength at 250 nm, as higher energy photons in the UV range have a greater probability of damaging biological molecules.

To understand the further requirements for a suitable optically active probe, the mechanism by which fluorescence and absorption occurs must be considered. Figure 2.1 shows a Jablonski diagram, used to illustrate relevant electronic transitions associated with chromophores. The diagram is arranged with the y-axis showing energy, which means that the energy gaps and subsequently emission wavelength shifts can be estimated. Each horizontal line indicates an eigenstate (energy level), with emission occurring from the lowest energy eigenstate. The most common states for traditional fluorophores are S_0, S_1 and S_1*, while molecules such as lanthanides can reach a triplet excited state (T). The solid lines pointing downwards indicate radiative transitions (photon release), while broken lines indicate non-radiative transitions, which often includes energy loss to the system, or intersystem crossing.

Absorption of a photon (solid blue arrow in Figure 2.1) results in a transition from an electron in the lowest energy S_0 state to a higher energy S_1* state. This occurs rapidly in the order of 10^{-15} s. Once in this excited state, an electron undergoes a non-radiative vibrational relaxation transition (solid yellow arrow in Figure 2.1) into a lower energy excited state (S_1), with energy loss to vibrations/rotations or to the system at roughly 10^{-10} s. Finally, photon emission occurs during the $S_1 \rightarrow S_0$ transition, resulting in a fluorescence response (solid green arrow in Figure 2.1). The ΔE from this process dictates the emission

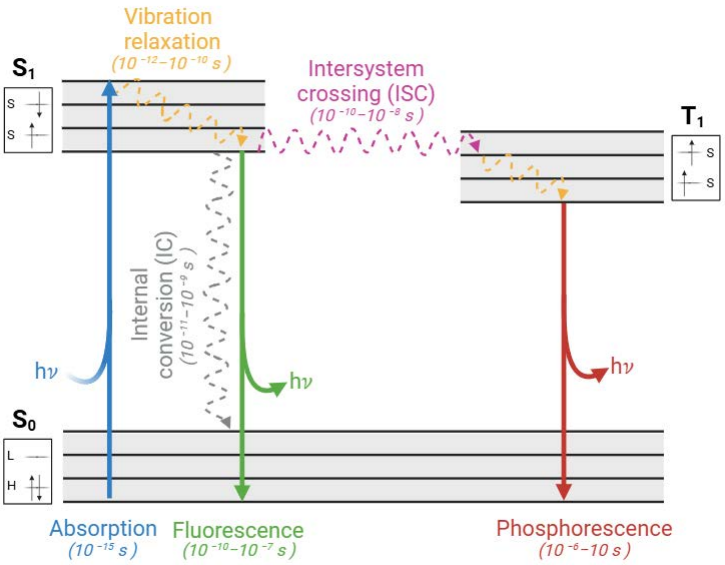

Figure 2.1: Jablonski diagram illustrating the main processes associated with fluorescence. Broken line arrows indicate non-radiative processes. Solid arrows indicate transitions associated with a simple system, while solid black lines indicate eigenstates.

wavelength, and gives rise to Kashas' rule indicating that fluorescence will occur from the lowest energy $S_1 \rightarrow S_0$.[98] Conformers by bond rotation may also have respective $S_1 \rightarrow S_0$ transitions at different wavelengths, due to processes such as intramolecular charge transfer (ICT) or twisting around bonds.

The difference in energy between absorption and emission is known as the Stokes' shift. As the electron decays from $S_1 \rightarrow S_0$, emission occurs with a defined HOMO-LUMO energy gap, resulting in a emission at a certain wavelength. Chemical modifications can be performed on the fluorophore to modify the HOMO-LUMO gap, thereby resulting in varied emission wavelengths and altered Stokes' shifts. For applications, the minimum Stokes' shift is around 50 nm.[99]

Fluorescent sensors for guests can operate through a range of mechanisms. The main mechanisms include chelation enhanced fluorescence (CHEF) or quenching (CHEQ), forster resonance energy transfer (FRET), photoinduced electron transfer (PET) and intramolecular charge transfer/twisted intramolecular charge

transfer (ICT/TICT). These mechanisms will now be explored in more detail.

Chelation enhanced fluorescence (CHEF) relies on the complexation of a non-redox active metal with a suitable metal binding ligand to produce an enhancement in fluorescence. Sensors using this mechanism are often used used for the recognition of heavy transition metals such as Cd(II), Zn(II), Al(III), Ni(II) and Hg(II), while CHEQ sensors designed for Cu(II) typically undergo quenching upon metal binding.[100] An example of a CHEF based sensor for guest recognition is presented in Figure 2.2,[101] in which **57** was utilised to image Hg(II) selectively in fibroblasts. The receptor only exhibited a CHEF response to Hg(II), Fe(II) and Zn(II), with no response observed for Li(I), Na(I), K(I), Cs(I), Mg(II), Ca(II), Ba(II), Cu(II), Ni(II), Co(II) and Cd(II) in MeOH/H_2O (9:1 v/v).

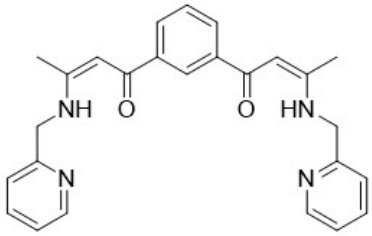

57

Figure 2.2: Molecular probe for Hg(II) imaging in fibroblasts.

Forster Resonance Energy Transfer (FRET) is classified as a through-space based interaction, in which energy transfer occurs between two fluorophores. The energy transferred is dependent on the distance between the fluorophores, which can be in different molecules. In the circumstance that analyte binding causes a positional shift of one fluorophore relative to the other, the FRET associated energy will also change, altering the emission spectrum.[102] FRET may produce a dual emissive response, in which the emission intensity of each fluorophore is modulated ratiometrically. An example of a FRET sensor used for analyte recognition is the quinoline-benzothiazole **58** containing a rhodamine fluorophore (Figure 2.3), which was used for the recognition of Cd(II) through live cell imaging.[103] Upon metal binding, the spiro ring of the rhodamine opens, resulting in a strong

emission attributed to FRET. Studies performed in 1:4 MeOH:aq HEPES (1 mM, pH 7.2) indicated that **58** was selective for Cd(II) (LogK_a 5.27) over K(I), Ca(II), Ni(II), Mn(II), Zn(II), Cu(II), Fe(III), Cr(III), Hg(II) and Pb(II).

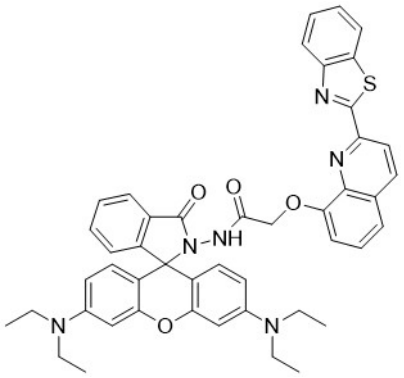

58

Figure 2.3: Rhodamine based FRET sensor for Cd(II) sensing.

Photoinduced electron transfer (PET) is the process by which electron transfer occurs between a lone electron pair on a molecule to a conjugated fluorophore. This typically occurs when a fluorophore is conjugated with an electron-rich substituent including amino- or mercapto functional groups. PET induces quenching of the fluorophore, and the fluorescence is restored upon binding of the electron pair to an analyte.[104] This can be altered by the introduction of a spacer, which will limit the effects of PET quenching. This approach was used in Hu *et al.*[105] who appended a thio-aza-crown-ether to a rhodamine fluorophore to give **59** (Figure 2.4), which was used for the fluorescent recognition of Ag(I) in MCF-7 cells. Fluorescence titrations in aqueous HEPES (20 mM containing 100 mM $NaNO_3$) indicated a turn-on response to metals, with LogK_a 5.66 for Ag(I), and 5.19 for Hg(II) and 5.16 for Cu(II).

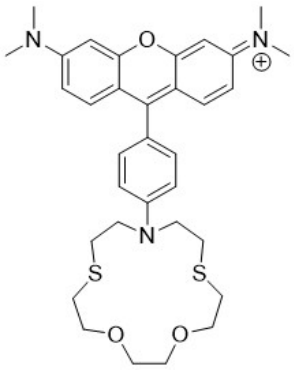

59

Figure 2.4: Rhodamine based PET sensor for Ag(I) sensing.

Finally, ICT and TICT rely on charge transfer (CT) between a charged donor (D) and a charge deficient acceptor (A). ICT relies on charge transfer in a conjugated system, and often occurs in combination with other mechanisms such as PET. TICT relies on bond rotation in a conjugated systen. In TICT, the typical emission state is referred to as the ^1L_b state, while the TICT emission band is referred to as the ^1L_a state,[106] and occurs in tandem with a D $\rightarrow$ A transition to produce an excited perpendicular state. This produces a dual emission type character arising from both the $S_1 \rightarrow S_0$ transition of the ^1L_b state, as well as lower energy transition from the ^1L_a state,[107] as represented in Figure 2.5, resulting in a darker state with lower luminescence.

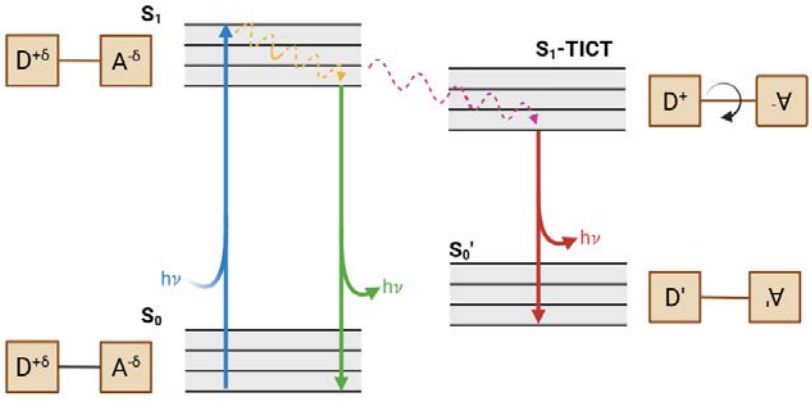

Figure 2.5: Jablonski diagram illustrating the main processes associated with TICT and the D-A conformations. Broken line arrows indicated non-radiative processes. Solid arrows indicate transitions associated with a simple system, while solid black lines indicate eigenstates.

An example of utilising this mechanism for guest recognition shows that the ICT state can be affected differently depending on the metal, in which Dash *et al*[108] used **60** (Figure 2.6) as an ICT sensor for metals. The response to metals varied, with Zn(II) resulting in a fluorescence colour change attributed to ICT inhibition ($LogK_a$ 5.57), while Ni(II) and Co(II) addition resulted in a complete quenching of emission ($LogK_a$ 4.44 and 3.20 respectively) through formation of ground state complexes. This is contrasted with the addition of Li(I), Na(I), Ca(II) ($LogK_a$ 2.84), Mg(II) ($LogK_a$ 3.11), Ba(II) and Cd(II) ($LogK_a$ 4.00) as calculated through fluorescence spectroscopy, for which no change in fluorescence was observed in MeCN. This was applied to the detection of Zn(II) in HeLa cells.

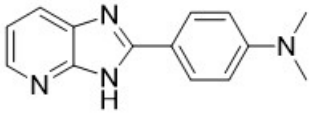

60

Figure 2.6: ICT based sensor for metals.

Ratiometric sensors which operate by multiple mechanisms can also be employed. These sensors yield dual emissive responses, either by containing two fluorophores (FRET), or by emission from two excited states. A ratiometric response, where the ratio of the two signals at different λ_{max} correlates to guest concentration, can be used for calibration and analyte quantification.[100] A recent example is found in Xu *et al.*[109], in which a calibration curve was generated for Cd(II) using a benzothiazole derivative **61** (Figure 2.7). Studies performed in DMF:H_2O:EtOH (1:1:98) indicated a response to Cd(II), Cu(II) and Ag(I), with Cd(II) complex formation producing a red shift in emission, while addition of Ag(I) and Cu(II) induced a turn-off response. There was no response to Zn(II), Al(III), Ga(III), In(III), Na(I), K(I), Mg(II), Ca(II), Ba(II), Pb(II), Cr(III), Hg(II), Fe(II), Fe(III), Mn(II), Co(II) and Ni(II). This receptor was used to image Cd(II) in A549 cells using fluorescence microscopy.

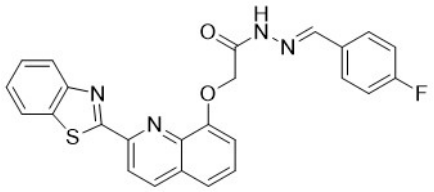

61

Figure 2.7: ICT based ratiometric sensor for Cd(II).

Finally, UV-vis based sensors which rely on changes in absorbance can be used for analyte recognition, and the changes may be in absorbance intensity or result in a change in wavelength. These sensors are typically less sensitive to analytes when compared to fluorescent sensors, requiring higher receptor concentrations that may increase the chances of aggregative effects.

It can be seen that there are a range of mechanisms which are present in optical based sensors, including using UV-vis absorbance and a range of emission pathways. To determine which mechanisms are at play or to exploit these for guest recognition, the photophysical characteristics of receptors should be elucidated, with these methods outlined below.

2.1.1 Methods for photophysical characterisation

In order to elucidate the photophysical properties of novel receptors, experiments must be performed to provide some insight into the potential fluorescence mechanism. Firstly, the excitation and emission responses need to be determined for use in subsequent experiments. The appropriate concentration also needs to be determined through dilution studies, which also determines any effects of aggregation. pH studies can be used to determine if charge transfer processes are occurring, and viscosity studies may be used to indicate if TICT is contributing. Finally, quantum yield (ϕ_y) and decay lifetimes (τ) are used to explore photon absorption efficiency and rate of excited state decay (the $S_1 \rightarrow S_0$ transition).

Firstly, ϕ_y is defined as the ratio of emitted photons to absorbed photons

and is related to decay from $S_1 \rightarrow S_0$ (Figure 2.1).[98] Fluorophores where ϕ_y approaches unity have the greatest emission, which may include fluorophores such as rhodamines and Alexa Fluor, but ϕ_y can be affected by substituents on the fluorophore, such as the introduction of electron donors which are capable of PET.[110] Additionally, -NO_2 substitution can increase non-radiative decay processes, leading to lower ϕ_y values. ϕ_y is solvent dependent, as low viscosity solvents can induce rotation (TICT), increasing non-radiative decay and increasing quenching. ϕ_y can be calculated using equation 2.1

$$\phi_y = \frac{\Gamma}{\Gamma + k_{nr}} \tag{2.1}$$

where k_{nr} = non radiative decay rate and Γ = fluorescence lifetime

There are two methods for the determination of ϕ_y, which are absolute and relative. Relative ϕ_y tends to be simpler to measure, requiring only a traditional fluorimeter, increasing ease of accessibility and reducing cost. Because fluorimeters are unable to measure all light emitted from a sample, in order to determine an accurate value of ϕ_y, a comparative standard is required, with that standard having almost identical optical properties to the novel molecule. Depending on the fluorophore, this may be difficult to obtain.

The determination of absolute ϕ_y requires a more complex experimental set up, and is typically performed using an integrating sphere. It requires no comparative standard, however the cost of the integrating sphere set-up is quite high. An integrating sphere is able to detect all emitted light as the light reflects off the inner surface to reach the monochromator.[111] Because of this, the absolute method is often the preferred route to determine ϕ_y, with Figure 2.8 demonstrating the optical principle involved in measuring ϕ_y.

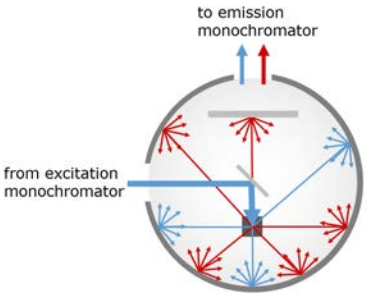

Figure 2.8: Diagram showing how an integrating sphere works for quantum yield determination.[112]

The fluorescent lifetime τ relates to the average length of time that the molecule spends in the excited state, and is presented as an exponential decay function. τ can be very small (in the range of picoseconds), but is typically in the nanosecond range for small molecules. τ can be in the form of mono-exponential decay, indicating a singular transition, or multi-exponential, indicating more than one excited state decay process. The value of τ gives an indication as to if there are multiple decay processes, as smaller values indicate faster decay, attributed to multiple non-radiative transitions. τ is measured using a single wavelength excitation source (diode), however cost limitations prevent the ability to excite every sample with the exact required wavelength. After excitation by the diode, the time of is decay measured and lifetime calculated. In order to remove the response of the instrument, an instrument response function (IRF) is measured under the same instrumental set up, to allow for signal de-convolution of the decay function. Equation 2.2 shows the equation to calculate fluorescence lifetime.[98]

$$\tau = \frac{1}{\Gamma + k_{nr}} \tag{2.2}$$

Where

k_{nr} = non radiative decay rate and τ = fluorescence lifetime

Excitation-emission matrices (EEM) and excitation/emission spectra are a useful technique for determining photophysical properties. The EEM is an in-

strumental techniques which generates information as to the presence of multiple structures, including conformers or impurities. An EEM is obtained by scanning the emission at a range of λ_{ex}, generating a 3D heat map. From this, the λ_{ex} corresponding to a λ_{em} is rapidly determined. If multiple species are present in solution, a multi-emission profile may be observed.

A simpler version of this is simply measuring the 2D excitation and emission spectra. This is useful to determine if multiple species are present, as multiple species will produce a varied emission profile as the λ_{ex} is changed. If one species is present in solution, changing the λ_{ex} will only result in a decreased emission intensity. While the λ_{ex} related to the $S_1 \rightarrow S_0$ transition, the intensity relates to the efficiency of both the excitation and emission transition efficiency. While EEM is a useful technique, it is typically performed as an initial starting point to determine the λ_{ex} and λ_{em} values, which must be confirmed by excitation and emission studies.

Dilution studies are a suitable approach to determine if there are effects on emission as a result of aggregate formation. This is typically required for fluorophores containing aromatic regions, as these can participate in π-π stacking, which can lead to modulations such as aggregation induced emission (AIE), quenching or excimer formation as is seen in the case of pyrenes.[113] Therefore, it is important to determine if these effects may arise throughout a fluorescence experiment. Aggregation may arise through solvent variation, and is concentration dependent.

To determine if aggregative effects are present, a solution of the desired solvent is titrated with increasing concentrations of the receptor molecule. Each aliquot is thoroughly mixed and the emissive response measured. Aggregation is often characterised by the presence of a broad, long wavelength emission signal, and the intensity of this signal increases linearly with the main emission signals. The absence of this indicates that aggregation is not playing a role in the emission

mechanism.

In order to determine the effects of PET induced quenching, pH studies can be performed if a protonatable group is present e.g a free amine. As the lone electron pair in this group can donate charge to the fluorophore to induce quenching, protonation of this group will prevent this process. pH studies are performed by slowly changing the pH of a receptor solution and measuring the absorbance and emission at each pH value. After measuring this response, the absorbance or emission at λ_{max} can be plotted against pH and fit to a sigmoidal Boltzmann function to extract the pK_a. Ideally, a greater ϕ_y at a pH $<$ pK_a indicates protonation of the electron donor, supporting PET as a potential mechanism.

Finally, viscosity studies can be an invaluable tool to elucidate the effects of TICT. The effects of TICT (quenching) increases in low viscosity solvents, as bond rotation occurs with greater ease, leading to increased quenching. Conversely, TICT is decreased in higher viscosity solvents leading to higher emission intensity. This can be experimentally determined by measuring the emission response in a range of solvents with varying viscosities, or varying the temperature in a solvent such as glycerol, which changes viscosity as a function of temperature. Ideally, one emission band will decrease in intensity as viscosity decreases, providing evidence for the presence of TICT.

All the techniques discussed above can be used in tandem to explore the fluorescence mechanisms of novel receptors. Understanding these properties allows for them to be exploited for assay purposes, such as designing receptors to be a ϕ_y based or a τ based sensor. Additionally, understanding these properties allows for comparisons to similar literature systems and builds upon the currently existing suite of receptors.

2.1.2 Probe Design and studied receptors

When considering an appropriate metal for use in a metal extrusion assay, particularly in bodily fluids, the targeted metal should not be biologically relevant e.g Na(I) or Ca(II). The reason for this is that using these metals leads to potential interference. As the metal is extruded from the binding site, if the receptor is primed to bind to biologically available metals, then new complexes may form. This could result in significant fluctuations in the absorbance or emission spectrum, yielding inaccurate results. Ba(II) is not found naturally in the body, and its concentration in sea-water is negligible. Therefore, Ba(II) was determined to be an appropriate metal binding centre due to its low natural concentrations in media of interest, so the ligands selected need to somewhat selective for this metal. In terms of the binding motifs employed, aza-crown ethers have been shown to bind well to Ba(II) as the intrinsic binding properties induce moderate size selectivity, which can be further altered through substitution, as outlined in Chapter 1.

A range of receptors were studied, with a combination of ligands and fluorophores. The first set of receptors contained either 1-aza-18-crown-6 ether (receptor **52**) or 1-10,di-aza-18-crown-6 ether (receptor **62**) appended to an anthracene fluorophore as presented in Figure 2.9. It has been shown that these aza-crown-ether ligands are capable of discriminating group (I)/group (II) metal ions.[81,87,90] Due to the binding properties of these ligands to Ba(II), this was utilised as the binding motif for metal binding and subsequent extrusion.

52 **62**

Figure 2.9: Anthracene based receptors synthesised in this study.

The next class of receptors contain naphthalimides appended with derivatives of 1,10-di-aza-18-crown-6 ether. Four novel receptors were synthesised, which were receptors **63**, **64**, **65** and **66**. These were synthesised taking inspiration from Thapa *et al.*,[75] in which altering the heteroatoms in the binding motif was shown to have a pronounced effect on metal binding. It was envisaged that changing the binding ligand by heteroatom variation could therefore alter the binding profile to Ba(II) to inform subsequent metal extrusion assays.

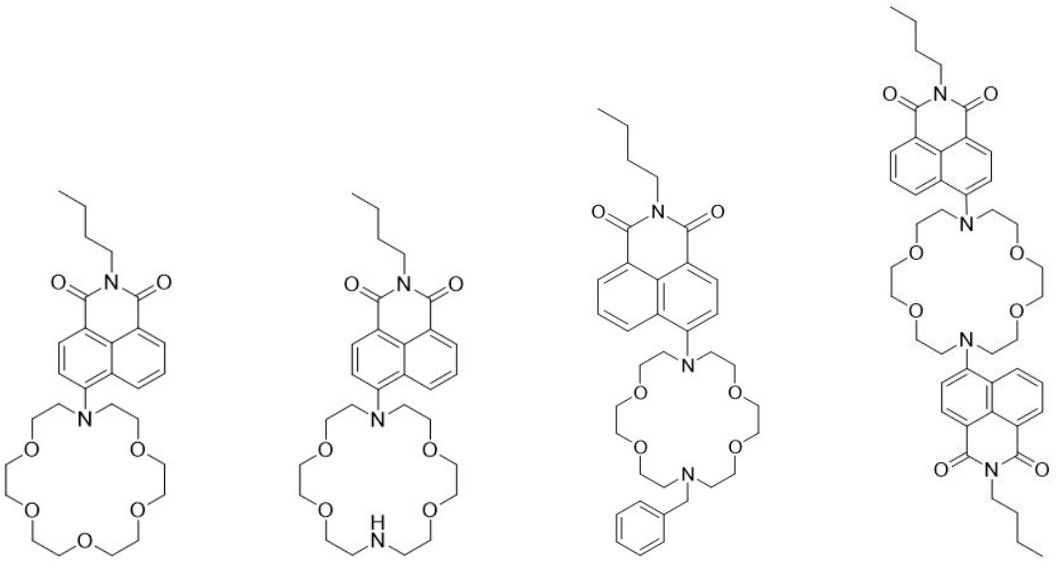

63 **64** **65** **66**

Figure 2.10: Naphthalimide aza-18-crown-6-ether receptors synthesised in this study.

A third group of receptors contained a di-carboxylate ligand for guest binding (Figure 2.11), inspired by ligands that have been reported as metal sensors.[59,79,114]

The receptors were synthesised as the Ba(II) salt, to allow for immediate use in metal extrusion assay applications. It was envisaged that the increased water solubility of the salt would increase the likelihood of utilising these receptors in aqueous assays in environments such as biological fluids or environmental fluids. These Ba(II) complexes were designed specifically for metal extrusion assay applications, and were not investigated as metal binding receptors.

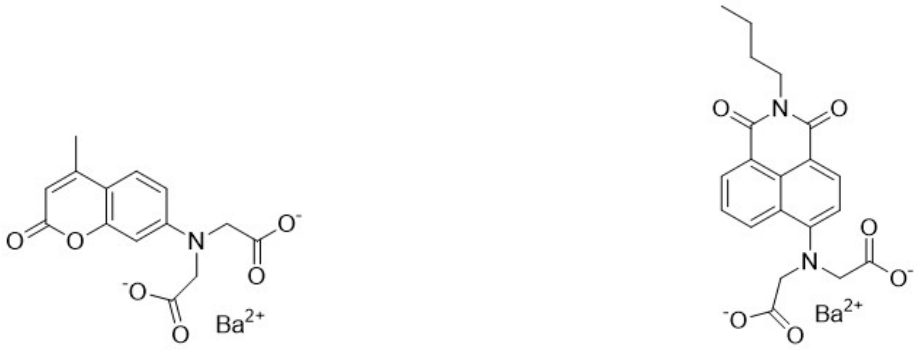

67 **68**

Figure 2.11: Dicarboxylate based receptors synthesised in this study.

Overall, three different fluorophores were used; 9-chloromethyl anthracene, *n*-butyl naphthalimide and 7-amino-4-methyl coumarin. Anthracene receptors have been reported to bind to group (I) and group (II) metals,[85,88,115] and anthracene based sensors are known to have low ϕ_y and exhibit multiple excited state decay pathways which can be modulated upon binding. Due to the lower ϕ_y of these anthracene fluorophores, *n*-butyl naphthalimide was also used as a fluorophore with a greater ϕ_y, potentially decreasing interference upon recording emission spectra. Similar receptors have been shown to bind to group (I) and group (II) metals,[75] while the fluorophore provides opportunity to create alternative structural combinations. Finally, 7-amino-4-methyl coumarin was also used, due to the high ϕ_y of the fluorophore, as well as the readily accessible starting material allowing for simple modifications of the core structure.

2.2 Synthesis

Anthracene crown receptors

The anthracene bearing aza-18-crown-6 receptors **52** and **62** were synthesised using slight modifications to literature precedent.[115] As shown in Scheme 2.1 and Scheme 2.2, a S_N2 substitution was performed between the respective aza-18-crown-6 ether and 9-chloromethyl anthracene. The addition of a non-nucleophilic base in the form of Et_3N to remove the HCl by-product in the form of a salt allows for the reaction to proceed with high conversion. The two receptors required slightly different reaction conditions, with the synthesis of receptor **62** requiring milder conditions with a shorter reaction time, in order to avoid substitution of both nitrogen atoms of the aza-crown ether. While the addition of iodide has been shown to increase reaction rate and yield in substitution reactions,[114,116] the addition of NaI was not found to significantly improve the yields or reaction rate.

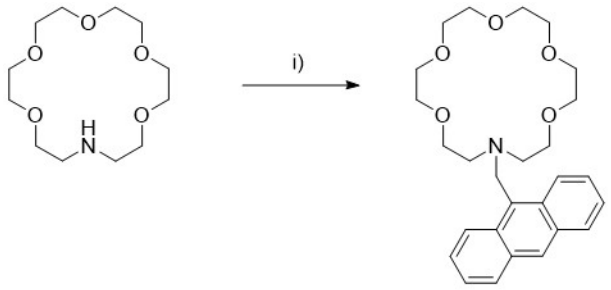

69 **52**

Scheme 2.1: i) 9-chloromethyl anthracene (0.9 eq), DMF (100°C), Et_3N (1.3 eq), K_2CO_3 (2 eq), 72 h, 22%

While both reactions proceeded to completion as determined by TLC analysis, isolation of the product resulted in loss of yield. To isolate the product, multiple pH based extractions were employed, causing loss of some desired product as a result of partial solubility in the aqueous acid used. Further receptor purification was performed through column chromatography. Compound **52** required isocratic elution with EtOAc/1% Et_3N using silica, while purification of **62** required a more polar eluent in the form of CH_2Cl_2/MeOH in combination with a neutral alumina

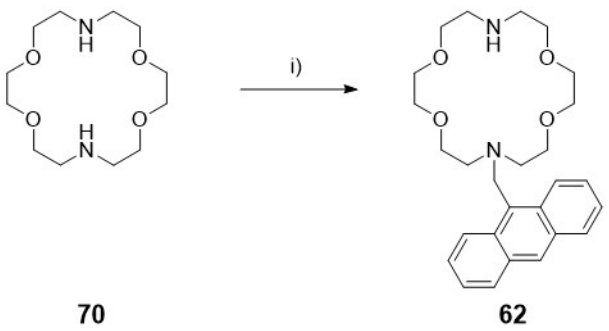

Scheme 2.2: i) 9-chloromethyl anthracene (1 eq), DMF (70°C), Et_3N (1 eq), 16 h, 40%

solid phase to reduce band broadening.

The NMR spectra of these receptors are shown in Figure 2.12 and Figure 2.13. For both receptors, the signals attributed to the crown ether protons are observed as a broad multiplet at 3.6 ppm. These are slightly more resolved in the case of receptor **62**, presumably due to the slight differences in the chemical environment due to the secondary amine. The formation of product was also confirmed by comparing to the spectrum of 9-chloromethyl anthracene starting material, with an upfield shift of the signal attributed to the methylene protons observed after product formation in both cases. Mass spectrometry also confirmed formation of both **52** and **62** (m/z 454 and 453.2745 respectively).

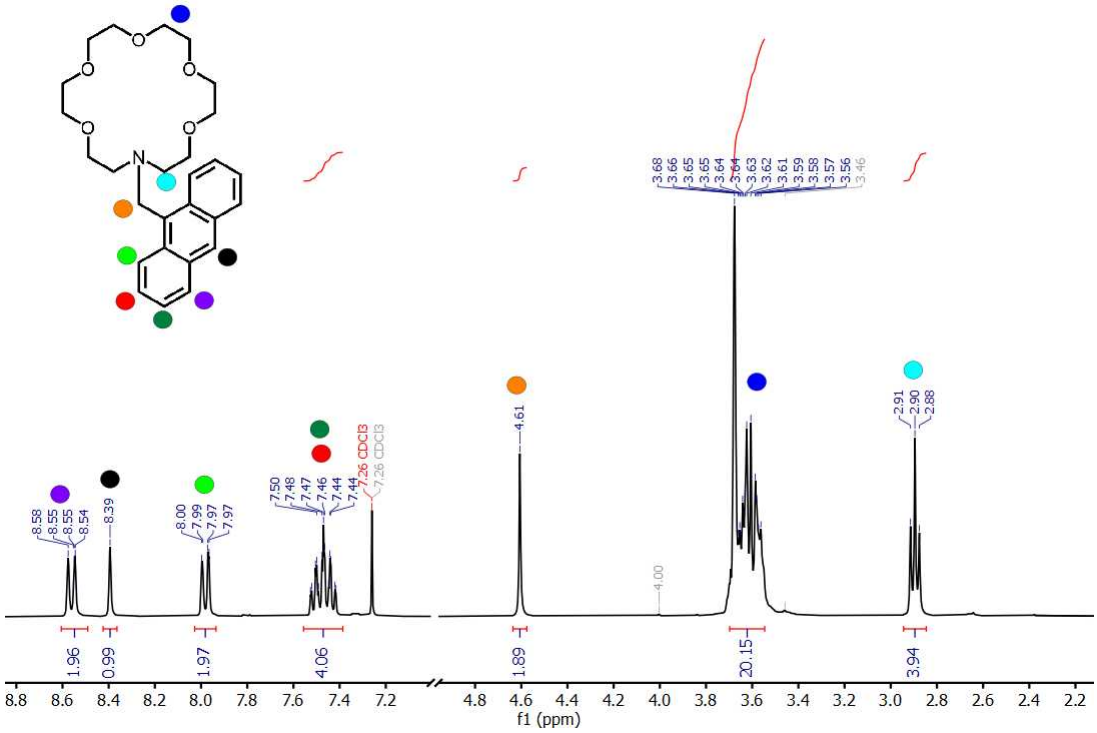

Figure 2.12: Annotated ^{1}H NMR of receptor **52** in $CDCl_3$.

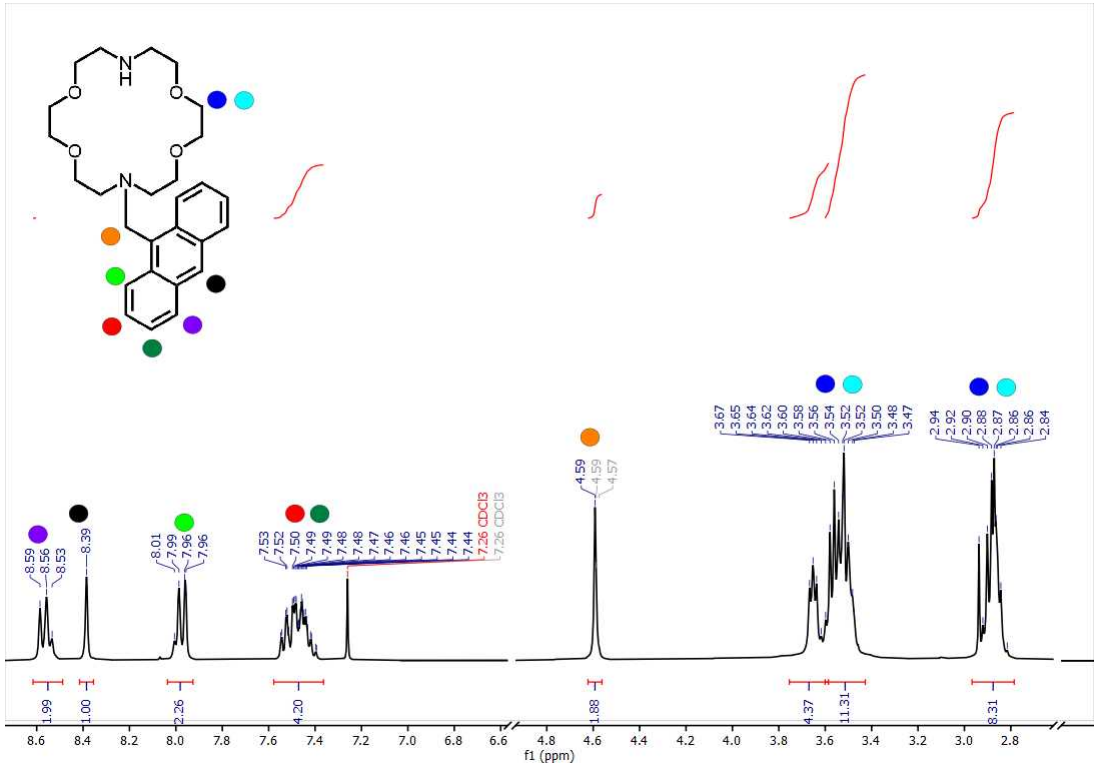

Figure 2.13: Annotated ^{1}H NMR of the receptor **62** in $CDCl_3$.

Naphthalimide crown receptors

Initial attempts to synthesise **38**, which was previously reported as a Ba(II) sensor,[75] were unsuccessful. Several difficulties were encountered in this synthesis (Scheme 2.3). The initial S_NAr of 1-aza-18-crown-6-ether with *p*-nitrofluorobenzene was found to proceed, with difficulties also encountered in the subsequent hydrogenolysis. The most significant difficulty was in the final step, with installation of *n*-butylamine in the 4-position of the naphthalimide. Using NMP as a solvent in high temperatures, this reaction was found to be low yielding. Isolation of the final product was also difficult, due to the poor elution on silica in high polarity solvents, and low water solubility preventing reverse phase chromatography from being utilised. Due to the low yields after both the reaction and purification steps, which would minimise the amount of product available for testing, the receptor design was modified, such that the aza-crown ether motif was directly conjugated to the fluorophore, with *n*-butylamine installed at the imide to prevent further reactivity.

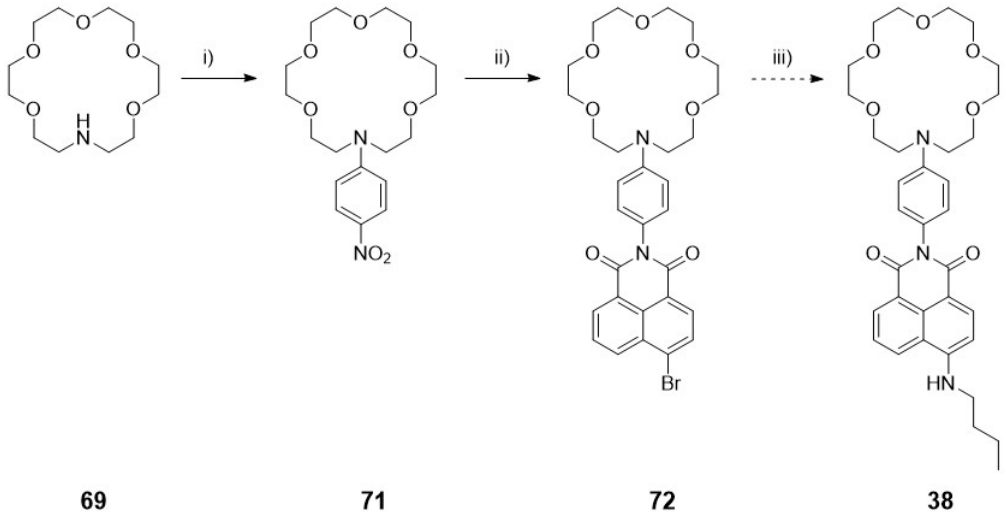

Scheme 2.3: i) *p*-Nitrofluorobenzene, K_2CO_3, DMF, 100°C ii) Pd/C, HCOOH, EtOH then **73**, EtOH, Δ iii) *n*-butylamine, NMP, 120°C

The first step in the synthesis of **63** involved the known synthesis of receptor **74** using previously reported conditions (Scheme 2.4). Reaction of *n*-

butylamine with 4-bromo-1,8-naphthalic anhydride gave the desired 4-bromo-1,8-naphthalimide.[117] The reaction proceeded in excellent yield and required only an acid wash with 1 M HCl of the crude solid to provide **74** without need for further purification. The ^{1}H NMR spectrum of the product is presented in Figure A.2.7 and matches data reported in the literature (*m/z* 332).[117]

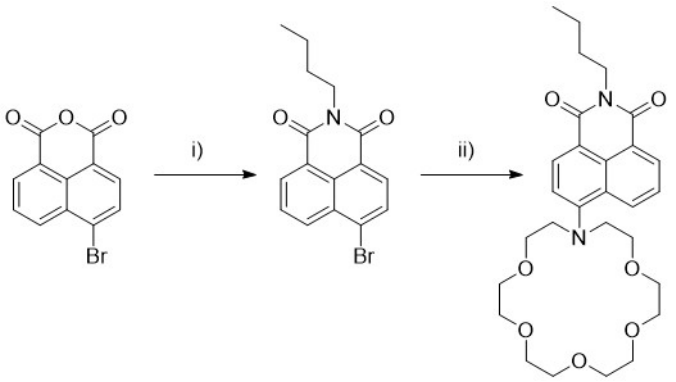

73 **74** **63**

Scheme 2.4: i) *n*-Butylamine (1.1 eq), EtOH, Δ, 18 h, 98% ii) **74** (4 eq), Na_2CO_3 (2 eq), DMSO, 140°C, 72 h, 56%

Compound **74** was then reacted with aza-18-crown-6-ether in a S_NAr reaction which required extensive optimisation as it was found that harsher conditions were required to achieve the S_NAr reaction. After a solvent screen to optimise the S_NAr, DMSO was determined to be the best solvent, as high temperatures were required for step ii) in Scheme 2.4. However, even with long reaction times (72 h), the reaction did not proceed to completion.

Purification of **63** was challenging, requiring a normal phase silica column eluted with 20% MeOH/EtOAc, followed by a reverse phase (C_{18}) chromatography with slow elution in TFA/H_2O/MeCN. Long elution times were required due to the presence of an unidentified impurity of similar polarity, with the extensive purification resulting in a highly reduced yield. Attempts at purification through preparative HPLC were made, however long experimental run times and low mass recovery made this unsuitable. The ^{1}H NMR spectrum of receptor **63** as shown

in Figure 2.14 shows upfield shifts of the signals associated with the aromatic protons when compared to that of **74**, however contains small impurities. Mass spectrometry also confirmed formation of **63** (m/z 515.2755).

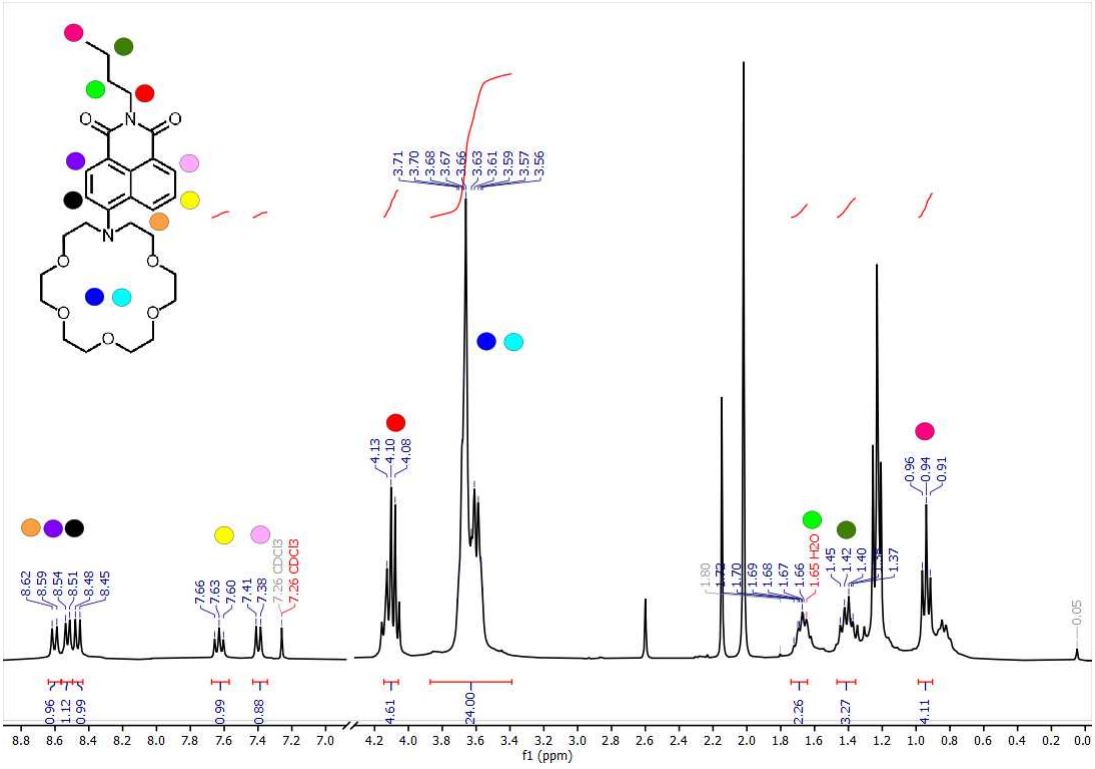

Figure 2.14: Annotated ^{1}H NMR of receptor **63** in $CDCl_3$.

Initial attempts at synthesising **64** using un-protected 1,10-di-aza-18-crown-6-ether resulted in a mixture of mono/di-substituted receptors. Therefore, the mono-protected aza-crown-ether **75** was first synthesised according to a literature protocol.[118] The starting 1,10-di-aza-18-crown-6 ether was treated with di-*tert*-butyl dicarbonate in 1,4-dioxane with gentle heating to aid dissolution and dropwise addition of the protecting agent to minimise by-product formation. Purification of this receptor was straightforward, as the starting 1,10-diaza-crown ether precipitated out of solution upon the addition of diethyl ether. Purification of the residue was performed *via* column chromatography in up to 20% $MeOH/CH_2Cl_2$ on alumina. The ^{1}H NMR spectrum shown in Figure A.2.3 in the Appendix confirmed formation of **75** with a signal at 1.4 ppm corresponding to the *tert*-butyl protecting group. Mass spectrometry also confirmed formation of **75** (m/z 362).

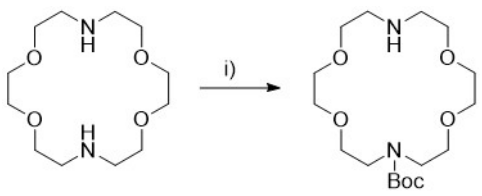

70 **75**

Scheme 2.5: i) Di-*tert*-butyl dicarbonate (1 eq), 1,4-dioxane, 40°C (40 minutes) then R.T (6 h), 24 %.

Similar difficulties in purification were encountered in the synthesis of **64**, resulting in low overall yield. Following the S_NAr reaction and purification *via* column chromatography, Boc deprotection of **75** was achieved upon treatment with TFA/CH_2Cl_2 (Scheme 2.6), and the product purified using reverse phase C_{18} column chromatography. Attempts were made at purification of the product prior to Boc deprotection, however this did not result in an increase in the yield. Mass spectrometry also confirmed formation of **64** (*m/z* 537.2572).

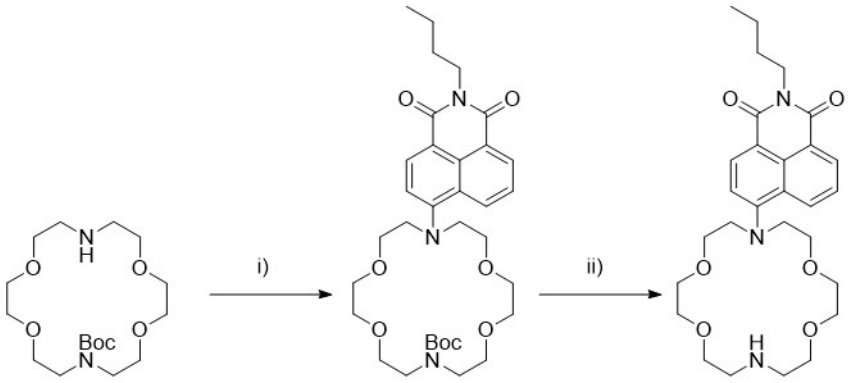

75 **76** **64**

Scheme 2.6: i) **74** (4 eq), Na_2CO_3 (2 eq), DMSO, 140°C, 72 h, ii) TFA/CH_2Cl_2, R.T, 1 h, 7%

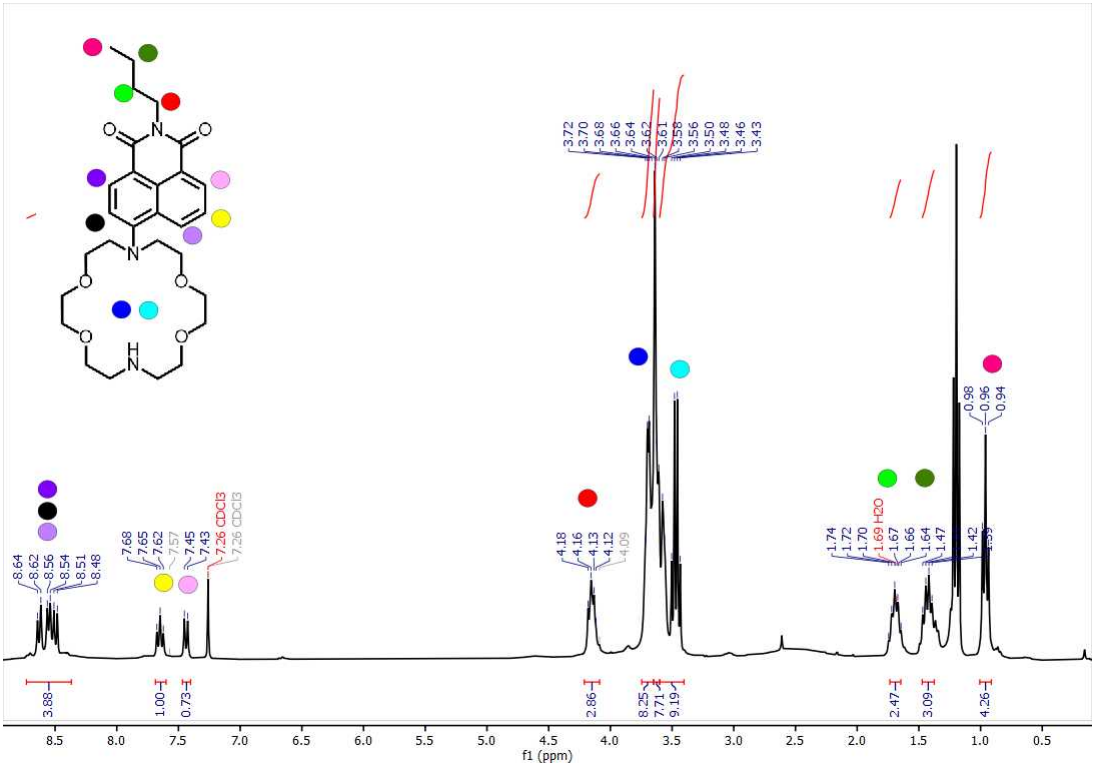

Figure 2.15: Annotated ^{1}H NMR of receptor **64** in $CDCl_3$.

The initial synthetic approach to receptor **65** involved performing a substitution reaction with receptor **64** with benzyl bromide. However, this did not provide **65** in high yield, so an alternative approach was investigated. A reductive amination was performed using 1,10-diaza-18-crown-6 ether and benzaldehyde with sodium triacetoxyborohydride as the reducing agent to afford the mono-benzylated aza-crown-ether **77** (m/z 353.2438). Reaction of **77** with **74** under similar conditions to those described above for **63** and **64** gave **65** in 5% yield after extensive purification. The ^{1}H NMR spectrum of **65** (Figure 2.16) indicates installation of the benzyl functional group, evidenced by signals at 7.24 ppm, attributable to the aromatic benzylic protons. A shift was observed from 4.6 ppm to 3.53 ppm attributable to methylene protons of the benzyl group indicating installation compared to **74**. Mass spectrometry also confirmed formation of **65** (m/z 604.3379).

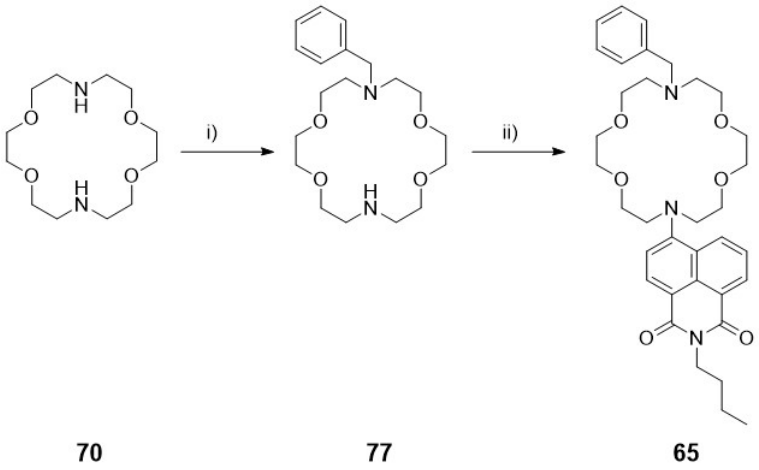

Scheme 2.7: i) Benzaldehyde (1 eq), glacial AcOH (1.1 eq), sodium triacetoxyborohydride (2 eq), DMF, R.T, 1h, 77% ii) **74** (6 eq), Na_2CO_3 (2.5 eq), DMSO, 100°C, 72 h, 5%

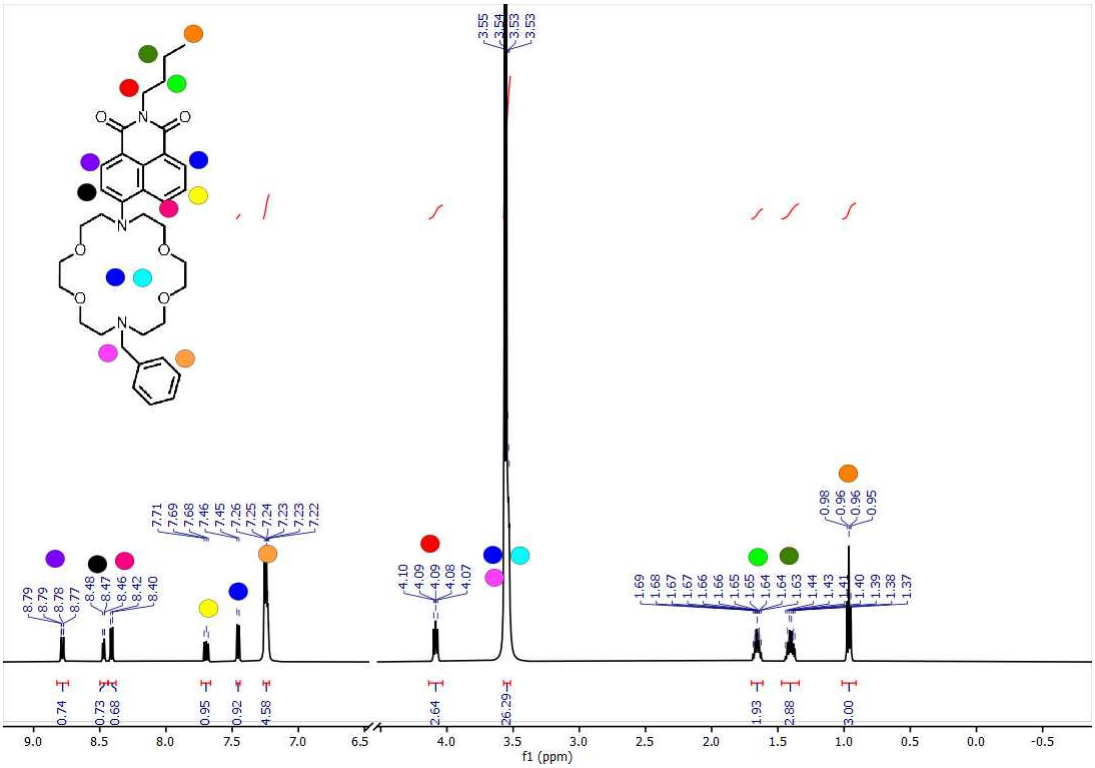

Figure 2.16: Annotated ^{1}H NMR of receptor **65** in CD_3CN. Due to solvent peaks dwarfing the product peaks, these have been removed.

Attempts to synthesise **65** resulted in the formation of **66**, which was initially isolated following column chromatography of the crude **65**. The formation of this product was confirmed through ^{1}H NMR analysis, in which a doubling of all aromatic signals was observed, while the signals associated with the aza-crown-ether ligand remained unaffected. Receptor **66** was then synthesised using conditions similar to those used for the prior naphthalimide containing receptors. Greater equivalents of **74** were required to ensure conversion to the product, however purification *via* column chromatography presented less difficulties compared to the previously synthesised receptors. Receptor **66** was isolated in poor yields after a long reaction time, indicating poor conversion to the product with minor impurities. Mass spectrometry also confirmed formation of **77** (*m/z* 787.3692).

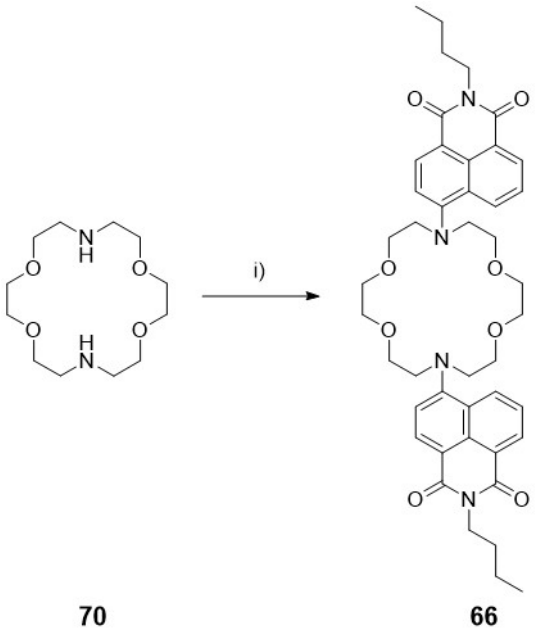

70 **66**

Scheme 2.8: i) **74** (7 eq), Na_2CO_3 (2 eq), DMSO, 100°C, 6d, 10%

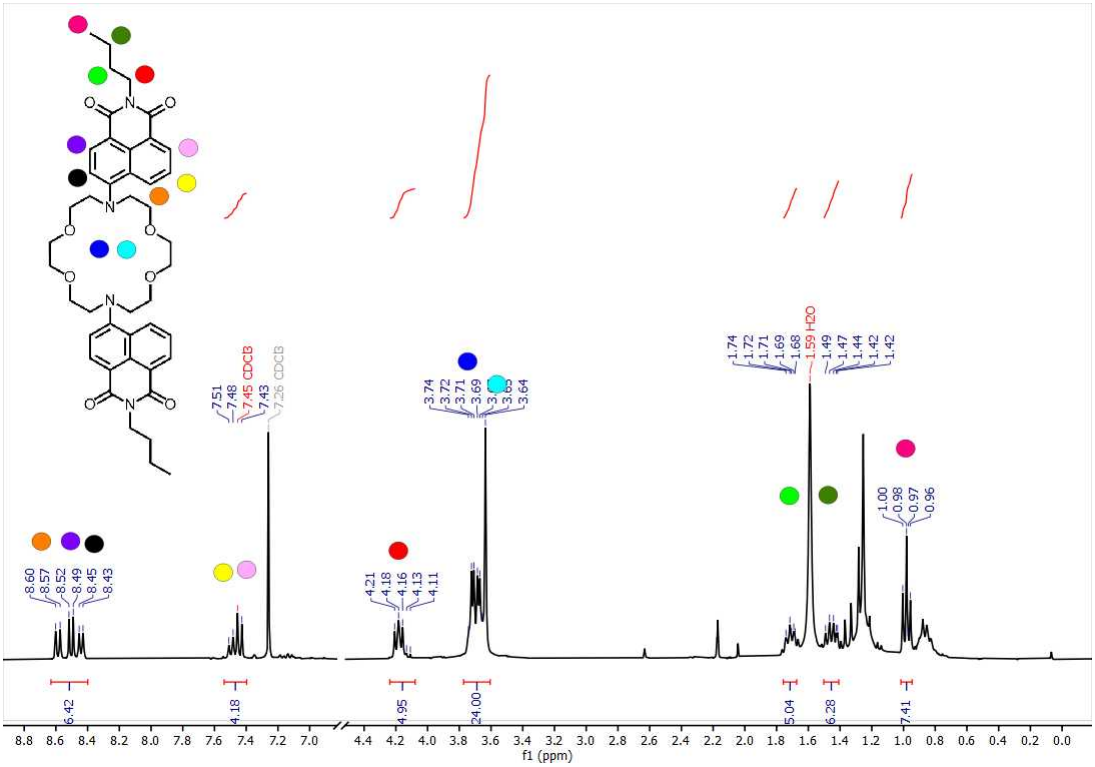

Figure 2.17: Annotated ^{1}H NMR of receptor **66** in $CDCl_3$.

Ba(II) salt receptors

Receptor **67** was synthesised using a modified literature procedure by Hagen *et al* (Scheme 2.9).[119] 7-Amino-4-methyl coumarin was reacted with *tert*-butyl bromoacetate in the presence of sodium iodide, affording a mixture of the mono-substituted **80** and the desired **79** (*m/z* 312 and 426 respectively). Compound **80** could be further reacted under the same conditions to afford **79** (Scheme 2.9). This reaction consistently yielded a 5:1 ratio of **80**:**79**, as confirmed by ^{1}H NMR of the crude reaction mixture. These products were efficiently separated by normal phase column chromatography without further purification.

Subsequent acid catalysed *tert*-butyl ester deprotection in a mixture of TFA/ CH_2Cl_2 proceeded cleanly to afford **81** as confirmed by the disappearance of the signal at 1.43 ppm associated with the *tert*-butyl esters in the ^{1}H NMR spectrum (Figure A.2.2) (*m/z* 290). Following this, **81** was converted to **67** upon reaction with $Ba(OH)_2$ in a $MeOH/H_2O$ solvent. Excess base was used to ensure full deprotonation of the receptor, however this was also repeated with exactly 1

equivalent of base to ensure no excess Ba(II) remained. Product formation was also confirmed by an increase in the water solubility from the **81** to **67**. Mass spectrometry also confirmed formation of **67** (m/z 449).

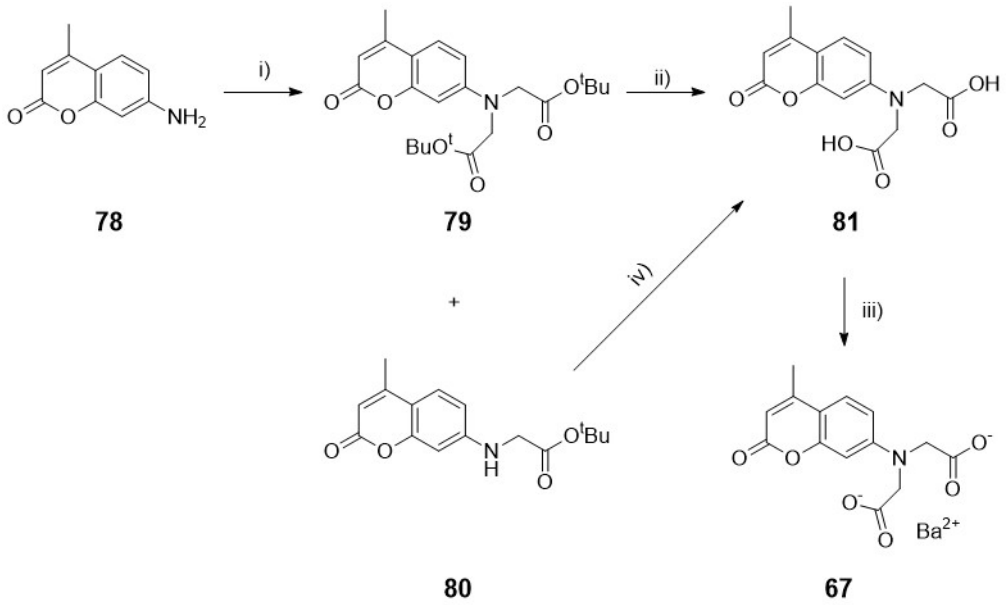

Scheme 2.9: i) *tert*-butyl-bromoacetate (8 eq), K_2CO_3 (6 eq), NaI (8 eq), MeCN, Δ, 72 h, 41%; ii) TFA/CH_2Cl_2, R.T, 0.5 h, 87%; iii) $Ba(OH)_2$ (2 eq), MeOH/H_2O, R.T, 1 h, quant iv) Steps i – ii

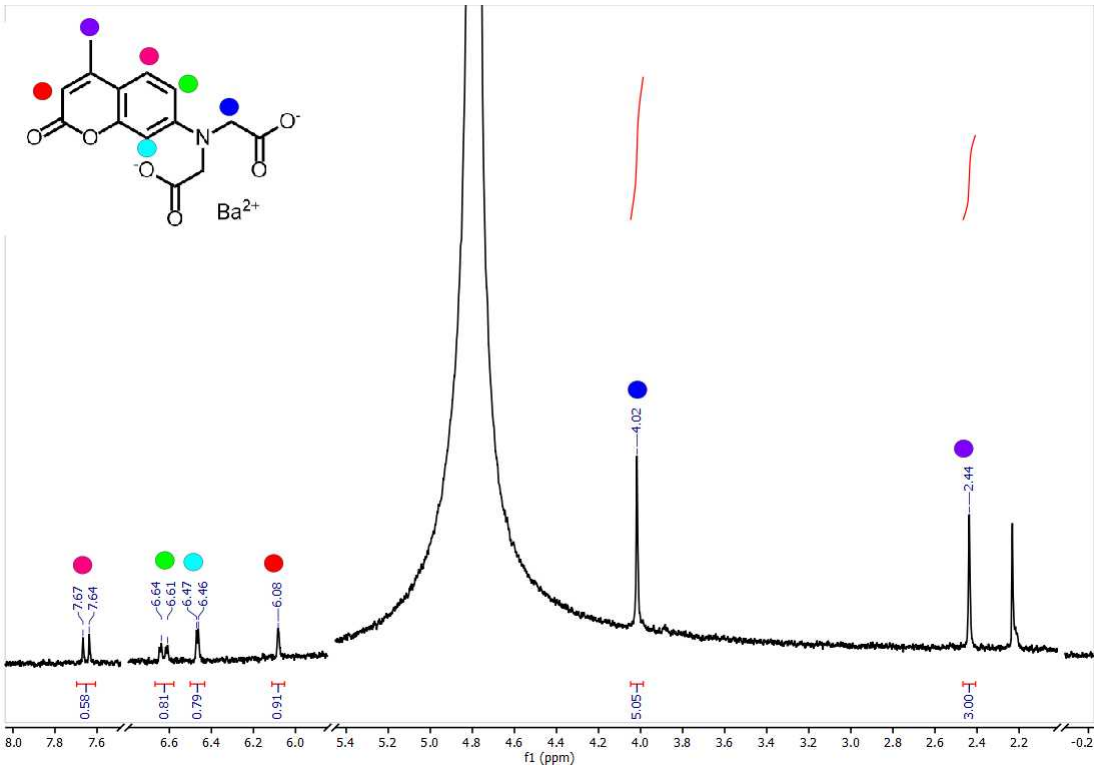

Figure 2.18: Annotated ^{1}H NMR of receptor **67** in D_2O. Cut sections contain no peaks.

A second receptor (**68**) containing the same recognition motif but replacing the coumarin fluorophore with a naphthalimide was also synthesised. The first step required synthesis of receptor **84**. Initial attempts to use a literature procedure by Wang *et al.*[120] by reacting 4-nitro-1,8-naphthalic anhydride with 1.4 equivalents of butylamine led to a mixture of the desired product and **82** in which the nitro group of 4-nitro-1,8-naphthalic anhydride also underwent substitution in a S_NAr reaction as presented in Figure A.2.9. Reduction in the number of equivalents of butylamine to 0.9 equivalents, together with shortening of the reaction time from 12 h to 2 h reduced the amount of doubly substituted **82** formed and provided the best yields of the desired product **84** (m/z 321), which could be isolated using column chromatography and further reacted to form **85** (m/z 267).

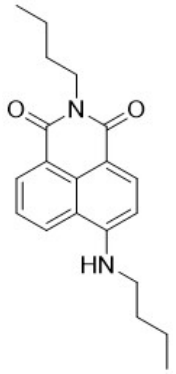

82

Figure 2.19: Isolated by-product of 4-nitro-1,8-naphthalic anhydride S_NAr.

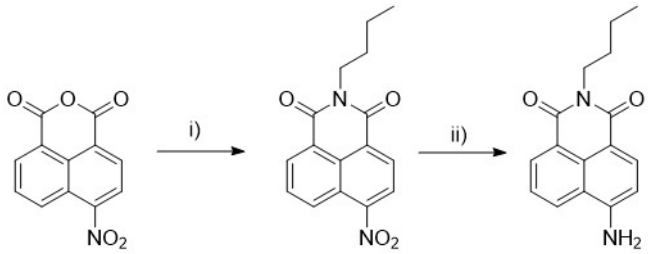

83 **84** **85**

Scheme 2.10: i) *n*-butylamine (0.9 eq), EtOH, Δ, 2 h, 35%; ii) Pd/C (1 mol%), EtOH, R.T, 2 h, 44%

Compound **85** was next reacted with *tert*-butyl bromoacetate to give the diester **86**. Formation of **86** was confirmed by ^{1}H NMR (Figure A.2.5) and mass spectrometry (*m/z* 519.2465). The 5:1 ratio of **87**:**86** was observed, similar to that seen in the synthesis of **79**, while **87** could be converted to **86** using the same reaction conditions. Compound **86** was converted to **68** under the same conditions used to convert **79** to **67**. The ^{1}H NMR is **68** is presented in Figure 2.20 with slight impurities, however only one product is present. Mass spectrometry also confirmed formation of **68** (*m/z* 521.0290).

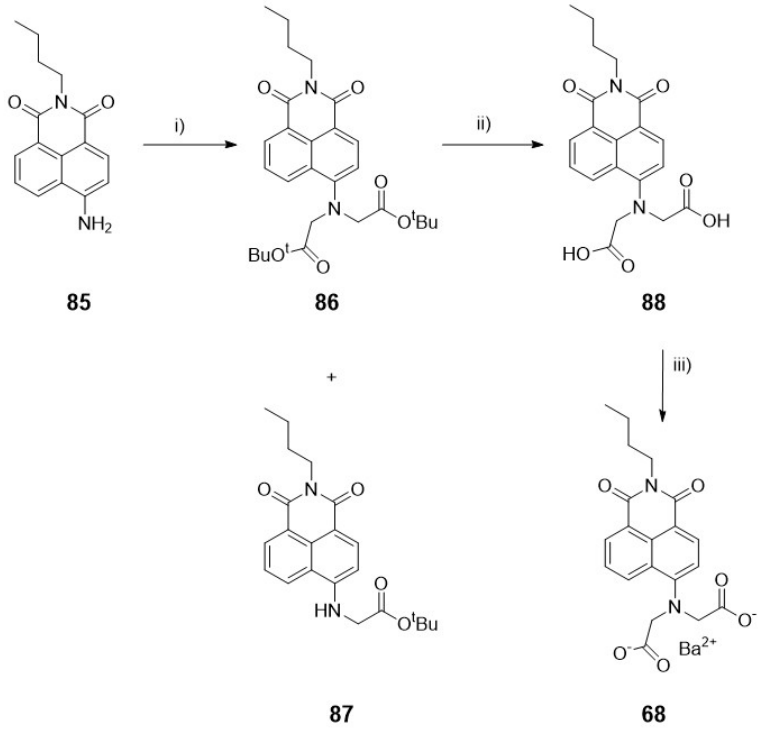

Scheme 2.11: i) K_2CO_3 (6 eq), NaI (3 eq), *tert*-butyl bromoacetate (8 eq), MeCN, Δ, 72 h, 67%, ii) TFA/CH_2Cl_2, R.T, 0.5 h, 13%, iii) $Ba(OH)_2$ (2 eq), MeOH/H_2O, R.T, 1 h, 32%

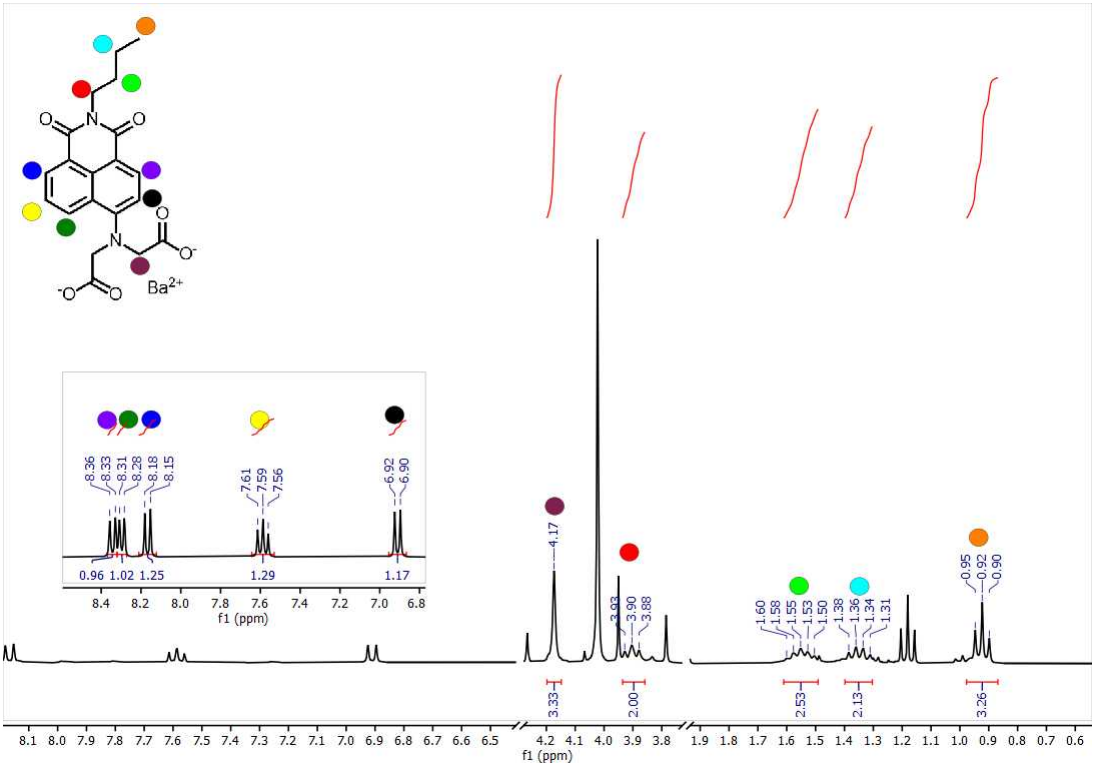

Figure 2.20: Annotated ^{1}H NMR of receptor **68** in D_2O. Cut sections contain no peaks.

2.3 Results

The photophysical properties of the synthesised receptors were explored using the techniques stated in Section 2.1.1. Excitation and emission studies were performed to determine appropriate λ_{ex}, and solvent screens performed to determine the appropriate solvent for studies. Dilution studies were performed by both UV-vis and fluorescence spectroscopy to examine aggregation effects.

In addition to this, pH studies were performed for receptor **63**, receptor **64** and receptor **67**, and viscosity studies were performed for receptor **63** and receptor **64** to examine mechanistic effects. ϕ and τ were determined for all receptors to better understand these fluorescent systems.

2.3.1 Anthracene receptors

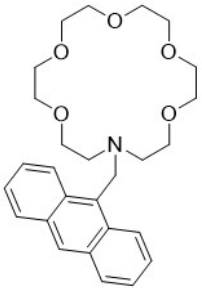

52

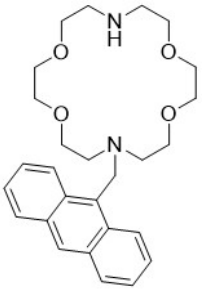

62

Excitation and Emission

Excitation and emission spectra were first obtained for both **52** and **62** (Figure 2.22). Anthracenes are known to exhibit multiple emission wavelengths, as well as multiple excitation wavelengths.[98,121] Due to the overlap at 375 nm between the excitation and emission spectra of **52** and **62**, a suitable λ_{ex} is 354 nm, consistent with previous studies of similar receptors.[122–124]

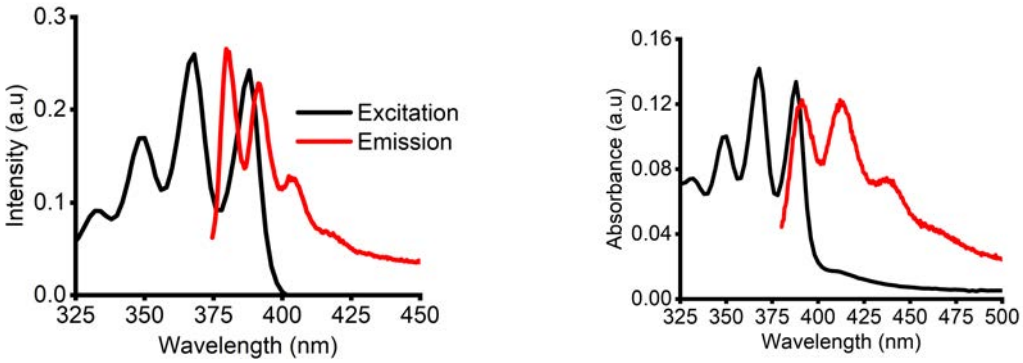

(a) 52 **(b) 62**

Figure 2.22: Excitation (black) and emission (red) spectrum of **52** and **62** in 1% Water/MeCN. $[\text{Probe}]_{ex} = 40\ \mu\text{M}$ and $[\text{Probe}]_{em} = 5\ \mu\text{M}$.

Dilution studies

Dilution studies for **52** were performed by both UV-vis and fluorescence spectroscopy. In the absence of aggregation, the intensity and absorbance are expected to increase linearly with respect to concentration. Excimeric species can be identified by the formation of a broad, long wavelength emission signal.

The absorbance and emission spectra of **52** in 100% MeCN at varying concentrations are presented in Figure 2.23. The absorbance response shows a roughly linear increase in absorbance with increasing receptor concentration. From this, a concentration of 40 μM was deemed suitable for UV-vis studies. The emission response illustrates a sharper increase in intensity due to the higher sensitivity of fluorescence spectroscopy, with no noticeable quenching effects occurring. Each signal undergoes slight red shifting, with the signal at roughly 430 nm undergoing $\Delta\lambda$ of 3 nm, the signal at roughly 410 nm undergoing $\Delta\lambda$ of 6 nm and the signal at roughly 390 nm undergoing $\Delta\lambda$ of 6 nm. No excimeric effects were observed in this solvent system, and given the structural similarities a similar response was assumed for **62**. From this study, a concentration of 5 μM was deemed acceptable for fluorescence studies.

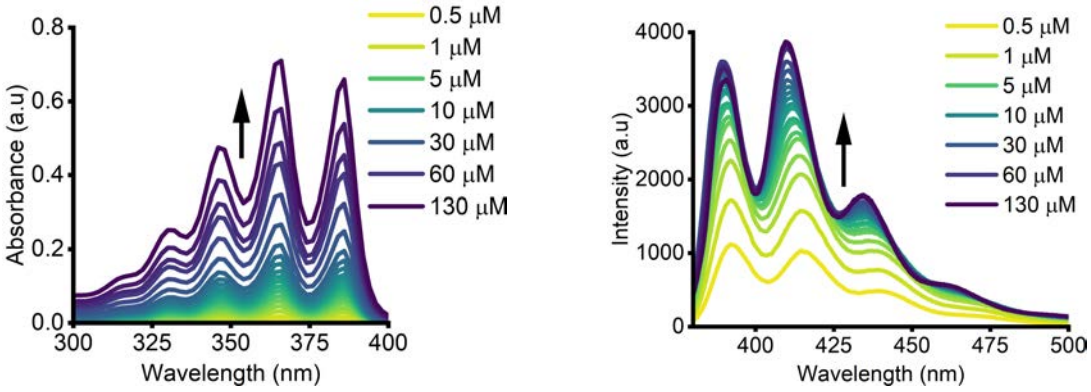

(a) UV-vis **(b)** Fluorescence

Figure 2.23: Dilution studies of **52** in 100% MeCN. For fluorescence, the excitation bandpass used was 20 nm and the emission bandpass was 1 nm, λ_{ex} = 354 nm. Dilution study isotherms are presented in A.3.1a and A.3.1b in the Appendix.

Determination of suitable solvent for spectroscopic studies

When determining the ideal solvent system for the upcoming optical studies, several parameters must be considered. The most obvious factor is the receptor solubility to ensure full dissolution of the receptor, as insolubilities affect the concentration of receptor in solution, while the presence of precipitates can lead to light scattering, yielding unreliable spectroscopic results.

Another factor is the effect of solvent on binding properties such as the strength of the H-G interaction. When considering the application of these molecules in a metal extrusion assay, the solvent composition should ensure that the metal is fully complexed by the ligand to minimise excess metal salt, as free metal cations may coordinate to the anion being studied in solution and alter the assay results. This can be determined by measuring the metal response in different solvent compositions.

Receptor **52** was used to determine a suitable solvent system. To explore the effects of water concentration on the binding relationship of **52** to metal, the response to Ba(II) was explored in an organic solvent and an aqueous system. In this case, the aqueous system comprised of a buffer, as future applications

will benefit from functionality in aqueous buffered systems. This study was performed by fluorescence spectroscopy given the higher sensitivity of this technique compared to UV-vis spectroscopy.

Firstly, Ba(II) (as the perchlorate salt due to the non-coordinating nature of this anion) was added to a solution of receptor **52** in 100% MeCN, with MeCN used as an aprotic solvent. Increasing aliquots of $Ba(ClO_4)_2$ were added to a solution of **52**, and fluorescence intensity at 430 nm plotted as a function of concentration (2.24a). The fluorescence intensity sharply increases and plateaus at 1 equivalent of Ba(II), indicating full formation of the 1:1 complex in this solvent system. No further changes were observed upon addition of excess Ba(II) up to 8 equivalents. As can be seen, the overall fluorescence intensity in the absence of guest is low, due to the PET occurring between the ligand and the anthracene.

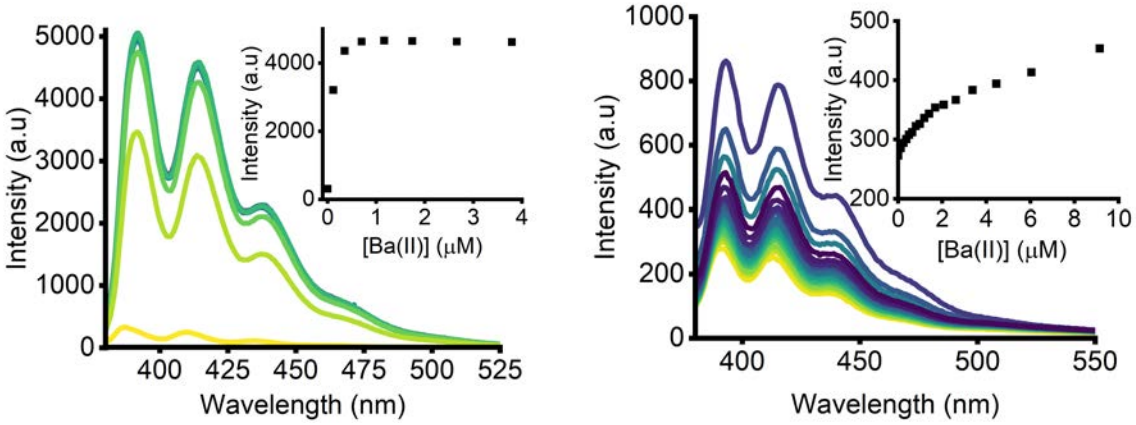

(a) 100% MeCN **(b)** MeCN/Tris buffer pH 10 (1:1)

Figure 2.24: Fluorescence titration of **52** with increasing equivalents of $Ba(ClO_4)_2$ in two different solvent systems. The emission bandpass was 5 nm and the excitation bandpass was 10 nm. ([Probe] = 5 μM and λ_{ex} = 354 nm).

In comparison, the same study was performed in a 1:1 mixture of Tris base buffer (pH 10):MeCN (2.24b). Since Ba(II) ions are more strongly solvated in water than MeCN, this was expected to decrease binding affinity of **52** for Ba(II). In this mixed solvent, the binding isotherm has substantially changed, to a more gradual increase in intensity. This isotherm continues to slope upwards, sug-

gesting that full complexation of Ba(II) is not achieved after addition of > 10 equivalents of metal salt, and the overall fluorescence intensity is lower in this buffered system compared to MeCN.

The above studies suggested that for the intended metal extrusion application, a suitable solvent system for this class of receptors cannot contain a significant aqueous content. Increasing the water content also limits the solubility of the receptor. In order to introduce some water to allow use of these receptors for aqueous applications, 1% Water/MeCN chosen as the solvent system. In order to ensure consistency across all receptors with the aza-crown-ether motif, this was the solvent used for all further studies with these receptors.

Quantum yield and lifetime

The ϕ values were next determined in 1% Water/MeCN. As seen in Table 2.1, in the absence of Ba(II) both **52** and **62** have a high degree of fluorescence quenching with ϕ close to 0. This can be attributed to the intrinsic quenching mechanism due to PET transfer from the lone nitrogen of the aza-crown-ether to the fluorophore. Receptor concentrations of 3 μM were used due to the instrumental requirements.

Table 2.1: Quantum yields of **52** and **62** expressed as a ratio.

Receptor	ϕ
52	0.002
62	0

Following this, the fluorescent decay lifetimes were measured for both receptor **52** and receptor **62**. Due to instrumental requirements requiring a concentration at which Abs < 0.05 a.u, receptor concentrations of 3 μM were used. The Instrument Response Function (IRF) was measured for each sample under the same experimental conditions, and was used to extract the exponential decay function from the measured signal. Due to instrumental limitations, a non-ideal excitation source was used in the form of a 405 nm diode, meaning that the overall intensity was quite low. Performing the study with a 370 nm diode did not significantly

impact the results.

The obtained data was fit using the DecayFit software using both mono-exponential and multi-exponential decay equations. Goodness of fit was evaluated by observing the χ^2 value, with lower values indicating a better fit. The residual pattern was also observed, with randomly distributed residuals along the x-axis indicating a better fit. Both receptors showed a good fit to a bi-exponential decay after considering χ^2 and random residual scattering. The τ_{amp} values were calculated using Equation 6.1, and the relevant decay graphs are presented in the Appendix.

There are two methods for the calculation of τ_{ave}: Amplitude average (τ_{amp}) and Intensity average (τ_i). τ_i is used in situations where the observed fluorescence intensity correlation to photon output is of importance, such as in fluorescence microscopy applications. This is because this method emphasises species with longer lifetimes, providing a better match to the emission intensity in microscopy images. In comparison, τ_{amp} is used where there may be multiple populations in a sample, and negates each species' brightness. To compare the lifetimes of different molecules or complexes, the use of τ_i may lead to bias of complexes with longer lifetimes or greater brightness. Due to this, τ_{amp} provides a better point of comparison.

Table 2.2: Bi-exponential lifetimes of receptor **52** and receptor **62**. Amplitudes for calculations are presented in Table 4 and Table 6 in the Appendix.

Receptor	τ_1 (ns)	τ_2 (ns)	τ_{amp} (ns)
52	0.79	8.12	7.55
62	0.00051	5.87	5.87

In general, a faster τ is indicative of more decay pathways, which tend to be non-radiative. Additionally, two lifetimes may be indicative of different environments such as partially hydrated or non hydrated species, altering the fluorescence properties to induce different decay pathways. These include conformational changes and energy lost to the solvent as heat. When comparing the

obtained τ_{amp} values, receptor **62** has a faster rate of decay, indicating more non-radiative transitions. This can be attributed to the greater propensity for PET to the fluorophore due to the presence of two electron donors in comparison to the single amine present in **52**.

2.3.2 Naphthalimide crown ether receptors

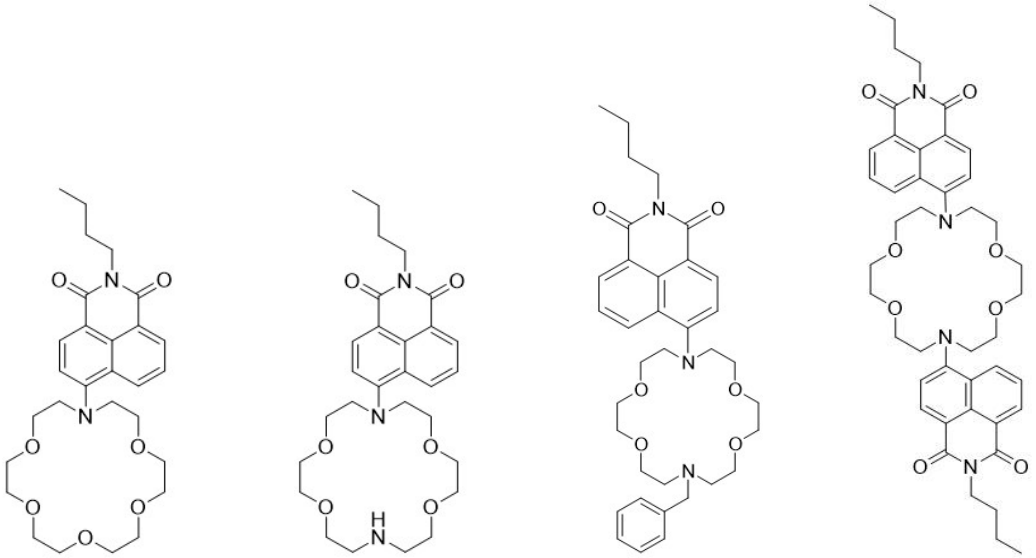

63 **64** **65** **66**

The photophysical properties of receptors **63** − **66** were next evaluated. Due to the difficulties in synthesis and purification, these receptors are as analytically pure as possible, but may contain slight impurities which could not be removed.

Excitation and Emission

Excitation and emission data were collected for receptors **63** − **66** in 1% water/MeCN, with the collated data for each naphthalimide aza-crown ether receptors presented in Table 2.3. Receptors **63** and **64** were found to have two excitation wavelengths of λ_{ex} 370 nm and λ_{ex} 430 nm with corresponding λ_{em} of 460 nm and 530 nm. Due to the small Stokes' shift observed, λ_{ex} 370 nm was used for subsequent experiments. This dual emission profile was not observed for **65** and **66**.

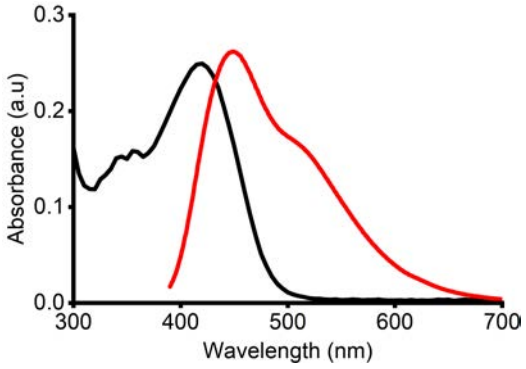

63 (λ_{ex} = 370 nm)

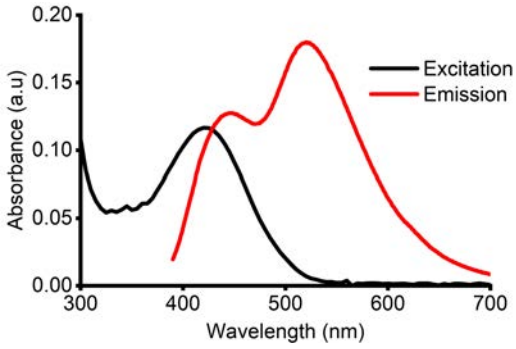

64 (λ_{ex} = 370 nm)

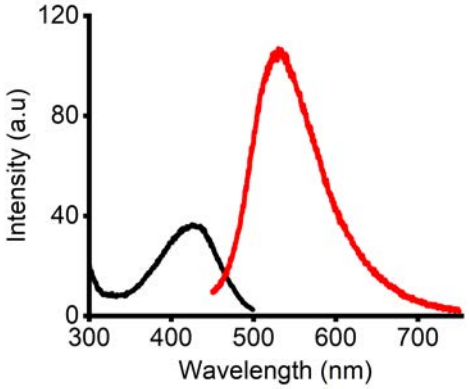

65 (λ_{ex} = 425 nm)

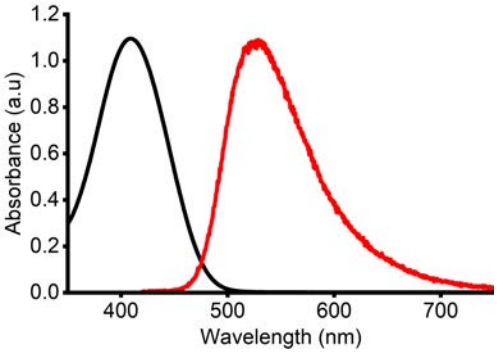

66 (λ_{ex} = 410 nm)

Figure 2.26: Excitation (black) and emission (red) spectra in 1% Water/MeCN. The excitation and emission bandpasses used were 5 nm/5 nm for **63**, **65** and **66**, and 3 nm/5 nm for **64**. Spectra for **63** and **66** were normalised for clarity.

Table 2.3: Excitation, emission wavelengths and Stokes' shifts for receptors **63** – **66**.

Receptor	λ_{ex}	λ_{em}	$\Delta\lambda$
63	370, 430	460, 530	30
64	370, 430	460, 525	30
65	428	533	105
66	409	576	167

Dilution studies

Dilution studies in 1% Water/MeCN were performed for receptors **63** – **66**. In all cases, the absorbance response was linear with respect to increasing receptor concentration (Figure 2.27). A concentration of 40 μM was determined to be the best concentration for UV-vis experiments for **63**, **64** and **66**, while 80 μM was chosen for **65** due to the weak absorbance profile of the receptor.

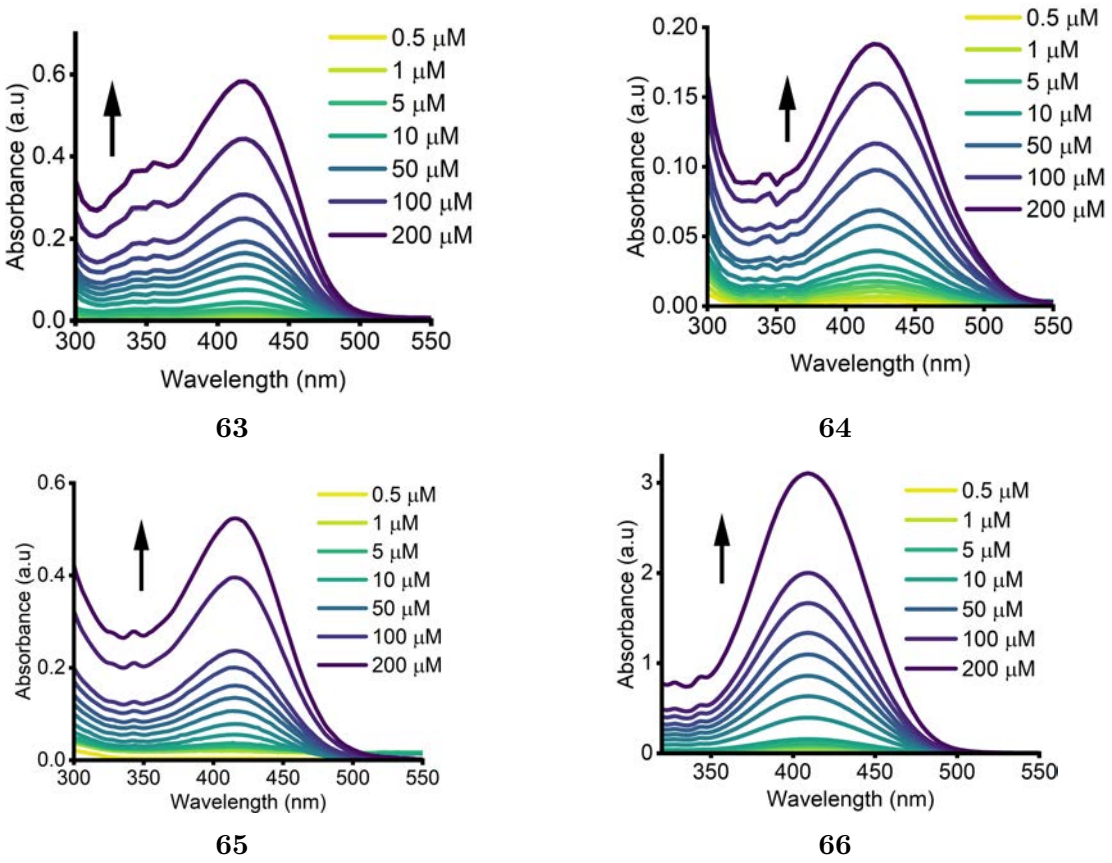

Figure 2.27: Dilution studies of **63** – **66** in 1% water/MeCN through UV-vis spectroscopy. Isotherms presented in the Appendix.

Fluorescence studies performed using the same procedure indicated that a concentration of 5 μM was appropriate for receptors **63** – **66**, with no excimer formation observed (Figure 2.28). Receptors **63**, **64** and **65** exhibited a mostly linear response as receptor concentration increased, while **66** exhibited a linear increase in fluorescence intensity up to 50 μM receptor. After this point, the intensity linearly decreases with concentration

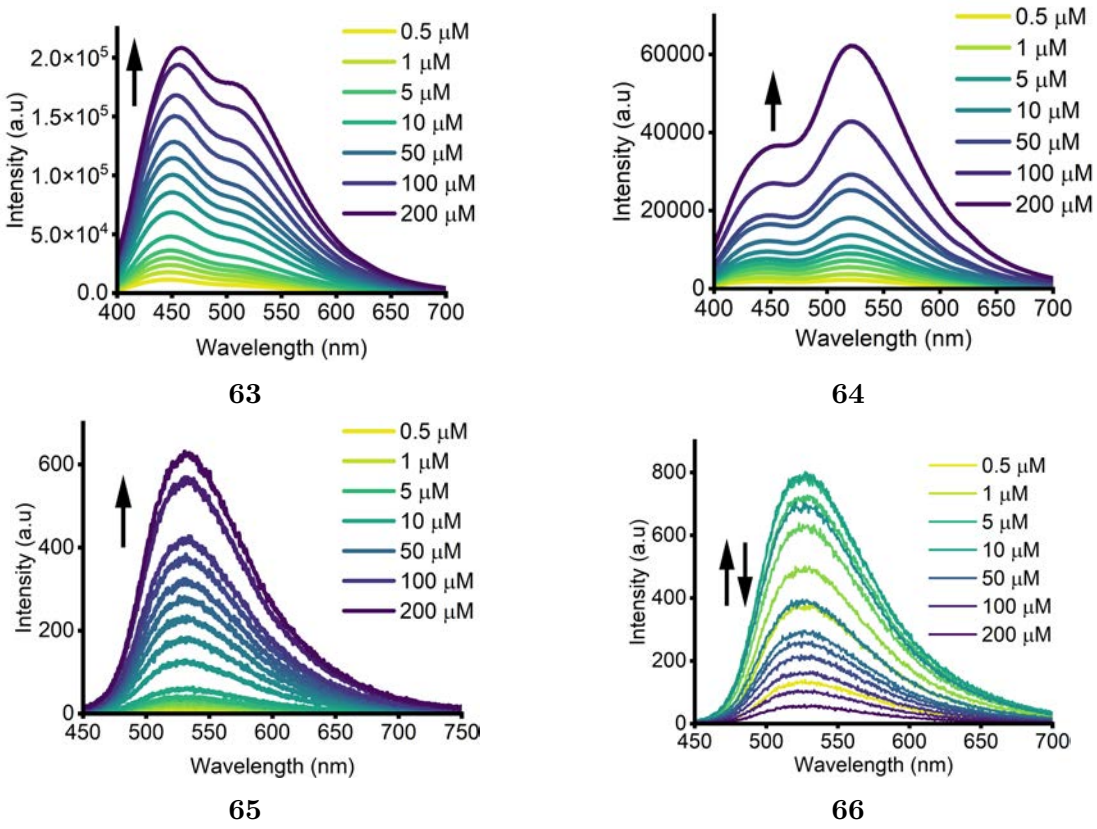

Figure 2.28: Dilution studies of **63** – **66** in 1% water/MeCN through UV-vis spectroscopy. Isotherms presented in the Appendix. (λ_{ex} = of 370 nm, 370 nm, 425 nm and 410 nm respectively).

Determination of suitable solvent for spectroscopic studies

Solvent screens were performed on receptor **63**. Due to the structural similarities and similar optical responses of **64**, this study was only carried out with **63**. To determine whether solvent polarity or viscosity influence the emission response, fluorescence spectra were obtained in different solvents with differing dielectric constants and differing viscosities. The solvents used were glycerol, EtOH, hexanes, DMSO, THF and CH_2Cl_2, and the receptor concentration was kept constant at 5 μM in each experiment.

The results show that the fluorescence response of **63** is highly dependent on the solvent (Figure 2.29). In nonpolar hexane, there is a single emission signal at 487 nm, whereas in ethanol two λ_{max} (441 and 503 nm) are observed. In more viscous solvents like glycerol and DMSO, the fluorescence intensity is almost

completely quenched, while exhibiting this dual emissive response. As this study was performed at the same concentration with the same λ_{ex} value, this response must be due to a property of the solvent. It is known that naphthalimides exhibit solvatochromic properties, which also explains the observed responses.[125]

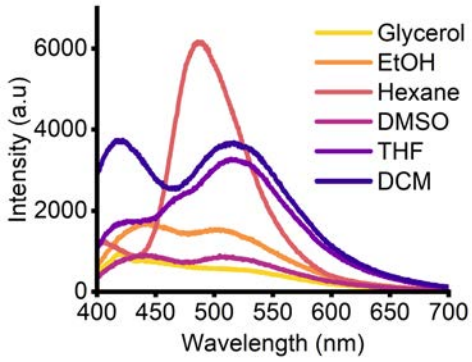

Figure 2.29: Solvent screen of receptor **63** at 5 μM. An excitation wavelength of λ_{ex} = 370 nm was used. The excitation band-pass was set to 5 nm and the emission band-pass was set to 5 nm.

To explore this response further, emission intensity was plotted against the dielectric constant (ε) of the solvents (Figure 2.30a). Fluorescence mechanisms such as CT can be solvent dependent, and may be affected by the solvent properties. ε indicates solvent polarity, with higher ε indicating greater ease of solvent polarisation, leading to potentially stronger interactions between the receptor and solvent. A stronger receptor-solvent interaction implies greater charge on the electron donating portion, increasing charge transfer to the naphthalimide portion, inducing further quenching. This effect has been demonstrated in receptors containing BODIPY functional group undergoing ICT,[126] suggesting that this may also occur for the naphthalimide receptors.

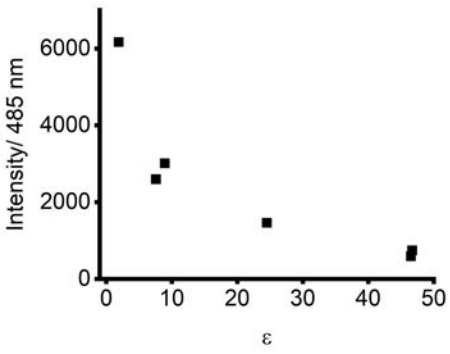

(a) Dielectric constant against intensity at 485 nm.

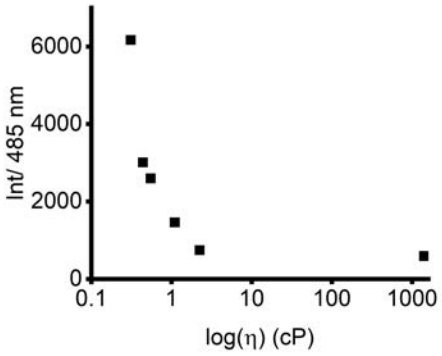

(b) Log(viscosity) against intensity at 485 nm.

Figure 2.30: Graphs extracted from solvent screen of **63** ([probe] = 5 μM, λ_{ex} = 370 nm). The excitation band-pass was 5 nm and the emission band-pass was 5 nm.

In hexane, the least polar solvent studied, a highest intensity fluorescence emission signal at 500 nm is observed, with the absence of a secondary emission signal suggesting that ICT may be occurring as a fluorescence mechanism. As shown in Figure 2.30a, as solvent ε increases, the fluorescence intensity decreases, suggesting greater degrees of CT leading to quenching of the 485 nm signal. As the receptor-solvent interaction increases,the intensity of both λ_{max} varies, suggesting that this may be as a result of CT.

When intensity was plotted against log(viscosity), an unexpected result was observed. Increasing viscosity should increase fluorescence intensity, as collisional deactivation pathways are minimised and bond rotation decreased.[127] However, receptor **63** exhibited a decrease in emission intensity as viscosity increased as shown in Figure 2.30a, alluding to a complex emission mechanism in which internal deactivation pathways are increased as solvent viscosity increases. This response is unexpected, as it has been shown that piperidinyl naphthalimides,[127] which are able to undergo bond rotation at the C-N bond, exhibit decreasing emission intensity with decreasing viscosity. The results obtained have the same trend as the dielectric constant, suggesting that both viscosity and polarity affect emission. Since the changing viscosity also correlated with a changing dielectric

constant, more experiments are required to understand this effect.

After consideration of the solubility of the receptors, it was determined that a 1% water/MeCN mixture was appropriate for all the aza-crown-ether naphthalimides. This allows for easy comparison to the anthracene based receptors. While those system was used, it is clear that the fluorescence properties are complex and reliant on both the viscosity and polarity of the solvent.

Viscosity

To further explore the effects of viscosity on emission, viscosity studies were performed for both **63** and **64**. The receptors were dissolved in glycerol, and the intensity measured with increasing temperature, with increased temperatures reducing the viscosity. This eliminates any effects from changing the solvent to achieve variations in viscosity. As the viscosity decreases, quenching mechanisms such as TICT should increase due to increased rotation and an overall decrease in the fluorescence intensity is expected.

Both **63** and **64** were found to have dual emissive properties. Because the two emission signals overlap, Gaussian deconvolution was performed on the emission spectra, to extract the two signals and plot emission intensities against the viscosity of the solvent (2.31b). The emission intensity increases at both 450 nm and 530 nm as the solution viscosity increases. This suggests that as viscosity increases, bond rotation decreases, leading to increased fluorescence, indicating that a mechanism similar to TICT is contributing to the fluorescence response. For **64**, there is a similar response compared to **63**, with intensity increasing at both 450 nm and 530 nm as viscosity increases as shown in Figure 2.32.

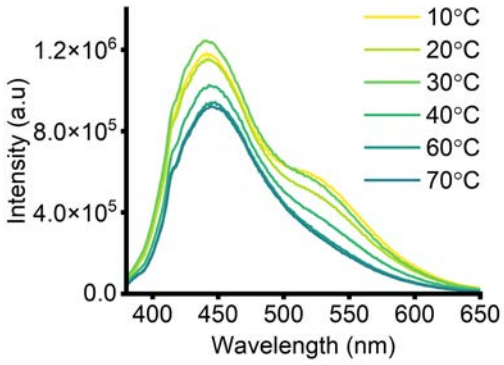

(a) Intensity of **63** as a function of temperature.

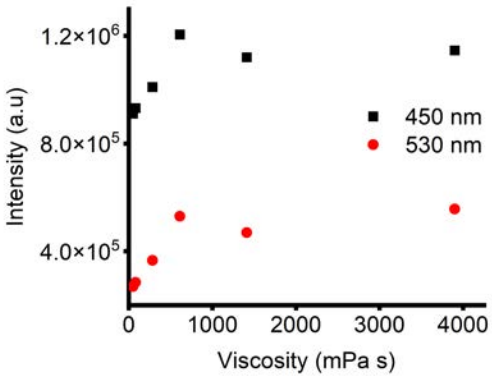

(b) Viscosity plot of **63**.

Figure 2.31: Unnormalised emission data from the viscosity study of **63** in 100% glycerol ([probe] = 5 μM, λ_{ex} = 370 nm).

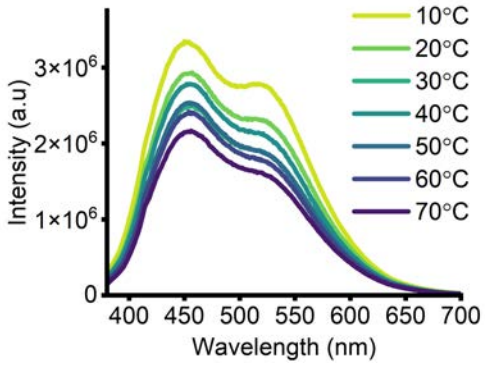

(a) Intensity of **64** as a function of temperature.

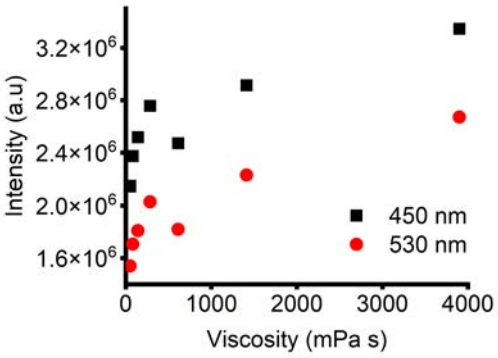

(b) Viscosity plot of **64**.

Figure 2.32: Unnormalised emission data from the viscosity study of **64** in 100% glycerol ([probe] = 5 μM, λ_{ex} = 370 nm).

pH studies

In order to explore the effects of pH on the excitation and emission response of these receptors, a pH study was performed. This was first performed for **63** in 1% water/MeCN. This was done by first acidifying the receptor solution with HCl. To maintain the solvent composition, the water was replaced with aqueous HCl. The pH was altered by addition of the receptor at the same concentration in a basic solution to minimise receptor dilution over the titration.

Examining the emission response in Figure 2.33, the fluorescence intensity of the receptor decreases with increasing pH, and is almost completely quenched at pH 11. This can be reasoned by considering that at this pH the amine is fully deprotonated, maximising the effects of PET quenching. Additionally, examining the excitation spectrum shows almost no change from pH 1.5 to pH 9, however there is a noticeable blue shift at pH 11, with presumably an increase in electron donating capability as pH increases, contributing to an altered HOMO-LUMO gap. This phenomena has been observed in 15-aza-crown-5-ether BODIPY probes,[128] suggesting that this may occur with the naphthalimide systems. The longer wavelength 530 nm emission signal is shown to be present at pH $3-9$. This signal may be attributed to CT processes, suggesting that below the pK_a, the amine is protonated and cannot undergo efficient CT to the fluorophore. The effect of pH is also observed in the excited state as well, as indicated by the excitation spectrum. The rough pK_aH value for similar secondary amines is in the range of 10–11, suggesting that this process results from deprotonation.

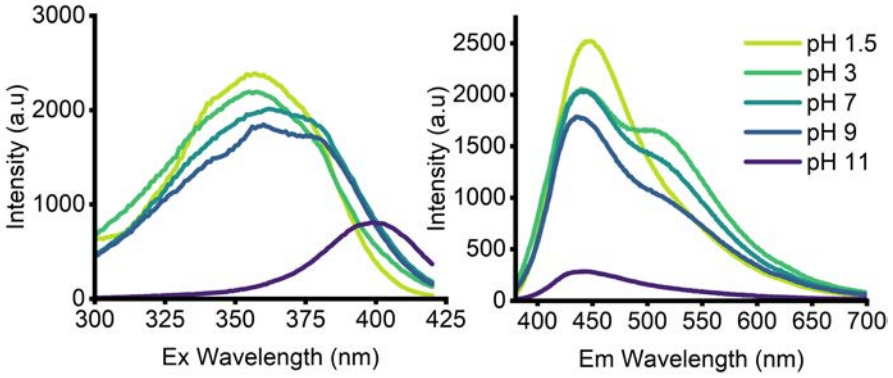

Figure 2.33: Excitation and emission spectra of **63** in 1% Water/MeCN with addition of TBAOH ([probe] = 5 μM, λ_{ex} = 370 nm). The excitation band-pass was 3 nm and the emission band-pass was 3 nm.

Receptor **64** contains two binding sites that can be protonated. The fluorescence intensity increases from pH 2 to pH 7 (Figure 2.34), suggesting that **64** exists in the protonated form in this range. The emission intensity reached a maximum at pH 3 and 7, resulting in an overloading of the detector, causing a distorted signal. As the pH of the solution increases, the intensity decreases, suggesting that above pH 7, the receptor exists in the deprotonated form. The dual emission type character, particularly observed at pH 2, may indicate the existence of two species, in which either amine is protonated. This suggests that metal binding studies performed below pH 11 may result in binding to either species, which may contribute to variation in λ_{max}. This response is observed for **63**, suggesting different protonation states at different pH values, which may influence the observed change in emission after metal addition.

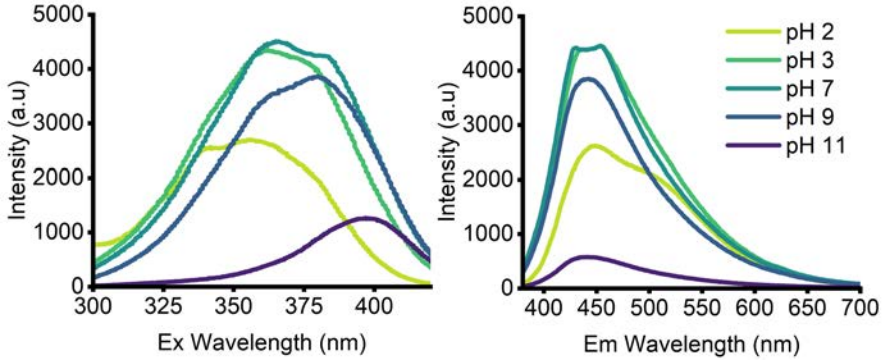

Figure 2.34: Excitation and emission spectra of **64** in 1% Water/MeCN with addition of TBAOH ([probe] = 5 μM, λ_{ex} = 370 nm). The excitation band-pass was 3 nm and the emission band-pass was 3 nm.

Quantum yield and lifetime

The quantum yields for the naphthalimide crown ethers are presented in Table 2.4 and are very low. Increasing the number of nitrogen heteroatoms increased the degree of quenching, with a ϕ of 0.13 for **63** and 0.085 for **64**. This supports the theory that the extra nitrogen lone pair is available for donation to the fluorophore, increasing the rate of PET quenching. Of all four naphthalimide aza-crown-ether receptors, receptor **63** exhibited the highest ϕ. Of the three receptors containing two nitrogen heteroatoms, there is no significant difference when comparing the ϕ values, suggesting that substitution pattern does not have a major effect on brightness.

Table 2.4: Quantum yields of receptor **63**, **64**, **65** and **66** expressed as a ratio.

Receptor	ϕ	**Concentration** (μM)
63	0.13	10
64	0.085	10
65	0.058	5
66	0.063	2

Following this, the fluorescent decay lifetimes were measured for receptors **63** – **65** in 1% water/MeCN. Due to instrumental malfunctions, the lifetime for receptor **66** could not be obtained. Similarly to the anthracene receptor experiments, instrumental requirements required a receptor concentration at which Abs

< 0.05 a.u. Data was analysed and ϕ extracted using the same methods as for the anthracenes.

Table 2.5: Multi-exponential lifetimes of receptor **63**, **64** and **65**. Amplitudes for calculations are presented in Table 7, Table 8 and Table 9 in the appendix.

Receptor	τ_1 (ns)	τ_2 (ns)	τ_{amp} (ns)
63	1.91	9.39	5.50
64	1.39	9.89	9.47
65	4.87	0.55	1.42

The data obtained was analysed in the same way as for **52** and **62**. When comparing the τ_{amp} values, receptor **65** has a faster rate than both **63** and **65** of decay (τ 1.42 compared to 5.50 and 9.47 respectively), indicating more non-radiative transitions such as PET or TICT mechanisms. Interestingly, receptor **63** had a faster decay compared to receptor **64**. Due to the presence of an additional secondary amine in **64**, **64** should exhibit a faster τ due to the potential for more PET quenching between the ligand and the fluorophore. The lower τ for **63** must result from greater degrees of quenching, so it could be reasoned that the structure of **63** may prime it for other quenching mechanisms such as rotational quenching, however this can not be determined from simple photophysical studies.

2.3.3 Barium salt probes

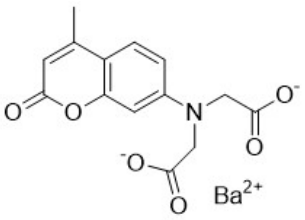

67

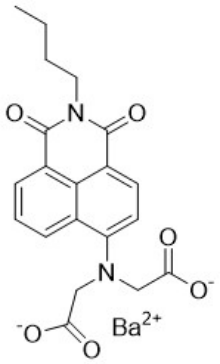

68

This final portion will now focus on the photophysical characterisation **67** and **68**. It will also touch on the characterisation of the isolated intermediates in the form of the ester **79** and **86**, as well as the acid **81** and **88**. In the synthesis

of these receptors, excess $Ba(OH)_2$ was not removed, however the studies were repeated after salt formation with 1 equivalent of $Ba(OH)_2$ and shown to have minimal impact on results. Limitations reduced the experiments performed, with instrumental errors preventing lifetime determination and some naphthalimide characterisation.

Determination of suitable solvent for spectroscopic studies

For these receptors, the best solvent system is one in which the formation of the Ba(II) salt results in a shift in the spectroscopic property, while taking into consideration any potential impacts of pH fluctuation. This is because there needs to be a clear difference in the spectral properties of the complex compared to the free ligand, so extrusion of the metal can be clearly monitored. In order to determine the most ideal solvent system, multiple tests were performed. Firstly, the presence or absence of buffer was tested, followed by buffer type, the ratio of buffer to organic solvent and the nature of the organic solvent.

Un-buffered aqueous systems were explored first with the response of receptor **67**, as the proportion of organic solvent changed. For solubility reasons, mixtures of MeCN and H_2O were used. Through the excitation and emission spectra in Figure 2.36, a fluctuation in excitation intensity was observed as water content varied in addition to the emission intensity, which has been observed in other studies in both naphthalimide[129] and coumarin.[130] Solubility limitations prevented studies of **67** in solvent systems with higher percentages of MeCN.

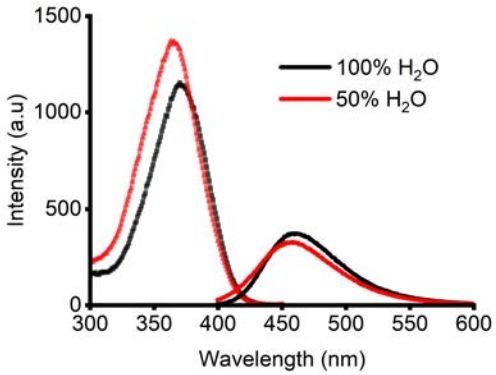

Figure 2.36: Excitation and emission spectra of **67** in unbuffered solvent with MeCN used as the organic solvent ([probe] = 60 μM, λ_{ex} = 370 nm). The excitation bandpass was 5 nm and the emission bandpass was 5 nm.

Following this, the emission profiles of Ba(II) complex **67** and the acid precursor **81** were contrasted to determine if the emission profile changes upon salt formation which would be used to indicate successful metal extrusion in resultant assays. As presented in 2.37a, there is no significant change in emission from receptor **81** to receptor **67**, suggesting that in a completely aqueous system, the metal may be too loosely bound to yield an observable response, or may suggest that there is a higher degree of solvation which is interfering in the emission profile. In comparison, the formation of the salt in 50% water/MeCN was substantially more significant with a fluorescent turn on shown in 2.37b. Due to the substantial change observed upon formation of the Ba(II) salt in a 50% MeCN/Water mixture, this serves as a suitable solvent system for analytical studies.

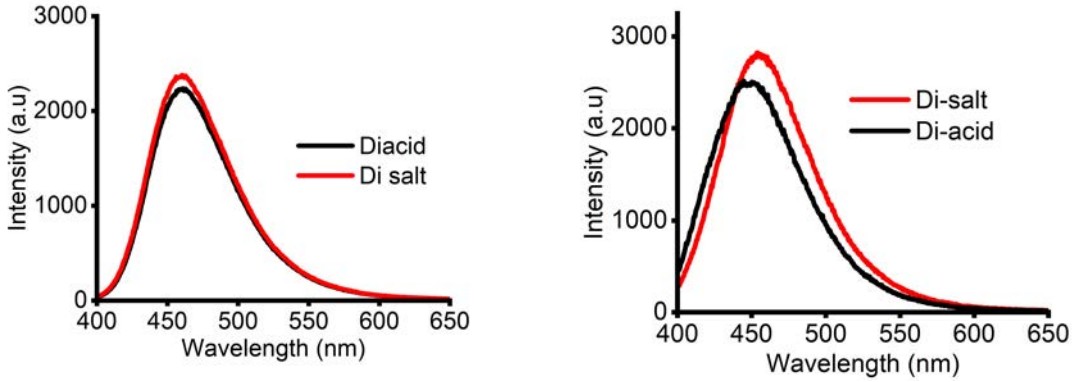

(a) 100% water **(b)** 50% water

Figure 2.37: Comparison of emission profiles between receptor **67** and receptor **81** in 100% water and 50% water/MeCN ([probe] = 10 μM, λ_{ex} = 390 nm). The excitation bandpass was 5 nm and the emission bandpass was 5 nm.

The emission profile of **67** was also explored in a range of buffered systems containing either HEPES, borate or Tris buffers to examine if aggregation or quenching was induced in biological assay systems. In general, the emission of **67** in buffered systems was not quenched, suggesting that aggregative quenching did not occur as presented in the appendix. It cannot be determined if the change in fluorescence intensity was between **81** and **67** was significant in these buffered systems, as this was not explored.

Ultimately, the solvent screens indicated that the emission profile of **67** varies depending on the solvent. A 50% H_2O:MeCN system showed a large change between the acid precursor and the Ba(II) complex. The emission varied depending on the water content of the solvent system, while the results obtained in buffered systems present no discernible trend in the emission profile. Because of the large change in emission between **81** and **67** in the 50% H_2O:MeCN system, this was chosen as a suitable system.

Excitation and Emission

After determining a suitable solvent system, the excitation and emission spectra were obtained for both receptor **67** and receptor **88**. To determine if there was

re-formation of the respective acid, the responses of **67** and **81** were compared in the same solvent system.

To begin, the excitation and emission spectra were obtained for receptor **67** in 100% Water (Figure 2.38). Receptor **67** has a λ_{ex} of roughly 372 nm with a corresponding λ_{em} of 462 nm. This results in a large Stokes' shift, with $\Delta\lambda$ of 90 nm.

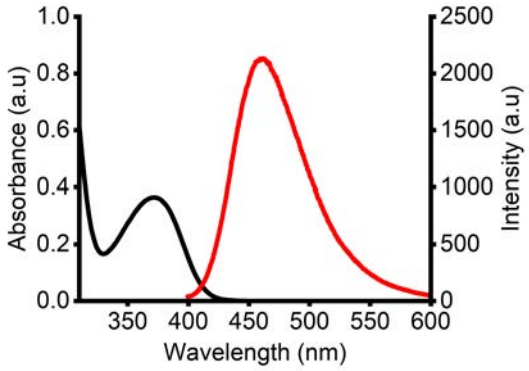

Figure 2.38: Excitation (black) and emission (red) spectrum of receptor **67** in 100% Water (λ_{ex} = 390 nm). The excitation bandpass was 10 nm and the emission bandpass was 10 nm.

Following this, the excitation and emission spectra were determined for receptor **88** in 50% Water/MeCN to maintain receptor solubility as presented in Figure 2.39. As established previously with the coumarin receptors, the response of the acid form closely mimics that of the salt, so these results are assumed to hold true for receptor **68**. From this, the receptor has a λ_{ex} of 431 nm with a corresponding λ_{em} of 534 nm. This results in a $\Delta\lambda$ of 103 nm.

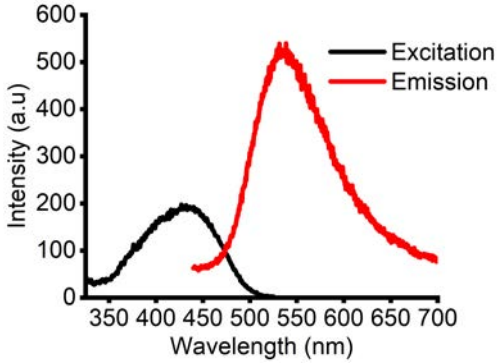

Figure 2.39: Excitation (black) and emission (red) spectrum of **88** in 50% Water/MeCN (λ_{ex} = 430 nm). The excitation bandpass was 5 nm and the emission bandpass was 5 nm.

Dilution studies

Dilution studies were performed using receptor **67** in 50% water/MeCN. Subsequent assays were performed in water, however are at a low enough concentration that the dilution study results are still applicable. The absorbance responses were measured and are presented in 2.40a. Monitoring the absorbance response shows a roughly linear increase in absorbance with increasing receptor concentration. From this, a concentration of 50 μM was deemed suitable for UV-vis studies. The emission response can also be observed in 2.40b. This illustrates a gradual increase in intensity until 100 μM of receptor, at which point quenching is observed along with a slight bathochromic shift. No excimeric effects were observed in this solvent system. From this study, a concentration of 10 μM was deemed acceptable for fluorescence studies.

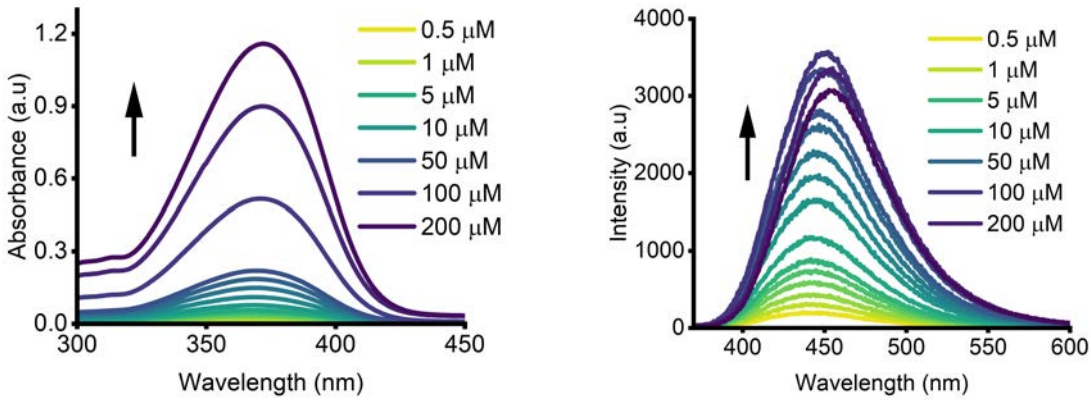

(a) UV-vis **(b)** Fluorescence

Figure 2.40: Dilution study of **67** performed in 50% Water/MeCN (λ_{ex} = 390 nm). The excitation band-pass was 5 nm and the emission band-pass was 5 nm. Dilution study isotherms are presented in the Appendix.

In order to determine the response of **68**, the photophysical properties of **88** were studied to determine appropriate concentrations and solvent systems. Dilution studies were performed using receptor **88** in 50% water/MeCN. The absorbance responses were measured and are presented in 2.41a. Monitoring the absorbance response shows a linear increase in absorbance with increasing receptor concentration. From this, a concentration of 50 μM was deemed suitable for UV-vis studies. The emission response can also be observed in 2.41b. This illustrates a gradual increase in intensity until 150 μM of receptor, at which point slight quenching is observed. No excimeric effects were observed in this solvent system. From this study, a concentration of 5 μM was deemed acceptable for fluorescence studies.

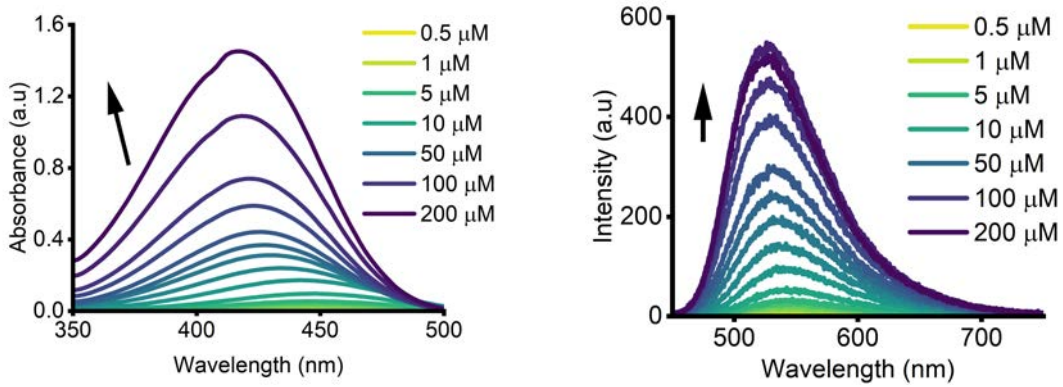

(a) UV-vis **(b)** Fluorescence

Figure 2.41: Dilution study of **88** performed in 50% Water/MeCN (λ_{ex} = 430 nm). The excitation band-pass was 5 nm and the emission band-pass was 5 nm. Dilution study isotherms are presented in the Appendix.

pH studies

It was envisaged that the pH of the solution may have an impact on the metal binding nature of **67**, as pH could change the protonation state of the receptor, and therefore change the MA interaction strength. This changes could occur as presented in Figure 2.42, showing changes in protonation states with pH, which may affect the interaction to the Ba(II) centre. It is anticipated that in basic media, PET quenching would occur, while this would not be observed in acidic or neutral media. In acidic media, there would be no free electrons available for PET quenching, while in neutral media, these electrons are contributing to the MA interaction.

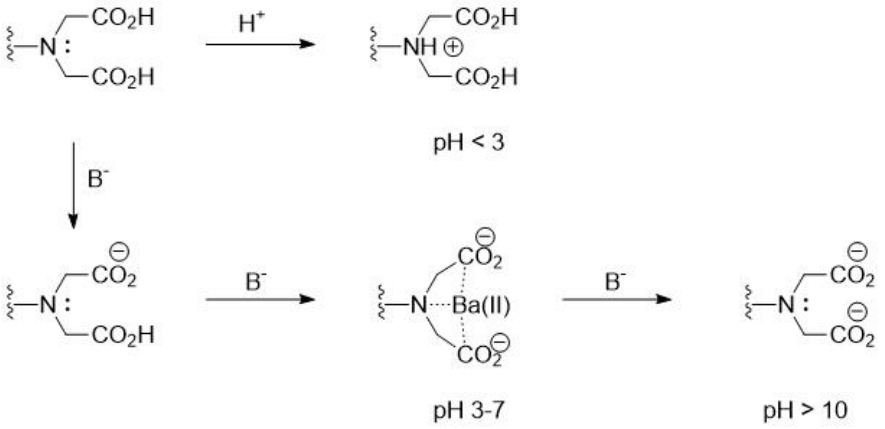

Figure 2.42: Expected changes in ligand for **67** as pH changes.

When examining the effects of pH on **67**, the presence of multiple equilibria processes also complicates the data. As the ligand undergoes protonation at various sites as presented above, each process has it's own pK_a value, while the metal centre itself will form hydrated species in an equilibrium process.[131] The first process involves amine protonation (equation 2.3), while the metal centre undergoes hydrolysis in aqueous solutions (equation 2.4) and the carboxylic acid ligand also has separate equilibrium processes with separate pK_a (equation 2.5). These processes contribute to the fluctuations in the spectral properties as pH changes.

$$NH - R_2 + H_2O \rightleftharpoons NH_2^+R_2 + OH^- \tag{2.3}$$

$$Ba^{2+} + H_2O \rightleftharpoons Ba(OH)_2 + H^+ \tag{2.4}$$

$$H^+ + COO^- \rightleftharpoons COOH \tag{2.5}$$

To attempt to simplify the pH titration data to remove the effects of metal complexation, a pH study was performed on **81** in 50% H_2O:MeCN. Compound **81** was due to fewer equilibrium processes, with only a change in protonation state as a function of pH. Analysis of the pH isotherm indicates a pK_a value of 6 through UV-vis spectroscopy. Fluorescence studies could not be used to evaluate this, as the change in emission intensity was too significant to be satisfactorily fit, however a decrease in intensity was observed from pH 5 until pH 7.5, at which point no further change was observed. From the titration isotherm, studies performed at a pH > pK_a will ensure the ligand is in the anionic form and may be complexed by a metal. This suggests that studies using the corresponding metal salt **67** performed at pH > 7 will involved the complexed metal ligand.

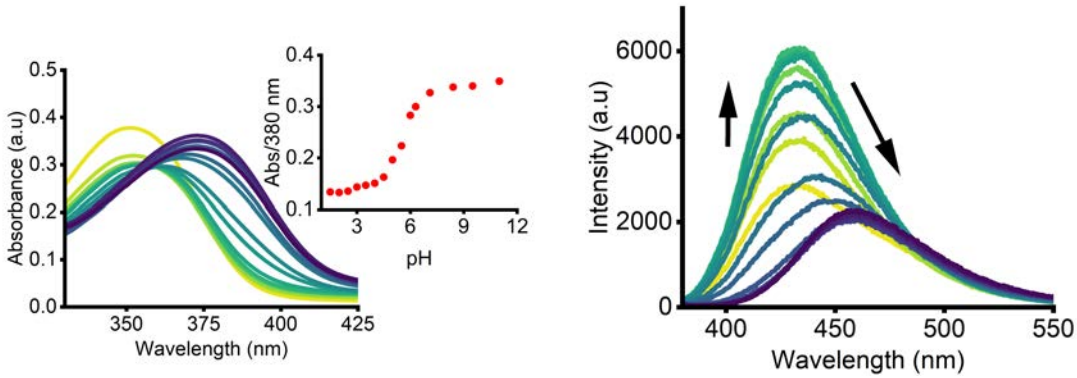

(a) UV-vis **(b)** Fluorescence

Figure 2.43: pH titrations of **81** performed in 50% H_2O:MeCN. Receptor concentration was 10 μM for fluorescence (λ_{ex} = 370 nm, excitation bandpass set to 5 nm and emission bandpass was set to 5 nm) and 60 μM for UV-vis.

These titrations were then performed on **67** to examine if the Ba(II) centre remains bound to the ligand in the desired pH ranges. Through fluorescence spectroscopy (2.44a), quenching was observed at pH > 10 suggesting extrusion of the metal leading to PET quenching from the amine. Quenching was not observed in acidic and neutral media from pH 2 − 7, and it is hypothesised that Ba(II) complexation occurs within this range, as also suggested by the studies performed on **81** showing the anionic form of **81** at pH 6. In contrast, the results obtained through UV-vis spectroscopy indicate that the absorbance of **67** varies depending on pH (2.44b). This may explain the results observed in the solvent screen with varying water concentrations, as fluctuations in solution pH can have a significant impact on the measured spectrum. As the pH of the solution increases, there is a shift in λ_{max}, suggesting that **67** in undergoing a structural change. Due to the substantial changed in the UV-vis spectrum, it could be hypothesised that studies performed using **67** would be more susceptible to solution pH changes.

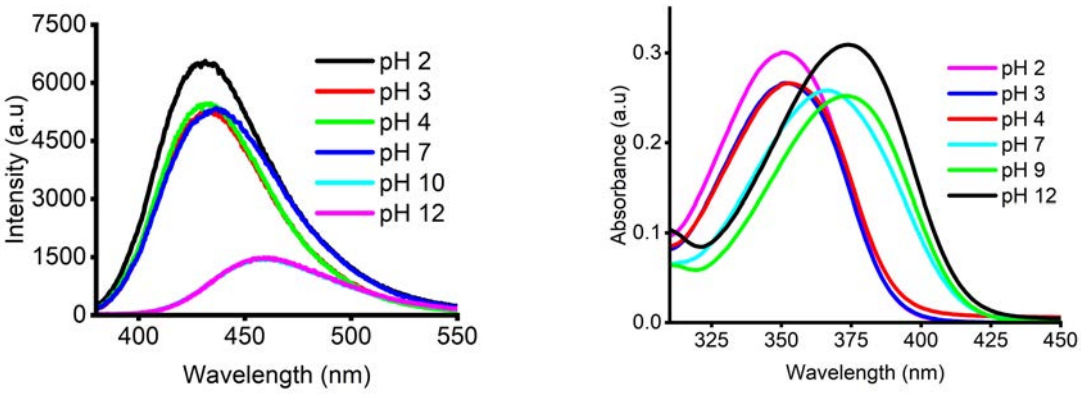

(a) Fluorescence **(b)** UV-vis

Figure 2.44: pH titrations of **67** performed in 50% H_2O:MeCN. Receptor concentration was 10 μM for fluorescence (λ_{ex} = 390 nm, excitation bandpass set to 5 nm and emission bandpass was set to 10 nm) and 60 μM for UV-vis.

Quantum yield

Quantum yields were also obtained for all coumarin and naphthalimide compounds. When comparing the naphthalimides, the studies were performed in the same solvent system of 50% Water/MeCN. The ϕ of the studied compounds decreases from ester **86** to acid **88** (0.61 to 0.013), which may be attributed to increased charge transfer to the fluorophore as a result of the carboxylic acid ligand. After deprotonation to form the salt, the ϕ increases to 0.084 for **68**, but does not return the initial ratio. This slight increase in brightness may be attributed to the acid groups now binding to the metal, reducing the charge transfer properties.

When comparing the coumarin compounds, solubility issues required that receptor **79** needed to be studied in 50% Water/MeCN, so a valid comparison to **81** and **67** cannot be performed, as they were studied in 100% H_2O. This is because quantum yield is solvent dependent. There is still a decrease in brightness when comparing **79** to **81** (0.64 to 0.25). After formation of receptor **67**, there is a slight decrease to 0.22, however the values are roughly the same. All ϕ values are presented in Table 2.6. Equipment malfunctions prevented the collection of lifetime data for compounds **86** – **67**. Due to this, the only photophysical comparison which could be performed was a comparison of ϕ.

Table 2.6: Quantum yields of **86** − **67** expressed as a ratio. The concentrations of each receptor and their respective solvent systems are presented in Table 6.3.

Compound	ϕ
86	0.61
88	0.013
68	0.0841
79	0.64
81	0.25
67	0.22

2.4 Chapter Conclusion

The aim of this thesis is to develop MEAs for sulfate. In order to monitor the extrusion of the metal, and therefore the formation of the free ligand, the photophysical characteristics of the free ligand need to first be determined. A range of techniques were employed to determine the properties of the receptors studied. This chapter first focused on the synthesis of these receptors, and explored difficulties in both synthesis and purification. Following that, the receptors were characterised with standard photophysical methods, which included excitation/emission spectra, solvent, pH studies and viscosity studies for crown ether naphthalimide receptors, quantum yield and lifetime decay determination. Instrumental malfunctions prevented the collection of data for some receptors.

For the anthracene receptors **52** and **62**, the λ_{ex} was determined to be 354 nm, and an appropriate solvent of 1% Water/MeCN was used. The ϕ values were determined to be 0.002 and 0 respectively, indicating high degrees of quenching. Both receptors exhibited a bi-exponential decay, with τ_{amp} of 7.55 and 5.87 respectively, indicating that **62** had more decay pathways leading to a faster decay rate. Dilution studies indicated the concentrations used for both UV-vis spectroscopy and fluorescence spectroscopy were appropriate.

Following this, receptors **63**, **64**, **65** and **66** were studied. λ_{ex} was determined to be 370 nm, 370 nm, 428 nm and 409 nm respectively, and an appropriate solvent of 1% Water/MeCN was used. The emission profile of **63** and **64** was viscosity

dependent and altered by pH. The ϕ values of **63** − **66** were determined to be 0.13, 0.085, 0.058 and 0.063 respectively, suggesting a a low degree of fluorescence intensity. **63**, **64** and **65** all exhibited bi-exponential decay, with τ_{amp} of 5.50, 9.47 and 1.42, suggesting more decay pathways for **65**. Dilution studies indicated that no aggregation was occurring at the concentrations used for both UV-vis spectroscopy and fluorescence spectroscopy.

Finally, **67** and **88** were studied. λ_{ex} was determined to be 372 nm and 431 nm respectively, and an appropriate solvent of 100% water and 50% Water/MeCN was used. The spectroscopic properties of **67** were found to be pH dependent. The ϕ values were determined to be 0.22 and 0.084. Dilution studies indicated the appropriate concentration for studies and were performed by both UV-vis spectroscopy and fluorescence spectroscopy.

Table 2.7: Photophysical properties of receptors explored in this chapter.

Compound	λ_{ex} **(nm)**	λ_{em} **(nm)**	ϕ	τ **(ns)**
52	354	390, 410, 430	0.002	7.55
62	354	390, 410, 430	0	5.87
63	370, 430	460, 530	0.13	5.50
64	370, 430	460, 525	0.085	9.47
65	428	533	0.058	1.42
66	409	576	0.063	-
67	372	462	0.22	-
88	431	534	0.084	-

Understanding these properties will allow for determination of the fluorescence mechanism, and inform the upcoming studies on metal assays for sulfate sensing. The next chapter will focus on the responses of these receptors to a range of metals, to be used in the final chapter for sulfate recognition.

Chapter 3

Metal Recognition

3.1 Introduction

This chapter will focus on the responses of the anthracene and naphthalimide aza-crown-6 ethers described in Chapter 2 to Group (I) and Group (II) metals. These responses are studied through UV-Vis and fluorescence spectroscopy as a tool for monitoring binding events which will build upon the currently existing receptors for these metals and present an opportunity for distinguishing these cations.

3.1.1 Alkali Metal Binding

There are numerous examples of fluorophore appended crown ethers and aza-crown ethers and their ability to bind to and discriminate between Group (I) and Group (II) metals has been extensively investigated. A selection of relevant receptors, such as those with naphthalimide fluorophores, are discussed below.

Two benzocrown-naphthalimide receptors **89a** and **89b** were prepared and their responses to both Mg(II) and Ba(II) investigated in MeCN.[132] These were found to operate *via* PET, which was determined through the minimal change in the UV-vis absorbance spectra in addition to the increase in emission intensity upon M(II) addition to either **89a** or **89b**. This unique response was attributed to the orbital localisation of the HOMO, in which the localisation position varied from **89a** to **89b**. For **89a**, it was observed that the addition of Ba(II) led to initial quenching of emission, followed by an increase in intensity, correlated to

the formation of a 2:1 sandwich complex at low Ba(II) concentrations. As Ba(II) concentrations increased, formation of the 1:1 complex was favoured. In comparison, addition of M(II) to **89b** resulted in an increase in emission intensity with a concomitant wavelength shift, with no 2:1 complex formation, while the overall emissive properties (FEF and ϕ) were lower for the **89b**-Ba(II) complex compared to the **89b**-Mg(II) complex. This example highlights that the functionalisation of the fluorophore can have an overall substantial impact on the binding profile to Group (II) metals, which provides valuable information in the further development of selective M(II) sensors. This also indicates that the optical properties of a naphthalimide sensor may very depending on the metal added, and the fluorescence mechanism can be elucidated.

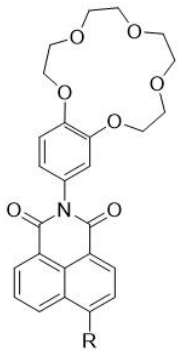

R = NH_2 (**a**), NHCOMe (**b**)

89a and **89b**

Compound	λ_{abs} **(nm)**	λ_{em} **(nm)**	ϕ_y	**LogK**
89a	414	519	0.43	-
89a-Mg(II)	417	521	0.49	-
89a-Ba(II)	417	522	0.45	11.5
89b	366	456	0.003	-
89b-Mg(II)	368	454	0.61	5.33
89b-Ba(II)	368	454	0.071	4.58

Figure 3.1: Benzocrown naphthalimide for Mg(II) and Ba(II) and respective photophysical properties.

The BODIPY based aza-18-crown-6 ether **90** shown in Figure 3.2 was reported to exhibit a ratiometric response with high selectivity for K(I) in MeCN.[133] As the inner cavity of the 1-aza-18-crown-6-ether closely matches the radius of K(I), this was expected to impart size selectivity for K(I). Based on the structure of **90**, the

direct attachment of the aza-crown-ether donor to the BODIPY core resulted in an ICT based sensor, in which the ground state of **90** is initially dark, attributed to direct quenching of the BODIPY core from the donor. Upon the formation of the **90**-K(I) complex, the electron donating capacity of the 1-aza-18-crown-6-ether donor is limited in the excited state, further imparting selectivity for K(I). While this selectivity was observed when compared to Na(I), Li(I) and Cs(I), responses were also observed upon the addition of Mg(II) and Ca(II) to **90** suggesting no inherent selectivity for Group (I) metals over Group (II). The selectivity of **90** for K(I) was explored through molecular dynamics, in which a conformational change was observed upon addition of K(I), indicating encapsulation of K(I) by the 1-aza-18-crown-6-ether and the BODIPY core, however as molecular dynamics was not explored for the remaining Group (I) metals, the observed selectivity cannot be directly correlated to the conformational change. This example indicates that conformational changes arise as a result of receptor binding to M(I) or M(II), which may impart selectivity.

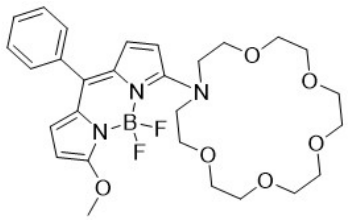

90

Figure 3.2: BODIPY probe for K(I).

The solvatochromic *N*-methyl aza-18-crown-6 ether naphthalimide **91** (Figure 3.3) was studied in response to Group (I) and Group (II) metals.[134] Upon comparison of the emissive properties of **91** to dialkylamino naphthalimides, ICT was determined as the main fluorescence mechanism, in which the 1-aza-18-crown-6-ether donor participates in the π naphthalimide system, changing the resultant energy levels for the $S_1 \rightarrow S_0$ transition. Through spectroscopic studies, the calculated $LogK_a$ was found to not be directly correlated to the observed change in emission. It was further determined that the change in observed emission

was influenced by the nitrogen portion of the ligand, while the LogK_a behaviour was attributed more to the oxygenated portion of the ligand, suggesting that changes in the ligand atoms can influence metal affinity. Photoinduced recoordination was observed upon M(I) and M(II) addition to **91**, in which excitation resulted in a partially coordinated metal complex in which the M-N bond of the 1-aza-18-crown-6-ether is broken, however the M-O bonds remain, which has been postulated in other systems,[135] providing a mechanism of binding. Spectroscopic studies performed in MeCN yielded LogK_a values for Li(I) (2.22), Na(I) (3.76), K(I) (3.56), Cs(I) (2.75), Mg(II) (2.36), Ca(II) (5.69) and Ba(II) (5.26). Due to the similarities to **63**, this example provides a comparison point for the studies performed in this thesis, however the lack of further studies in addition to the sparse experimental conditions and data reported provide a limited comparison. This example also indicates how M(I) and M(II) may bind to 1-aza-18-crown-6-ether receptors, and provides a mechanism of fluorescence through photoinduced recoordination.

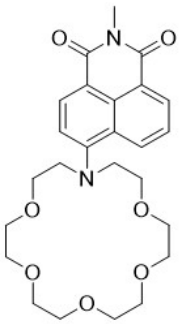

91

Metal	λ_{abs} **(nm)**	λ_{em} **(nm)**	ϕ_y	**LogK**	τ **(ns)**
None	414	540	0.069	-	1.8
Li(I)	414	540	-	2.22	-
Na(I)	400	535	0.29	3.76	4.8
K(I)	378	538	-	3.56	-
Cs(I)	344	552	-	2.75	-
Mg(II)	387	525	-	2.36	-
Ca(II)	385	515	0.75	5.69	8.3
Ba(II)	360	520	0.38	5.26	4.7

Figure 3.3: *N*-methyl aza-18-crown-6-ether naphthalimide for non-selective Group (I) and Group (II) metal recognition and respective photophysical properties in MeCN.

3.1.2 Dual emission sensors

Within the field of fluorescence for analyte recognition, there exists a small number of receptors which have exhibited dual emissive properties, mostly for the detection of transition metals. Examples of the small range of these receptors available for Group (I) or Group (II) metals, with a specific focus on those containing crown ethers or aza-crown-ethers are described below. While there are dual emission sensors which present complex electronic structures and higher order excited states (such as lanthanides emitting from triplet excited states in phosphorescence),[136] there are also simple fluorescent systems exhibiting dual emissive properties, which may arise from multiple different $S_1 \rightarrow S_0$ transitions, such as receptors may exhibit both PET and ICT transitions.

There exists a small amount of information on the use of dual emission sensors, particularly for cation recognition and discrimination. This differs from ratiometric probes, where-by peaks change at a ratio. This dual emission can arise from altering excitation wavelength, or with multiple emission mechanisms. This can be estimated experimentally or computationally. These can potentially be used to identify different metal in a system by monitoring different wavelengths.

In the 4-piperidinyl-1,8-naphthalimide **92**, TICT was found to play a particular role in the dual emissive properties,[127] in which electron donating groups at the 4-position of the naphthalimide have been shown to increase both charge and electron donation to the dicarboximide portion of the fluorophore. This results in an observed long wavelength emission band containing the dark state TICT band. This dark state band was found to be influenced by solvent polarity, in which an increase in ϕ was observed as the solvent polarity decreased, which may be attributed to a reduced charge transfer capability from the donor to the fluorophore. Additionally, TICT was also confirmed through an increase in emission intensity as the viscosity of the solvent decreased. Due to the presence of the dual emission attributed to the dark state TICT $S_1 \rightarrow S_0$ transition, a bi-exponential

τ was observed due to the multiple excited state decay pathways, while Time Dependent-Density Functional Theory (TD-DFT) indicated that conformational changes occur in solution attributed to TICT. This example highlights that M(I) and M(II) sensors may undergo conformation changes when fluorophore substitution of naphthalimides occurs at the 4-position, indicating that the observed emission response may contain multiple complex processes.

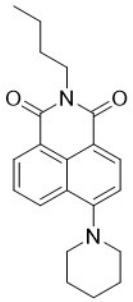

92

Figure 3.4: 4-piperidinyl-1,8-naphthalimide.

A study was performed by Panchenko *et al.*[137] to explore the effects of substitution on 1-aza-15-crown-5 ether naphthalimide receptors shown (Figure 3.5) for the sensing of Ca(II) in MeCN. Substitution of the binding motif at the imide position in **93** and **94** resulted in PET operating as the main emission mechanism, while substitution with the ligand at the 4-position of the naphthalimide resulted in the ICT-based sensor **95**. Calculations attributed this change in emission mechanism to a lower energy HOMO(-1) transition which was observed through a broad absorption band as a result of an increased inductive effect for **95**. This inductive effect arises as the tertiary amine of the ligand exists twisted to minimise repulsion with *peri* hydrogens of the naphthalimide which increases donor ability, while the nitrogen also contributes to the π system leading to the spectral changes. As described for the aza-18-crown-6-ether analogue **91** above,[134] the metal can often be partially coordinated by the oxygenated portion of the ligand, resulting in spectral changes. This example signifies that the fluorescence mechanism of naphthalimide sensors can be changed depending on the substitution

pattern of the receptor.

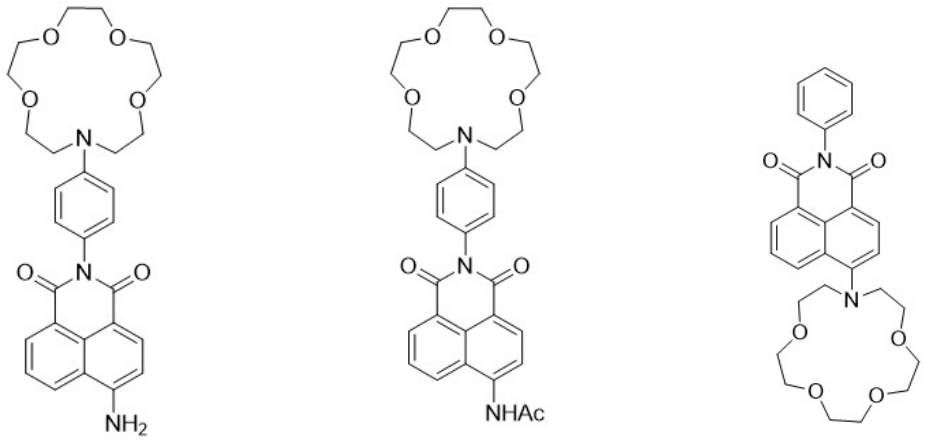

93 **94** **95**

Figure 3.5: 1-aza-15-crown-5-ether PET and ICT based sensors for Ca(II).

Two benzocrown-ether compounds **96** and **97** were developed by Yang *et al.*[138] utilising a *trans*-4-(*N*-arylamino)stilbene recognition motif for the sensing of Mg(II), Ca(II), Sr(II) and Ba(II) in MeCN. This receptor was found to exhibit dual emission based on locally excited-planar intramolecular charge transfer (LE-PICT) as a result of metal ion induced deprotonation of the fluorophore ammonium group under acidic conditions. The addition of $HClO_4$ to both receptors results in the formation of a protonated LE state, with PICT dual emission arising from subsequent M(II) addition, with a comparison of **96** and **97** finding that **97** was more sensitive to Mg(II). While the exact cause of this selectivity was not discussed in detail, it is attributed to the effect of the cyano group on the basicity of the amine. The overall binding profile and $LogK_a$ values for **96** were determined for Mg(II) (4.2), Ca(II) (4.1), Sr(II) (3.9) and Ba(II) (3.8), while for **97** affinities for Mg(II) (5.2), Ca(II) (5.0), Sr(II) (4.8) and Ba(II) (4.7) were determined. This example indicates that dual emission may arise from alternative pathways, such as metal ion induced deprotonation, however this does not alter the selectivity of these receptors.

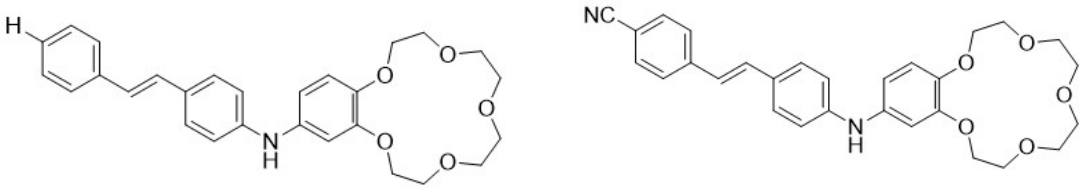

96 **97**

Receptor	Cation	LogK$_a$
96	Mg(II)	4.2
	Ca(II)	4.1
	Sr(II)	3.9
	Ba(II)	3.8
97	Mg(II)	5.2
	Ca(II)	5.0
	Sr(II)	4.8
	Ba(II)	4.7

Figure 3.6: Benzocrown derivatives for Group (II) metal sensing and corresponding LogK$_a$ values in MeCN.

3.2 Results

This section will focus on the photophysical responses of the previously synthesised aza-crown-ether receptors to metal ions to inform subsequent Metal Extrusion Assays. The responses of the receptors to metal ions were characterised using fluorescence and UV-vis spectroscopy, as well as competition studies, ϕ and τ in the presence of Group (I) and Group (II) metals. For all titrations, results are presented for 3 titrations, τ results show the average of 3 trials per sample, while ϕ was recorded once per compound.

3.2.1 Anthracene Receptors

52 **62**

Initially a screen was performed to determine which metals induced a UV-vis

or fluorescent response when added to compounds **52** and **62**. For all receptors, screens were performed by adding excess (> 100 equivalents) metal salt containing the non-coordinating counter-ion into a solution containing the receptor at constant concentration of 40 μM for UV-vis spectroscopy and 5 μM for fluorescence spectroscopy. While the perchlorate salt was used for most cases, limitations in obtaining this counterion for some metals existed. A range of Group (I) and Group (II) metals were screened using cations commonly found in biological assay samples. Additionally, Zn(II), Cs(I) and Sr(II) were screened, in order to identify any binding trends in each group. Zn(II) was included as an example of a biologically relevant transition metal.

The results obtained in the UV-Vis spectroscopy metal screens are presented in Figure 3.8 for **52** and **62**. With the exception of Li(I), the addition of Group (I) metals did not result in significant changes in the absorption spectra for either **52** or **62**. The addition of Li(I) resulted in a small shift in λ_{max} for **52**, with a larger change in λ_{max} observed upon the addition of Li(I) to a solution of **62**. Upon the addition of Group (II) metals and Zn(II), a small shift in λ_{max} was observed upon the addition of Zn(II) to either **52** or **62**. In all cases, the observed change was greater upon metal addition to a solution of **62** when compared to the response of **52** to the same metals, suggesting a higher level of sensitivity in the receptor containing two nitrogen heteroatoms. However, these responses were not substantial enough. Therefore, fluorescence spectroscopy was used to further evaluate these receptors.

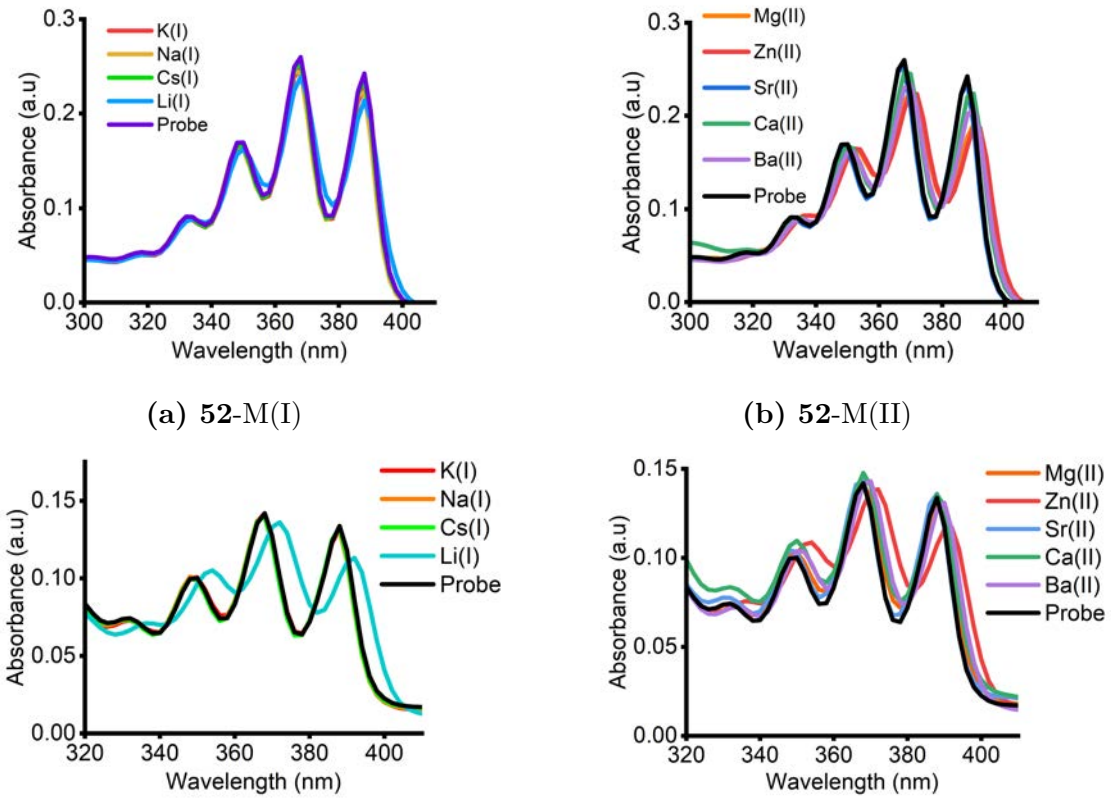

(a) **52**-M(I) **(b)** **52**-M(II)

(c) **62**-M(I) **(d)** **62**-M(II)

Figure 3.8: Response of **52** and **62** to various metal salts in excess performed in 1% H_2O/MeCN through UV-vis ([probe] = 40 μM).

The responses of **52** and **62** to metal ions obtained using fluorescence spectroscopy are presented in Figure 3.9. In general, more pronounced changes were observed in the fluorescence spectra upon metal ion addition than were observed with UV-vis spectroscopy. Upon the addition of Group (I) metal ions, an increase in emission intensity was observed for K(I) and Li(I) for both **52** and **62**, with **52** exhibiting a larger response to Li(I) while **62** had the largest response to K(I). Upon the addition of Cs(I) to these receptors, minimal change was observed, however this may be attributed in part to the low solubility of the cesium carbonate salt used. **62** also showed a response upon the addition of Na(I), in addition to K(I) and Li(I). Upon the addition of Group (II) metals and Zn(II), there was an observed turn-on response observed upon addition of Mg(II), Zn(II), Ca(II) and Ba(II), however this degree of turn-on for Mg(II) was lower for **62** when compared to **52**. It is noted that the addition of Mg(II), Ba(II) and Zn(II)

to **52** resulted in an overloaded detector when obtaining the emission profile due to the large increase in emission intensity in this screening experiment. Due to detector overload, a sensitivity comparison cannot be performed between **52** and **62**.

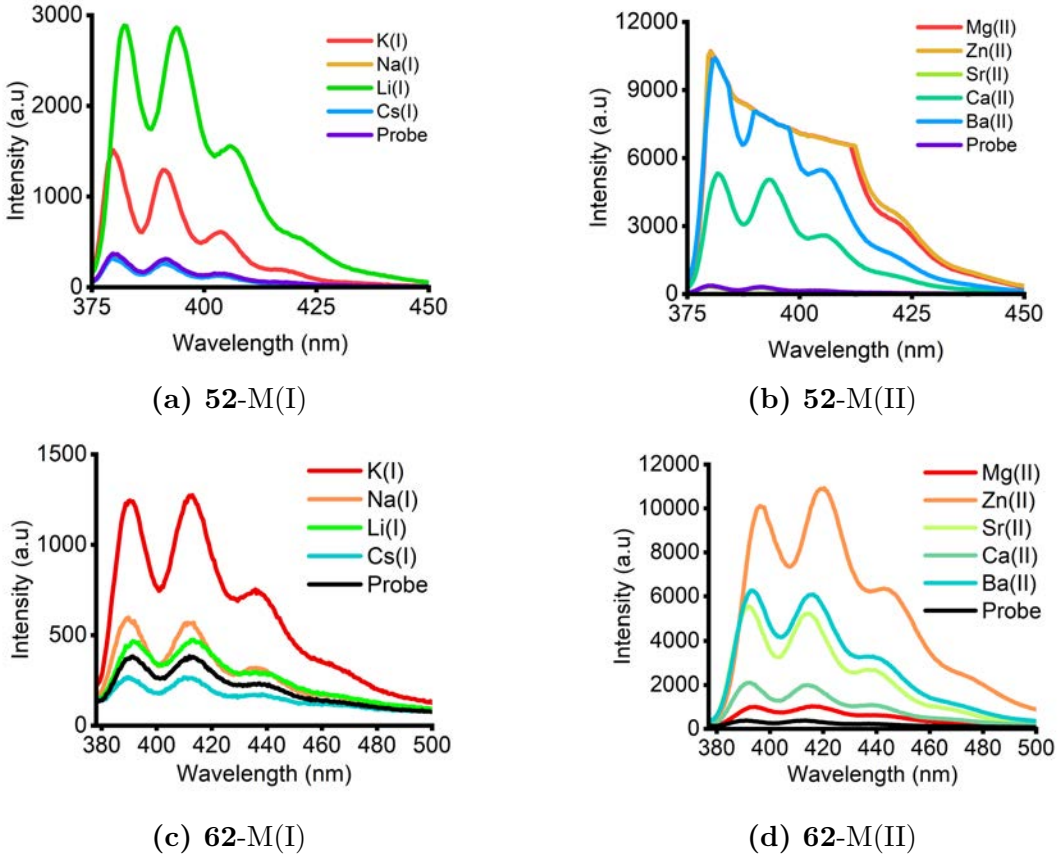

(a) 52-M(I) **(b) 52**-M(II)

(c) 62-M(I) **(d) 62**-M(II)

Figure 3.9: Response of compound **52** and **62** to various metal salts in excess performed in 1% H_2O/MeCN through UV-vis ([probe] = 5 μM, λ_{ex} = 354 nm).

By taking the ratio of the intensity of the metal complex and the intensity of the free receptor, the results of the metal screens for **52** and **62** are presented by the fluorescence enhancement factor (FEF) in 3.10a and 3.10b respectively. While the addition of Zn(II), Ba(II) and Mg(II) to **52** seemingly resulted in the same FEF, this is attributed to the overloaded detector, which skews the results and prevents comparison between these three metals. Regardless, Group(II) metals induced a larger FEF compared to Group(I) for both receptors. Upon addition of metal ions of the same ionic radii, such as in the case of K(I) and Ba(II), a higher sensitivity was observed for both **52** and **62** for the doubly charged ions.

FEF studies at lower concentrations were not performed as it was believed that comparison of titrations isotherms provided more valuable information, however this study could be performed in future at a lower concentration to determine sensitivity. The response of **62** follows the cation-cavity size relationship also seen in 18-crown-6-ethers, where optimally sized cations (K(I) and Ba(II)) induced the largest changes in emission while larger and smaller cations resulted in reduced emission.

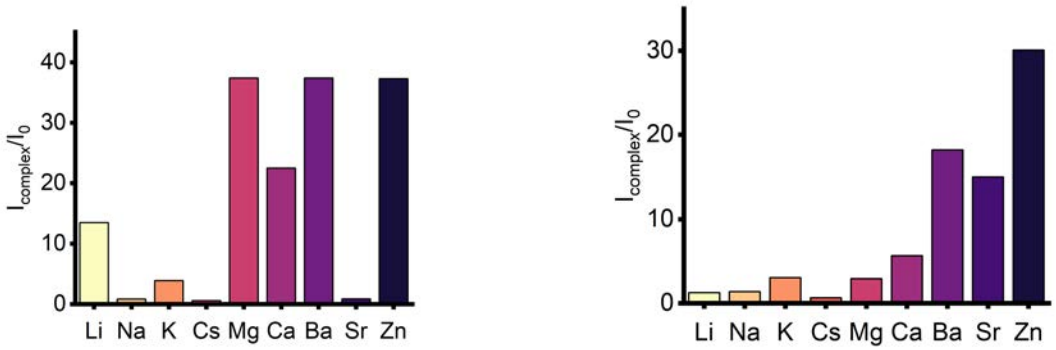

52 **62**

Figure 3.10: Calculated FEF upon addition of excess metal salts (> 100 equivalents) performed in 1% H_2O/MeCN ([probe] = 5 μM) using the instrumental conditions above. Detector saturation was observed for **52** for Mg(II), Ba(II) and Zn(II).

For all titrations in this thesis involving both the anthracene and naphthalimide receptors, two isotherm fitting programs were utilised- BindFit and the Hyperquad HypSpec program. Using BindFit, data was fit to a 1:1 model, and further stoichiometries explored if a poor fit (based on error analysis) was observed. Hypspec can provide more detailed information in cases where complex equilibria may be present, such as for metal-ligand binding (where there may be multiple stoichiometries). Additionally, HypSpec performs full spectrum analysis, which is useful where there may be overlapping spectra due to partial complexation between metal and ligand.[139] Where HypSpec was employed for $LogK_a$ determination, no isotherm fit line is provided as HypSpec performs global fitting at all wavelengths and does not provide single wavelength isotherms, presenting a technical limitation of the program.

Fluorescence spectroscopic titrations were then performed through the addition of Li(I), K(I), Mg(II), Ba(II), Zn(II) and Ca(II) salts to a solution of **52** and Sr(II), K(I), Mg(II), Ba(II), Zn(II) and Ca(II) to **62** in 1% H_2O/MeCN (Figure 3.11 and Figure 3.12). In all cases, an increase in emission intensity was observed, with the resultant data fit to the appropriate binding models using both BindFit and HypSpec. With the exception of Ba(II), Ca(II) and Zn(II) for **52** and Sr(II), Ca(II) and Zn(II) for **62**, the other metal complexes were found to fit to a 1:1 binding stoichiometry, with $LogK_a$ values obtained as summarised in Table 3.1.

Table 3.1: Tabulated $LogK_a$ values for **52** and **62** in 1% H_2O/MeCN upon the addition of Group (I) and Group (II) salts obtained through fluorescence spectroscopy with errors presented in the Appendix (n = 3)

Receptor	**Metal**	**LogK_a**
52	Li(I)	3.51
	K(I)	5.71
	Mg(II)	4.69
62	K(I)	4.08
	Mg(II)	4.09
	Ba(II)	5.14

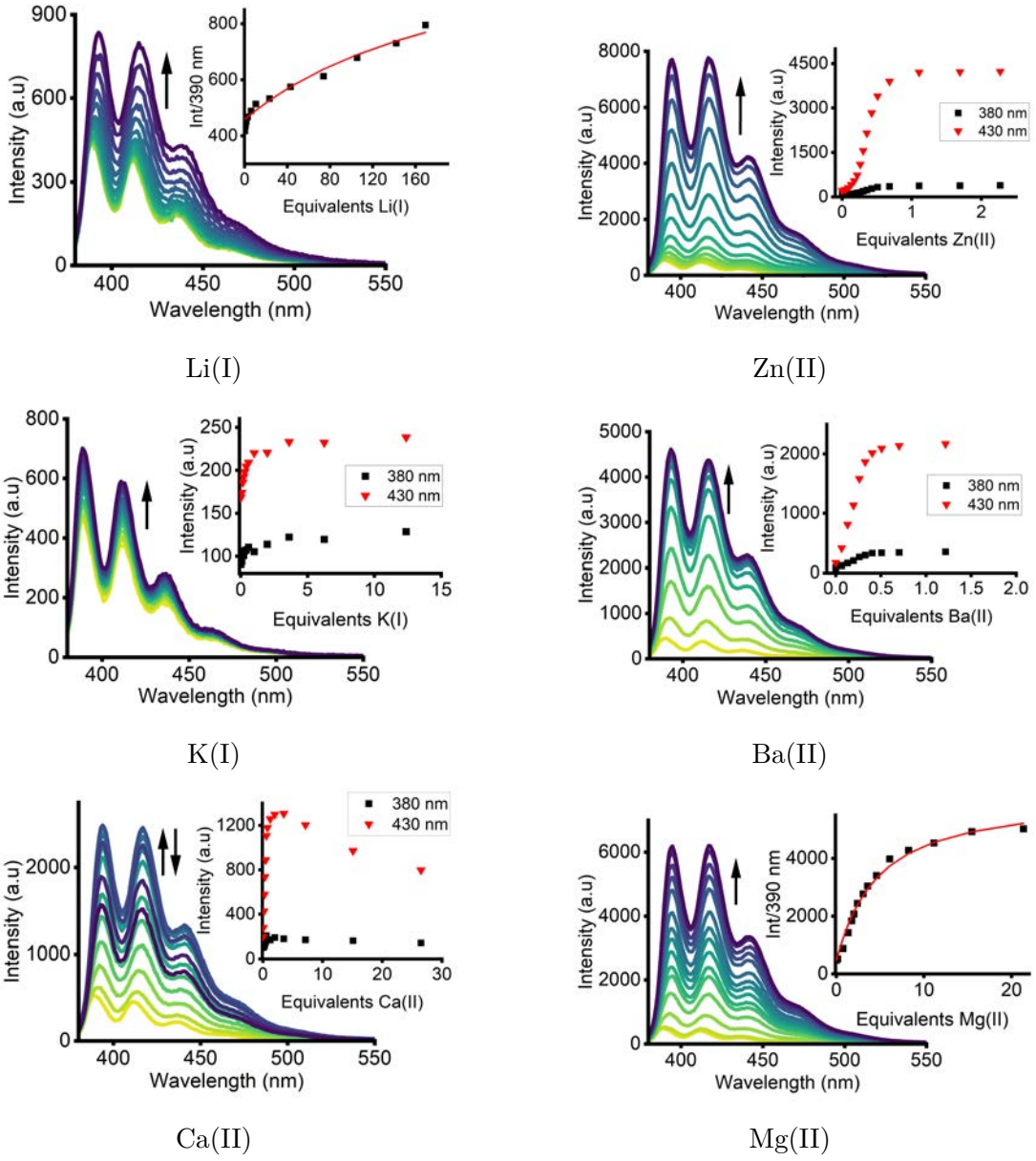

Figure 3.11: Fluorescence titrations of **52** to increasing equivalents metal salts performed in 1% H_2O/MeCN ([probe] = 5 μM, λ_{ex} = 354 nm). The excitation band-pass was 10 nm and the emission band-pass was 5 nm. The red line indicates the fit generated by BindFit. Ba(II) isotherm was fit using HypSpec resulting in no fit line generated.

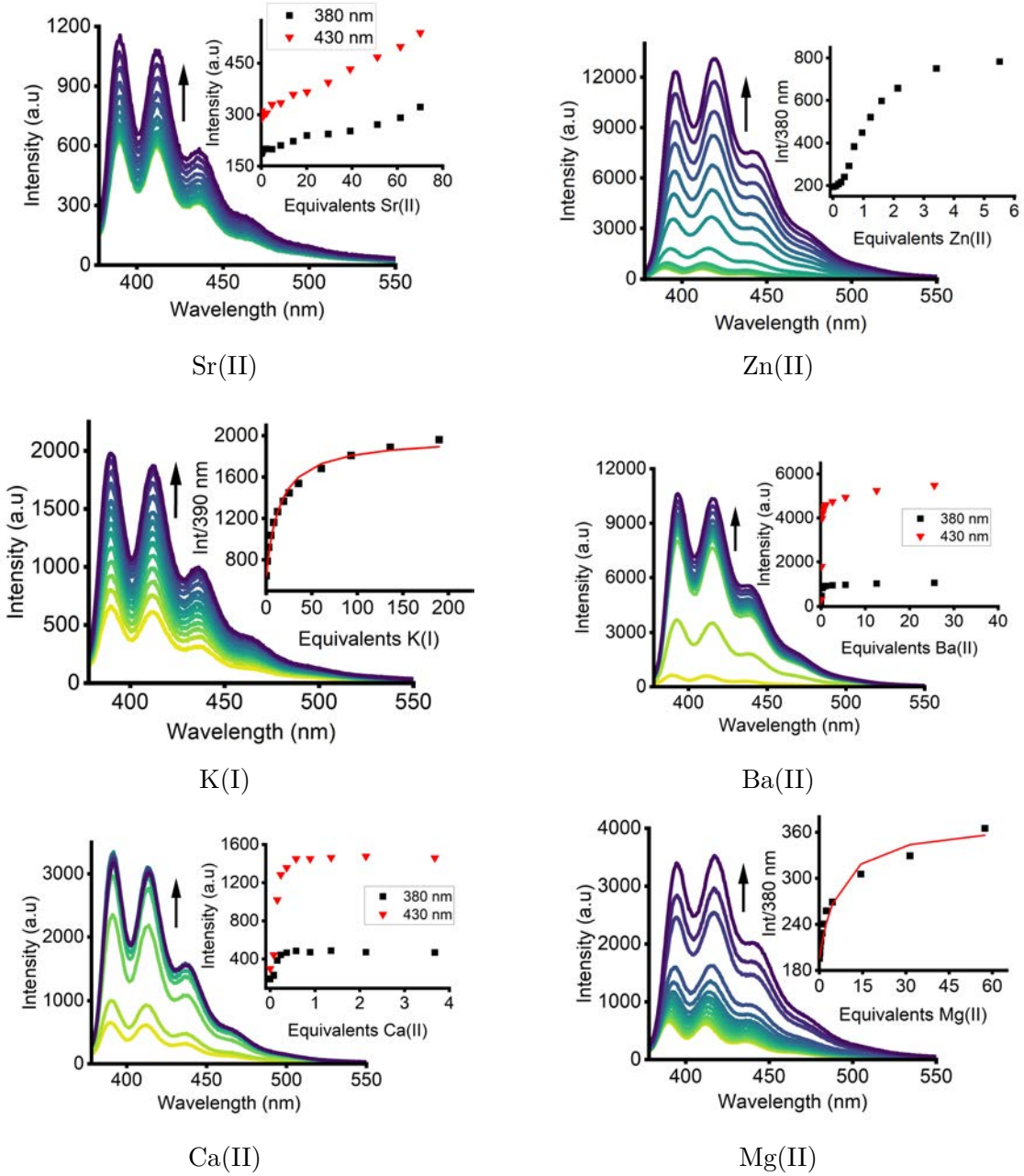

Figure 3.12: Fluorescence titrations of **62** to increasing equivalents metal salts performed in 1% H_2O/MeCN ([probe] = 5 μM, λ_{ex} = 365 nm). The excitation band-pass was 10 nm and the emission band-pass was 10 nm. The red line indicates the fit generated by BindFit.

Inspection of the binding isotherms of **52** with Ba(II) and Zn(II) indicates that a maximum intensity is observed upon addition of approximately 0.5 equivalents of metal ion in both cases, suggesting the formation of a 2:1 binding stoichiometry in 1% H_2O/MeCN. However, the binding data could not be fit to a 2:1 model in either case, while the isotherm for Ca(II) indicates complex equilibria occurring (a decrease in emission intensity after 2 equivalents), preventing isotherm fitting. For **62**, inspection of binding isotherms indicates that a maximum intensity is observed upon addition of approximately 0.5 equivalents of metal ion for Ca(II), suggesting the formation of a 2:1 binding stoichiometry in 1% H_2O/MeCN, while the addition of Sr(II) resulted in weak binding with full complexation of the receptor not occurring over the titration. The binding data for Ca(II) could not be fit to a 2:1 model, while the binding data for Sr(II) could not be fit to a 1:1 binding model. Upon the addition of Zn(II), cooperativity a sigmoidal binding isotherm was observed, also observed for **52**, suggesting that both compounds bind in different stoichiometries to the other metal ions. An overall trend in $LogK_a$ values of K(I) > Mg(II) > Li(I) for **52** was obtained, and Ba(II) > Mg(II) > K(I) for **62**.

The binding data indicate that the strongest interaction arises with the formation of the Ba(II)-**62** complex, demonstrating that this may arise from the differences in donor atoms, with the additional Nitrogen heteroatom seeming to increase ML interactions. While size complementarity may influence these interactions, both binding motifs have the same size internal cavity, implying that this does not influence binding interaction strength. Due to the complex processes preventing $LogK_a$ values from being determined for all metal complexes, a valid comparison exploring the effect of ligand heteroatom variation between **52** and **62** is difficult to perform.

The receptors can additionally be characterised by monitoring the ϕ and τ. In the instance in which a receptor may not be selective through fluorescence

spectroscopy, or where guest introduction has minimal effect on the emission intensity, receptors may exhibit a selective ϕ or τ response, allowing them to be used for selective recognition using these methods. For ϕ and τ measurements, these were only performed with metal complexes which induced a change in emission as observed in the prior metal screens. Upon the addition of Li(I), K(I), Ca(II), Mg(II), Ba(II) or Zn(II) (Table 3.2) to a solution of **52** (with a ϕ of 0.002), an increase in ϕ was observed, which can be attributed to the prevention of internal quenching between the aza-crown ether nitrogen to the fluorophore. The largest $\Delta\phi$ was observed upon formation of the **52**-Ba(II) complex ($\phi = 0.21$). The addition of K(I) to **52** resulted in minimal changes in ϕ, suggesting that similarly sized cations may be distinguished using this method, as K(I) and Ba(II) have similar ionic radii however induced a noticeably different response in ϕ.

Table 3.2: Quantum yields of **52** and **62** metal complexes expressed as a ratio with a [probe] of 3 μM (n =1).

Metal complex	ϕ
52	0.002
52-Li(I)	0.15
52-K(I)	0.0097
52-Ca(II)	0.022
52-Mg(II)	0.11
52-Ba(II)	0.21
52-Zn(II)	0.2

Metal complex	ϕ
62	0
62-Ba(II)	0.11
62-Ca(II)	0.032
62-Zn(II)	0.28
62-Mg(II)	0.019
62-Sr(II)	0.002
62-K(I)	0.015

Upon the addition of Ba(II), Ca(II), Zn(II), Mg(II), Sr(II) or K(I) (Table 3.2) to a solution of **62** (with a ϕ of 0), an increase in ϕ was observed, which can be attributed to the prevention of internal quenching between the aza-crown ether nitrogen to the fluorophore. The largest $\Delta\phi$ was observed upon formation of the **62**-Zn(II) complex ($\phi = 0.28$), followed by Ba(II) ($\phi = 0.11$). These results are similar to those obtained for **52**, in which the addition of K(I) results in minimal $\Delta\phi$, suggesting that these receptors could be used to distinguish K(I) from Ba(II) by monitoring $\Delta\phi$.

Upon the addition of Group (I) and Group (II) metals to a solution of **52**, the

τ was measured using a bi-exponential decay model (suggesting multiple excited state decay pathways from $S_1 \rightarrow S_0$), which was determined by observing the χ^2 values. In analysis of τ, it can be determined that a decrease in τ upon metal complex formation when compared to the free ligand, suggests increased rates of non-radiative decay, as a result of electronic quenching processes or bond rotations, causing energy loss to the environment. Upon the addition of Ba(II), Ca(II), Zn(II), Mg(II), Li(I) or K(I) (Table 3.3) to a solution of **52**, a decrease in τ was observed only upon the formation of the Ba(II) complex (7.55 ns for **52** to 7.23 ns as the **52**-Ba(II) complex), suggesting that this receptor could be used to selectivity detect Ba(II) as a τ sensor. This also suggests that complex formation induces a faster rate of decay, which contributes to the complex titration data obtained. This effect was not observed for metals of the same charge, or metals of similar ionic radii. In contrast, upon the addition of Ba(II), Ca(II), Zn(II), Mg(II), Sr(II) or K(I) (Table 3.3) to a solution of **62**, all metals resulted in an increase in τ in contrast to **52**, suggesting no metal selectivity through monitoring τ, indicating that the variation of the ligand to incorporate a second nitrogen atom diminished the selectivity of the anthracene receptors as a τ sensor.

Table 3.3: Bi-exponential lifetimes of **52** and **62** metal complexes in 1% H_2O/MeCN with a [probe] of 3 μM. Amplitudes for calculations are presented in Table 4 and Table 6 in the appendix (n =3).

Complex	τ_{amp} (ns)
52	7.55
52-Ba(II)	7.23
52-Ca(II)	10.85
52-Zn(II)	9.10
52-Mg(II)	8.99
52-Li(I)	10.99
52-K(I)	19.23

Complex	τ_{amp} (ns)
62	5.87
62-Ba(II)	8.15
62-Ca(II)	6.60
62-Zn(II)	10.27
62-Mg(II)	8.77
62-Sr(II)	8.13
62-K(I)	6.86

3.2.2 Naphthalimide Receptors

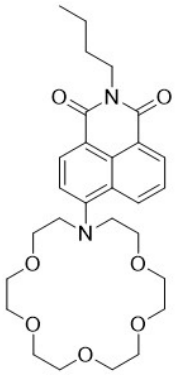

63

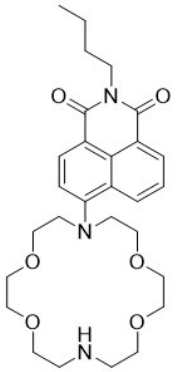

64

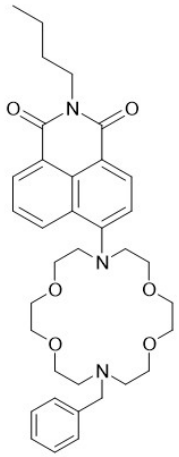

65

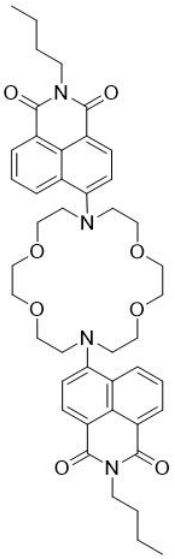

66

The analysis of fluorescence spectroscopy data upon guest addition to a host solution presents additional challenges in the data analysis process. This complexity arises from excited-state association processes, resulting in titration isotherm inflection points which may be due to properties which do not directly correlate with binding constants. In the instance in which a fluorescence system contains two excited state species and two ground state species (potentially attributed to multiple fluorescence mechanisms), the 1:1 binding system can be portrayed below in Figure 3.14, with this presenting the simplest case of solution behaviour. In this simple case, it can be assumed that the true binding mechanism may consist of multiple complexation events, or multiple equilibrium events of the molecules in solution in addition to quenching mechanisms.[140] Due to the complexity associated in this process, the K_a determination considers the rate constants of each process according to equation 3.1, which is not typically considered in traditional binding software. In order to avoid these complexities in binding isotherm analysis, UV-vis spectroscopy is often used, as these ground state transitions cannot be observed through UV-vis spectroscopy, hence resulting in easier calculations.

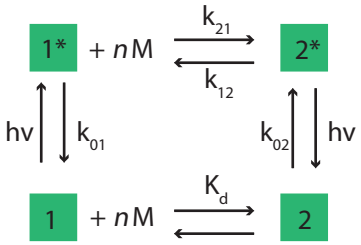

Figure 3.14: Fluorescent receptor-ion binding general mechanism where n is the stoichiometry for a 1:n system.[140] **M** represents a guest/analyte and k represents the rate constants.

$$K_d = \frac{k_{01}(k_{02} + k_{01})}{k_{02}k_{21}}, \quad K_a = \frac{1}{K_d} \tag{3.1}$$

The results obtained in the UV-Vis spectroscopy metals screens are presented in Figure 3.15 for **63**, Figure 3.16 for compound **64**, Figure 3.17 for **65** and 3.18b for **66**. With the exception of compound **66**, which exhibited no response to any metal, the addition of K(I) resulted in a λ_{max} shift, with this change being smaller for **65** than for **63** and **64**. A similar, but smaller, response was also observed upon the addition of Na(I), while the addition of Cs(I) and Li(I) resulted in minimal changes in the absorbance spectra. Upon the addition of Group (II) metals to a solution of each receptor (barring **66**), Ba(II) resulted in the formation of a new defined signal at $\lambda_{max} = 360$ nm in addition to reduction of the signal at 430 nm, with this response only observed for Ba(II). The formation of a broad signal with similar λ_{max} was observed for the addition of Mg(II) to **63**, but in this case there was no reduction of the signal at 430 nm. The addition of Zn(II) to **64** and **65** resulted in a broad signal. In all cases, no response was observed for Sr(II) and Ca(II), with the unique spectral trace only observed for the Ba(II) complexes.

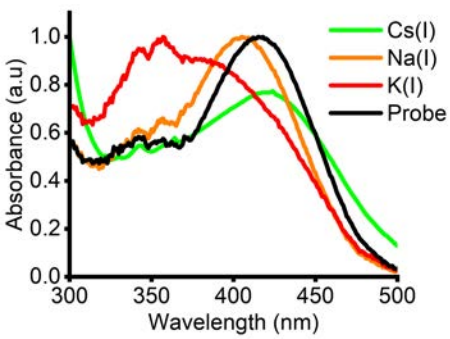

(a) Group (I)

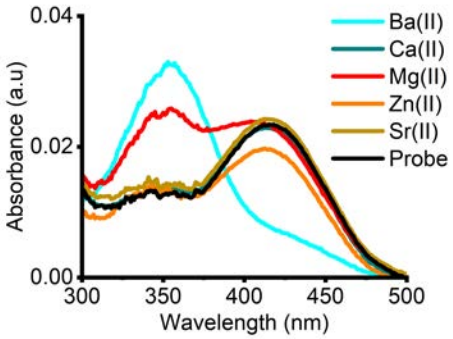

(b) Group (II)

Figure 3.15: Response of **63** to a range of metal salts through UV-vis in 1% H_2O/MeCN ([probe] = 40 μM).

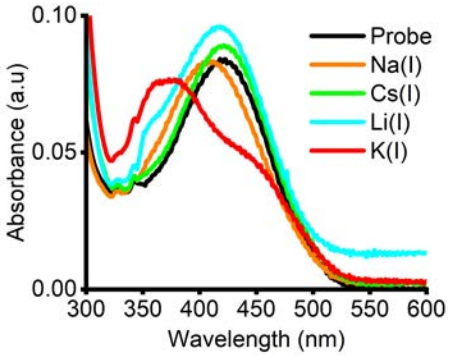

(a) Group (I)

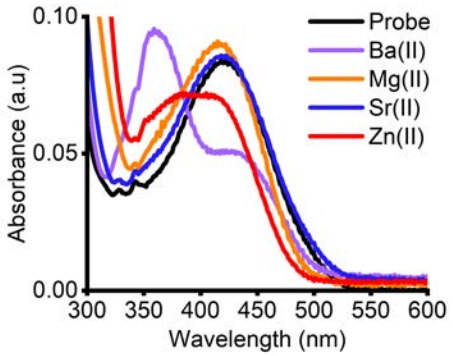

(b) Group (II)

Figure 3.16: Response of **64** to a range of metal salts through UV-Vis in 1% H_2O/MeCN ([probe] = 40 μM).

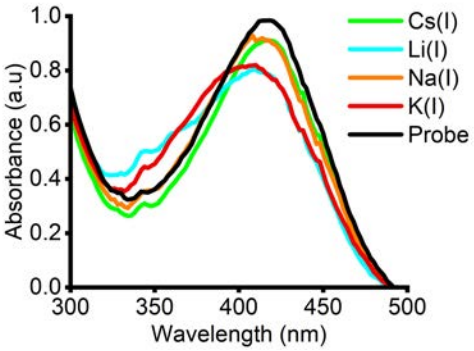

(a) Group (I)

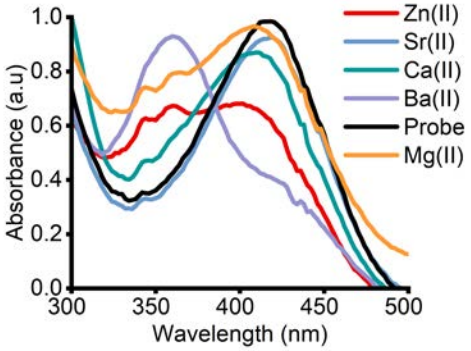

(b) Group (II)

Figure 3.17: Response of **65** to a range of metal salts through UV-Vis in 1% H_2O/MeCN ([probe] = 80 μM).

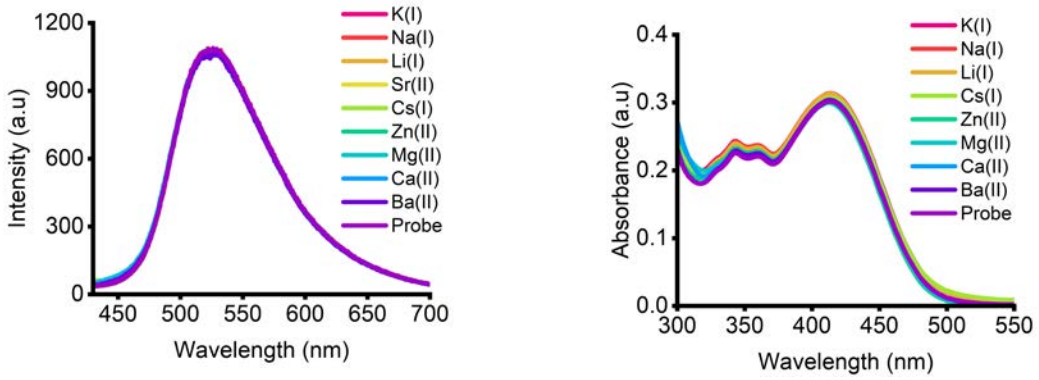

(a) Fluorescence **(b)** UV-Vis

Figure 3.18: Response of **66** to a range of metal salts ([probe] = 5 μM for fluorescence and 40 μM for UV-Vis, λ_{ex} = 410 nm). The excitation band-pass was 10 nm and the emission band-pass was 20 nm.

Comparing the response of **64** to the *N*-substituted **65**, it was observed that the response in UV-Vis spectroscopy for Group (I) metals was reduced upon replacing the secondary amine with a tertiary amine. It was also observed that **65** exhibited changes more to Group (II) metals compared to **64**, implying a lower degree of selectivity. The comparison between the mono and di-aza-crowns can also be made by comparing the profile of **63** and **64**. Both receptors were found to bind to K(I) and Ba(II) with a different spectral trace when compared to other Group (I) and Group (II) metals. However, the addition of the second nitrogen atoms resulted in a lower response to Mg(II). This was also accompanied by an increased response to Zn(II). This suggests that the UV-vis spectroscopic binding properties of these receptors can be altered and tuned depending on substitution pattern.

In addition, the results of the fluorescence spectroscopy metal screens are presented in Figure 3.19 for compound **63**, Figure 3.20 for **64**, Figure 3.21 for **65** and 3.18a for **66**. **66** did not exhibit a change in emission for either Group (I) or Group (II) metals. For receptors **63** – **65**, in contrast to the UV-Vis spectroscopic studies, the response of these receptors through fluorescence spectroscopy varies substantially. In all cases, the initial emission intensity is low, attributed to internal quenching mechanisms, with these mechanisms inhibited upon metal

addition. The response of the benzyl-substituted **65** is significantly lower than those of **63** and **64** with both Group (I) and Group (II) metal addition, with only Ca(II) inducing a small increase in intensity. When considering responses to Group (I) metals, **64** was found to be less selective than **63**, with all Group (I) metals inducing a change in emission, in comparison to the seemingly selective response upon the addition of K(I) to a solution of **63**. The emission profile of **63** and **64** presents two λ_{max}, with the change in relative emission of these signals being metal dependent.

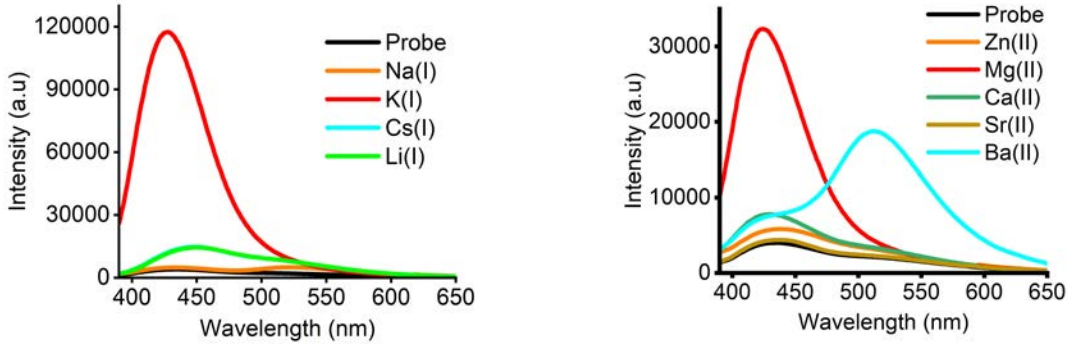

(a) Group (I) **(b)** Group (II)

Figure 3.19: Response of **63** to a range of metal salts through fluorescence in 1% H_2O/MeCN ([probe] = 5 μM, λ_{ex} = 350 nm). The excitation band-pass was 3 nm and the emission band-pass was 5 nm.

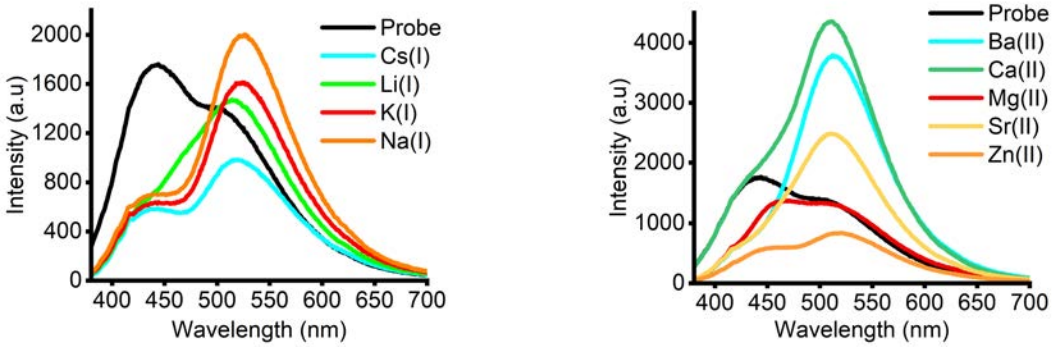

(a) Group (I) **(b)** Group (II)

Figure 3.20: Response of **64** to a range of metal salts through fluorescence in 1% H_2O/MeCN ([probe] = 5 μM, λ_{ex} = 370 nm). The excitation band-pass was 10 nm and the emission band-pass was 10 nm.

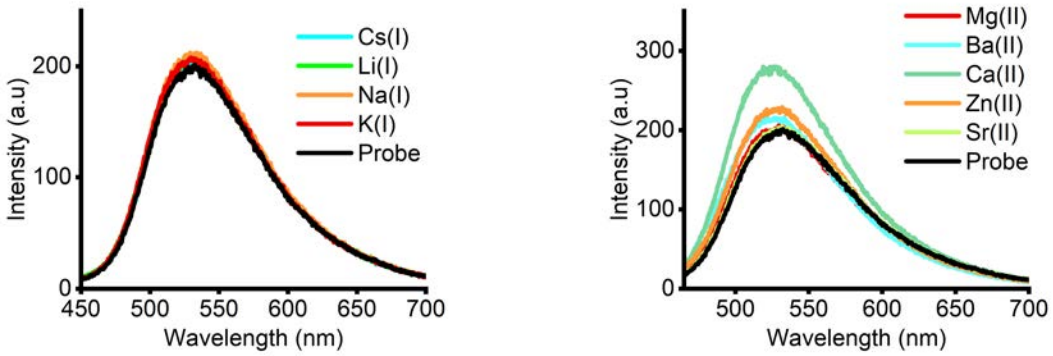

(a) Group (I) **(b)** Group (II)

Figure 3.21: Response of **65** to a range of metal salts through fluorescence in 1% H_2O/MeCN ([probe] = 5 μM, λ_{ex} = 425 nm). The excitation band-pass was 10 nm and the emission band-pass was 10 nm.

Additionally, the change in emission upon addition of Group (II) metals was also explored. Receptor **63** has a seemingly selective response to Ba(II) as evidenced by the increase in emission intensity of λ_{max} = 530 nm, which is not observed for any other metal for this receptor, while an increase intensity of λ_{max} = 430 nm is only observed upon formation of the **63**-Mg(II) complex. While this response is observed for **64**, there is less selectivity as this change in λ_{max} = 530 nm is seen for all other Group (II) metals to varying degrees. As was observed with the UV-vis spectroscopic titrations, the increased substitution of the binding ligand results in a decreased selectivity profile of the receptors, determined when comparing the results of **63** to **64** and **64** to **65** and **66**.

UV-vis spectroscopic titrations were then performed through the addition of Na(I), K(I), Mg(II), Ba(II) and Ca(II) salts to a solution of **63** and **64** in 1% H_2O/MeCN (Figure 3.22 and Figure 3.23). In all cases except for Mg(II), the formation of an isosbestic point was observed, suggesting a 1:1 binding stoichiometry. The data generated were fit to the appropriate binding models using both BindFit and HypSpec. All metal complexes were found to fit to a 1:1 binding stoichiometry, with LogK_a values obtained as summarised in Table 3.4, with an overall trend in LogK_a values of Ba(II) > Mg(II) > Ca(II) > K(I) > Na(I) for **63**. In general, **63** exhibits larger LogK_a for Group (II) metals, and cations of similar

sizes such as Ba(II) and K(I) have vastly different affinities for **63**. Additionally, **63** exhibits the highest affinity for Ba(II) over all other Group (II) and Group (I) metals tested.

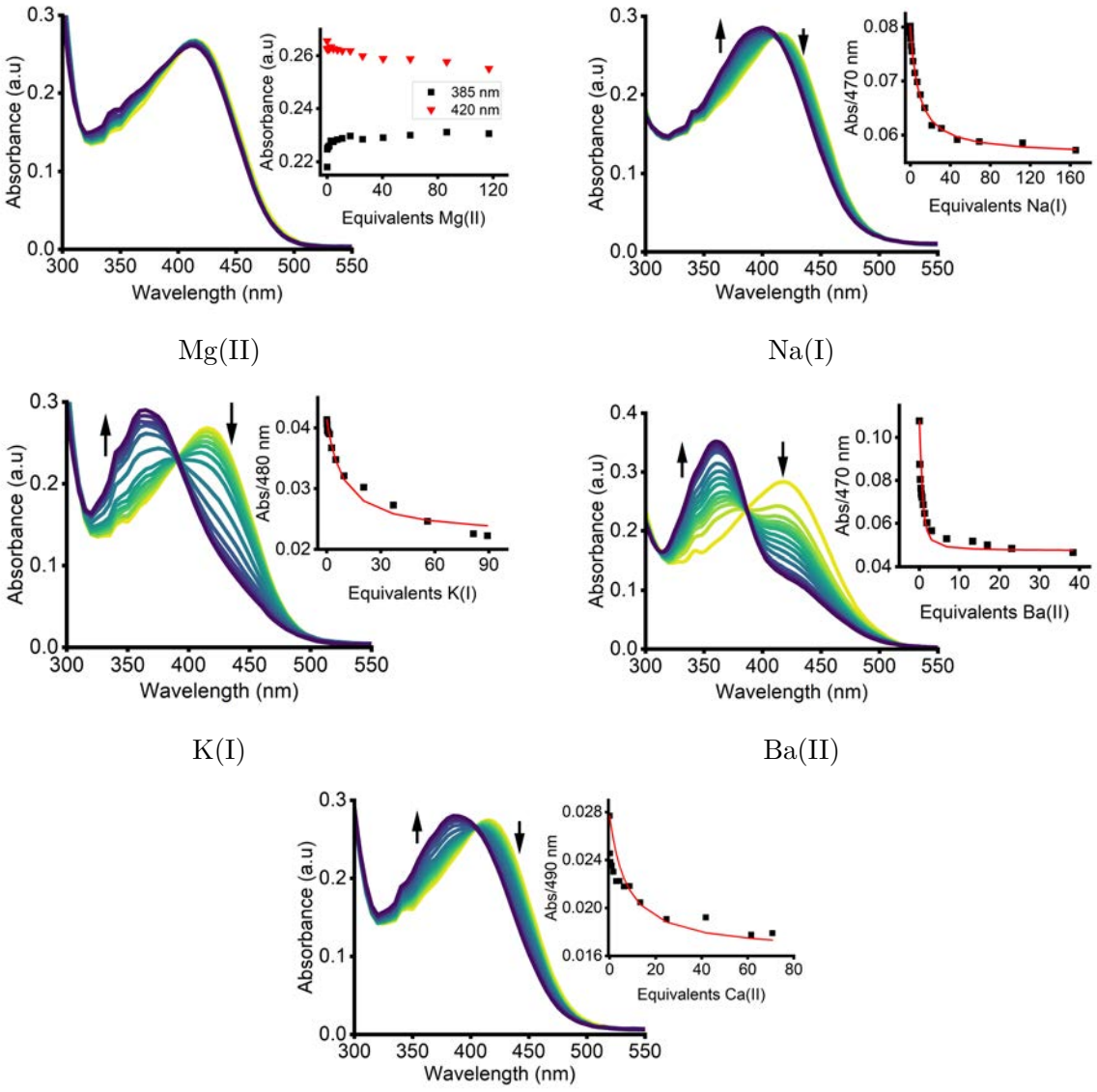

Figure 3.22: UV-vis spectroscopic titrations of **63** to increasing equivalents metal salts performed in 1% H_2O/MeCN ([probe] = 40 μM). The red line indicates the fit generated by BindFit.

For **64**, with the exception of Mg(II), the titration data successfully fit to a 1:1 binding stoichiometry, and can be summarised as Ba(II) > Ca(II) > K(I) > Na(I), which is similar to the trend obtained in the spectroscopic titrations of **63**, suggesting that the binding profile is not altered upon addition of a second

nitrogen atom in the binding ligand. Similar to **63**, **64** exhibits the highest affinity for Ba(II) over all other Group (II) and Group (I) metals tested.

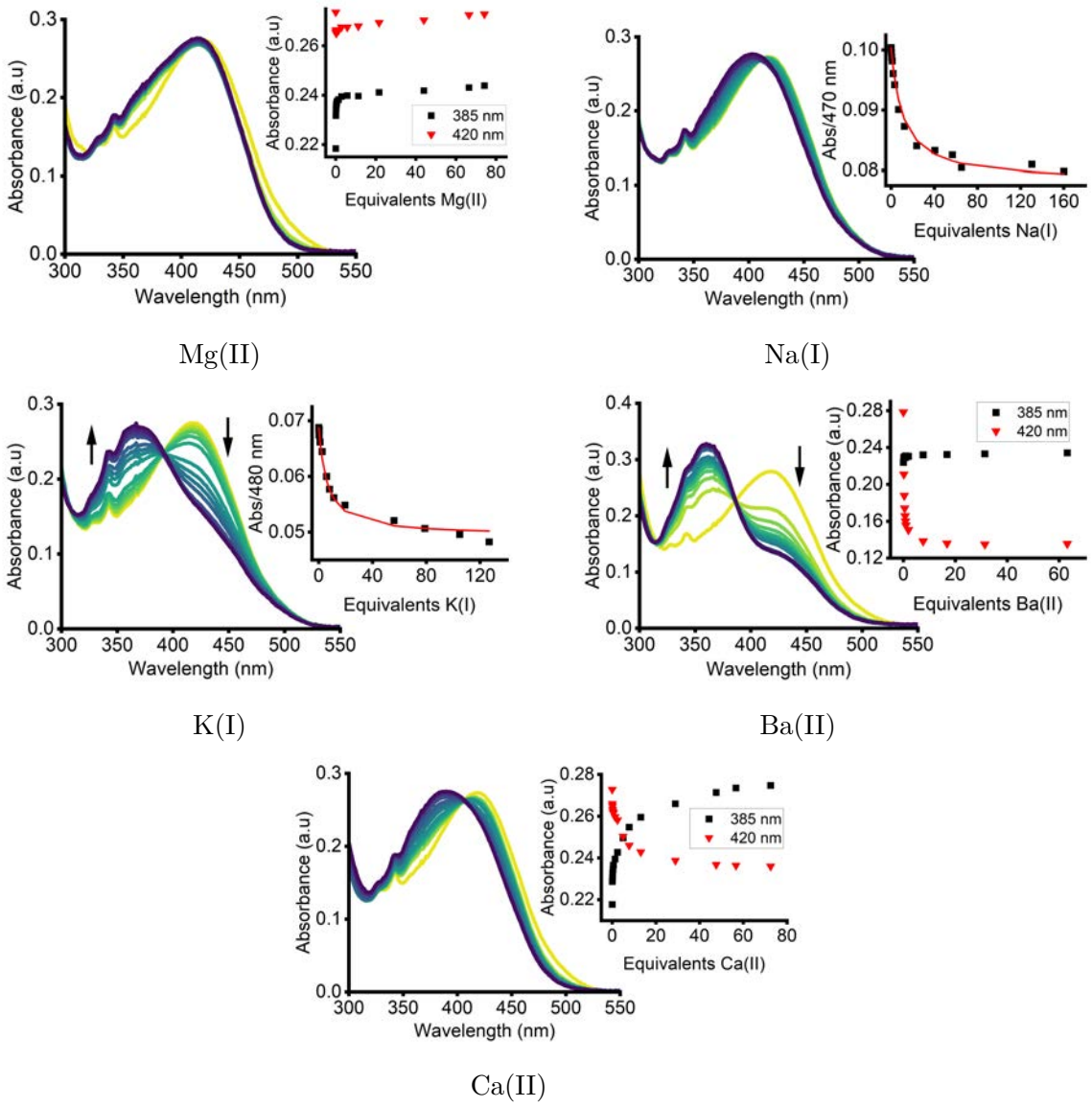

Figure 3.23: UV-vis spectroscopic titrations of **64** to increasing equivalents metal salts performed in 1% H_2O/MeCN ([probe] = 40 μM). The red line indicates the fit generated by BindFit.

Finally, the UV-vis spectroscopic titrations of **65** against Li(I), K(I), Zn(II), Ba(II) and Ca(II) (Figure 3.24) indicate a 1:1 binding profile of Ba(II) > Ca(II) > K(I), while Zn(II) and Li(I) could not be fit to an appropriate model. This binding trend is similar to that obtained for **63** and **64**. Again, Ba(II) exhibits the highest affinity, while the overall affinities were found to be lower compared to the other naphthalimide receptors. The similarities to **63** and **64** suggest the size

complementarity between the cation and the ligand, while also suggesting that the binding profile is not altered upon functionalisation of the second nitrogen atom in the binding ligand. **65** exhibits higher LogK_a for Group (II) metals.

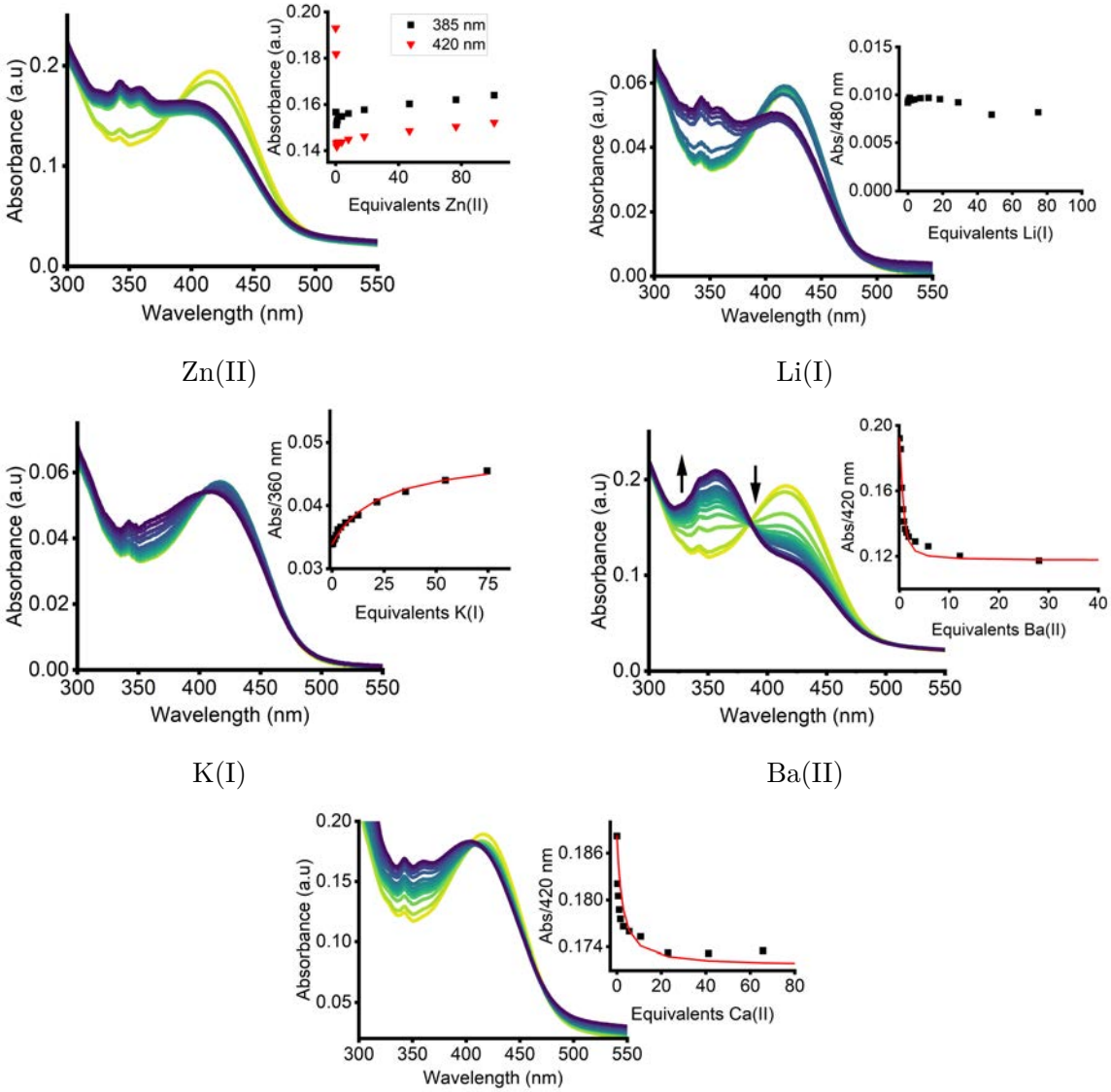

Figure 3.24: UV-vis spectroscopic titrations of **65** to increasing equivalents metal salts performed in 1% H_2O/MeCN ([probe] = 80 μM). The red line indicates the fit generated by BindFit.

Table 3.4: Tabulated $LogK_a$ values for **63**, **64** and **65** in 1% H_2O/MeCN upon the addition of Group (I) and Group (II) salts obtained through UV-vis absorbance spectroscopy with errors presented in the Appendix (n = 3).

Receptor	Metal	$LogK_a$
63	Na(I)	3.37
	K(I)	3.40
	Mg(II)	3.83
	Ca(II)	3.43
	Ba(II)	4.87
64	Na(I)	3.36
	K(I)	3.42
	Ca(II)	3.70
	Ba(II)	4.98
65	Li(I)	2.44
	K(I)	2.21
	Ca(II)	3.63
	Ba(II)	4.70

Finally, spectroscopic titrations for **66** presented in the Appendix indicate no further modulation in absorbance or fluorescence spectra up to > 100 equivalents Ba(II). Complex equilibrium processes or changes in binding stoichiometry over the titration were observed for the **63**-Ca(II), **63**-K(I), **64**-Mg(II), **65**-Zn(II) and **65**-Li(I) complexes, resulting in poorer fits to the calculated binding models in 1% H_2O/MeCN.

Fluorescence spectroscopic titrations were then performed through the addition of Na(I), K(I), Mg(II), Ba(II) and Ca(II) salts to a solution of **63** and **64** in 1% H_2O/MeCN with results (Figure 3.25 and Figure 3.26). Titration isotherms were fit at 470 nm and 600 nm, as the degree of change at these wavelengths was smaller, allowing for more accurate fitting to binding models. This is due to higher sensitivities at other wavelengths due to larger degrees of change, with resulted in poorer fits. For all metals (except for Mg(II) in the case of **63**), 1:1 binding stoichiometries were utilised to obtain $LogK_a$ values as summarised in Table 3.5. The overall trend in $LogK_a$ values was Ba(II) > K(I) > Ca(II), with the $LogK_a$ of the **63**-Ba(II) similar to that obtained through UV-vis spectroscopy. In general, **63** exhibits larger $LogK_a$ for Group (II) metals, and cations of similar

sizes such as Ba(II) and K(I) have vastly different affinities for **63**. Additionally, **63** exhibits the highest affinity for Ba(II) over all other Group (II) and Group (I) metals tested.

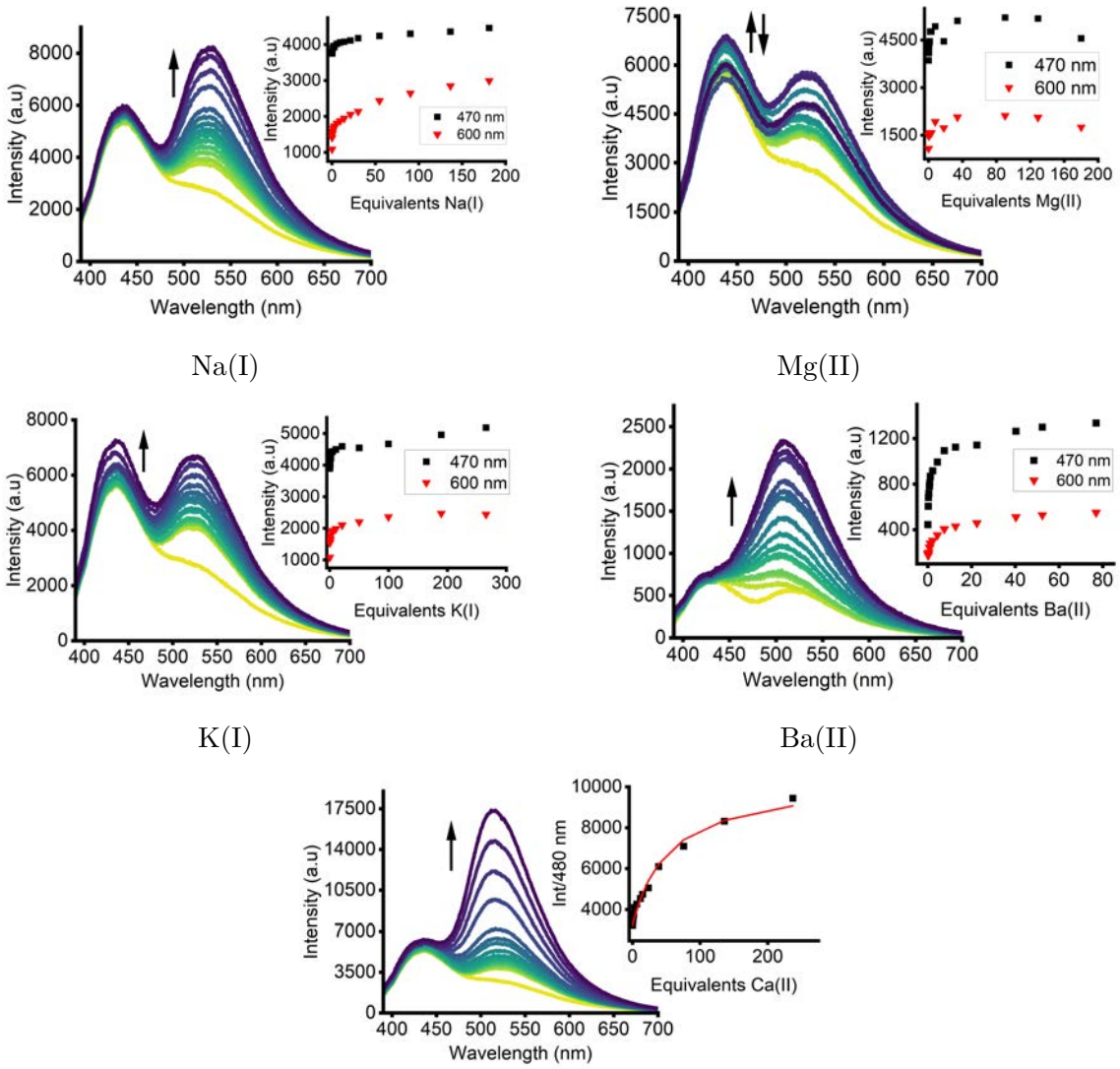

Figure 3.25: Fluorescence titrations of **63** to increasing equivalents metal salts performed in 1% H_2O/MeCN ([probe] = 5 μM, λ_{ex} = 370 nm). The excitation band-pass was 5 nm and the emission band-pass was 20 nm. The red line indicates the fit generated by BindFit.

For **64**, with the exception of Mg(II), the titration data successfully fit to a 1:1 binding stoichiometry, and can be summarised as Ba(II) > Ca(II) > Na(I) > K(I) (Table 3.5). In comparison to **63**, the binding profile has changed between Na(I), K(I) and Ca(II), however the affinity for Ba(II) is still the largest. This

suggests that changing the number of nitrogen atoms in the aza-crown-ether had minimal impact on binding affinity for Ba(II). However, increasing the number of nitrogen atoms seemed to favour stronger binding to Group (II) metals over Group (I) metals, as shown by the higher LogK$_a$ for Ca(II).

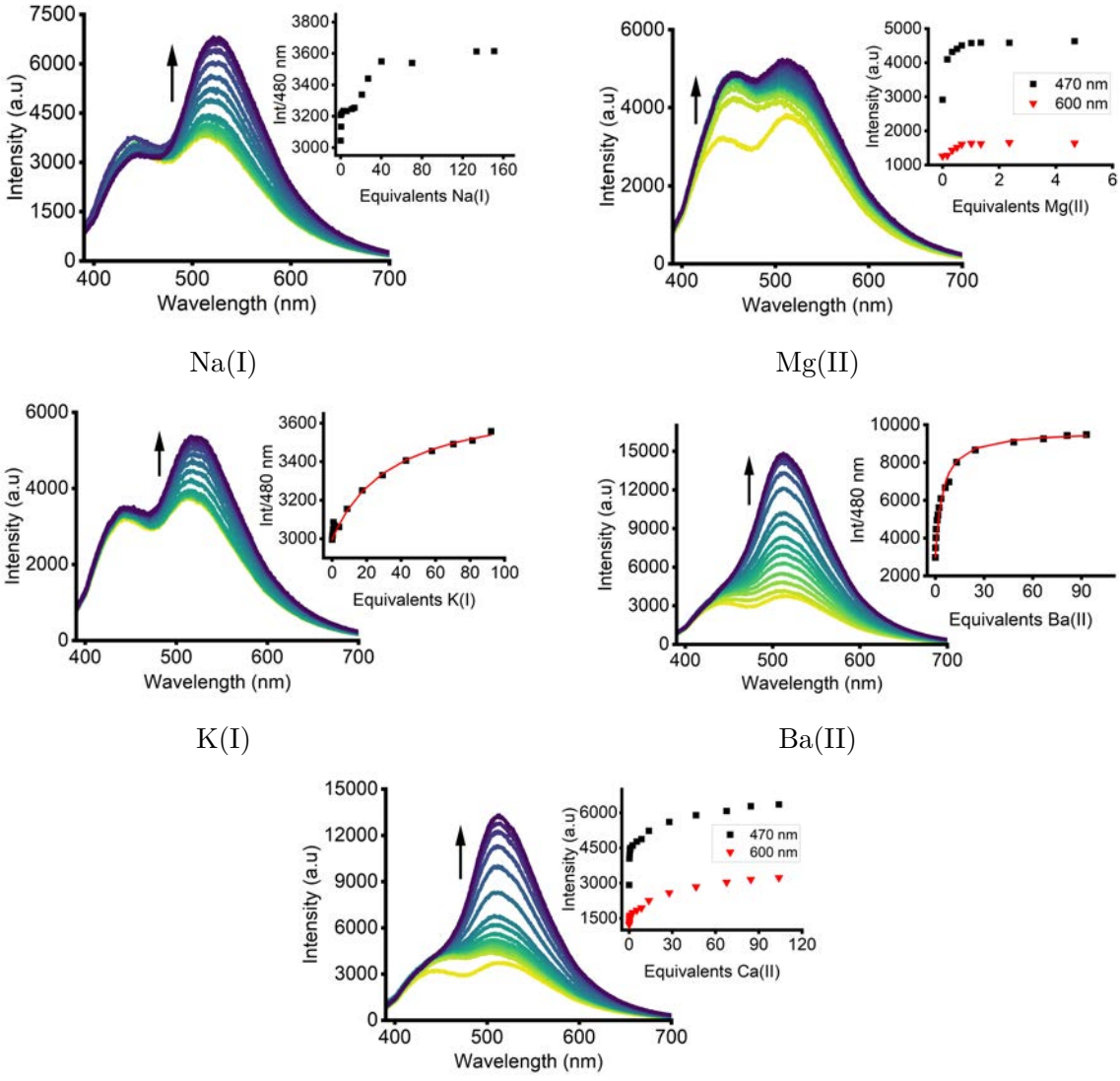

Figure 3.26: Fluorescence titrations of **64** to increasing equivalents metal salts performed in 1% H_2O/MeCN ([probe] = 5 μM, λ_{ex} = 370 nm). The excitation band-pass was 5 nm and the emission band-pass was 20 nm. The red line indicates the fit generated by BindFit.

Finally, fluorescence spectroscopy titrations were performed through the addition of Ba(II), Ca(II) and Zn(II) salts to a solution of **65** in 1% H_2O/MeCN with results presented in Figure 3.27. In all cases, a small turn-on response

was observed upon addition of the metal ions, while the increase in emission intensity varied depending on the metal similar to that observed in the screening experiments. The data generated were fit to the appropriate binding models using BindFit and HypSpec, and Ba(II) and Ca(II) data fit well to a 1:1 binding model, with LogK values of 4.46 and 3.65 respectively, while the binding data for Zn(II) could not be fit to a model. The binding data indicate that the strongest interaction arises with the formation of the Ba(II)-**65** complex similar to that observed for **63** and **64**.

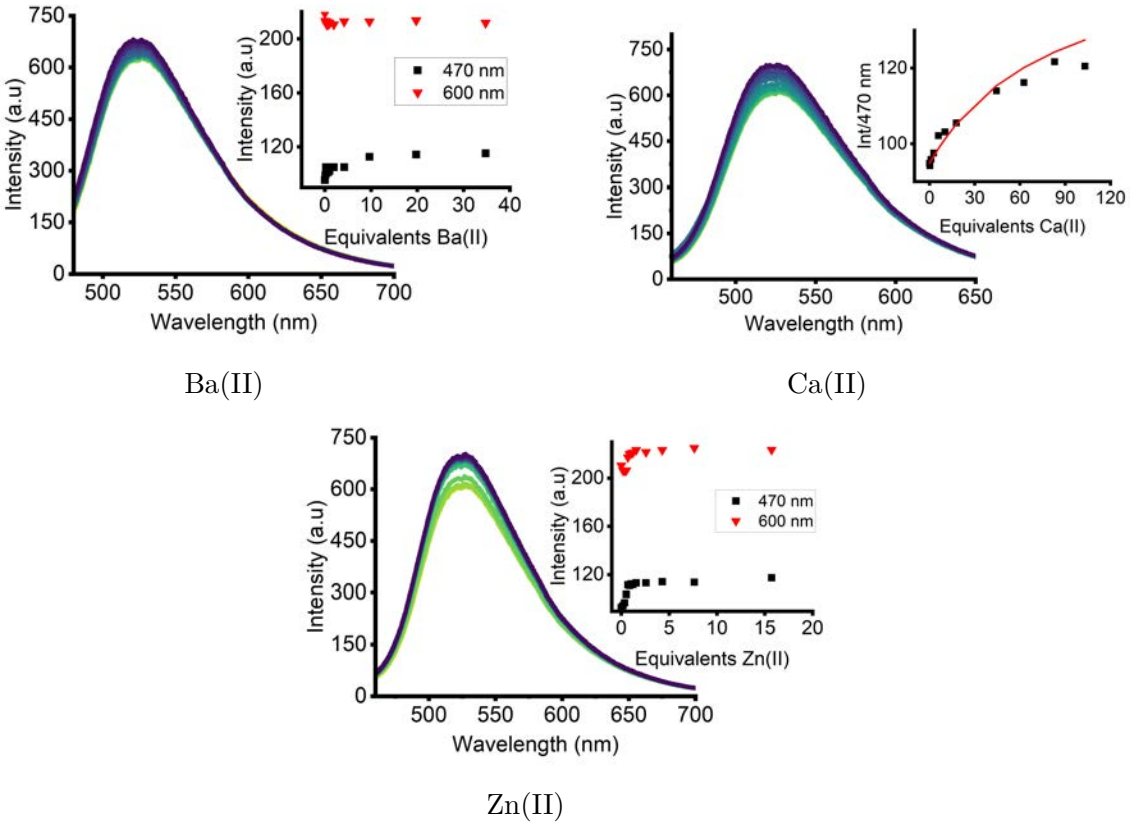

Figure 3.27: Fluorescence titrations of **65** to increasing equivalents metal salts performed in 1% H_2O/MeCN ([probe] = 5 μM, λ_{ex} = 425 nm). The excitation band-pass was 10 nm and the emission band-pass was 10 nm. The red line indicates the fit generated by BindFit.

The overall trend in LogK_a values from the fluorescence spectroscopic titrations of **65** can be summarised as Ba(II) > Ca(II), with the trend in the LogK_a of the **65**-Ba(II) complex similar to that observed fluorescence titrations of **63** and **64**. Due to the minimal change in the fluorescence spectrum observed for

65 complex formation, this indicates that **65** would provide minimal information in a metal extrusion assay. Complex equilibrium processes or changes in binding stoichiometry over the titration were observed for the **63**-Mg(II), **64**-Mg(II), **64**-Na(I) and **65**-Ca(II) complexes, resulting in poorer fits to the calculated binding models in 1% H_2O/MeCN.

Table 3.5: Tabulated LogK_a values for **63**, **64** and **65** in 1% H_2O/MeCN upon the addition of Group (I) and Group (II) salts obtained through fluorescence spectroscopy (n = 3).

Receptor	**Metal**	**LogK_a**
63	Na(I)	3.95
	K(I)	3.90
	Ca(II)	3.64
	Ba(II)	4.79
64	Ba(II)	4.83
	K(I)	3.54
	Ca(II)	3.14
65	Ca(II)	3.65
	Ba(II)	4.46

The change in fluorescence intensity upon metal addition can be summarised by calculating the FEF at 530 nm. It was observed that the degree of intensity change upon Ba(II) addition was reduced as substitution of the ligand increased, when comparing **63** to **64** and **65**, as presented in Figure 3.28. Within each group, there is no identifiable trend in the FEF based on cation size or cation charge density. These results indicate that **63** has a seemingly selective response to Ba(II) when monitoring the FEF, while plotting this FEF at 550 nm did not result in a higher degree of selectivity for Ba(II). This selectivity profile diminishes with substitution, while **64** and **65** are more selective to Ca(II).

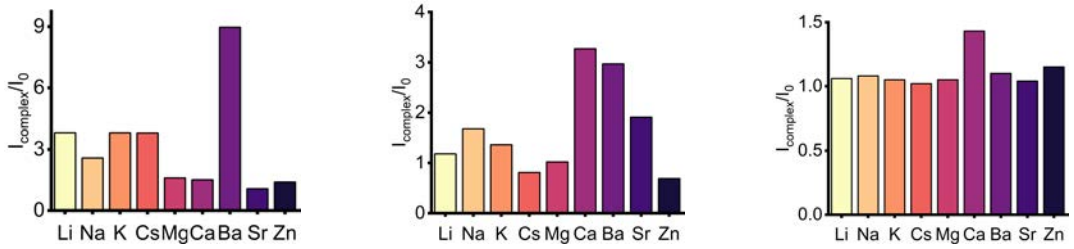

63 **64** **65**

Figure 3.28: Calculated FEF at 530 nm upon addition of excess metal salts (> 100 equivalents) performed in 1% H_2O/MeCN ([probe] = 5 μM). The excitation band-pass for **63** was 3 nm and the emission band-pass was 5 nm (λ_{ex} = 370 nm). The excitation band-pass for **64** was 10 nm and the emission band-pass was 10 nm (λ_{ex} = 370 nm). The excitation band-pass for **65** was 10 nm and the emission band-pass was 10 nm (λ_{ex} = 425 nm).

To determine the relative stability of the receptor-Ba(II) complex, competition studies were performed. This involved the addition of excess Group (I) or Group (II) salt to the receptor to ensure formation of the metal complex, then the addition of equivalent concentrations Ba(II) salt and measuring the intensity as presented in Figure 3.29. In all cases except the **65**-Ca(II) and **65**-Zn(II) complex, the addition of Ba(II) resulted in an significant increase in emission intensity, indicative of metal displacement upon Ba(II) addition. These results suggest that if performed in a system containing these competing metal ions, Ba(II) would successfully displace them from these ligand, allowing for these receptors to be used for MEAs in systems containing these cations. This also suggests that **65** would not be useful for the desired metal extrusion assay applications in a biological system, as Ca(II) would bind to the receptor and interfere with the fluorescence spectroscopic data.

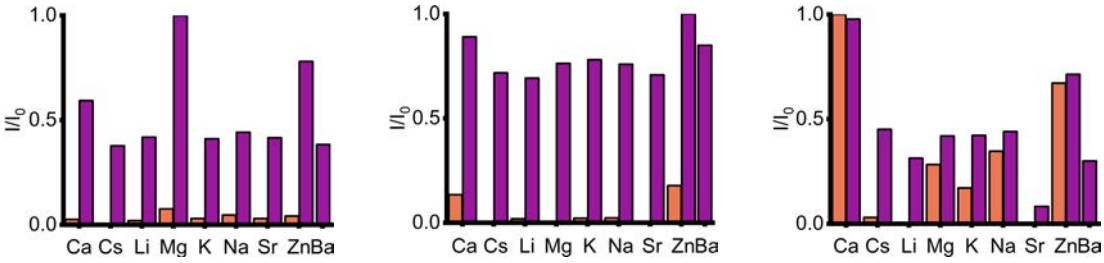

Figure 3.29: Competition studies upon addition of excess $Ba(ClO_4)_2$ to the Receptor-M(I) or Receptor M(II) complex performed in 1% H_2O/MeCN ([probe] = 5 μM). Orange = no barium, purple = addition of barium.

Following on from this, metal binding was studied using ϕ in 1% H_2O/MeCN. Upon the addition of Ba(II), Ca(II), Na(I) or K(I) to a solution of **63** (Table 3.6) (with a ϕ of 0.13), and Ca(II), K(I), Na(I) or Ba(II) to **64** (with a ϕ of 0.085). For both **63** and **64**, an increase in ϕ was observed for all complexes with the exception of K(I) which led to a reduction in ϕ for **63** and only a slight increase in ϕ for **64**. The increases in ϕ were larger for **64** than **63**, but the responses for **64** did not allow for differentiation of Ca(II) and Ba(II) with both complexes having $\phi = 0.16$. The results contrast with the responses observed in the case of the anthracenes **52** and **62**, in which much larger changes in ϕ were observed upon complexation.

Table 3.6: Quantum yields of **63** and **64** metal complexes expressed as a ratio with a [probe] of 3 μM (n = 1).

Metal complex	ϕ
63	0.13
63-Na(I)	0.17
63-Ca(II)	0.19
63-K(I)	0.11
63-Ba(II)	0.17

Metal complex	ϕ
64	0.085
64-Ca(II)	0.16
64-K(I)	0.092
64-Na(I)	0.11
64-Ba(II)	0.16

The values of ϕ were then determined upon the addition of Ca(II), Zn(II) or Ba(II) (Table 3.7) to a solution of **65** (with a ϕ of 0.058), in which a significant increase in ϕ was observed only upon the addition of Ba(II), suggesting some selectivity of **65** as a ϕ based Ba(II) sensor ($\phi = 0.12$). This is in stark contrast to the responses observed for **63** and **64**, in which no selectivity for Ba(II) was

observed upon determination of ϕ.

Table 3.7: Quantum yields of **65** metal complexes expressed as a ratio with a [probe] of 5 μM (n = 1).

Metal complex	ϕ
65	0.058
65-Ba(II)	0.12
65-Ca(II)	0.087
65-Zn(II)	0.094

Upon the addition of Ba(II), Ca(II), K(I), Li(I), Sr(II), Mg(II), Cs(I) or Na(I) (Table 3.8) to a solution of **63** (τ = 10.46 ns), the largest decrease in τ was observed upon the formation of the Ca(II) complex (τ = 8.05 ns), with smaller decreases for the Sr(II) (τ = 10.21 ns) and Mg(II) (τ = 9.60 ns) complexes, with the remaining metals inducing small increases in τ. Similarly, upon the addition of Ba(II), Ca(II), K(I), Li(I), Sr(II), Mg(II), Cs(I) or Na(I) (Table 3.8) to a solution of **64** (τ = 9.47 ns), a decrease in τ was observed upon the formation of the Ca(II) complex (τ = 7.90 ns), as well as the Sr(II) (τ = 9.43 ns), Mg(II) (τ = 9.24 ns) and Li(I) (τ = 8.77 ns) complexes, with the remaining metals inducing small increases in τ. Finally, upon the addition of Ba(II), Ca(II) or Zn(II) (Table 3.9) to a solution of **65** (τ = 1.42 ns), small increases in τ were observed upon the formation of all metal complexes. In all cases, this lack of selectivity is in contrast to the anthracene receptors, suggesting that the naphthalimide compounds could not be applicable as a selective τ sensors.

Table 3.8: Bi-exponential lifetimes of **63** and **64** metal complexes in 1% H_2O/MeCN ([probe] = 5 μM). Amplitudes for calculations are presented in Table 7 and Table 8 in the appendix (n = 3).

Complex	τ_{amp} (ns)
63	10.46
63-Ba(II)	10.54
63-Ca(II)	8.05
63-K(I)	10.95
63-Li(I)	10.61
63-Sr(II)	10.21
63-Mg(II)	9.60
63-Cs(I)	10.68
63-Na(I)	11.15

Complex	τ_{amp} (ns)
64	9.47
64-Ba(II)	9.52
64-Ca(II)	7.90
64-K(I)	9.59
64-Li(I)	8.77
64-Sr(II)	9.43
64-Mg(II)	9.24
64-Cs(I)	9.54
64-Na(I)	9.81

Table 3.9: Bi-exponential lifetimes of **65** metal complexes in 1% H_2O/MeCN ([probe] = 5 μM). Amplitudes for calculations are presented in Table 9 in the appendix (n = 3).

Complex	τ_{amp} (ns)
65	1.42
65-Ba(II)	2.22
65-Ca(II)	2.08
65-Zn(II)	1.77

3.3 Chapter Conclusion

In order to construct a suitable MEA, the optimal metal-ligand pair needs to be determined. The response after metal addition to the ligand also needs to be identified, which allows for the identification of a free ligand after the metal has been extruded. The ideal metal has a low biological concentration and induces a substantial shift in the fluorescence or UV-vis spectrum (or through ϕ or τ). In order to determine the ideal metal for the MEAs performed in the next chapter, this chapter set out to explore the metal binding responses of a range of receptors.

This chapter focused on the photophysical characterisation of the responses of **52**, **62**, **63**, **64**, **65** and **66** in the presence of a variety of Group (I) and Group (II) metals. Competition studies were performed for the naphthalimide containing receptors. ϕ and τ values were also experimentally determined and calculated. Bi-exponential decays were obtained for all compounds both in the presence and absence of metal ions.

For compound **52**, metal screens indicated higher sensitivity for Group (II) and Zn(II) metals with the greatest change in fluorescence intensity observed for Ba(II) and Zn(II). The order of LogK_a fluorescence spectroscopic titrations was K(I) > Mg(II) > Li(I), while for **62** the order was found to be Zn(II) > Ba(II) > Ca(II) > Mg(II) > K(I) as presented in Table 3.1. This suggests that the introduction of the second nitrogen heteroatom in the binding ligand decreased the overall selectivity when comparing **62** to **52**, with this second nitrogen atom increasing the propensity for strong binding to Group (II) metals. While this trend may appear, binding isotherms for some metals could not be obtained, so a definitive trend cannot be determined. Due to the complex equilibria processes occurring over the course of the metal titrations definitive comparison between **52** and **62** on the introduction of the second nitrogen atom's influence on overall LogK_a values cannot be confidently assessed as some data could not be accurately fit to standard 1:1 models.

Furthermore, analysis was performed on the influence of M(I) and M(II) addition to solutions of **52** and **62** through ϕ and τ determination. For **52**, it was observed that the addition of Ba(II) to **52** selectively resulted in a decrease in τ, in contrast to the response observed for **62** in which a non-selective increase in τ was observed upon the addition of both Group (I) and Group (II) metals. When comparing the influence of Group (I) and Group (II) metal addition to a solution of **52** versus **62** on the ϕ of the receptor complexes, the **52**-Ba(II) complex had a higher ϕ value when compared to the **62**-Ba(II) complex. This suggests that Ba(II) is able to modulate the excited state properties of these receptors differently when compared to other Group (I) and Group (II) metals, which may arise due to intrinsic properties of Ba(II), with this effect confirmed using both τ and ϕ.

The photophysical responses of **63**, **64**, **65** and **66** were studied. It was found that the overall UV-vis absorbance and fluorescence response upon metal addition was diminished as substitution of the second nitrogen in the ligand increased, as the change in intensity and absorbance were minimised when comparing **64** to **65**. This response was further reduced in the case of **66**, which exhibited no change upon addition of any Group (I) or Group (II) metal, presumably due to the absence of nitrogen lone pair available for metal complexation, showing the effect of nitrogen substitution on the metal binding profile. Additionally, the emission profile of **63** and **64** exhibited dual-emission like properties, as the intensity of each λ_{max} varied depending on the metal. In contrast, compounds **65** and **66** exhibited only a single emission band.

Through spectroscopic metal screens, it was observed that altering this substitution pattern changed the selectivity of the receptor. All receptors were found to exhibit selectivity for Ba(II). Competition studies performed indicated that Ba(II) was able to displace metals from complexes of **63** and **64**, however Ba(II) could not displace Ca(II) from **65**. This was confirmed by monitoring the change

in emission upon addition of Ba(II) to these complexes. This change observed in the competition study for **65** may be attributed to the absence of the second nitrogen lone pair available for binding, and may suggest that the inner cavity diameter may change depending on substitution, or that there are potential conformational changes occurring upon substitution of the second amine.

The order of $LogK_a$ for UV-vis spectroscopic titrations for **63** was found to be Ba(II) > Mg(II) > Ca(II) > K(I) > Na(I), while for **64** this was found to be Ba(II) > Ca(II) > K(I) > Na(I) and for **65** this was Ba(II) > Ca(II) > Li(I) > K(I) as summarised in Table 3.4. As summarised in Table 3.5, this order of binding is somewhat maintained when studying these receptors through fluorescence spectroscopy, however small differences arise due to the dual emission observed for **63** and **64**, altering the fluorescence results. These receptors maintain the highest affinity for Ba(II) over other Group (I) and Group (II) metals, while substitution of the second nitrogen seemed to have minimal impact on the overall $LogK_a$ values when comparing **64** to **65** as was confirmed by both fluorescence and UV-vis spectroscopy, with the obtained $LogK_a$ values through both techniques are in the same order of magnitude as each other.

Furthermore, analysis was performed on the influence of M(I) and M(II) addition to solutions of **63**, **64** and **65** through ϕ and τ determination. For **63**, there was no selective modulation of τ, in contrast to the response observed for **52** containing the same ligand, with this non-selective response also observed for both **64** and **65**. In contrast to the anthracene compounds, substitution did not alter the selectivity observed in τ analysis. When comparing the influence of Group (I) and Group (II) metal addition to a solution of **63** versus **64** and **65** on the ϕ of the receptor complexes, all tested metals induced an increase in ϕ as anticipated. In general, the addition of 2 nitrogen atoms reduced overall ϕ of the receptors when comparing **63** to **64** due to increased quenching. As was observed for the anthracene compounds, the Ba(II) complexes tended to have the largest

$\Delta\phi$ when compared to the other metals tested, suggesting the ability of Ba(II) to modulated excited state properties differently to other Group (I) and Group (II) metals.

It was observed that all naphthalimide receptors exhibited higher LogK_a values for Ba(II), implying that these receptors will be suitable for MEAs utilising Ba(II). The anthracene receptors were found to be not useful for metal detection through UV-vis absorbance spectroscopy, however **52** was found to exhibit a selective change in both τ and ϕ upon formation of the Ba(II) complex, suggesting that this receptor could be employed for Ba(II) detection using these methods. The slight variation in ligand composition was shown to have a slight effect on the binding profile by both UV-Vis spectroscopy and fluorescence spectroscopy. Additionally, the naphthalimide receptor was found to exhibit dual emissive properties which varied depending on the metal added, while substitution of the second nitrogen heteroatom was found to influence the binding profile of the naphthalimide aza-crown-ethers.

It was observed that the fluorescence intensity upon addition of M(I) and M(II) to the naphthalimides does not directly correlate with the LogK_a. In the cases of **63**, **64** and **65**, the addition of Ca(II) resulted in the greatest change in fluorescence intensity, however Ba(II) was found to have the highest LogK_a, which is consistent with literature, suggesting that the change in emission cannot be used to determine the binding affinity. For **52**, detector saturation means that the selectivity cannot be determined, as the metal ion responses cannot be distinguished. For **62**, the FEF suggests that this is selective for Zn(II), however this cannot be confirmed as LogK_a could not be determied. For **63**, **64** and **65**, the FEF shows selectivity for Ba(II), Ca(II) and Ca(II) respectively, with this selectivity not directly correlated to LogK_a for the case of **64** and **65**.

The results from this chapter aim to inform the next chapter, with receptors **52** and **63** used for Metal Extrusion Assays for $SO_4{}^{2-}$ due to their changes in

optical properties after Ba(II) addition. The information obtained in this chapter allows for the determination of the ideal metal for the following MEAs, and provides a benchmark for the expected response after metal extrusion upon anion addition.

Chapter 4

Assays for Use in Sulfate Detection

4.1 Chapter Introduction

As discussed in Chapter 1, the task of developing tools for SO_4^{2-} recognition, particularly in complex aqueous media, is monumental. The optimal tools involve using fluorescence spectroscopy or UV-vis spectroscopy, and while the ultimate goal is to develop tools for the direct recognition of SO_4^{2-} using UV-vis or fluorescent sensors, indirect detection can achieved through assays such as MEA and IDA.

MEAs rely on the formation of an insoluble metal salt, as a Metal-Ligand (M-L) bond is broken in the presence of anion. This requires initial formation of a M-L complex, in which the strength of this bond is weak enough to ensure extrusion. Ideally, conditions are employed under which full metal complexation occurs and a clear spectroscopic change is observed when comparing the free ligand to the metal complex to avoid substantial effects from background signals.

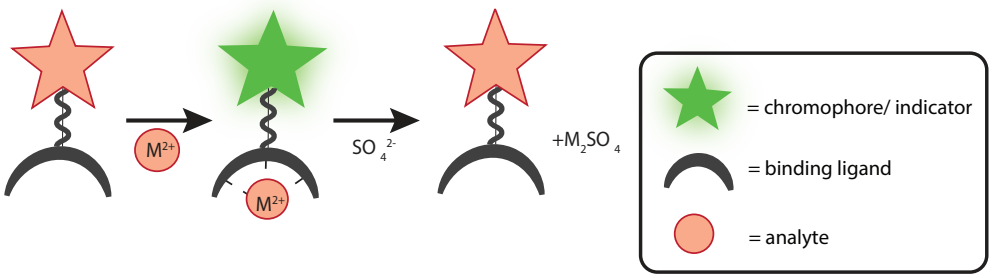

Figure 4.1: Generalised scheme displaying MEA.

An alternative indirect detection method involves a competition assay using an indicator which binds to the receptor and can be displaced upon addition of SO_4^{2-} leading to a modulation of indicator absorbance or emission. The indicator is released and remains unbound, and a H-G complex forms allowing for indirect detection. Indicator displacement assays can be performed using either chromogenic or fluorogenic indicators, with IDA often resulting in a colour change of the solution to provide a visual determination.

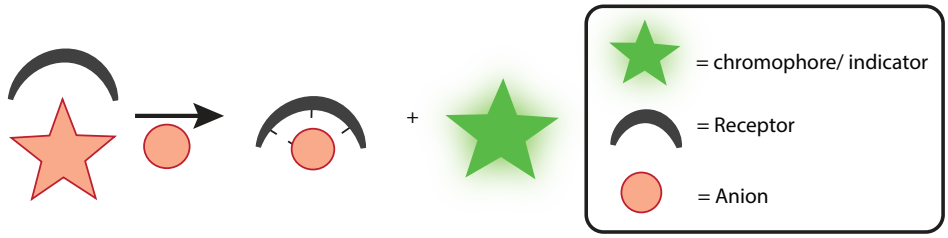

Figure 4.2: Generalised scheme displaying IDA.

4.1.1 Ion Chromatography for Anion Sensing

To evaluate the efficiency and selectivity of MEA and IDAs for SO_4^{2-} detection, a comparison to a robust detection method is required. A common analytical technique for anion recognition is Ion Chromatography (IC). In comparison to photophysical techniques, IC tends to be more robust, as elution profiles of ions are consistent for a specific system. In combination with standard sample analysis, the identity of each peak is easily determined. In contrast to these benefits, IC is known to be time and cost ineffective, with long sample preparation and data analysis times. It is also important to consider the protonation state of the ion, as this will vary depending on the buffer, which can alter elution profiles.

Ion chromatography works on the principle of ion exchange. A charged stationary phase is used, while the sample containing oppositely charged ions is injected. The stationary phase is functionalised with a functional group, such as NH_4^+ for anion analysis and OH^- for cation analysis. The ions in the sample

are attracted to the stationary phase through Couloumbic interactions. As the sample passes through, stronger interactions result in greater affinity to the stationary phase, leading to longer elution times.

The instrumental set up of IC as presented in Figure 4.3. The eluent (mobile phase) is moved through the system by a pump. The sample is injected through a sample loop of a particular size by the injection valve. The sample then moves to the guard column which acts as a filter to remove contaminants and impurities which may taint the column. After this, the sample moves to the separator column and then ions move to the suppressor, which removes any conductive ions from the eluent (increasing S/N ratio), removes the counterions (improves peak resolution) and converts ions into more conductive forms which are detected by the conductivity cell.

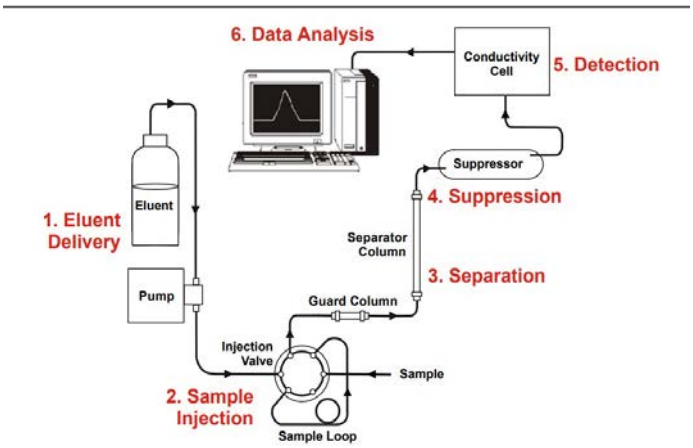

Figure 4.3: Diagram illustrating main components of Ion Chromatography.

In order to maximise separation and efficiency in IC, a range of parameters should be considered. The first set of conditions is the eluent, including the buffer pH, buffer type and flow rate. An increase in flow rate leads to reduced run times at the risk of decreasing peak resolution. The buffer nature should also be considered. For instance, carbonate/carbonic acid buffers are typically used for anion detection and quantification, as it ensures most anions are dissociated and easily ionisable. On the other hand, hydroxide based buffers can greatly basify the eluent, and can degrade tubing and columns while also altering elution

order.

The other parameters to be considered are injection volume, column type and temperature. Smaller injection volumes can reduce the size of the band and result in a greater peak resolution. Temperature has been shown to influence efficiency, as increased temperatures increases the exchange rate between mobile and solid phase. However, some IC may not be equipped with the functionality to increase temperature, presenting instrumental limitations. Finally, the column functional groups needs to be considered and matched to the desired analytes when optimising IC, such as the use of strong or weak ion-exchange groups, which affect the degree of ionisation of the functional groups, ultimately affecting attraction to analytes of interest.[141]

Due to the reliability in determining the nature of elution peaks, it is relatively easy to construct calibration curves to determine analyte concentration in a given system. This is performed by measuring the peak area of the analyte of interest and comparing it to the elution profile of a known standard. Retention time is used to identify the analytes, and so standardised experimental conditions are required.

Typically a standard solution is made at varying concentrations through serial dilution to minimise error propagation. The peak areas of the standards are plotted as a function of concentration. The unknown sample is then analysed, and the peak area corresponding to the ion of interest is identified. The unknown concentration is then determined using the line-of-best fit. Validity of the curve is analysed through sample spiking, in which a known concentration of the standard is added. The observed response is compared to the predicted response to determine % recovery. If the predicted response does not match the observed response, then it can be assumed that there are limitations with the experimental conditions and may indicate that the method chosen is not suitable for quantification of analyte concentration.

Statistical calculations can be used to evaluate both limit of detection (LOD) and limit of quantification (LOQ). The LOD indicates the lowest sample concentration which can be accurately detected. Mathematically it is calculated by:

$$LOD = \frac{3.3\sigma}{s} \tag{4.1}$$

Where

σ = standard deviation

s = slope of the calibration curve

In comparison, the LOQ indicates the limit of quantification. This represents the lowest concentration which can be accurately quantified by a calibration curve. This can mathematically be written as:

$$LOQ = \frac{10\sigma}{s} \tag{4.2}$$

Through a combination of calibration curve validation with samples of known concentration, LOD and LOQ, new assays can be compared to IC to determine whether they are equally effective.

In an example of utilising IC for anion detection from Bak *et al.*,[142] newly developed low capacity columns were used for SO_4^{2-} analysis with the ability to discriminate between SO_4^{2-} and thiosulfate, for the ultimate goal of detection in lake-water sediments. To ensure proper elution of the targeted analytes, a traditional $NaHCO_3$ buffered eluent was used, with experimental variations including manual sample filtration in lieu of guard columns to improve separation while modifying the eluent reduced separation, signifying that sample preparation can influence analyte separation. In comparison to previous techniques for separation of these two anions, the authors improved upon the reproducibility when com-

pared to these methods, allowing for the successful detection of bacterial SO_4^{2-} reduction, as well as detection of SO_4^{2-} reduction in sediment slurries. This example highlights that SO_4^{2-} can be detected from similar species, and indicates that sample preparation and conditions can vastly affect this separation.

A study from Jun *et al.*[143] has shown that changing the nature of the column to a C_{18} column alters the affinity of SO_4^{2-} for the stationary phase, resulting in longer elution times when compared to traditional columns surfaces. Due to the nature of the stationary phase, the eluent was modified to be an aqueous solution of $K_3[Fe(CN)_6]$, and was used for the detection of trace SO_4^{2-} levels in water samples on the picogram scale. This example signifies that the column type and eluent can be substantially modified for analyte detection, and can be used to detect picogram quantities of anions, in comparison to most systems with a millimolar detection level.

IC can be extended for SO_4^{2-} detection in biological samples, such as body tissues as presented in Rozman *et al.*[144] This study aimed to improve upon the previously existing techniques for SO_4^{2-} detection methods, while modifying the experimental conditions for further detection of inorganic SO_4^{2-} species. To improve separation of anions in this medium, MeCN was introduced into the mobile phase with 1 mM NaOH, while high sample dilution conditions were required to minimise contamination of the guard and analytical column, which would negatively impact subsequent runs. This slight alteration in the instrumental conditions allowed for the determination of SO_4^{2-} concentration in a range of tissues and biological fluids (serum, urine, bile, kidney and liver) with a high % recovery of around 100% for serum, bile, liver and kidney samples. This study indicates the versatility of IC, while also highlighting the importance of method modification as the sample medium changes.

Another example showcases the ability to utilise IC for SO_4^{2-} detection in complex systems such as STEALTH liposomes as presented in Wang *et al.*[145]

Due to membrane disruption in previous studies of these liposomes during SO_4^{2-} detection, IC was employed to minimise these disruptions for accurate detection in the millimolar range. A carbonate buffer eluent was used at 7 mM Na_2CO_3/2 mM $NaHCO_3$ with % recoveries close to 100% and LOD of 0.06 μM SO_4^{2-}. Additionally, this technique was found to be highly robust with high precision from day-to-day studies, again solidifying that IC can be applicable to further complex systems.

Finally, IC can also be utilised for SO_4^{2-} detection with high % recoveries in sea-water by employing a KOH eluent.[146] A variation on the sampling loop was used referred to as cycling-column-switching to allow for the separation of closely eluting anions, while also reducing the level of interference by reducing matrix ion effects. A highly linear response was observed for SO_4^{2-} with improved peak shapes compared to traditional sampling loops with % recoveries around 100%. This study indicates that IC can be modified to improve resolution and increase separation of closely eluting anions in complex aqueous solutions.

Despite the disadvantages of IC, it is a useful benchmark for comparing novel methods to established methods. It has been shown in the discussed papers that it is an effective tool for monitoring SO_4^{2-} in aqueous systems, and provides a point of comparison for new methods. By using IC, new techniques can be developed to determine if they improve upon the pre-existing methods.

4.1.2 Synthesis

Prior literature shows that **29** and **28** can be used for the quantification of SO_4^{2-} in complex mixtures using IDAs. However, there is limited detail as to how effective these receptors are in SO_4^{2-} recognition in complex mixtures. Due to their promising response as discussed in Chapter 1, **29** and **28** were synthesised to test their effectiveness in complex aqueous systems.

Macrocycle **101** was prepared following literature procedures. Firstly, excess

diethyl squarate was reacted with *N*-*N*-bis-(3-aminopropyl)methylamine to give **99** (*m/z* 469). Following this, **99** was reacted with an equimolar amount of *N*-*N*-bis-(3-aminopropyl)methylamine. Interestingly, this reaction did not require the high dilutions conditions typically found in the syntheses of other squaramide macrocycles. This reaction afforded **100** in high yields with simple purification. This compound was found to be insoluble at the concentrations required for standard characterisation, so was used in the next reaction as is.

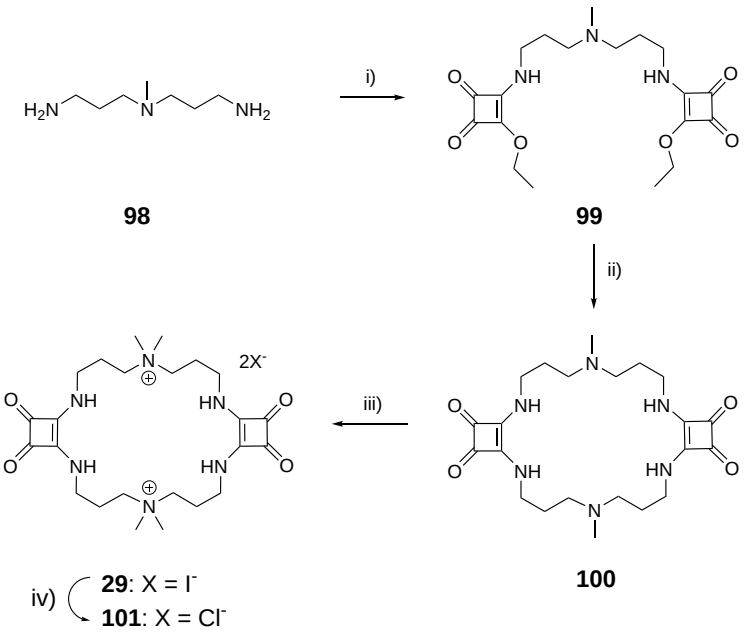

Scheme 4.1: Synthetic route to access compound **101** i) 3,4-diethoxy-3-cyclobutene-1,2-dione (3 eq), Et_2O, N_2, r.t, 22 h, 59%, ii) *N*-*N*-bis(3-aminopropyl)methylamine (1 eq), EtOH, r.t, 18 h, 72%, iii) MeI (7 eq), DMF, N_2, 70 °C, 21 h, quant, iv) chloride exchange resin (0.5 g), deionised water (dH_2O), r.t 12 h, quant.

The final step to access the final squaramide macrocycle **29** involved *N*-alkylation with excess iodomethane. Purification of **28** was performed according to literature procedures to afford **28** in high yields. As the iodide salt, the solubility in any solvents was far too low for routine characterisation, and so the salt was converted into the water soluble chloride form **105**. The reaction was visibly

observed as the chloride salt gradually dissolved into water, while the iodide salt was insoluble. In order to ensure an effective ion exchange, the reaction was performed under vigorous stirring to ensure efficient adsorption to the resin surface. The formation of the product was confirmed by ^{1}H NMR (Figure 4.4), ^{13}C NMR and Mass spectrometry (m/z 370.3592). In D_2O, the signals attributed to the NH protons were not observed.

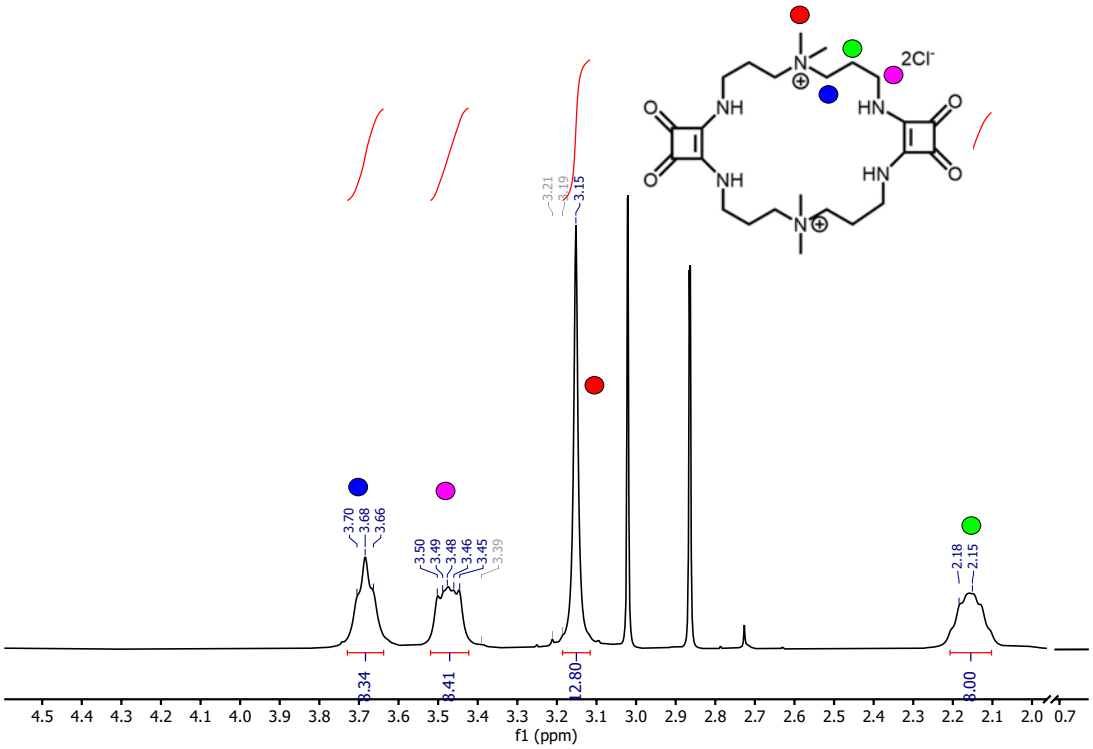

Figure 4.4: NMR spectrum of compound **101** in D_2O.

To access the linear squaramide receptor **28**, the first compound made was **103**. To access this, the starting 3-(dimethylamino)-1-propylamine was used in an asymmetric substitution of diethyl squarate. Diethyl squarate was used in a slight excess to prevent over-substitution. Compound **103** was obtained in good yields with straight-forward purification (m/z 227).

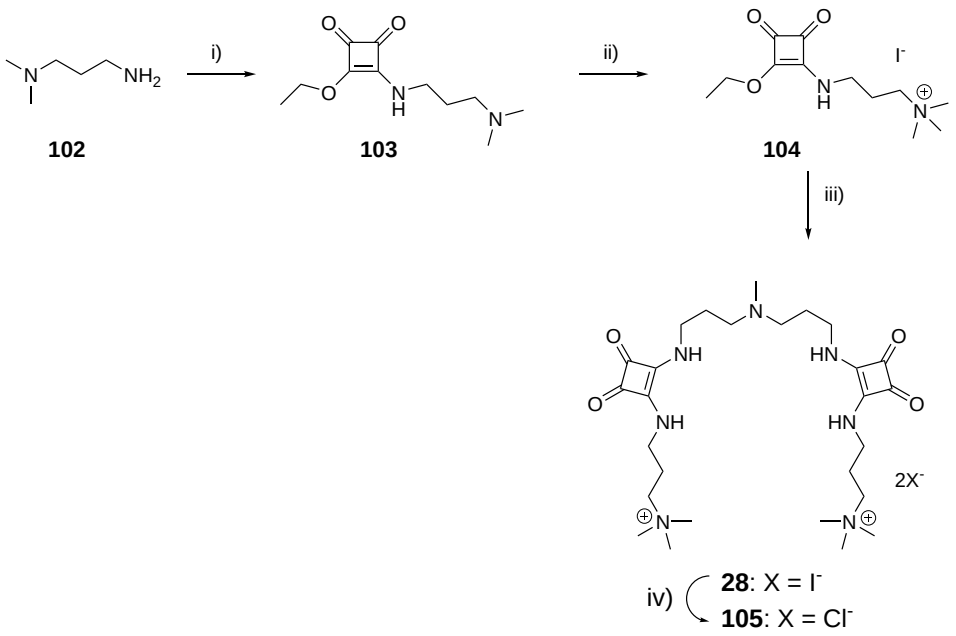

Scheme 4.2: Synthetic route to access compound **105** i) 3,4-diethoxy-3-cyclobutene-1,2-dione (1.2 eq), Et_2O, N_2, r.t, 1 h, quant, ii) MeI (1.9 eq), Acetone, N_2, Δ, 21 h, 52%, iii) *N*-*N*-bis(3-aminopropyl)methylamine (0.56 eq), MeOH, N_2, r.t, 24 h, 21%, iv) chloride exchange resin (0.5 g), dH_2O, r.t 12 h, quant.

Following this, the asymmetrical intermediate then under went a Menshutkin reaction to give **104**. Iodomethane was used in excess as the alkylating agent, while acetone used as the solvent to aid in solubility. *N*-*N*-bis-(3-aminopropyl) methylamine was then reacted with excess **104** to produce **28** in modest yields with the product purified according to literature procedures (*m/z* 242).[147] Attempts to obtain satisfactory ^{1}H NMR of **28** were unsuccessful due to the low solubility of the iodide salt in common NMR solvents. Additionally, a sealed vial of **28** was found to undergo a colour change from a yellow solid to a purple solid, attributed to potential oxidation of the salt over time when unprotected from light, suggesting instability of the product. To mitigate these effects, **28** was converted to the water soluble chloride salt **105** using ion-exchange resin, allowing for suitable ^{1}H NMR spectra to be obtained in D_2O to indicate successful product

formation in conjunction with mass spectrometry (m/z 606.3296).

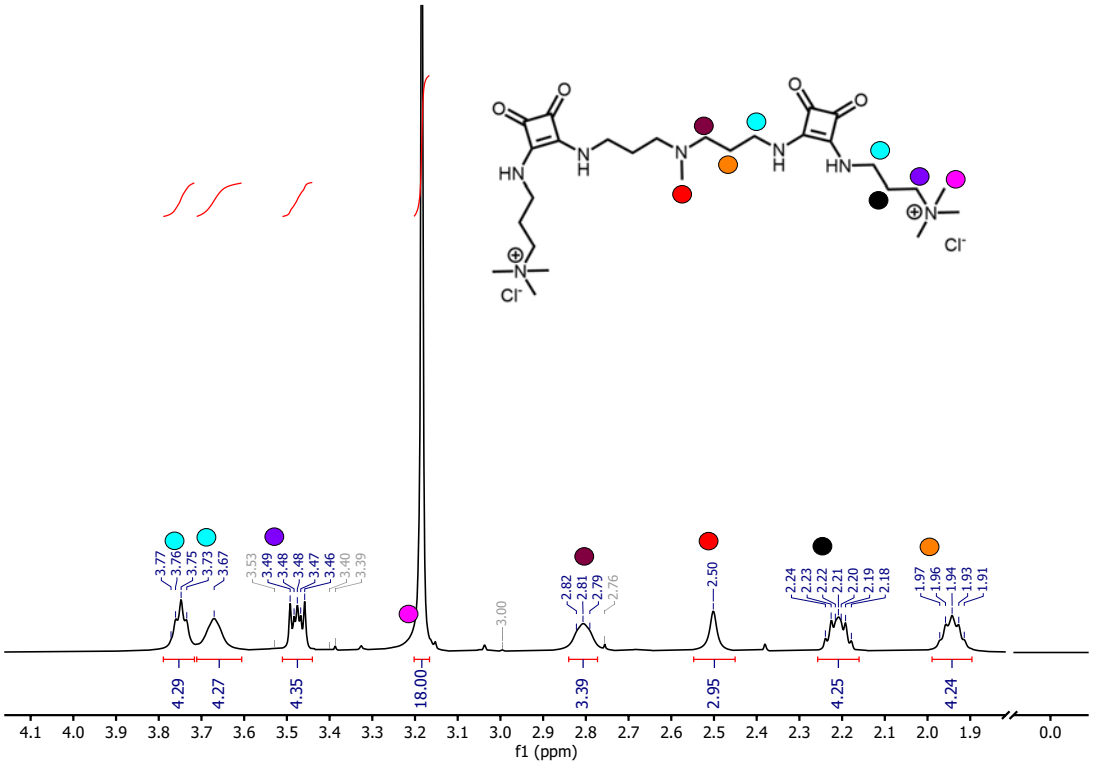

Figure 4.5: NMR spectrum of compound **105** in D_2O.

4.2 Results

4.2.1 Indicator Displacement Assays

In the following section, assays were performed three times, to ensure that the results obtained were reproducible over multiple days. By performing the assays three times, this allowed for a more accurate response to be observed, as calibration curves could be compared between the three runs. Calibration curves were evaluated by comparing R^2 values as obtained by statistical analysis performed by OriginLabs software. Ion Chromatography calibration curves were evaluated by sample spiking as mentioned further in this section, and were validated by using multiple injections. Furthermore, Ion Chromatography studies were also performed over multiple days to ensure reliability and reproducibility.

UV-vis Spectroscopy

As previously mentioned, UV-vis spectroscopy based IDAs were performed using the **28**:CR and **28**:BG chemosensing ensembles to quantify SO_4^{2-} in the presence of phosphate.[147] To increase the strength of the I:H complex in both cases, the indicators were employed as the di-anionic form to complement the di-cationic receptor, with the protonation state of the indicator ensured by performing studies at pH > pK_a. In the literature study, **28** was successfully used to quantify SO_4^{2-} from 0 – 120 ppm in 9:1 EtOH:Tris (10 mM) apparent pH 8.9.

To explore the suitability of **28** for UV-vis IDAs, and to confirm the literature response, **28** was titrated into a solution of CR to form the **28**:CR complex. This experiment aimed to determine the required **28**:CR ratio to maximise the observable colour change for subsequent SO_4^{2-} titrations to ensure a noticeable indication of sulfate binding. The initial literature conditions were used, with the study performed in a 9:1 EtOH:Tris buffer mixture, with an apparent pH of 8.9. As presented in Figure 4.6, the addition of **28** to CR induced an increase in absorbance at λ_{max} = 590 nm along with a decrease in absorbance at λ_{max} = 430 nm, which correlated to an observed colour change from blue to yellow over the course of the titration. Isotherm fitting to a 1:1 stoichiometry from this titration using HypSpec returned a $LogK_a$ of 3.18, suggesting a strong **28**:CR interaction.

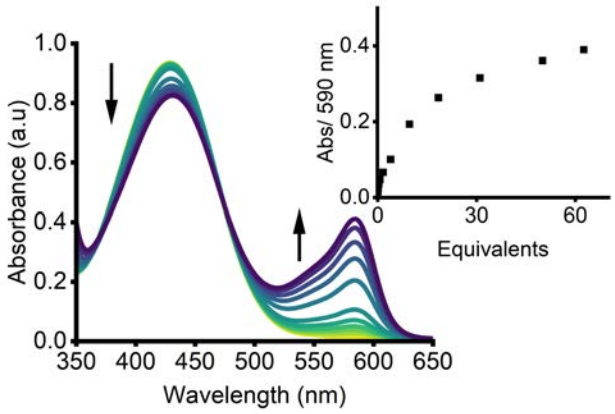

Figure 4.6: UV-vis spectroscopy titration of **28** with CR in 9:1 EtOH:Tris 10 mM pH 8.9. [Indicator] = 40 μM.

While this response was similar to that observed in the initial literature study,

serious solubility issues of **28** were encountered. Attempts to create stock solutions for titrations were hindered by the low solubility of **28** in the EtOH:Tris mixture. Additionally, the observed change in colour in the initial literature study suggested full complexation of **28** after the addition of 10 equivalents of **28**, which was not observed in the initial literature study,[147] with this response attributed to the low solubility of **28** resulting in inaccurate concentration calculations.

In attempts to achieve the same degree of colour change upon addition of **28** to CR, the proportion of organic solvent was varied from 80% EtOH, and increased to 95% EtOH (4.7a and 4.7b), as changing the percentage of water in the solvent system will change the competition between **28** and water, leading to a change in the titration isotherm while also impacting the solubility of **28**. Unexpectedly, increasing the EtOH content did not substantially increase the colour change upon addition of **28** to CR and only resulted in the formation of a precipitate as shown by the abnormal dark purple trace in 4.7b which indicated scattering due to insoluble particulates, attributed to the aforementioned solubility limitations of **28**. While decreasing the EtOH content avoided these solubility issues, the anticipated full complexation at 10 equivalents of **28** still did not occur. This study was also performed with a newly purchased bottle of CR to indicate if impurities were altering the response, however this was determined to not be the cause of the reduced response. Ultimately, the mis-match to the previous literature study may be attributed to general insolubilities of **28**, in addition to difficulties in maintaining the apparent pH of the ethanolic solution.

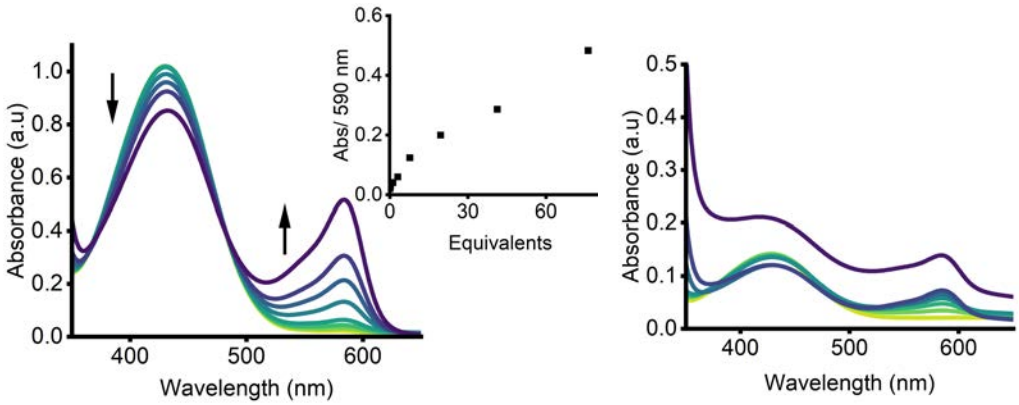

(a) 80% EtOH:1 mM Tris. **(b)** 95% EtOH:1 mM Tris.

Figure 4.7: Response of CR to increasing concentration of **28** performed by UV-vis spectroscopy in the indicated solvent. Inset graph presents absorbance against concentration of the salt. [Indicator] = 40 μM.

From these studies, it was determined that the **28**:CR complex would not result in a satisfactory colour change, and so the following studies were only performed with the **28**:BG complex.

The above study was then performed with **28** and BG to confirm the literature results, using the same solvent system above but with an apparent pH of 4.5. As presented in Figure 4.8, the addition of **28** to BG induced an increase in absorbance at λ_{max} = 630 nm along with a decrease in absorbance at λ_{max} = 430 nm, which correlated to an observed colour change from blue to red over the course of the titration. Isotherm fitting to a 1:1 stoichiometry from this titration using HypSpec returned a LogK_a of 2.91, suggesting a slightly weaker **28**:BG interaction when compared to CR.

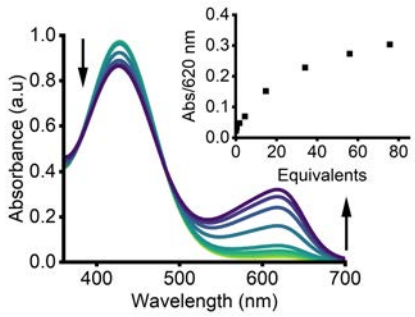

Figure 4.8: UV-vis spectroscopy titration of **28** with BG in 9:1 EtOH:Tris (10 mM) pH 4.5. [Indicator] = 40 μM.

Similar to the experiment performed with CR, the percentage of aqueous buffer was varied to observe the colour change upon addition of **28** to BG. The percentage of EtOH was decreased to 80% (4.9a) and increased to 95% (4.9b). It was found that either increasing or decreasing the proportion of EtOH resulted in a greater colour change upon addition of **28** to BG, albeit higher concentrations of **105** was required. The observed colour change in the BG system was greater when compared to CR, signifying that the **28**-BG complex will be more suitable for SO_4^{2-} sensing. Additionally, the lower LogK for **28**-BG compared to **28**-CR suggests that this indicator is more valuable for an IDA, as the weaker interaction suggests a greater chance of indicator displacement upon sulfate addition.

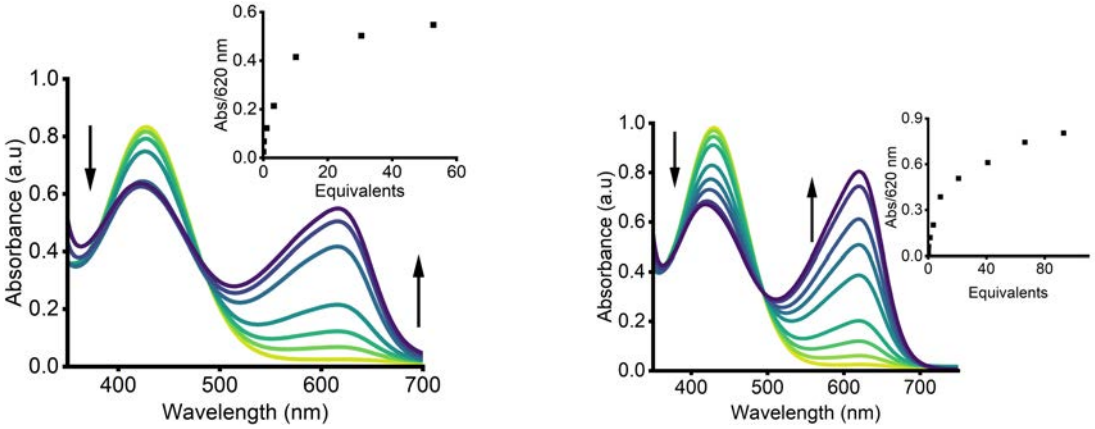

(a) 95% EtOH:1 mM Tris. **(b)** 80% EtOH:1 mM Tris.

Figure 4.9: Response of BG to increasing concentration of **28** performed by UV-vis spectroscopy. Inset graph presents absorbance against concentration of the salt. [Indicator] = 40 μM.

With this information in hand, the next step was to perform a SO_4^{2-} titration with the **28**-BG complex. From the previous study, a solvent system of 95% EtOH:1 mM Tris buffer was used with a 1:4 BG:**28** stoichiometry. Upon the gradual addition of SO_4^{2-} to this complex, an increase in absorbance was observed at λ_{max} = 430 nm along with a decrease at λ_{max} = 620 nm attributed to displacement of the indicator and formation of a **28**-SO_4^{2-} complex with a colour change from yellow to blue. Monitoring the change in absorbance at λ_{max} = 620 nm resulted in the construction of a linear calibration curve (R^2 0.99) from 0 μM up to 70 μM SO_4^{2-}.

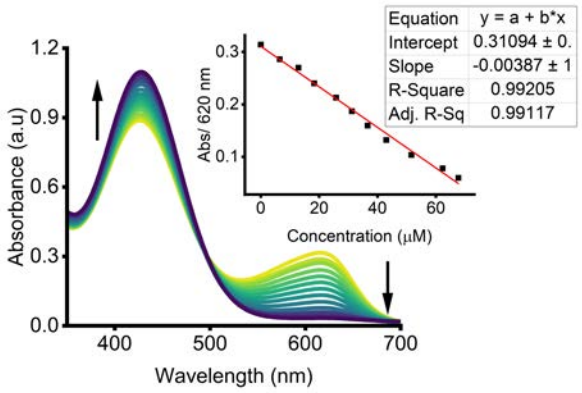

Figure 4.10: UV-vis spectroscopy SO_4^{2-} titration of **28** complexed with Bromocresol green (160 μM:40 μM) in 95% EtOH:Tris (1 mM pH 4.5). Inset presents calibration curve generated by Origin.

To test the limits for SO_4^{2-} detection using the **28**-BG complex, a second titration was performed in the presence of 4 mM NaCl, 9 μM $CaCl_2$, 9.4 mM $MgCl_2$ and 7 μM KCl. As the competition of the solvent system was increased through the introduction of these salts, minimal change was observed over the course of the SO_4^{2-} titration, suggesting that the **28**-BG complex would not be suitable to quantify SO_4^{2-} concentrations in complex aqueous mixtures similar to those found in biological systems, suggesting this would be ineffective for sulfate sensing.

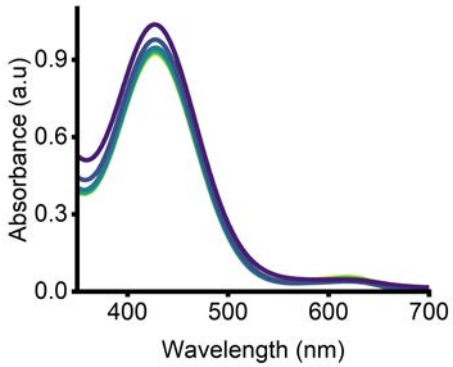

Figure 4.11: UV-vis spectroscopy SO_4^{2-} titration of **28** complexed with BG (160 μM:40 μM) in 95% EtOH:Tris (1 mM pH 4.5). Final concentration of salts is 4 mM NaCl, 9 μM $CaCl_2$, 9.4 mM $MgCl_2$ and 7 μM KCl.

Due to the low solubility of **28** in the aforementioned solvent system, the response of the water-soluble **105** upon addition of SO_4^{2-} was explored as the

105-BG complex in the same conditions as above. While this receptor exhibited greater solubility in the EtOH:Tris mixture, the observed response to SO_4^{2-} was not substantially different to that observed for **28**. The I:H ratio was additionally altered to be 1:8 BG:**105** (Figure 4.12) to improve the observed colour change upon SO_4^{2-} addition, however this did not provide an improved response. This suggests that while the formation of **105** resulted in a more soluble receptor, this had no substantial impact on the SO_4^{2-} sensing capabilities due to the poor colour change in the presence of a salt solution that mimics the composition of physiological fluids.

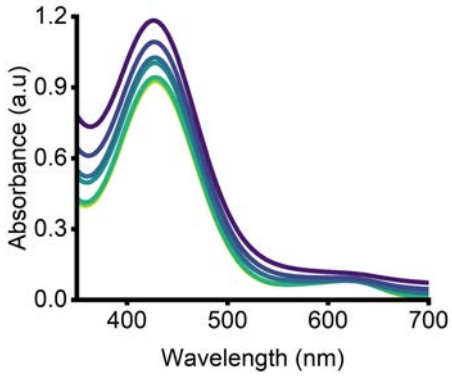

Figure 4.12: UV-vis spectroscopy SO_4^{2-} titration of **105** complexed with BG (320 μM:40 μM) in 95% EtOH:Tris (1 mM pH 4.5). Final concentration of salts is 4 mM NaCl, 9 μM $CaCl_2$, 9.4 mM $MgCl_2$ and 7 μM KCl.

Fluorescence IDA

While the IDAs using the linear receptor **105** were not effective in complex mixtures, a fluorescent IDA using macrocycle **29** in combination with fluorescein has been reported previously.[50] This system was reported to have higher affinity for SO_4^{2-} than the linear receptor **28** with a $LogK_a$ for SO_4^{2-} of 6.7, suggesting strong binding of SO_4^{2-} by **29**.

Therefore, this system was also evaluated. Firstly, a fluorescence titration was performed observing the response upon addition of **29** into a solution of FNa_2 in MeOH:H_2O (9:1) following the literature protocol.[50] While the expected fluorescence quenching was observed, an excess of **29** was required to induce this

response, contrary to that observed in the prior literature. This can be attributed to the low solubility of **29** in the MeOH:H_2O mixture, similar to that observed in the UV-vis spectroscopic titrations of **28**. Due to this unexpected result and the poor receptor solubility, the remainder of the studies with the squaramide macrocycle were performed with the water soluble compound **101**.

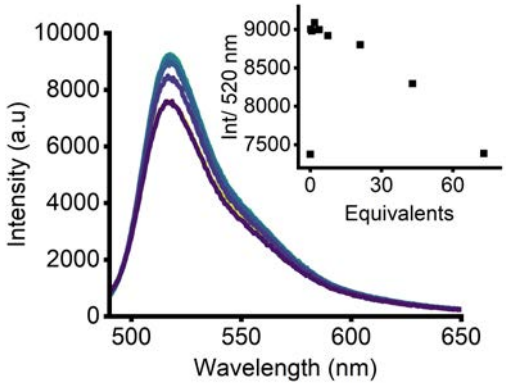

Figure 4.13: Fluorescence titration of FNa_2 with increasing equivalents of **29** performed in 10% H_2O:MeOH ([Indicator] = 14 μM, λ_{ex} = 490 nm). The excitation bandpass was 3 nm and the emission bandpass was 5 nm. Inset graph presents emission intensity as a function of guest equivalents.

Upon formation of the water-soluble **101**, a titration with FNa_2 was performed in the same solvent system. In this case, addition of **101** to FNa_2 resulted in the expected turn-off emission response in 10% H_2O:MeOH with an observable colour change from a bright green solution to a pale yellow solution over the course of the titration. While the titration isotherm could not be fit to a standard binding model, visual inspection of the generated isotherm indicated no further change in emission intensity after addition of 1 equivalent of macrocycle **101** to FNa_2 suggesting strong binding and formation of a 1:1 complex. This informs the required indicator:guest ratio for future studies, requiring them to be equimolar. With this information in hand, this system was then used for SO_4^{2-} titrations.

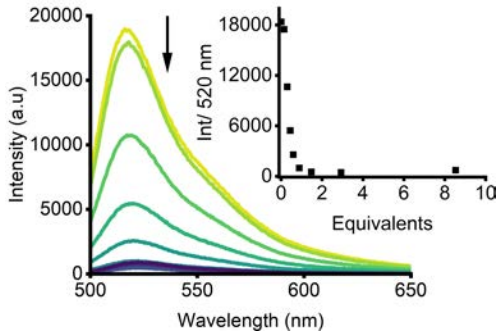

Figure 4.14: Fluorescence titration of FNa_2 with increasing equivalents of compound **101** performed in 10% H_2O:MeOH ([Indicator] = 14 μM, λ_{ex} = 490 nm). The excitation bandpass was 3 nm and the emission bandpass was 10 nm. Inset graph presents emission intensity as a function of guest equivalents.

The fluorescence response upon addition of SO_4^{2-} to a 1:1 FNa_2:**101** complex was observed in 10% H_2O:MeOH. The initial expected turn-on response was observed after addition of less than 1 equivalent of SO_4^{2-}, however quenching was observed upon the addition of greater concentrations of SO_4^{2-}, which could be attributed to excess SO_4^{2-} interacting with FNa_2 after displacement of **101** from the complex. The interaction between FNa_2 and SO_4^{2-} was confirmed in a titration of SO_4^{2-} into a solution of FNa_2, in which quenching was observed up to 8 equivalents of SO_4^{2-} (see Figure A.3.22 in the Appendix). While this was unexpected, it resulted in a linear calibration curve (R^2 0.99) from 12 μM to 320 μM SO_4^{2-} (7 to 185 ppm) as presented in Figure 4.15.

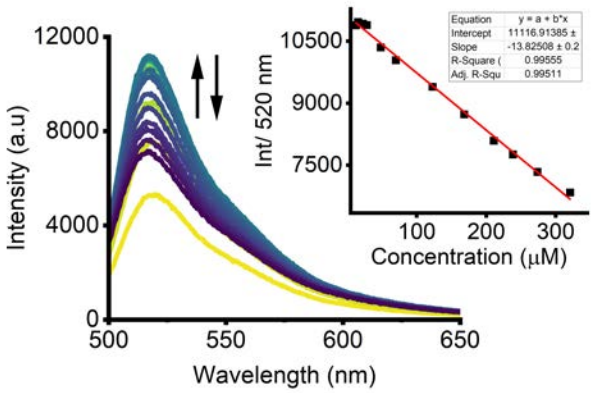

Figure 4.15: Fluorescence titration of the 1:1 FNa_2:**101** complex with increasing concentration of TBA_2SO_4 performed in 10% H_2O:MeOH ([Indicator] = 14 μM, λ_{ex} = 490 nm). The excitation bandpass was 3 nm and the emission bandpass was 5 nm. Inset graph presents the calibration curve fit using Origin.

This response was further explored by repeating this experiment in a complex solvent system containing a range of salts (4 mM NaCl, 9 μM $CaCl_2$, 0.4 mM $MgCl_2$ and 7 μM KCl), with the salt concentration was intended to mimic that of biological serum. Due to the solubility limitations of the added chloride salts, the water content of the solvent system was increased to 15%, with a large excess of **101**, relative to FNa_2, required to induce a substantial colour change. This resulted in a linear calibration curve (R^2 0.99) from 240 μM to 410 μM SO_4^{2-} (139 to 238 ppm) as presented in Figure 4.16, suggesting lower sensitivity for SO_4^{2-} in a more complex solvent system.

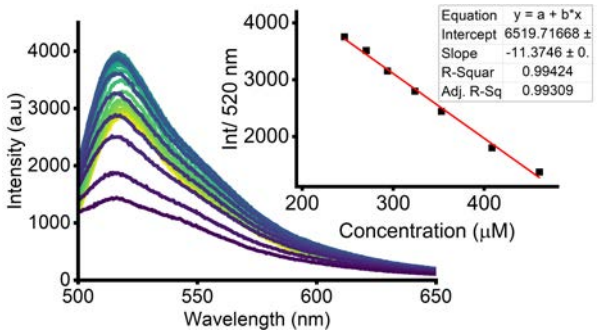

Figure 4.16: Fluorescence titration of FNa_2:**101** complex with increasing concentration of TBA_2SO_4 performed in 15% H_2O:MeOH, containing 4 mM NaCl, 9 μM $CaCl_2$, 0.4 mM $MgCl_2$ and 7 μM KCl ([Indicator] = 14 μM, [**101**] = 420 μM, λ_{ex} = 490 nm). The excitation bandpass was 3 nm and the emission bandpass was 5 nm. Inset graph presents the calibration curve fit using Origin.

This shows that this fluorescent IDA can be used for SO_4^{2-} calibration curve construction, while the results reported in the literature were improved upon through the use of the more soluble receptor **105**, allowing **105** to be utilised in SO_4^{2-} recognition through a fluorescence-based IDA as the FNa_2 complex. However, it was observed that the response upon the addition of SO_4^{2-} to a solution of the **105**:FNa_2 complex in a salt solution was not consistent. Instead of a gradual increase in fluorescence intensity over the whole course of the titration, this non-linear increase in intensity was observed up to 200 μM SO_4^{2-}, after which point an unexpected turn off response was observed, suggesting interaction of SO_4^{2-} with **105**. These results suggest that while this method is suitable for indirect SO_4^{2-} detection, the inconsistent response observed in the biologically

relevant SO_4^{2-} concentration range[4] suggests limitations in the applications.

4.2.2 Metal extrusion assays

When considering the experimental conditions used for MEAs, the traditional techniques of spectroscopic titrations need to be partially modified due to the formation of a potentially insoluble salt upon metal extrusion. Traditional titrations involve gradual addition of guest to a cuvette containing receptor, with a constant concentration and molecules which remain dissolved in solution. However, the presence of precipitate can interfere with spectroscopic measurements and removal of this salt by filtration results in a significant reduction in sample volume. Therefore, a 'titration' method was developed in which different amounts of guest were added to individual receptor aliquots of the same volume and same concentration, to ensure that filtration can occur without interfering with sample volume over the course of the titration.

The development of this assay aims to introduce a new tool for SO_4^{2-} recognition, as this class of technique has seldom been used for SO_4^{2-}. While turbidometric systems have been used using $BaCl_2$ for precipitation of SO_4^{2-},[148] this does not allow for optical determination of this response by fluorescence or UV-vis spectroscopy.

Anthracene compound 52 and 62

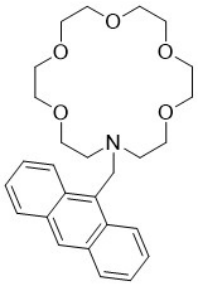

52

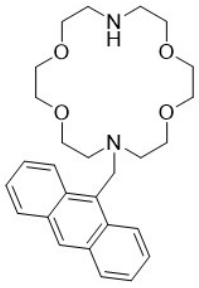

62

While the MEA performed is relatively straightforward, the ultimate goal is to apply this concept in a biological system. Due to this, a small handful of studies

were required to determine if MEAs could be performed in a complex medium mimicking that of blood. To do this, SO_4^{2-} titrations were firstly performed using a pre-formed 1:1 **52**-Ba(II) complex in order to construct calibration curves for quantification, with Ba(II) used for all receptors due to the changes in optical properties upon Ba(II) addition. As a proof of concept, a titration was first performed in MeCN. Upon gradual addition of SO_4^{2-} to a 1:1 complex of **52**-Ba(II), a decrease in fluorescence intensity was observed (Figure 4.18). As the Ba(II) is extruded from the ligand and forms insoluble $BaSO_4$, the inhibited internal quenching becomes prevalent once more. As expected, this is the opposite response to that observed in the metal titrations in Chapter 3, indicating that the MEA works as intended in an organic solvent, however slight inconsistencies in the emission spectra limit the utility of this receptor.

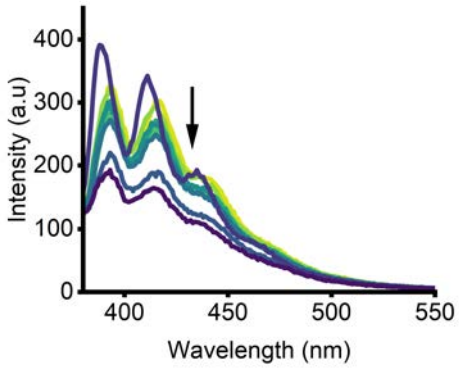

Figure 4.18: Fluorescence titration of **52**-Ba(II) 1:1 complex with increasing concentration of TBA_2SO_4 performed in MeCN ([probe] = 5 μM, λ_{ex} = 354 nm). The excitation bandpass was 5 nm and the emission bandpass was 5 nm.

The response to SO_4^{2-} in a 1:20 20 mM Tris:MeCN (Figure 4.19) mixture at pH 10.1 was next evaluated, as the addition of a buffer more closely resembles conditions used with biological samples. In this system, addition of guest (up to 100 μM) resulted in an unexpected initial turn on response, which then reduced in intensity over the course of the experiment. This unexpected response meant that a linear calibration curve could not be constructed. This could be attributed to the solution pH, as this study was performed in a basic medium. While a pH study was not performed with this receptor, the results observed in the pH

titration of **63** in Chapter 2 suggest that the pH of the solution has a significant impact on the emission profile of the aza-crown ether ligand. It may stand to reason that upon the addition of SO_4^{2-} to this system, the multiple potential equilibria processes occurring in solution are affected, resulting in a variation in the emission profile.

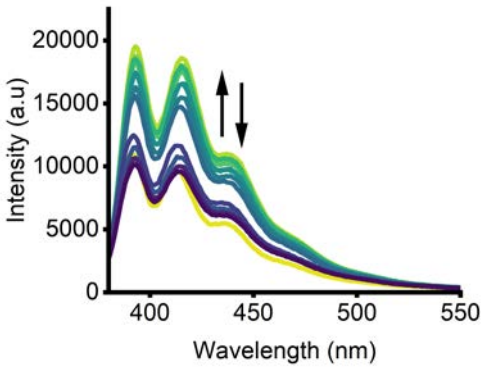

Figure 4.19: Fluorescence titration of **52**-Ba(II) 1:1 complex with increasing concentration of TBA_2SO_4 performed in 1:20 20 mM pH 10.2 Tris:MeCN ([probe] = 5 μM, λ_{ex} = 354 nm). The excitation bandpass was 5 nm and the emission bandpass was 5 nm.

Given that the use of buffer appeared to alter the probe behaviour, a further titration was performed in a mixture of 1% H_2O/MeCN containing Na(I), K(I), Mg(II) and Ca(II) as the chloride salts to mimic the cations present in a biological sample (Figure 4.20). In this case, the gradual decrease in intensity as SO_4^{2-} was added (up to 280 μM) to **52**-Ba(II) was observed, attributed to $BaSO_4$ formation reinstating quenching. Unfortunately, the response was monotonic but non-linear, meaning that it would not be useful for calibration curve construction in aqueous media. In some instances, it is possible to construct non-linear calibration curves. However, there are many disadvantages to this approach. Firstly, the construction of these curves requires complex mathematical functions such as polynomials or quadratics, which must be calculated specifically to suit the system, as opposed to linear regression which requires no further computation. This implies that slight errors in the calculation of this function may lead to inaccurate concentration calculations. Additionally, for systems in which the expected response is linear

(such as fluorescence studies), matrix effects may result in inaccurate calculations in non-linear calibration, which is applicable to this system as the experimental procedure was modified to filter a solid precipitate upon each SO_4^{2-} addition.

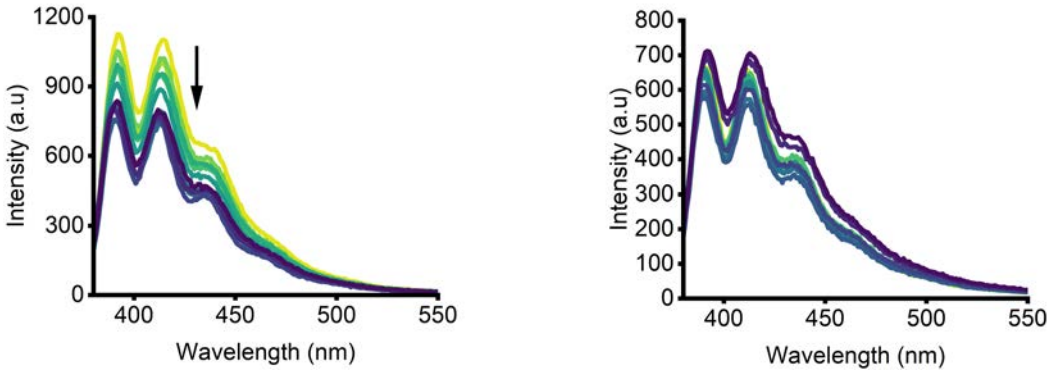

(a) 52 **(b) 62**

Figure 4.20: Fluorescence titration of **52**-Ba(II) 1:1 complex and the **62**-Ba(II) 1:1 complex and with increasing concentration of TBA_2SO_4 performed in 1% Water:MeCN, with final salt concentrations of 4 mM NaCl, 9 μM $CaCl_2$, 0.4 mM $MgCl_2$ and 7 μM KCl ([probe] = 5 μM, λ_{ex} = 354 nm). The excitation bandpass was 10 nm and the emission bandpass was 10 nm for **62** and 5 nm/5 nm for **52**.

MEA were then performed using compound **62** in the same conditions as 4.20a. As expected, a modulation in fluorescence intensity with increasing SO_4^{2-} concentrations, attributed to $BaSO_4$ formation as the M-L bond breaks. In contrast to that observed for the **52**-Ba(II) complex, this modulation was not consistent, as a gradual decrease in emission intensity was not observed. From Chapter 3, it was observed that the relative $LogK_a$ for the aza-crown-ether receptors decreased from 1 nitrogen atom to 2 nitrogen atoms in the ligand, with **62** subsequently exhibiting lower $LogK_a$ values for tested metals. It could be reasoned that this inconsistent change in emission is attributed to competition between the Ba(II) ion and the other metal cations in solution, with the M-L bond breaking and re-forming with other cations in solution. This suggests that **62** would not be suitable for MEA purposes due to greater effects of competition when compared to **52**.

Taken together, the MEAs performed for both compound **52** and **62** for SO_4^{2-} as the 1:1 Ba(II) complex provide proof of principle for the use of Ba(II) extrusion

assays to quantify SO_4^{2-} concentrations in solution, however care must be taken to consider potential interferants in solution. Due to the minimal overall change in both the fluorescence and UV-vis spectra, receptors containing naphthalimide fluorophore were then employed.

Naphthalimide Aza-crown ether 63

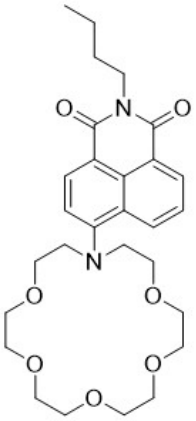

63

Since compound **63** displayed the greatest change in emission upon addition of Ba(II) out of the compounds evaluated (**63** – **65**), the **63**-Ba(II) complex was deemed suitable for MEA construction. As observed in Chapter 3, the selective response for Ba(II) over other Group (I) and Group (II) metals commonly found in biological samples, suggesting less effects from interference.

Due to the high emission intensity of the complexed receptor, fluorescence spectroscopy was initially used. SO_4^{2-} was introduced into a 1:1 **63**-Ba(II) system, with the solutions filtered with a 5 μm filter after each addition. As presented in Figure 4.22, SO_4^{2-} introduction led to a drastic decrease in intensity at 530 nm, correlated to the removal of Ba(II) and reintroduction of PET quenching. A large decrease in emission intensity was observed when monitoring λ_{max} = 530 nm, which was the anticipated response when compared to the initial Ba(II) titrations of **63** presented in Chapter 3. However, this substantial change in emission upon addition of 1 equivalents of SO_4^{2-} indicated that fluorescence spectroscopy was too sensitive resulting in large fluctuations in the spectrum, and a linear

calibration curve could not be constructed.

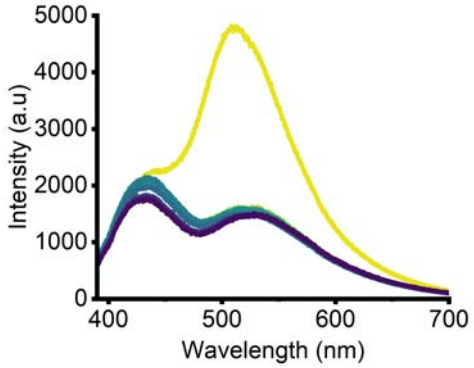

Figure 4.22: SO_4^{2-} titration of the 1:1 complex compound **63**-Ba(II) in MeCN ([probe] = 5 μM, λ_{ex} = 370 nm). The excitation bandpass was 5 nm and the emission bandpass was 20 nm.

Therefore, this study was then performed using UV-vis spectroscopy. As shown in Figure 4.23, the addition of SO_4^{2-} to the 1:1 **63**-Ba(II) complex indicated reformation of the free ligand, with a ratiometric change observed upon gradual addition of SO_4^{2-}. The appearance of a λ_{max} at 416 nm was associated with the free ligand, indicating successful displacement of Ba(II) from **63**, resulting in a linear calibration curve when plotting absorbance at 416 nm/360 nm from 0 – 40 μM SO_4^{2-} (R^2 0.96).

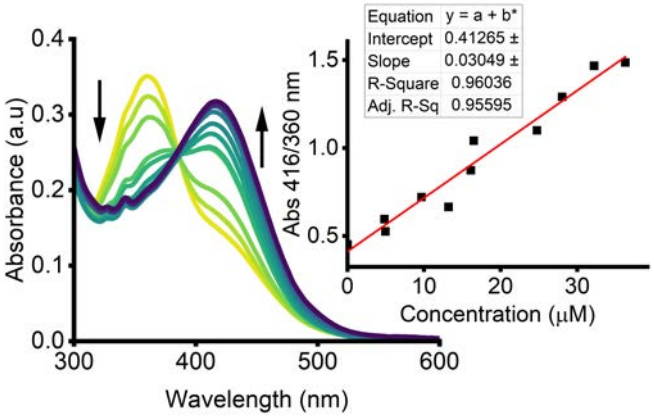

Figure 4.23: SO_4^{2-} titration of the 1:1 complex compound **63**-Ba(II) in MeCN through UV-vis ([probe] = 40 μM). Inset presents calibration curve generated by Origin.

The impact of increasing water content on the response of this probe was evaluated (1% H_2O/MeCN) as shown in Figure 4.24 to determine if the **63**-Ba(II)

complex maintains solubility and a linear response to SO_4^{2-}. The small addition of water was found to not significantly impact the ML binding stoichiometry as a 1:1 ML stoichiometry was observed in UV-vis spectroscopic titrations in Chapter 3, however the addition of higher % volumes of water was restricted due to the low aqueous solubility of **63**. Once again, a linear response was observed, with the highest linearity obtained through plotting of the absorbance at 360 nm (in contrast to the ratiometric approach taken in 100% MeCN). This plot was linear in the range of $0 - 40$ μM SO_4^{2-} with R^2 of 0.95 indicating no decrease in the working range of the receptor when moving to slightly more aqueous conditions.

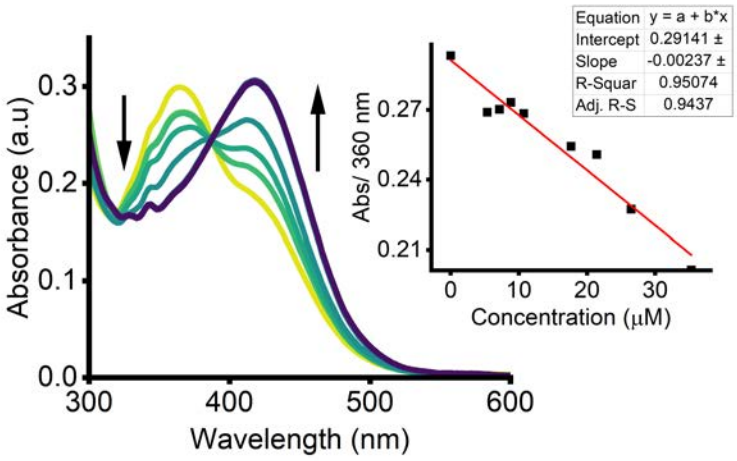

Figure 4.24: SO_4^{2-} titration of the 1:1 complex compound **63**-Ba(II) in 1% Water:MeCN through UV-vis ([probe] = 40 μM). Inset presents calibration curve generated by Origin.

The next step was to determine if the **63**-Ba(II) complex would retain a linear response in the presence of common interferants at relevant concentrations. These included other metals which could bind to the crown ether ligand or form SO_4^{2-} salts. As shown in Figure A.3.7 in the Appendix, the addition of a mixture of metal chloride salts led to a diminished response. Therefore, a set of experiments were performed to determine which salts were interfering the most.

The response upon the addition of SO_4^{2-} to **63** was observed in 1% water/MeCN in the presence of either 140 mM $NaBF_4$, 2 mM KPF_6, 2.5 mM $Ca(ClO_4)_2$ or 120 mM $MgCl_2$ (Figure A.3.11 in the Appendix) to determine if ex-

cess competing cations resulted in interference in the UV-vis absorbance spectra. High concentrations were used to saturate the solution to push the limits of the working range. It was observed that high salt concentration led to no significant change in the UV-vis absorbance spectra of **63**-Ba(II), with the λ_{max} attributed to the free ligand observed and no metal complex formation. As the concentration of the competing cations decreased as presented in Figure 4.25, the λ_{max} of the **63**-Ba(II) metal complex was observed with the exception of in the presence of Mg(II) suggesting that the presence of Mg(II) prevents formation of any metal complex. While the LogK$_a$ for **63** was highest in the instance of Ba(II), Mg(II) seems to interfere with Ba(II) binding, while also indicating no formation of the Mg(II) complex.

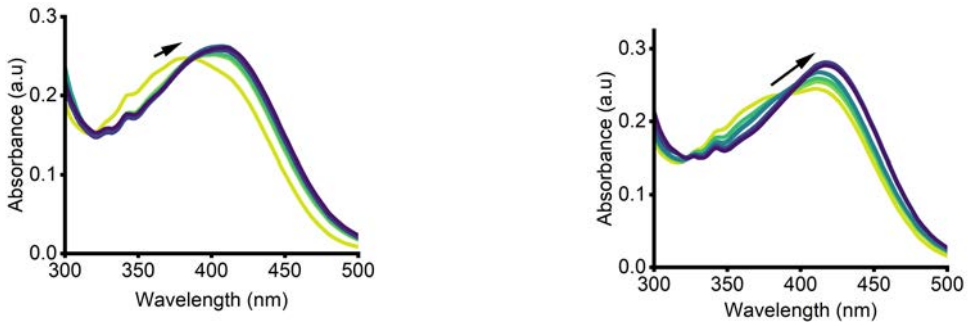

(a) 1 mM $NaBF_4$ **(b)** 23 μM $CaCl_2$

(c) 1 mM $MgCl_2$ **(d)** 18 μM KPF_6

Figure 4.25: UV-vis spectroscopic titration of **63**-Ba(II) with increasing equivalents of TBA_2SO_4 in 1% water/MeCN ([probe] = 40 μM) containing the mentioned salts (concentration indicative of final salt concentration).

One experiment was performed with a mixed salt concentration at 200 x dilution, with this representing concentration in a diluted sample of serum plasma in Figure A.3.9 in a system containing 5 mM NaCl, 9 μM KCl, 12 μM $CaCl_2$ and

0.5 mM $MgCl_2$, in comparison to 4.26b containing 4 mM NaCl, 7 μM KCl, 9 μM $CaCl_2$ and 0.4 mM $MgCl_2$. As the overall matrix salt concentration continued to decrease, a larger change in the UV-vis spectra was observed, however this resulted in an inconsistent overall change which could not be fit to linear regression up to 900 μM of SO_4^{2-}, signifying that while **63**-Ba(II) functions effectively in MEA in simple solutions, limitations are observed as the complexity of the media increases. This can be attributed to the competitive binding of other Group (I) and Group (II) metals to **63**, as described in Chapter 3.

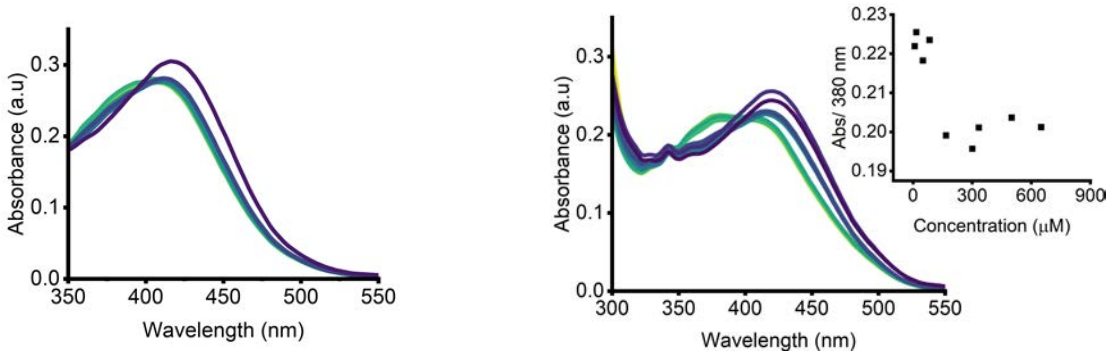

(a) 5 mM NaCl, 9 μM KCl, 12 μM $CaCl_2$ and 0.5 mM $MgCl_2$.

(b) 4 mM NaCl, 7 μM KCl, 9 μM $CaCl_2$ and 0.4 mM $MgCl_2$.

Figure 4.26: UV-vis spectroscopic titration of **63**-Ba(II) with increasing equivalents of TBA_2SO_4 in 1% water/MeCN ([probe] = 40 μM) containing the mentioned salts (concentration indicative of final salt concentration).

The effects of sample preparation were also briefly studied to determine whether to diminished response was attributed to precipitates forming at a different stage of sample preparation, however this was shown to have no affect on the observed results (Figure A.3.8 in the Appendix).

Ultimately, compound **63** was able to function in a MEA. Due to the high sensitivity of fluorescence spectroscopy, this was limited to UV-vis spectroscopy. Reduced responses were observed in complex solvent mixtures, with a decrease in calibration curve linearity as complexity increased when comparing Figure 4.24 to 4.26b. No MEA was performed with compounds **64** or **65**, due to the fact that compound **63** indicated that this method begins to fail in complex systems. However, this indicates that a MEA can be used for SO_4^{2-} recognition in complex

mixtures containing competing cations and anions, once more presenting one of the first example of MEA for SO_4^{2-} recognition.

Coumarin 67

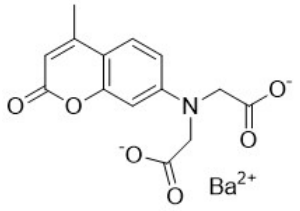

67

The final compound studied for MEA was compound **67**. Due to the water solubility of this compound, it was anticipated that there was higher viability of performing this MEA in water. Due to excess $Ba(OH)_2$ used in the formation of **67**, the calculated receptor concentrations vary slightly from those calculated in most assays described below. Studies were also performed using **67** after complexation with 1 equivalent of $Ba(OH)_2$, however the observed response had no significant difference when prepared with 2 equivalents. This was repeated with the studies performed in varying % of water in the solvent system, and SO_4^{2-} titration in a solvent system mimicking seawater.

The highly water soluble nature of **67** led to determining if **67** would function as a SO_4^{2-} sensor in 100% water. Following from the results in Chapter 2, a preliminary SO_4^{2-} titration of the **67**-Ba(II) complex was performed in water (Figure 4.28). Minimal change was observed in the fluorescence and UV-vis spectrum, suggesting that the addition of up to 50 equivalents SO_4^{2-} did not induce displacement of Ba(II) from **67**.

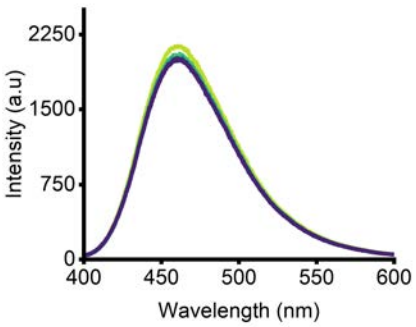

(a) Fluorescence. [Receptor] = 10 μM.

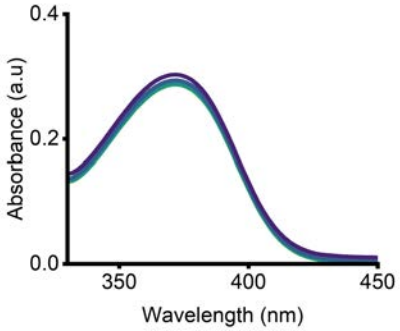

(b) UV-vis. [Receptor] = 50 μM

Figure 4.28: $SO_4{}^{2-}$ titration of **67** in Water (λ_{ex} = 390 nm). For the fluorescence study, the excitation bandpass was 10 nm and the emission bandpass was 10 nm.

Following this, the response of **67** upon $SO_4{}^{2-}$ addition in both 75% H_2O:MeCN was studied (Figure 4.29). Upon addition of $SO_4{}^{2-}$ to **67**, the expected response was a gradual decrease in fluorescence intensity, as this would allow for monitoring of $SO_4{}^{2-}$ concentrations over a wider range. The fluorescence intensity of **67** decreases as $SO_4{}^{2-}$ is added with no further change, with no change observed in the UV-vis spectrum. As displacement of Ba(II) from **67** was not observed to occur in this solvent system, potentially as a result of high competition with the solvent, this was deemed unsuitable for further studies.

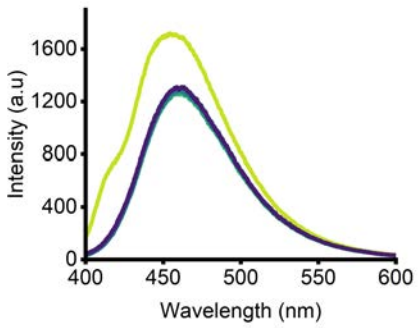

(a) Fluorescence. [Receptor] = 10 μM.

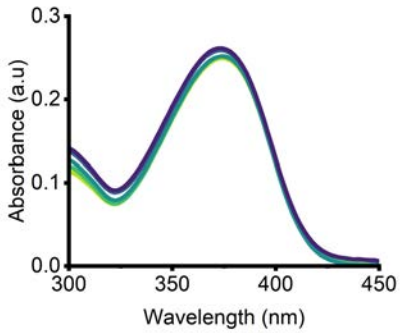

(b) UV-vis. [Receptor] = 50 μM

Figure 4.29: $SO_4{}^{2-}$ titration of compound **67** in 75% Water:MeCN (λ_{ex} = 390 nm). For the fluorescence study, the excitation bandpass was 10 nm and the emission bandpass was 10 nm.

To determine if a buffered system was required given the pH sensitivity of **67** (Chapter 2), experiments were performed to determine the response of varied buffer concentrations with 1:1 1 mM HEPES:MeCN and 1:1 5 mM HEPES:MeCN.

It is considered that the excess $Ba(OH)_2$ in the sample of **67** used may impact the fluorescence intensity. A large excess (50 equivalents) of added SO_4^{2-} induced a small change in emission intensity upon addition to **67** for both solvent systems as presented in Figure 4.30. This suggests that HEPES is not the ideal buffer for this system, as a large change in emission intensity is preferable for MEA applications.

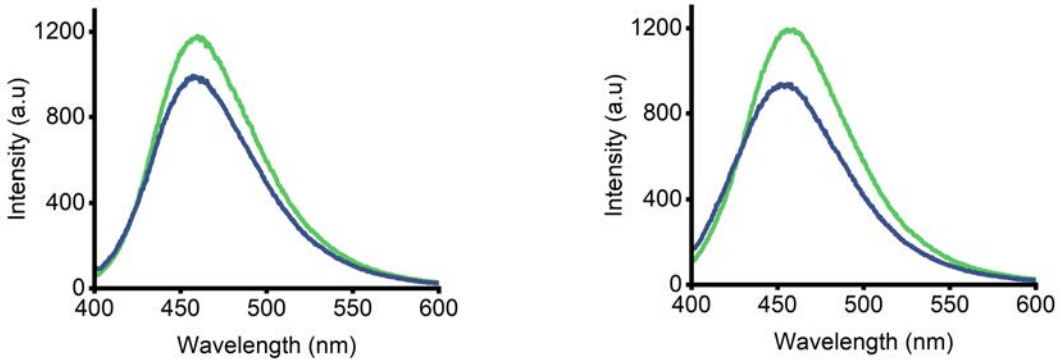

(a) 50% 1 mM HEPES:MeCN. **(b)** 50% 5 mM HEPES:MeCN.

Figure 4.30: SO_4^{2-} response of compound **67** in HEPES (pH 7.4):MeCN performed by fluorescence spectroscopy ([probe] = 5 μM, λ_{ex} = 390 nm). The excitation bandpass was 10 nm and the emission bandpass was 10 nm.

While the response in Figure 4.28 shows a small response upon the addition of up to 50 equivalents SO_4^{2-}, SO_4^{2-} titrations were next performed in water with higher concentrations of SO_4^{2-} added as presented in Figure 4.31 to determine if this was due to low sensitivity of **67** for SO_4^{2-}. As high concentrations of SO_4^{2-} were added (in the millimolar range, as opposed to the μM range used for the previous studies), a red shift was observed through fluorescence spectroscopy from λ_{max} 460 nm to 437 nm, resulting in a linear calibration curve (R^2 0.96) from 10 – 120 mM SO_4^{2-}, indicating that **67** is sensitive to SO_4^{2-} in water.

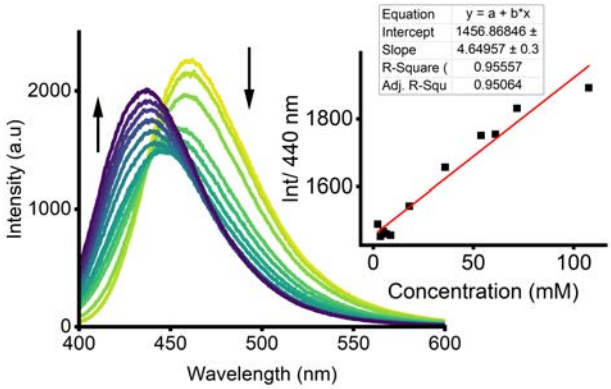

Figure 4.31: SO_4^{2-} titration of compound **67** in 100% Water ([probe] = 5 μM, λ_{ex} = 390 nm). The excitation bandpass was 10 nm and the emission bandpass was 10 nm.

The linear SO_4^{2-} range detectable was similar to that found in sea water. Therefore, the MEA was then performed in artificial sea water containing high concentrations of competing salts (1 M NaCl, 0.3 M $MgCl_2$, 70 mM Na_2SO_4, 45 mM $CaCl_2$ and 13 mM KCl) as shown in Figure 4.32. Addition of SO_4^{2-} to **67** resulted in a variation in intensity similar to that observed in Figure 4.28. While this response was observed, a quenching was observed upon the addition of 80 mM SO_4^{2-}, with no further change in emission observed, suggesting full displacement of Ba(II) from **67**. A linear calibration curve was generated from 10 – 70 mM SO_4^{2-} with good linearity and R^2 of 0.96.

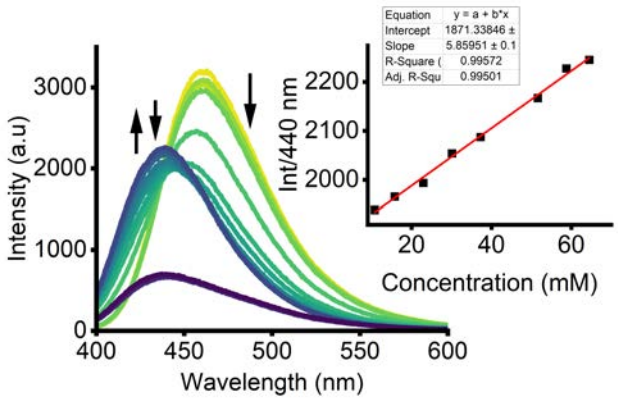

Figure 4.32: SO_4^{2-} titration of compound **67** in 100% Water ([probe] = 10 μM, λ_{ex} = 390 nm). The excitation bandpass was 10 nm and the emission bandpass was 10 nm. Solvent system contains 1 M NaCl, 0.3 M $MgCl_2$, 70 mM Na_2SO_4, 45 mM $CaCl_2$ and 13 mM KCl.

Spiking experiments were then performed to validate the generated calibration curve. SO_4^{2-} solutions at 70 mM, 30 mM and 120 mM were made in artificial seawater and the emission response obtained upon addition to a solution of **67**. From the linear regression analysis, negative x-values were obtained upon substituting the obtained emission intensities, suggesting that the measured y-values were outside of the valid range of the calibration curve. This may result from sample decomposition reducing overall emission intensity, as the sample was repeatedly excited and not kept protected from light during preparation, or may result from the formation of salts over the course of the titration, leading to skewed y-values. While this suggests that this MEA may not produce a reliable calibration curve, it represents a positive step forward to creating SO_4^{2-} assays in very complex water mixtures.

Overall, it was found that compound **67** was a viable option for use in a MEA for SO_4^{2-}. One benefit is that it was water soluble, and can be used to detect SO_4^{2-} in the mM range in comparison to the aza-crown ether receptors with a μM detection range. It can be hypothesised that altering the ligand to change the ML interactions can modulate the future sensing media and sensitivity.

4.2.3 Comparison to IC

The LOD and LOQ of **67** for SO_4^{2-} were calculated according to equation 4.1 and compared to those obtained by IC. Conditions for IC used were modified from Gros *et al.*[149] using sodium carbonate buffer as the eluent. The required calibration curves were constructed using standard conditions. Peak Area was plotted as a function of concentration obtained by IC and LOQ and LOQ calculated with LINEST (linear regression analysis tool) applied to determine the standard deviation. From IC, LOD = 1.2 mM and LOQ = 3.6 mM. In comparison, both LOD = 31 mM and LOQ = 94 mM were determined from the MEA with compound **67**. While the MEA functioned as a water soluble SO_4^{2-} sensor, it it less sensitive when compared to IC.

4.3 Chapter Conclusion

Two previously reported Indicator Displacement Assay systems were assessed for their ability to quantify SO_4^{2-} concentrations. Compound **105** was used in UV-vis IDAs with both Cresol Red and Bromocresol Green. The response to Cresol Red was found to not match that which was reported in the literature, and so was abandoned. In experiments performed with Bromocresol Green, the most promising result was observed in a 95% EtOH:1 mM Tris system, in which the SO_4^{2-} titration yielded a highly linear response ($R^2 = 0.992$) from $0 - 60$ μM of TBA_2SO_4. Attempts to move this into a higher complexity salt system failed due to salt insolubility, suggesting that this system would not be accurate when measuring SO_4^{2-} levels in biological samples.

101 was used in fluorescence IDAs with Fluorescein disodium salt. In a simple solvent system containing 10% H_2O:MeOH, a highly linear response ($R^2 = 0.996$) was observed from $12 - 320$ μM of TBA_2SO_4. Performing this same experiment in a complex salt water mixture yielded a linear response with a slightly worse fit ($R^2 = 0.988$) from $200 - 410$ μM of TBA_2SO_4. In these IDAs, the squaramide was required in high concentrations, producing difficulties in dissolution of the compound. Additionally, introduction of competing guests interfered with the response of the **101**:FNa_2 ensemble, suggesting that this system would not be accurate when measuring SO_4^{2-} levels in biological samples.

52 and **62** were studied to determine their effectiveness in MEAs. For compound **52**, titrations using TBA_2SO_4 in MeCN, 1:20 Tris:MeCN and 1% H_2O through fluorescence spectroscopy presented a response showing quenching upon guest addition, as proposed in the assay scheme. However, the change in emission fluctuated after the initial addition of TBA_2SO_4 to the **52**-Ba(II) complex in the solvents tested resulting in non-linear responses. Upon a change in the ligand to form the **62**-Ba(II) complex in the complex salt mixture, the response was negligible, with the results in Chapter 3 indicating lower overall $LogK_a$ values of

62, suggesting that the ligand may be complexing to other metals in solution, resulting in limited change in the fluorescence spectra.

For **63**, fluorescence spectroscopy was deemed unsuitable method for analysis, as the change observed in the fluorescence spectra upon the addition of SO_4^{2-} was too large to construct a valid calibration curve. To mitigate these effects, UV-vis spectroscopy was utilised for MEA studies of the **63**-Ba(II) complex. It was observed that this metal complex exhibited a linear response in a simple solvent system of 1% H_2O/MeCN ($0 - 40$ μM SO_4^{2-} with R^2 of 0.95), while the introduction of competing cations into the solvent system resulted a negligible change in the UV-vis absorbance of **63**-Ba(II) complex upon SO_4^{2-} addition. While using the 1-aza-18-crown-6-ether ligand presented a promising option for MEA, this system was only suitable for detecting SO_4^{2-} concentrations in simple solvent systems.

The response of **67** to SO_4^{2-} was observed through fluorescence studies. Solvent screens were performed to determine a suitable system, and it was found that this system can be used in 100% water. Fluorescence studies upon addition of TBA_2SO_4 in 100% water indicated a highly linear response ($R^2 = 0.956$) from $0 - 100$ mM. Performing this assay in artificial seawater also yielded a highly linear response ($R^2 = 0.956$) from $10 - 150$ mM SO_4^{2-}. This MEA was found to have LOD = 31 mM and LOQ = 94 mM which is less sensitive when compared to the 'gold standard' ion chromatography method.

The aim of this thesis was to develop MEAs for recognition of SO_4^{2-}, which has been successfully achieved in this chapter. In order to provide a comparison to existing systems, the MEAs were compared against IDAs and IC, with this comparison showing that MEAs provide a valid and suitable approach to SO_4^{2-} sensing. This thesis aimed to apply these MEAs in organic solvent, plasma, and seawater, which has been achieved by utilising various fluorophore. Additionally, pre-existing IDA methods have also been improved upon, improving their scope of

applications for use in complex and competitive solvent systems. However, more work must be done to improve the sensitivity of these receptors. Improvement of receptor solubility is also important, as many limitations were observed due to insolubility of species in the solvent.

Chapter 5

Thesis Conclusions and Future Directions

The aim of this thesis was to develop systems for quantification of SO_4^{2-} concentrations in simple and complex aqueous solutions. To achieve this, IDAs and MEAs were used. This aim was achieved, with sulfate recognition successfully performed in both simple and complex aqueous media. Pre-existing IDAs were improved upon from existing literature, while the first MEAs were designed and implemented. In this development, the unique metal binding properties of naphthalimide-aza-crown-ethers were explored.

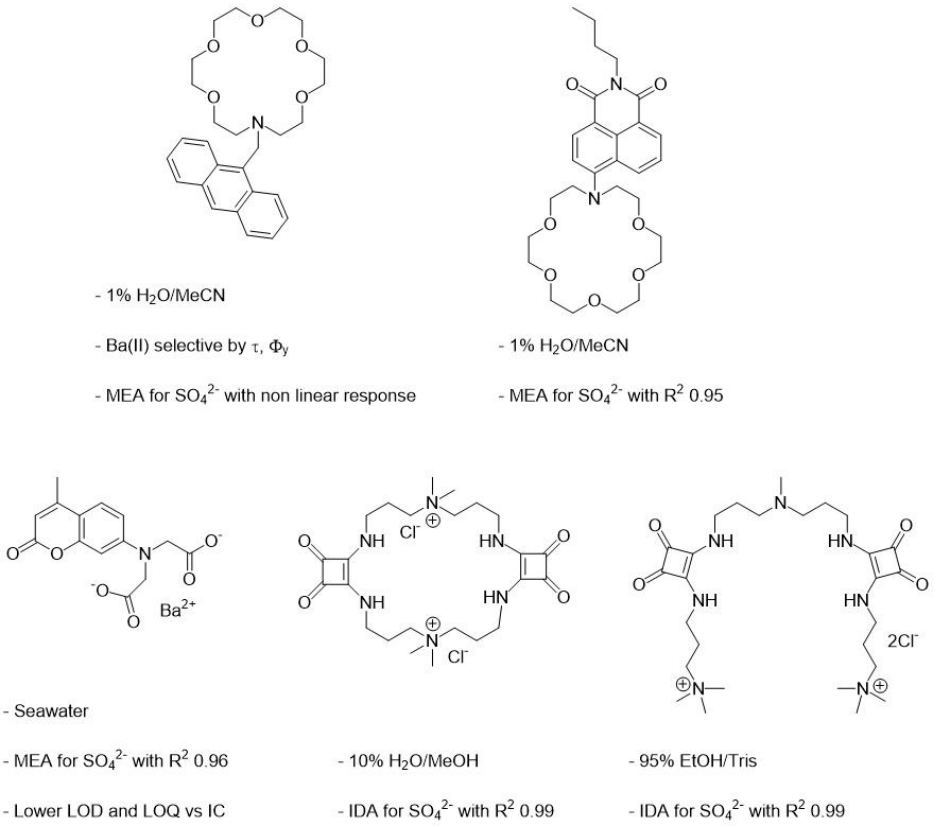

Figure 5.1: Summarised assay results

Chapter 2 described the synthesis of fluorescent receptors which contained a range of fluorophores, incorporating anthracene and naphthalimide as a fluorophore. The anthracene and naphthalimide fluorophores were appended with aza-18-crown-6 ether ligands, while coumarin and naphthalimides bearing aza-diacetates were also prepared as the Ba(II) complexes. The photophysical responses of the anthracene bearing receptors were compared in 1% water/MeCN, in which ϕ showed high degrees of internal quenching of both receptors, and τ indicating the rate of fluorescent decay, while standard characterisation (dilution studies and excitation/emission) was obtained. The naphthalimide bearing receptors were studied in the same solvent system, and the responses obtained were found to be dependent on pH and solvent viscosity.

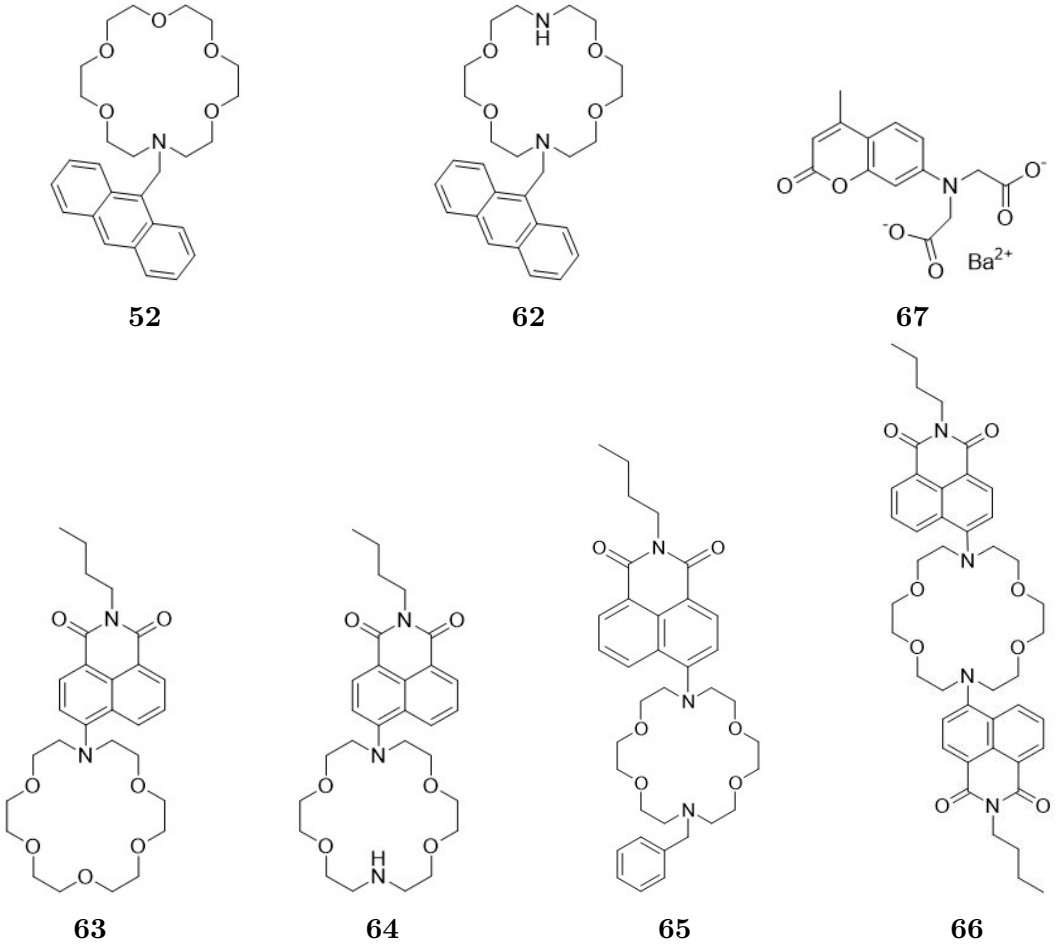

Figure 5.2: Receptors studied in this thesis.

Chapter 3 provided the photophysical characterisation of these receptors upon addition of a range of Group (I) and Group (II) metals to explore the effects of

coordination on their optical properties. The anthracene bearing receptors were most suitable for fluorescence spectroscopy studies, in which the introduction of a second nitrogen in the binding ligand reduced the selectivity of these receptors. In addition, the 1-aza-18-crown-6-ether bearing anthracene was found to be a promising selective ϕ and τ sensor for Ba(II). For the naphthalimide bearing receptors, the overall change in optical properties diminished with further diaza-18-crown-6-ether substitution of the second nitrogen atom in addition to a reduction in the propensity for selective Ba(II) binding, with minimal significant change on the binding affinity for Ba(II). Additionally, there was no selective ϕ or τ based response observed for these receptors.

Chapter 4 introduced two additional molecules which were used for IDA SO_4^{2-} recognition and contained squaramides as the binding motif. The linear squaramide receptor exhibited a linear response to SO_4^{2-} as a BG complex in an EtOH/Tris system, while the macrocyclic squaramide:FNa_2 complex exhibited a linear response upon SO_4^{2-} addition in a salt mixture. While these results were promising, limited solubility and high concentrations deemed these systems unsuitable for SO_4^{2-} sensing in complex biological systems, signifying that the pre-existing literature assay conditions are not suitable for biological SO_4^{2-} sensing. MEAs were performed with **52**-Ba(II) and **63**-Ba(II), in which it was observed that the **63**-Ba(II) complex could be used for SO_4^{2-} detection (in the micromolar range) through UV-vis spectroscopy in 1% H_2O/MeCN, with reduced responses observed in complex salt mixtures mimicking blood plasma. Finally, the coumarin-azadiacetate Ba(II) salt **67** was used for SO_4^{2-} detection in conditions mimicking sea-water, however this method was less robust when compared to ion chromatography. This indicates that variation of the fluorophore used (anthracene vs naphthalimide) changes the detection method used, while the water soluble Ba(II) salt could be used for SO_4^{2-} detection in higher concentrations, providing a range of options for MEAs depending on the natural concentrations of SO_4^{2-}.

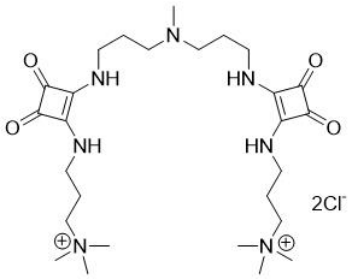

105

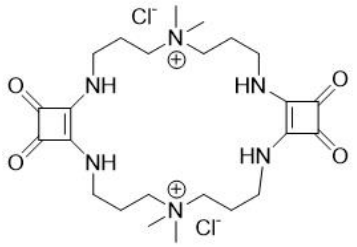

101

Figure 5.3: Squaramide based receptors.

This work presents a range of future directions. This technique could be extended to other anion-cation pairs, such as utilising lanthanide centres (as has been briefly explored in other literature) or Zn(II) sensors for phosphate extrusion, with motifs such as TACN or pyridine cores for metal complexation. This could also extend to utilising metals such as copper for extrusion of carboxylate species in biological cycles. The fluorescent receptors could be incorporated into a hydrogel, or polymerised and attached to a metal surface, and could be used as a technique to remove anions from a stream of flowing water by utilising this as a column. To increase the feasibility of the studied receptors, the fluorophores could be appended with water solubilising groups, such as at the *N*-imide of the naphthalimide. These receptors could be studied with extraction techniques to determine the levels of sulfate removed from a system, while further studies could be performed to understand the environments in which the anthracene receptors function as a τ or ϕ sensor. Additionally, mechanistic studies could also be performed to understand the origin of the emission profile of the naphthalimide receptors to Group (I) and Group (II) metals. Finally, the aza-crown ether systems have potential recyclabillity applications, whereby the metal could be continuously introduced and extruded. These could be achieved by functionalisation to a solid support, with barium streamed through the support, allowing sulfate to be introduced and removed from a sample. After this, the barium could be reintroduced, allowing for recycling of the system.

Chapter 6

Experimental

6.1 General Remarks

Melting points (M.p.) were observed manually using a Stanford Research Systems Optimelt apparatus and are uncorrected. Reactions were monitored using Thin Layer Chromatography on F254 silica plates and were visualised under UV light. Purification *via* column chromatography was performed on either a Biotage Isolera or Biotage Selekt with monitoring at 254 nm or the appropriate absorption wavelength of each fluorophore. Nuclear magnetic resonance (NMR) spectroscopy was conducted at 300 K using a Bruker NEO 500 spectrometer or a Bruker NEO 300 spectrometer. Proton NMR (^{1}H NMR) was conducted at the indicated frequency with chemical shifts (δ) recorded as parts per million (ppm) using deuterated chloroform (7.26 ppm), deuterated acetonitrile (1.94 ppm) dimethyl sulfoxide (2.50 ppm) or deuterium oxide (4.79 ppm) as internal references. Multiplicity (s = singlet, d = doublet, t = triplet, q = quartet, m = multiplet, pent = pentet), coupling constant (J Hz) and relative integral (nH) are reported. Carbon-13 NMR (^{13}C NMR) spectroscopy was conducted at the indicated frequency and chemical shifts are reported as parts per million (ppm) using deuterated chloroform (77.16 ppm), deuterated acetonitrile (118.26 ppm) or dimethyl sulfoxide (39.52 ppm) as internal references. Infrared (IR) absorption spectra were recorded on a Bruker Alpha-E FTIR spectrometer using attenuated total reflection (ATR) of a thin film or solid. Notable vibrational wavenumbers are recorded in ν_{max} cm^{-1}. Low resolution mass spectra (MS) were recorded

on a Bruker AmaZon SL mass spectrometer using electrospray ionisation (ESI) in positive or negative mode. High resolution mass spectra (HRMS) using ESI were obtained using a Bruker solariX 2xR. Commercial materials were used as received.

6.1.1 Ion Exchange

Amberlite chloride exchange resin was prepared by stirring overnight in deionised H_2O. Following this, the resin was filtered and rinsed with water. The iodide salt was then taken up in deionised H_2O and stirred overnight at R.T with 0.5 g of the resin. After 12 h, the mixture was filtered via vacuum filtration, the resin rinsed with deionised H_2O and the solvent evaporated to yield the chloride salt.

16-(Anthracen-9-ylmethyl)-1,4,7,10,13-pentaoxa-16-aza cyclooctadecane (52)

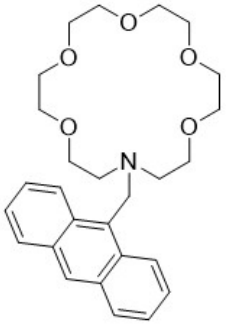

Compound **52** was synthesised using an adapted method from [88]. 9-Chlorome thyl anthracene (46 mg, 0.20 mmol) was dissolved in DMF (5 mL). To this, Et_3N (42 μL, 0.30 mmol) was added. Following this, 1-aza-18-crown-6-ether (54 mg, 0.21 mmol) was added and the solution stirred under a constant flow of nitrogen. After 30 minutes, the solution was heated at 100 °C for 24 h, K_2CO_3 (56 mg, 0.41 mmol) was added and heating continued for another 48 h. After completion, the solution was cooled to R.T and diluted with EtOAc (15 mL). The solution was extracted with 4 M HCl (3 x 15 mL). The combined aqueous layers were basified to pH 8 using K_2CO_3 then extracted with $CHCl_3$ (3 x 20 mL) and the

organic layer was evaporated under reduced pressure. The brown oil was purified *via* column chromatography (silica) in 1% Et_3N/EtOAc with isocratic elution to yield the product as a yellow solid (20 mg, 22%). **M.p:** 87 – 90 °C (lit[150] 93 °C); **^{1}H NMR** (300 MHz, $CDCl_3$): δ 2.90 (t, J = 5.7 Hz, 4H), 3.56 – 3.68 (m, 20H), 4.60 (s, 2H), 7.42 – 7.53 (m, 4H), 7.98 (d, J = 7.9 Hz, 2H), 8.39 (s, 1H), 8.56 (d, J = 8.8 Hz, 2H); **^{13}C NMR** (125 MHz, $CDCl_3$): δ 131.5, 130.6, 129.1, 127.4, 125.7, 125.3, 124.9, 70.7, 70.5, 70.4, 70.3, 70.2, 69.8, 49.1, 48.7; **LRMS (ESI)**: m/z 454 ($C_{27}H_{36}NO_5$) $[M+H]^+$. The data are in agreement with literature values.[151]

7-(Anthracen-9-ylmethyl)-1,4,10,13-tetraoxa-7,16-diazacyclo octadecane (62)

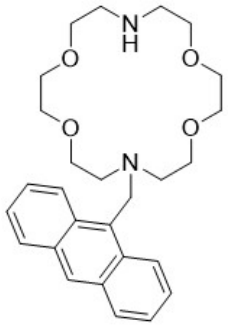

Compound **62** was synthesised using an adapted method from [88]. 9-Chloromethyl anthracene (53 mg, 0.23 mmol) was dissolved in DMF (3 mL). To this, Et_3N (34 μL, 0.24 mmol) was added. Following this, 1,10-diaza-18-crown-6 (65 mg, 0.23 mmol) was added and the solution stirred under a constant flow of nitrogen. After 30 minutes, the solution was heated at 70 °C for 16 h. After completion, the solution was cooled to R.T and diluted with MilliQ Water (20 mL). This was extracted with EtOAc (3 x 20 mL). The combined organic layers were extracted with 2 M HCl (3 x 20 mL). The aqueous extracts were combined then basified to pH 8 using NaOH and subsequently extracted with EtOAc (3 x 20 mL). The organic layers were combined and evaporated under reduced pressure. The crude product was purified using column chromatography (neutral alumina) using CH_2Cl_2/MeOH (0 – 20% MeOH) to yield the product as an orange solid

(45 mg, 40 %). **M.p:** 84 – 87 °C; **IR** (ATR): 2867, 1674, 1108 cm^{-1}; **^{1}H NMR** (300 MHz, $CDCl_3$): δ 2.82 – 2.94 (m, 8H), 3.48 – 3.67 (m, 12H), 3.75 (t, J = 4.5 Hz, 4H), 4.59 (s, 2H), 7.40 – 7.55 (m, 4H), 7.97 (d, J = 8.0 Hz, 2H), 8.39 (s, 1H), 8.56 (br t, 2H); **^{13}C NMR** (125 MHz, $CDCl_3$): δ 131.5, 130.6, 129.0, 127.5, 125.6, 125.4, 125.0, 70.9, 70.3, 70.2, 69.6, 54.3, 51.8, 49.3; **HRMS (ESI)**: m/z calc'd for $C_{27}H_{37}N_2O_4$ 453.2675, Found 453.2745 $[M+H]^+$. The data are in agreement with literature values.[115]

***tert*-Butyl 1,4,10,13-tetraoxa-7,16-diazacyclooctadecane-7-carboxylate (75)**

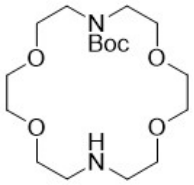

A solution of 1-aza-18-crown-6 (167 mg, 0.64 mmol) was dissolved in 1,4-dioxane (2 mL) and stirred at 40 °C. A solution of di-*tert*-butyl dicarbonate (142 mg, 0.65 mmol) in 1,4-dioxane (1 mL) was added dropwise over the course of 5 minutes. The resultant mixture was stirred at 40 °C for a further 30 minutes, then for a further 6 h at R.T. The solvent was evaporated and diethyl ether was added to the resultant oil to precipitate the starting material. The starting material was removed by filtration and washed with diethyl ether (30 mL) and the resultant filtrate evaporated to yield the crude product which was purified *via* column chromatography (neutral alumina) in CH_2Cl_2/MeOH (0 – 20% MeOH) and the appropriate fractions concentrated to yield the product as a yellow oil (71 mg, 24%). **IR** (ATR): 2867, 1682, 1097 cm^{-1}; **^{1}H NMR** (300 MHz, $CDCl_3$): δ 1.36 (s, 9H), 2.39 (s, 1H), 2.71 (t, J = 5.1 Hz, 4H), 3.42 – 3.52 (m, 4H), 3.53 – 3.70 (m, 16H); **^{13}C NMR** (125 MHz, $CDCl_3$): δ 155.6, 79.7, 70.5, 70.4, 70.0, 49.5, 48.0, 47.5, 28.6; **LRMS (ESI)**: m/z 362 ($C_{17}H_{35}N_2O_6$) $[M+H]^+$. The data are in agreement with literature values.[118]

7-Benzyl-1,4,10,13-tetraoxa-7,16-diazacyclooctadecane (77)

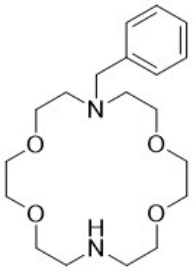

1,10-Diaza-18-crown-6 (0.52 g, 2.0 mmol) was stirred in DMF (10 mL). To this, benzaldehyde (0.2 mL, 2.0 mmol) was added, followed by glacial AcOH (0.13 mL, 2.3 mmol). Following this, sodium triacetoxyborohydride (0.84 g, 3.9 mmol) was added and the resultant solution stirred at R.T for 1 h. After completion, the solvent was evaporated and the residue taken up in EtOAc (15 mL), washed with aqueous 1 M NaOH (3 x 15 mL) and the resultant organic layer evaporated under vacuum to yield the pure product as a pale yellow oil (0.54 g, 77%). **IR** (ATR): 2862, 2821, 1118 cm^{-1}; **^{1}H NMR** (300 MHz, $CDCl_3$): δ 2.80 – 2.86 (m, 8H), 3.60 – 3.66 (m, 16H), 3.70 (s, 2H), 7.23 (t, J = 7.6 Hz, 1H), 7.31 (t, J = 7.4 Hz, 2H), 7.35 (d, J = 7.6 Hz, 2H), Product peaks overlapped the solvent peak, so NMR calibration was not performed; **^{13}C NMR** (125 MHz, $CDCl_3$): δ 139.8, 130.0, 128.3, 127.0, 71.0, 70.9, 70.4, 70.2, 60.1, 54.0, 49.5. One peak obscured; **HRMS (ESI)**: m/z calc'd for $C_{19}H_{33}N_2O_4$ 353.2362, Found 353.2438 $[M+H]^+$. The data are in agreement with literature values.[152]

6-Bromo-2-butyl-1*H*-benzo[*de*]isoquinoline-1,3(2*H*)-dione (74)

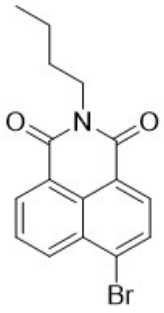

A mixture of 4-bromo-1,8-naphthalic anhydride (1.2 g, 0.43 mmol) and *n*-

butylamine (0.5 mL, 5.1 mmol) in EtOH (30 mL) was heated at reflux for 18 h. The reaction visually proceeded as the starting material formed a soluble product indicated by a disappearance of insoluble solid. After completion, the solution was cooled to R.T, at which point a dark brown solid formed. The mixture was further cooled in an ice bath, then the solid was collected by filtration and washed with ice cold EtOH. The solid was dissolved in EtOAc (30 mL) and washed with 1 M HCl (3 x 30 mL) followed by brine (3 x 25 mL). The organic layer was then dried (Na_2SO_4) and evaporated under reduced pressure to yield a light yellow solid (1.22 g, 98%). **M.p** 98 − 101 °C (lit[117] 98.6 − 99.4 °C), **IR** (ATR): 2953, 1653, 778 cm^{-1}; **^{1}H NMR** (300 MHz, $CDCl_3$): δ 0.97 (t, J = 7.6 Hz, 3H), 1.36 − 1.48 (m, J = 7.6 Hz, 2H), 1.63 − 1.73 (m, J = 7.6 Hz, 2H), 4.18 (t, J = 7.6 Hz, 2H), 7.85 (t, J = 8.0 Hz, 1H), 8.04 (d, J = 8.0 Hz, 1H), 8.42 (d, J = 8.0 Hz, 1H), 8.57 (d, J = 8.5 Hz, 1H), 8.66 (d, J = 7.3 Hz, 1H); **^{13}C NMR** (125 MHz, $CDCl_3$): δ 163.8, 133.4, 132.2, 131.4, 131.2, 130.8, 130.6, 129.2, 128.2, 123.4, 122.5, 40.5, 30.3, 20.5, 14.0. Two peaks obscured; **LRMS (ESI)**: m/z 332 ($C_{16}H_{15}BrNO_2$) $[M+H]^+$. The data are in agreement with literature values.[117]

2-Butyl-6-nitro-1*H*-benzo[*de*]isoquinoline-1,3(2*H*)-dione (84)

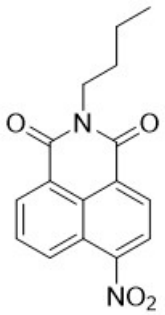

A mixture of 4-nitro-1,8-naphthalic anhydride (0.53 g, 2.2 mmol) and *n*-butylamine (0.19 mL, 1.9 mmol) in EtOH (30 mL) was heated at reflux for 2 h. After completion, the solution was cooled to R.T, at which point a dark brown solid formed. The mixture was further cooled in an ice bath, then the solid was collected by filtration and washed with ice cold EtOH. The solid was

dissolved in EtOAc (30 mL) and washed with 1 M HCl (3 x 30 mL) followed by brine (3 x 25 mL). The organic layer was then dried (Na_2SO_4) and evaporated under reduced pressure to yield a light brown solid (0.24 g, 35%). **M.p** 101 – 105 °C; **IR** (ATR): 2958, 2932, 2871, 1659, 1337 cm^{-1}; **^{1}H NMR** (500 MHz, $CDCl_3$): δ 0.99 (t, J = 7.6 Hz, 3H), 1.42 – 1.49 (m, J = 7.6 Hz, 2H), 1.69 – 1.77 (m, J = 6.1 Hz, 2H), 4.19 (t, J = 7.6 Hz, 2H), 7.98 (t, J = 8.0 Hz, 1H), 8.40 (d, J = 8.0 Hz, 1H), 8.69 (d, J = 8.0 Hz, 1H), 8.74 (d, J = 7.3 Hz, 1H), 8.84 (d, J = 8.7 Hz, 1H); **^{13}C NMR** (125 MHz, $CDCl_3$): δ 163.5, 162.7, 149.7, 132.6, 130.1, 129.9, 129.4, 127.2, 124.0, 123.2, 40.8, 30.3, 20.5, 13.9. One peak obscured; **LRMS (ESI)**: *m/z* 321 ($C_{16}H_{14}N_2O_4Na$) $[M+Na]^+$. The data are in agreement with literature values.[120]

6-Amino-2-butyl-1*H*-benzo[*de*]isoquinoline-1,3(2*H*)-dione (85)

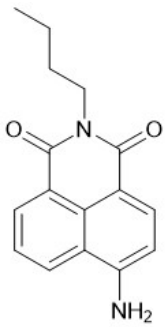

Compound **84** (0.281 g, 0.94 mmol) was dissolved in EtOH (10 mL) and stirred under an atmosphere of hydrogen. Pd/C (10% w/w, 50 mg) was added, with the atmosphere replaced with hydrogen, and the resultant suspension stirred under an atmosphere of hydrogen at R.T for 2 h. The mixture was filtered through Celite, and the Celite was washed with EtOH. The resultant filtrate was evaporated under reduced pressure to yield the pure product as an orange solid (0.11 g, 44%). **M.p:** 180 – 182 °C; **IR** (ATR): 3432, 2950, 1672 cm^{-1}; **^{1}H NMR** (300 MHz, $CDCl_3$): δ 0.97 (t, J = 7.4 Hz, 3H), 1.41 – 1.53 (m, J = 7.9 Hz, 2H), 1.68 – 1.78 (m, J = 7.9 Hz, 2H), 4.17 (t, J = 7.9 Hz, 2H), 4.90 (s, 2H), 6.89 (d, J = 8.2 Hz, 1H), 7.66 (t, J = 7.9 Hz, 1H), 8.10 (d, J = 8.2 Hz, 1H), 8.42 (d, J = 8.1

Hz, 1H), 8.61 (d, J = 7.2 Hz, 1H); **^{13}C NMR** (75 MHz, $CDCl_3$): δ 164.7, 164.2, 149.1, 133.9, 131.6, 129.9, 126.9, 125.1, 123.4, 120.3, 112.5, 109.7, 40.2, 30.4, 20.6, 14.0; **LRMS (ESI)**: m/z 267 ($C_{16}H_{15}N_2O_2$) $[M\text{-}H]^+$. The data are in agreement with literature values.[153]

2-Butyl-6-(1,4,7,10,13-pentaoxa-16-azacyclooctadecan-16-yl)-1*H*-benzo[*de*]isoquinoline-1,3(2*H*)-dione (63)

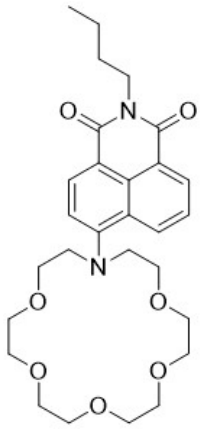

1-Aza-18-crown-6 (90 mg, 0.34 mmol) was dissolved in DMSO (5 mL). Compound **74** (0.5 g, 1.5 mmol) was added, followed by Na_2CO_3 (79 mg, 0.75 mmol). The solution was stirred at 140 °C for 72 h. The solution was cooled to R.T then diluted with EtOAc (40 mL). The solution was filtered and the resultant filtrate was evaporated under reduced pressure. Purification was performed *via* column chromatography (silica) using gradient elution from 100% EtOAc – 15% MeOH/EtOAc. The appropriate fractions were concentrated under reduced pressure to yield the product as a yellow oil (98 mg, 56%). **IR** (ATR): 2863, 1691, 1649, 1583, 1464, 1348, 1231, 1038 cm^{-1}; **^{1}H NMR** (300 MHz, CD_3CN): δ 0.97 (t, J = 7.4 Hz, 3H), 1.35 – 1.46 (m, J = 11.1 Hz, 2H), 1.60 – 1.75 (m, J = 15.0 Hz, 2H), 3.61 - 3.73 (m, 24H), 4.11 (t, J = 7.8 Hz, 2H), 7.51 (d, J = 7.8 Hz, 1H), 7.62 – 7.68 (m, J = 7.8 Hz, 1H), 8.47 (d, J = 8.2 Hz, 1H), 8.53 (d, J = 7.3 Hz, 1H), 8.75 (d, J = 8.2 Hz, 1H); **^{13}C NMR** (125 MHz, $CDCl_3$): δ 164.7, 164.2, 132.1, 131.3, 130.4, 126.0, 125.7, 123.5, 123.3, 117.8, 70.6, 70.4, 69.6 58.6, 40.7, 31.0, 30.4, 20.5, 14.0; **HRMS (ESI)**: m/z calc'd for $C_{28}H_{39}N_2O_7$ 515.2679,

Found 515.2755 $[M+H]^+$.

2-Butyl-6-(1,4,10,13-tetraoxa-7,16-diazacyclooctadecan-7-yl)-1*H*-benzo[*de*]isoquinoline-1,3(2*H*)-dione (64)

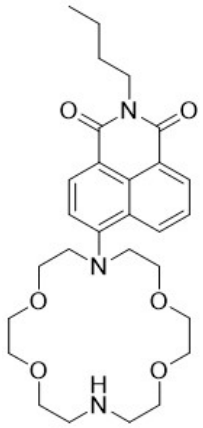

Compound **75** (163 mg, 0.5 mmol) was dissolved in DMSO (3 mL). Compound **74** (0.59 g, 1.7 mmol) was added, followed by Na_2CO_3 (95 mg, 0.90 mmol). The solution was stirred at 140 °C for 72 h. The solution was cooled to R.T then diluted with EtOAc (40 mL). The solution was filtered and the resultant filtrate was evaporated under reduced pressure. Purification was performed on the residue *via* column chromatography (silica) using gradient elution from 100% EtOAc – 15% MeOH/EtOAc. The appropriate fractions were combined and evaporated under reduced pressure. The residue was dissolved in TFA/CH_2Cl_2 (3:1 v/v, 5 mL) and stirred at R.T for 1 h. The solvent was evaporated under a stream of nitrogen, and CH_2Cl_2 (3 x 10 mL) added and removed by pipette. The resultant crude was further purified using reverse phase chromatography on C_{18} silica in water/MeCN (20 % - 100 % MeCN). The appropriate fractions were concentrated under vacuum to yield the product as a yellow oil (15 mg, 7 %). **IR** (ATR): 2955, 2923, 2868, 1724, 1685, 1652, 1577, 1550, 1393, 1348, 1257, 1230, 1188 cm^{-1}; **^{1}H-NMR** (300 MHz, $CDCl_3$): δ 0.96 (t, J = 7.1 Hz, 3H), 1.33 – 1.49 (m, 2H), 1.63 – 1.74 (m, 2H), 3.42 – 3.47 (m, 24H), 4.13 – 4.18 (m, 2H), 7.43 (d, J = 7.6 Hz, 1H), 7.65 (t, J = 7.9 Hz, 1H), 8.49 (d, J = 8.1 Hz, 1H), 8.55 (d, J = 7.5 Hz, 1H), 8.63 (d, J = 8.1 Hz, 1H); **^{13}C-NMR** (75 MHz, $CDCl_3$): δ 164.6,

164.1, 155.0, 132.0, 131.2, 131.1, 130.0, 125.6, 123.1, 118.2, 70.6, 70.4, 69.1, 65.6, 54.2, 40.2, 30.3, 20.4, 15.3, 13.9; **HRMS (ESI)**: *m/z* calc'd for $C_{28}H_{39}N_3O_6Na$ 537.2839, Found 537.2572 $[M+Na+H]^+$.

6-(16-Benzyl-1,4,10,13-tetraoxa-7,16-diazacyclooctadecan-7-yl)-2-butyl-1*H*-benzo[*de*]isoquinoline-1,3(2*H*)-dione (65)

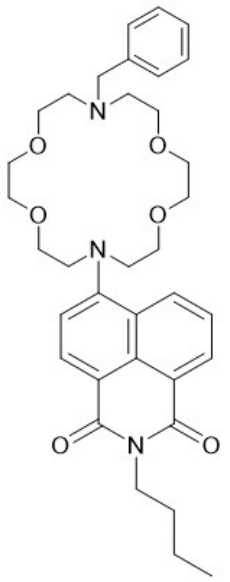

Compound **77** (93 mg, 0.26 mmol) was dissolved in DMSO (4 mL). To this, Na_2CO_3 (62 mg, 0.59 mmol) was added, followed by a solution of the starting naphthalimide **74** (0.52 g, 1.6 mmol) in DMSO (8 mL). The solution was stirred at 100 °C for 72 h. Following this, the mixture was diluted with EtOAc (30 mL) and washed with water (100 mL). The aqueous layer was further extracted with EtOAc (3 x 15 mL). The resultant organic layers were combined, dried with Na_2SO_4 and evaporated under reduced pressure. Purification was performed using column chromatography, first using reverse phase chromatography on C_{18} silica (gradient from H_2O – MeCN), followed by manual purification *via* column chromatography (silica) with EtOAc/MeOH (0 – 20% MeOH). This yielded the pure product as a yellow oil (9 mg, 5 %). **^{1}H NMR** (300 MHz, CD_3CN): δ 0.97 (t, J = 7.3 Hz, 3H), 1.38 – 1.43 (m, 2H), 1.63 – 1.67 (m, 2H), 3.52 – 3.58 (m, 26H), 4.07 – 4.10 (m, 2H), 7.19 – 7.27 (m, 5H), 7.46 (d, J = 8.0 Hz, 1H), 7.69

(dd, J = 7.4 Hz and 1.1 Hz, 1H), 8.41 (d, J = 8.3 Hz, 1H), 8.47 (d, J = 7.4 Hz, 1H), 8.78 (d, J = 8.3 Hz, 1H); **^{13}C NMR** (125 MHz, CD_3CN): δ 165.3, 164.2, 132.3, 131.5, 130.3, 129.7, 129.1, 129.0, 128.9, 128.0, 127.7, 127.6, 126.4, 71.3, 71.1, 70.9, 70.5, 70.3, 69.8, 69.3, 60.4, 59.8, 54.7, 40.5, 21.0, 21.0, 14.4; **HRMS (ESI)**: m/z calc'd for $C_{35}H_{46}N_3O_6$ 604.3308, Found 604.3379 $[M+H]^+$.

6,6'-(1,4,10,13-Tetraoxa-7,16-diazacyclooctadecane-7,16-diyl)bis(2-butyl-1*H*-benzo[*de*]isoquinoline-1,3(2*H*)-dione) (66)

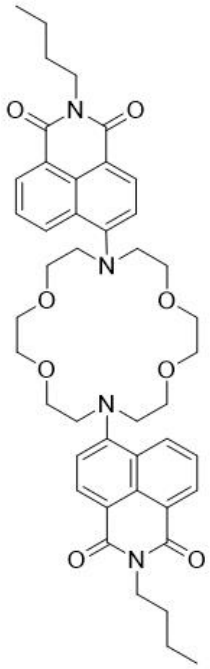

1,10-Diaza-18-crown-6-ether (81.4 mg, 0.3 mmol) was dissolved in DMSO (14 mL). Compound **74** (0.69 g, 2.1 mmol) was added, followed by Na_2CO_3 (72 mg, 0.68 mmol). The resultant solution was stirred at 100 °C for 6 days. Following this, the mixture was diluted with water (80 mL) and extracted with CH_2Cl_2 (3 x 40 mL). The combined organic layers were dried (Na_2SO_4) and evaporated under reduced pressure. Purification was performed *via* column chromatography (silica) using gradient elution with hexane/EtOAc (0 – 100% EtOAc). The appropriate fractions were combined and evaporated under reduced pressure to yield the product as a yellow oil (24 mg, 10%). **IR** (ATR): 2919, 1650, 1390, 1258, 1066, 1008 cm^{-1}; **^{1}H NMR** (300 MHz, $CDCl_3$): δ 0.96 (t, J = 6.6 Hz,

6H), 1.41 – 1.51 (m, 4H), 1.66 – 1.77 (m, 4H), 3.44 – 3.72 (m, 22H), 4.16 – 4.21 (m, 4H), 7.43 – 7.55 (m, 4H), 8.44 (d, J = 7.1 Hz, 2H), 8.51 (d, J = 8.3 Hz, 2H), 8.59 (d, J = 8.3 Hz, 2H); **^{13}C NMR** (75 MHz, $CDCl_3$): δ 164.5, 154.9, 131.9, 131.0, 130.9, 127.4, 125.5, 123.2, 117.7, 116.9, 71.1, 69.6, 54.0, 40.3, 30.4, 20.6, 14.0; **HRMS (ESI)**: *m/z* calc'd for $C_{44}H_{52}N_4O_8Na$ 787.3785, Found 787.3692 $[M+Na]^+$.

Di-*tert*-butyl 2,2'-[(2-butyl-1,3-dioxo-2,3-dihydro-1*H*-benzo[*de*]isoquinolin-6-yl)azanediyl]diacetate (86)

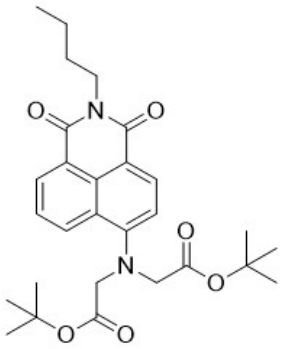

Compound **85** (0.089 g, 0.3 mmol) was dissolved in MeCN (20 mL). K_2CO_3 (0.28 g, 2 mmol) was added, followed by NaI (0.15 g, 0.99 mmol). The solution was stirred, and a solution of *tert*-butyl bromoacetate (0.4 mL, 2.7 mmol) in 10 mL MeCN was added. The mixture was heated to reflux under nitrogen for 72 h. Following this, the reaction mixture was cooled to R.T and the solvent was evaporated under reduced pressure. The residue was suspended up in EtOAc (50 mL) then filtered. The filtrate was concentrated under reduced pressure. Purification was performed *via* column chromatography (silica) using gradient elution with hexanes/EtOAc (10% – 100% EtOAc). The appropriate fractions were concentrated under pressure to yield the pure product as a yellow oil (0.1 g, 67%). **IR** (ATR): 1736, 1694, 1654, 1587, 1365, 1216 cm^{-1}; **^{1}H NMR** (500 MHz, $CDCl_3$): δ 0.97 (t, J = 7.4 Hz, 3H), 1.44 (s, 18H), 1.45 – 1.49 (m, 2H), 1.64 – 1.72 (m, 2H), 4.06 – 4.16 (m, 2H), 4.20 (s, 4H), 7.31 (d, J = 8.1 Hz, 1H), 7.67 (dd, J = 7.3 Hz and 1.1 Hz, 1H), 8.43 (dd, J = 8.4 Hz and 1.1 Hz, 1H), 8.48 (d,

J = 8.1 Hz, 1H), 8.58 (dd, J = 7.3 Hz and 1.1 Hz, 1H); **^{13}C NMR** (125 MHz, $CDCl_3$): δ 169.3, 164.6, 153.6, 132.0, 130.4, 126.3, 123.5, 117.7, 82.4, 68.7, 40.3, 30.4, 28.1, 20.5, 13.9; **HRMS (ESI)**: m/z calc'd for $C_{28}H_{36}N_2O_6Na$ 519.2573, Found 519.2465 $[M+Na]^+$.

***Tert*-butyl (2-butyl-1,3-dioxo-2,3-dihydro-1H-benzo[*de*]isoquinolin -6-yl)glycinate (87)**

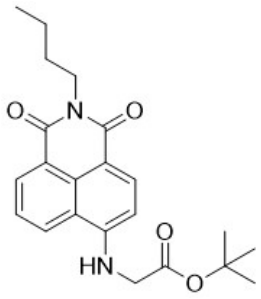

Compound **87** was also isolated as a yellow oil (25 mg, 22%). **IR** (ATR): 3391, 2872, 1734, 1578, 1347, 1230, 1149 cm^{-1}; **^{1}H NMR** (300 MHz, $CDCl_3$): δ 0.97 (t, J = 7.4 Hz, 3H), 1.38 – 1.51 (m, 2H), 1.55 (s, 9H), 1.65 – 1.77 (m, 2H), 4.04 (d, J = 4.6 Hz, 2H), 4.12 – 4.23 (m, 2H), 5.97 (br s, 1H), 6.56 (d, J = 8.5 Hz, 1H), 7.62 (dd, J = 7.7 Hz and 0.7 Hz, 1H), 8.18 (d, J = 8.5 Hz, 1H), 8.44 (d, J = 8.5 Hz, 1H), 8.56 (d, J = 7.5 Hz, 1H); **^{13}C NMR** (75 MHz, $CDCl_3$): δ 169.1, 148.3, 134.3, 131.4, 126.2, 125.3, 104.8, 83.5, 45.7, 40.2, 30.5, 28.3, 20.6, 14.0; **HRMS (ESI)**: m/z calc'd for $C_{22}H_{26}N_2O_4Na$ 405.1893, Found 405.1788 $[M+Na]^+$. While this compound has previously been reported in the literature, no characterisation data was provided.[154]

2,2'-[(2-Butyl-1,3-dioxo-2,3-dihydro-1*H*-benzo[*de*]isoquinolin -6-yl)azanediyl]diacetic acid (88)

Compound **86** (0.1 g, 0.2 mmol) was stirred in 9:1 v/v TFA:CH_2Cl_2 (2 mL) at R.T for 0.5 h. The solvent was evaporated under a stream of nitrogen and the residue was triturated with $CHCl_3$ (3 x 10 mL) to yield the pure acid as a yellow solid (10 mg, 13%). **IR** (ATR): 2962, 1709, 1583, 1394, 1206 cm^{-1}; **^{1}H NMR**

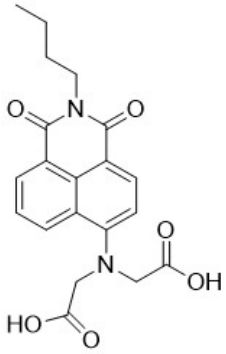

(300 MHz, CD_3CN/ 1% D_2O): δ 0.90 (t, J = 7.4 Hz, 3H), 1.29 – 1.42 (m, 2H), 1.53 – 1.66 (m, 2H), 3.97 – 4.03 (m, 2H), 4.29 (s, 4H), 7.30 (d, J = 8.5 Hz, 1H), 7.71 (dd, J = 7.7 Hz and 0.7 Hz, 1H), 8.34 (d, J = 8.5 Hz, 1H), 8.39 (dd, J = 8.5 Hz and 0.9 Hz, 1H), 8.45 (d, J = 7.4 Hz, 1H). The NMR spectra were calibrated to the CD_3CN solvent peak; **^{13}C NMR** (75 MHz, CD_3CN/ 1% D_2O): δ 175.5, 164.9, 164.3, 154.1, 132.1, 131.2, 130.9, 130.1, 126.3, 125.8, 123.2, 117.0, 116.5, 55.2, 40.1, 30.1, 20.3, 13.5; **HRMS (ESI)**: *m/z* calc'd for $C_{20}H_{19}N_2O_6$ 383.1321, Found 383.1253 $[M\text{-}H]^-$.

2,2'-[(2-Butyl-1,3-dioxo-2,3-dihydro-1*H*-benzo[*de*]isoquinolin -6-yl)azanediyl]diacetate barium (II) (68)

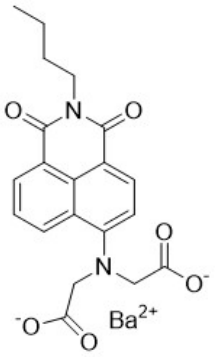

Compound **88** (74 mg, 0.2 mmol) was dissolved in 3.5 mL MeOH. An aqueous solution containing $Ba(OH)_2$ (69 mg, 0.4 mmol) was added dropwise to the methanolic solution. The solution was stirred at R.T for 1 h. The solvent was evaporated and the resultant solid triturated with CH_2Cl_2 (3 x 10 mL) and dried under vacuum to yield the pure salt as a yellow solid (32 mg, 32 %). **M.p:** 230

– 235 °C; **IR** (ATR): 1573, 1389, 1303 cm^{-1}; **^{1}H NMR** (300 MHz, D_2O): δ 0.93 (t, J = 7.3 Hz, 3H), 1.29 – 1.43 (m, 2H), 1.52 – 1.63 (m, 2H), 3.90(t, J = 7.5 Hz, 2H), 4.18 (s, 4H), 6.93 (d, J = 8.6 Hz, 1H), 7.61 (t, J = 7.9 Hz, 1H), 8.17 (d, J = 8.5 Hz, 1H), 8.21 (d, J = 8.6 Hz, 1H), 8.36 (t, J = 7.3 Hz, 1H). Due to insolubility of the product, a carbon NMR spectrum could not be obtained; **HRMS (ESI)**: *m/z* calc'd for $C_{20}H_{19}BaN_2O_6$ 521.0217, Found 521.0290 $[M+H]^+$.

Di-*tert*-butyl 2,2'-[(4-methyl-2-oxo-2*H*-chromen-7-yl) azanediyl]diacetate (79)

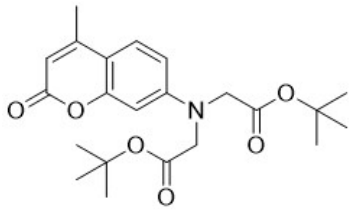

Compound **79** was synthesised based on a previously reported method [119]. 7-Amino-4-methylcoumarin (0.31 g, 1.77 mmol) was dissolved in MeCN (8 mL). To this, *tert*-butyl bromoacetate (2.1 mL, 14.2 mmol) was added, followed by K_2CO_3 (1.45 g, 10.5 mmol) and NaI (2.09 g, 13.9 mmol). The solution was heated to reflux for 72 h. After completion, the solution was cooled to R.T and the solids removed by filtration and washed with MeCN. The filtrate was evaporated under vacuum. The resultant residue was taken up in EtOAc (20 mL), partitioned with brine (3 x 25 mL) and the resultant organic layers isolated and dried ($MgSO_4$). The crude product was purified *via* column chromatography (silica) with gradient elution using hexane/EtOAc (10 % – 100 % EtOAc). The appropriate fractions were isolated and evaporated under vacuum to yield the pure product as a yellow oil (0.48 g, 41%). **IR** (ATR): 1735, 1714, 1606, 1148 cm^{-1}; **^{1}H NMR** (300 MHz, DMSO-d_6): δ 1.41 (s, 18H), 2.34 (s, 3H), 4.18 (s, 4H), 6.03 (s, 1H), 6.41 (d, J = 2.4 Hz, 1H), 6.57 (dd, J = 9.0 Hz and 2.4 Hz, 1H), 7.56 (d, J = 9.0 Hz, 1H); **^{13}C NMR** (125 MHz, DMSO-d_6): δ 168.9, 160.5, 154.9, 153.5, 151.2, 126.1, 109.9, 109.0, 108.9, 98.0, 81.0, 53.6, 27.7, 17.9; **LRMS (ESI)**: *m/z* 426 ($C_{22}H_{29}NO_6Na$)

$[M+Na]^+$. The data are in agreement with literature values.[119]

Tert-butyl (4-methyl-2-oxo-2*H*-chromen-7-yl)glycinate (80)

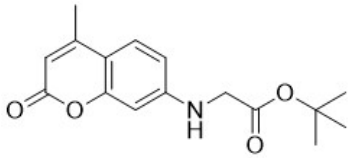

Compound **80** was also isolated as a brown oil (0.298 g, 58%). **IR** (ATR): 3384, 2976, 1720, 1608, 1449, 1393, 1219, 1145 cm^{-1}; **^{1}H NMR** (300 MHz, DMSO-d_6): δ 1.42 (s, 9H), 2.31 (s, 3H), 3.90 (d, 2H, J = 6.5 Hz), 5.94 (s, 1H), 6.38 (d, J = 2.1 Hz, 1H), 6.63 (dd, J = 8.7 Hz and 2.1 Hz, 1H), 6.89 (t, J = 6.1 Hz, 1H), 7.45 (d, J = 8.7 Hz, 1H); **^{13}C NMR** (125 MHz, DMSO-d_6): δ 169.7, 160.7, 155.4, 153.8, 152.0, 130.0, 110.3, 109.3, 108.0, 96.9, 80.9, 44.9, 27.7, 18.0; **LRMS (ESI)**: *m/z* 312 ($C_{16}H_{19}NO_4Na$) $[M+Na]^+$. The data are in agreement with literature values.[119]

2,2'-[(4-Methyl-2-oxo-2*H*-chromen-7-yl)azanediyl]diacetic acid (81)

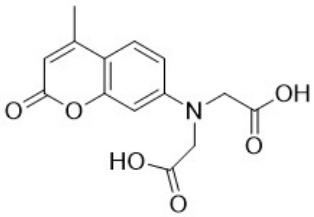

Compound **79** (0.136 g, 0.34 mmol) was stirred in 9:1 v/v TFA:CH_2Cl_2 (2 mL) at R.T for 0.5 h. The solvent was evaporated under a stream of nitrogen and the residue was triturated with diethyl ether (3 x 10 mL) to yield the pure acid as a yellow oil (85 mg, 87%). **IR** (ATR): 3391, 1711, 1605, 1523, 1400, 1192, 1023 cm^{-1}; **^{1}H NMR** (300 MHz, DMSO-d_6): δ 2.28 (s, 3H), 4.15 (s, 4H), 5.97 (d, J = 1.1 Hz, 1H), 6.35 (d, J = 2.5 Hz, 1H), 6.56 (dd, J = 6.5 Hz and 2.5 Hz, 1H), 7.52 (d, J = 9.0 Hz, 1H). The peak at 4.15 ppm was partially obscured

by water; **^{13}C NMR** (75 MHz, DMSO-d_6): δ 171.8, 161.2, 155.2, 154.2. 151.6, 121.6, 110.3, 109.4, 109.3, 98.2, 53.2, 18.3; **LRMS (ESI)**: m/z 290 ($C_{14}H_{12}NO_6$) $[M\text{-}H]^-$.

2,2'-[(4-Methyl-2-oxo-2*H*-chromen-7-yl)azanediyl]diacetate barium (II) (67)

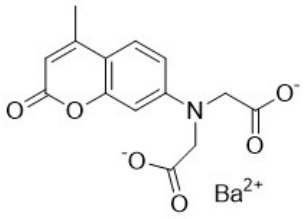

Compound **81** (30 mg, 0.1 mmol) was dissolved in 1.5 mL MeOH. An aqueous solution of $Ba(OH)_2$ (34 mg, 0.2 mmol) was added dropwise. The solution was stirred at R.T for 1 h. The solvent was evaporated, the resultant solid triturated with CH_2Cl_2 (3 x 10 mL) and dried to yield the pure salt as a yellow solid (54.6 mg, quant). **^{1}H NMR** (300 MHz, D_2O): δ 2.44 (s, 3H), 4.02 (s, 5H), 6.07 (s, 1H), 6.44 (d, J = 2.6 Hz, 1H), 6.60 (dd, J = 6.2 Hz and 2.6 Hz, 1H), 7.62 (d, J = 8.9 Hz, 1H). Due to insolubility of the product, a carbon NMR spectrum could not be obtained; **LRMS (ESI)**: m/z 449 ($C_{14}H_{11}BaNO_6Na$) $[M+Na]^+$.

4,4'-[(Methylazanediyl)bis(propane-3,1-diyl)]bis(azanediyl) bis(3-ethoxycyclobut-3-ene-1,2-dione) (99)

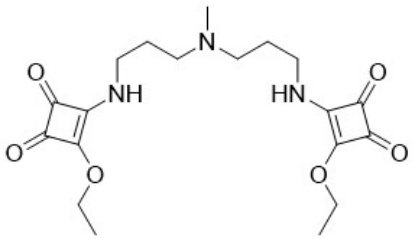

Compound **99** was synthesised based on a previously reported method [155]. *N*-*N*-Bis(3-aminopropyl)methylamine (0.12 mL, 0.76 mmol) in diethyl ether (20 mL) was added drop-wise to a solution of 3,4-diethoxy-3-cyclobutene-1,2-dione

(0.38 g, 2.2 mmol) in diethyl ether (1.5 mL). The resultant solution was stirred under nitrogen at R.T for 22 h. The solution was diluted with *n*-pentane (5 mL) and cooled in an ice bath. The resultant solid was centrifuged and the supernatant decanted. The solid was then washed with *n*-pentane/diethyl ether (9:1 v/v, 3 x 10 mL). The solid was dried under vacuum to yield the desired product as a yellow solid (0.17 g, 59%). **M.p**: decomposition from 210 °C; **IR** (ATR): 3220, 2943, 1795, 1655, 1539 cm^{-1}; **^{1}H NMR** (300 MHz, $CDCl_3$): δ 1.34 – 1.50 (m, 6H), 1.81 (br s, 4H), 2.23 (s, 3H), 2.52 (s, 4H), 3.54 (s, 3H), 3.72 (br s, 1H), 4.60 – 4.81 (m, 4H), 7.04 (br s, 0.4 H), 7.82 (br s, 0.7 H), 8.12 (br s, 0.3 H); **^{13}C NMR** (75 MHz, $CDCl_3$): δ 189.7, 183.0, 177.4, 172.6, 69.7, 55.7, 43.7, 41.5, 28.1, 16.0; **LRMS (ESI)**: *m/z* 416 ($C_{19}H_{27}N_3O_6Na$) $[M+Na]^+$. The data are in agreement with literature values.[147]

6,19-Dimethyl-2,6,10,15,19,23-hexaazatricyclo[22.2.0.0^{11,14}] hexacosa-1(24),11(14)-diene-12,13,25,26-tetraone (100)

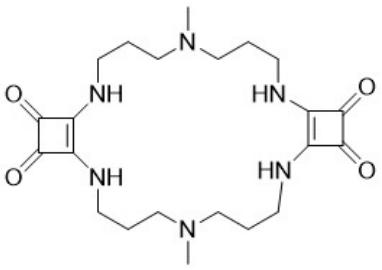

Compound **99** (0.1 g, 0.25 mmol) was dissolved in 4 mL EtOH. A solution of *N*-*N*-bis(3-aminopropyl)methylamine (41 μL, 0.25 mmol) in EtOH (1 mL) was added dropwise and the solution stirred at R.T for 18 h. The reaction mixture was then diluted with 10 mL *n*-pentane and further cooled in ice. The solution was centrifuged and the supernatant decanted off. The resultant yellow solid was washed with a mixture of *n*-pentane/EtOH (9:1 v/v, 3 x 10 mL). Drying under high vacuum yielded the desired product as a yellow solid (83 mg, 72%). **M.p**: decomposition from 230 °C; **IR** (ATR): 3161, 2941, 1798, 1643, 1557 cm^{-1}; **LRMS (ESI)**: *m/z* 469 ($C_{22}H_{34}N_6O_4Na$) $[M+Na]^+$. Due to insolubility of the

product, the product was used as is in the next step without further characterisation.

6,6,19,19-Tetramethyl-12,13,25,26-tetraoxo-2,6,10, 15,19,23-hexaazatricyclo[22.2.0.0^{11,14}]hexacosa-1(24),11(14)-diene-6,19-diium iodide (29)

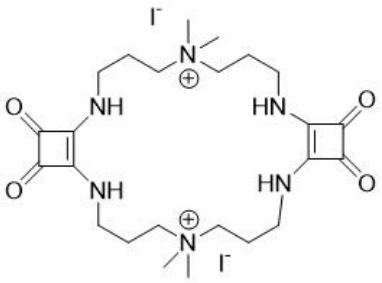

Macrocycle **100** (0.11 g, 0.25 mmol) was dissolved in DMF (15 mL). To this, iodomethane (0.11 mL, 1.8 mmol) was added and the resultant solution stirred at 70 °C under a flow of nitrogen for 21 h. The solution was cooled to R.T. *n*-Pentane (20 mL) was added and the resulting suspension was cooled in an ice bath and centrifuged. The supernatant was decanted, and the solid washed with a mixture of *n*-pentane/DMF (8:2 v/v, 3 x 20 mL). After drying under vacuum, the iodide salt was obtained as a pale yellow solid (0.19 g, quant).

6,6,19,19-Tetramethyl-12,13,25,26-tetraoxo-2,6,10, 15,19,23-hexaazatricyclo[22.2.0.0^{11,14}]hexacosa-1(24),11(14)-diene-6,19-diium chloride (101)

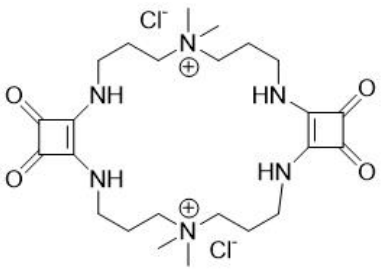

Due to insolubility of the product, macrocycle **29** was converted to the chloride salt following the procedure described in Section 6.1.1 to yield the desired chloride

salt as a pale yellow oil (0.1 g, 72%). **IR** (ATR): 3374, 2958, 1662, 1480 cm^{-1}; **^{1}H NMR** (300 MHz, D_2O): δ 2.12 – 2.21 (m, 8H), 3.15 (s, 12H), 3.42 – 3.53 (m, 8H), 3.63 – 3.73 (m, 8H); **^{13}C NMR** (125 MHz, D_2O): δ 181.7, 168.1, 61.4, 50.9, 41.0, 24.0; **HRMS (ESI)**: *m/z* calc'd for $C_{24}H_{40}Cl_2N_6O_4Na$ 569.2488, Found 570.3592 $[M+Na]^+$.

3-[(3-(Dimethylamino)propyl)amino]-4-ethoxycyclobut-3-ene-1,2-dione (103)

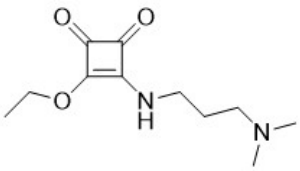

The squaramate was synthesised according to a literature method [147]. A solution of 3-(dimethylamino)-1-propylamine (0.31 mL, 2.4 mmol) in diethyl ether (3 mL) was added dropwise to a solution of 3,4-diethoxy-3-cyclobutene-1,2-dione (0.44 mL, 3 mmol) in diethyl ether (3 mL). The solution was then stirred under nitrogen at R.T for 1 h. The solution was cooled in ice and diluted with *n*-pentane (10 mL). The mixture was then centrifuged. The supernatant was decanted, and the solid washed with a mixture of *n*-pentane/diethyl ether (9:1 v/v, 3 x 10 mL). After drying under vacuum, the product was obtained as a yellow solid (0.61 g, quant). **M.p:** 72 – 77 °C; **IR** (ATR): 2990, 1791, 1695, 1477, 1466, 1445, 1247 cm^{-1}; **^{1}H NMR** (300 MHz, DMSO-d_6): δ 1.36 (t, J = 7.0 Hz, 3H), 1.57 – 1.72 (m, 2H), 2.10 (s, 6H), 2.22 (t, J = 7.1 Hz, 2H), 3.26 – 3.31 (br m, 0.6 x $2H_{anti}$), 3.46 – 3.52 (br m, 0.4 x $2H_{syn}$), 4.58 – 4.73 (br m, 2H), 8.58 (br s, 0.4 x NH_{anti}), 8.77 (br s, 0.4 x NH_{syn}); **^{13}C NMR** (75 MHz, DMSO-d_6): δ 189.3, 182.2, 176.5, 172.5, 68.7, 55.9, 45.0, 42.2, 28.4, 27.9, 15.7; **LRMS (ESI)**: *m/z* 227 ($C_{11}H_{18}N_2O_3$) $[M+H]^+$. The data are in agreement with literature values.[147]

3-[(2-Ethoxy-3,4-dioxocyclobut-1-en-1-yl)amino]-*N*,*N*,*N*-trimethylpropan-1-aminium iodide (104)

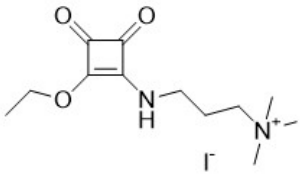

Compound **103** (0.473 g, 2.1 mmol) was suspended in acetone (21 mL). Iodomethane (0.25 mL, 4.0 mmol) was added to the squaramate suspension and the mixture was heated to reflux under nitrogen for 21 h. The solution was cooled to R.T and diluted with 25 mL *n*-pentane. The solution was then cooled in an ice bath and centrifuged. The supernatant was decanted and the solid washed with acetone/ *n*-pentane (8:2 v/v, 3 x 15 mL). The solid was placed under vacuum and dried to yield the pure product as a pale yellow solid (0.26 g, 52 %). **M.p:** 137 – 147 °C; **IR** (ATR): 3433, 1691, 1608, 1518, 1336, 1214 cm^{-1}; **^{1}H NMR** (300 MHz, DMSO-d_6): δ 1.39 (t, J = 7.2 Hz, 3H), 1.91 – 2.02 (m, 2H), 3.06 (s, 9H), 3.52 – 3.60 (m, 1H), 4.62 – 4.72 (m, 2H), 8.62 (br s, 0.5 x NH_{anti}), 8.80 (br s, 0.5 x NH_{syn}). Due to insolubility of the product, a carbon NMR spectrum could not be obtained; **LRMS (ESI)**: m/z 242 ($C_{12}H_{21}N_2O_3$) $[M\text{-}I]^+$. The data are in agreement with literature values.[147]

3,3'-[([(methylazanediyl)bis(propane-3,1-diyl)]bis (azanediyl)bis(3,4-dioxocyclobut-1-ene-2,1-diyl))bis(azanediyl)]bis (*N*,*N*,*N*-trimethylpropan-1-aminium) iodide (28)

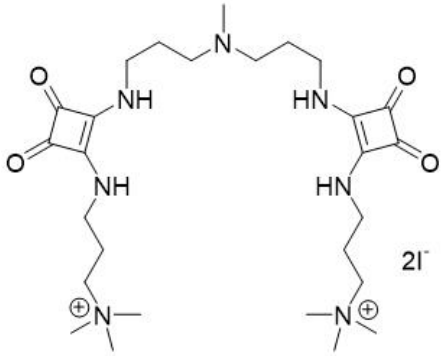

Compound **104** (0.3 g, 0.82 mmol) was dissolved in MeOH (1.5 mL). A solution of *N*-*N*-bis(3-aminopropyl)methylamine (0.11 mL, 0.69 mmol) in MeOH

(11 mL) was added drop-wise with stirring. The resultant solution was stirred at R.T under nitrogen for 24 h. The reaction mixture was diluted with 20 mL *n*-pentane and further cooled in an ice bath. The mixture was centrifuged and the supernatant decanted off. The resultant yellow solid was washed with a mixture of *n*-pentane/MeOH (9:1 v/v, 3 x 10 mL). Drying under high vacuum yielded the desired product as a white solid (0.11 g, 21%).

3,3'-[([(Methylazanediyl)bis(propane-3,1-diyl)] bis(azanediyl)bis(3,4-dioxocyclobut-1-ene-2,1-diyl))bis(azanediyl)] bis(*N*,*N*,*N*-trimethylpropan-1-aminium) chloride (105)

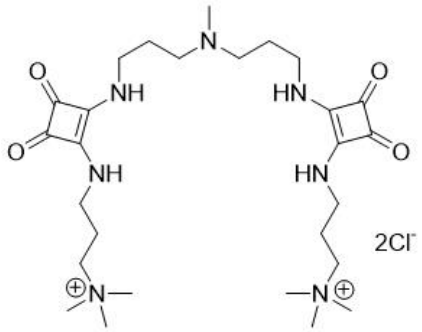

Due to insolubility of the product, compound **28** was converted to the chloride salt following the procedure set forth in Section 6.1.1 to yield the desired chloride salt as a pale yellow oil (0.047 g, 56%). **IR** (ATR): 3376, 3231, 2957, 1798, 1534 cm^{-1}; **^{1}H NMR** (500 MHz, D_2O): δ 1.90 – 1.99 (m, 4H), 2.16 – 2.26 (m, 4H), 2.50 (s, 3H), 2.80 (br s, 4H), 3.18 (s, 18H), 3.44 – 3.51 (m, 4H), 3.65 – 3.69 (m, 4H), 3.75 (t, J = 6.6 Hz, 4H); **^{13}C NMR** (125 MHz, D_2O): δ 181.9, 181.5, 168.3, 63.7, 53.0, 42.0, 41.1, 40.8, 26.5, 24.3; **HRMS (ESI)**: *m/z* calc'd for $C_{27}H_{50}Cl_2N_7O_4$ 606.3223, Found 606.3296 $[M+H]^+$. The data are in agreement with the literature, however this was compared to the data for compound **28**.[147]

6.2 Ion Chromatography

Ion Chromatography was performed on seawater samples collected from Cronulla Beach, Sydney Australia in August 2024. Calibration solutions were prepared

by dissolving Na_2SO_4 in freshly collected MilliQ Water. A stock solution was created with a Na_2SO_4 concentration of 100 mM, and standards created through serial dilution at concentrations of 20 mM, 15 mM, 10 mM, 8 mM, 6 mM, 4 mM and 2 mM. Calibration solutions were prepared immediately before running the samples. A 1.2 mL aliquot of sea water was diluted to 10 mL using MilliQ water. Ion chromatography was performed using 9 mM Na_2CO_3 eluent on a Waters 2695 Separation Module equipped with a Waters 432 Conductivity detector with scaling factor = 1000. A Waters 2996 PDA detector was equipped sampling a range from $210 - 600$ nm with a sampling rate = 5. A Dionex IonPac-AS9 HC column with dimensions 4 x 250 mm was used with isocratic elution with a 50 min run time. Samples were examined at ambient temperature with 90 μL injection and a flow rate of 1 mL/min. Samples were spiked by addition of a Na_2SO_4 standard to a seawater sample. The seawater sample using during spiking was prepared as stated above.

6.3 Spectroscopic Studies

6.3.1 UV-Vis Spectroscopic Titrations

UV-Vis titrations were performed on a Cary 4000 UV-Vis spectrophotometer or a Horiba Duetta spectrofluorometer at 25°C. To a one dimensional 1 cm quartz glass cuvette was added a solution of the receptor (1 mL) in the indicated solvent at the indicated concentration. After background correction, the receptor (at x μM) was added to the sample cuvette and the absorbance spectrum was recorded from $250 - 700$ nm. Aliquots of a solution containing the respective salt (y μM) and the receptor (x μM) were then added. After each addition, the resulting solution was stirred for 30 seconds before the absorbance spectrum was recorded. To determine association constants for the receptor-cation complexes, analysis of the absorbance data was carried out using a nonlinear least-squares curve fitting procedure using the commercially available software program bindfit v0.5[11] (http://supramolecular.org) and HypSpec. The obtained Ka values represent the

average of two or more independent titrations.

6.3.2 Fluorescence Spectroscopic Titrations

Fluorescence titrations were performed on a Horiba Duetta spectrofluorometer at 25°C. To a one dimensional 1 cm quartz glass cuvette was added a solution of the receptor (0.8 mL) in the indicated solvent at the indicated concentration and the fluorescence spectrum was recorded. Aliquots of a solution containing the respective salt (y μM) and the receptor (x μM) were then added to the sample cuvette. After each addition, the resulting solution was stirred for 30 seconds before the fluorescence spectrum was recorded. To determine association constants for the receptor-cation complexes, analysis of the fluorescence data was carried out using a nonlinear least-squares curve fitting procedure using the commercially available software bindfit v0.5[11] (http://supramolecular.org) and HypSpec. The obtained Ka values represent the average of two or more independent titrations.

6.3.3 Dilution Studies

Dilution studies were performed on a Horiba Duetta spectrofluorometer at 25°C. To a one dimensional 1 cm quartz glass cuvette, 0.8 mL of the desired solvent was added. Aliquots of a solution containing the receptor (x μM) were added to the sample cuvette. After each addition, the resulting solution was stirred for 30 seconds before the fluorescence or absorbance spectrum was recorded.

6.3.4 Competition Studies

Competition studies were performed on a Horiba Duetta spectrofluorometer at 25°C. For studies involving **63**, 0.8 mL of a 5 μM receptor solution was added to a one dimensional 1 cm quartz glass cuvette in 1% Water/MeCN. To this cuvette, 7 equivalents of metal salt was added, and the resultant solution was stirred for 30 seconds before the fluorescence spectrum was recorded. Following this, 7 equivalents of $Ba(ClO_4)_2$ was added. The resultant solution was

stirred for 30 seconds before the fluorescence spectrum was recorded. The metal salts used were $Ca(NO_3)_2.4H_2O$, $Zn(ClO_4)_2.6H_2O$, $LiBF_4$, $NaClO_4.H_2O$, KPF_6, $Mg(NO_3)_2.6H_2O$, $Sr(NO_3)_2$, Cs_2CO_3 and $Ba(ClO_4)_2.3H_2O$.

For studies involving **64**, 0.8 mL of a 5 μM receptor solution was added to a one dimensional 1 cm quartz glass cuvette in 1% Water/MeCN. To this cuvette, 7 equivalents of metal salt was added, and the resultant solution was stirred for 30 seconds before the fluorescence spectrum was recorded. Following this, 7 equivalents of $Ba(ClO_4)_2$ was added. The resultant solution was stirred for 30 seconds before the fluorescence spectrum was recorded.

For studies involving **65**, 0.8 mL of a 5 μM receptor solution was added to a one dimensional 1 cm quartz glass cuvette in 1% Water/MeCN. To this cuvette, 30 equivalents of metal salt was added, and the resultant solution was stirred for 30 seconds before the fluorescence spectrum was recorded. Following this, 30 equivalents of $Ba(ClO_4)_2$ was added. The resultant solution was stirred for 30 seconds before the fluorescence spectrum was recorded.

6.3.5 Sulfate Titrations for Metal Displacement Assay in Plasma Mimic

The final composition of the plasma mimic contained 4 mM NaCl, 0.4 mM $MgCl_2$, 7 μM KCl and 9 μM $CaCl_2$ in 1% Water/MeCN with a receptor concentration as indicated in Table 6.1. To prepare the solutions, a stock solution was made containing a 1:1 mixture of $Ba(ClO_4)_2.6H_2O$:Receptor in MeCN. To a vial, 6.7 μL of a concentrated salt water solution was added (initial concentration of 1 M NaCl, 100 mM $MgCl_2$, 1.8 mM KCl and 2.3 mM $CaCl_2$ made in MilliQ water). To the same vial, 0.79 mL of the 1:1 complex solution was added. An aliquot of a tetra-*n*-butylammonium sulfate solution (in MeCN) was added to the vial. The resultant solution was diluted to a final volume of 1.57 mL using MeCN. This was filtered with a 5 μM syringe filter. The background response was corrected and

the emission or absorbance response recorded. This was repeated with varying sulfate aliquots.

Table 6.1: Concentrations of receptor and super-stock used in studying responses in a plasma mimic.

Receptor	**Method**	[**Receptor**] (μM)
52	Fluorescence	5
62	Fluorescence	5
63	UV-Vis	40
67	Fluorescence	10

6.3.6 Sulfate Titrations for Metal Displacement Assay in Seawater Mimic

The receptor **67** was dissolved to a final concentration of 20 μM. This was made up in an aqueous solution containing 0.4 M NaCl, 60 mM $MgCl_2.6H_2O$, 28 mM Na_2SO_4, 18 mM $CaCl_2$ and 5 mM KCl in MilliQ Water. To perform this, tetra-*n*-butylammonium sulfate (860 μM) was added at varying aliquots to an eppendorf. A solution of the receptor in the salt solution above was made to 40 μM. A 0.59 mL aliquot of the 40 μM receptor was added to the eppendorf. The mixture was then diluted to 1.2 mL with the aqueous salt solution. The eppendorf was shaken, sonicated and filtered with a 5 μM syringe filter. The background was subtracted and the emission response recorded.

6.3.7 Indicator Displacement Assays for Squaramides

For the fluorescence studies, a stock solution of **101** was dissolved in a solution of Fluorescein disodium salt (9:1 MeOH: H_2O, 14 μM). A 0.65 mL aliquot of the Fluorescein solution was added to a one dimensional 1.4 mL cuvette. Aliquots of the squaramide solution were added incrementally to the indicator solution. After each addition, the resulting solution was stirred for 30 seconds before the fluorescence spectrum was recorded.

In order to perform the fluorescence IDA sulfate titrations, a 1:1 complex of Indicator: Compound **101** solution was made, with concentrations maintained at

14 μM. This was used to dissolved a sample of tetra-*n*-butylammonium sulfate. A 0.9 mL aliquot of the 1:1 solution was added to a 1.4 mL cuvette. Aliquots of the sulfate solution were added incrementally to the indicator solution. After each addition, the resulting solution was stirred for 30 seconds before the fluorescence spectrum was recorded.

To perform the UV-Vis studies in a simple medium, compound **105** (as the Iodide salt before performing Ion Exchange) was dissolved to a final concentration of up to 160 μM in a 40 μM solution of either Bromocresol Green or Cresol Red. The indicator was dissolved in a 9:1 EtOH: Tris (1 mM) solution. For studies performed with bromocresol green, the solution was acidified to pH 4.9 using AcOH. For studies performed with cresol red, the solution was basified to pH 8.9 using TBAOH. A 1.3 mL aliquot of the indicator solution was added to a one dimensional 2.5 mL cuvette. Aliquots of the receptor solution were added incrementally to the indicator solution. After each addition, the resulting solution was stirred for 30 seconds before the absorbance spectrum was recorded.

To perform the UV-Vis studies in a plasma medium mimic, **105** was dissolved to a final concentration of 600 μM in a 40 μM solution of Bromocresol Green. The indicator was dissolved in a 9:1 EtOH: Tris (1 mM) solution. The tris buffer solution contained 4 mM NaCl, 0.4 mM $MgCl_2$, 7 μM KCl and 9 μM $CaCl_2$ and was made using MilliQ water. The buffer was adjusted using AcOH to a pH of 4.5. A 1.3 mL aliquot of the indicator solution was added to a one dimensional 2.5 mL cuvette. Aliquots of the receptor solution were added incrementally to the indicator solution. After each addition, the resulting solution was stirred for 30 seconds before the absorbance spectrum was recorded. For the sulfate titrations, a mixture of Indicator:**105** (40 μM:600 μM) was created in the same solvent. Tetra-*n*-butylammonium sulfate was dissolved in this solution. Aliquots of the sulfate solution were added to a cuvette containing the 1:1 mixture. After each addition, the resulting solution was stirred for 30 seconds before the absorbance

spectrum was recorded.

6.3.8 Lifetime Experiments

Fluorescence decay was measured using a time-correlated single photon counting (TCSPC) set up on a Fluorolog-QM (HORIBA) spectrofluorometer system at 25°C. This system was equipped with DeltaDiode that provided an excitation light source at 405 nm with a pulsed rate at 25 MHz, a cooled PMT controller (HORIBA), a DH-HT high throughput TCSPC controller (HORIBA) and a DD-C1 picosecond diode controller (HORIBA). The fluorescence decay curves (TCSPC data) were acquired with the software FelixFL (HORIBA) and the DeltaHub TCSPC controller settings, with a total count of 10,000 photons under 100 ns. Solutions of the receptor at a concentration indicated in Table 6.2 in the indicated solvent were prepared. For each fluorescence lifetime measurement, the slit width was adjusted so that the ratio of single photon events counted by the detector to the pulse rate of the lamp is between 1% to 5% of the lamp frequency. An instrument response function (IRF) of the set up was measured in 0.4% LUDOX AS-40 colloidal silica (Sigma-Aldrich) diluted with distilled water, using a neutral density (ND) filter to control the amount of light reaching the detector.

The fluorescence decay curves were fitted using two-exponential decay function convolved with the IRF using DecayFit. For data displaying more than one lifetime component, the amplitude weighted mean fluorescence decay lifetime (τ_{amp}) was calculated[156] using equation 6.1:

$$\tau_{amp} = \frac{a_1\tau_1 + a_2\tau_2}{a_1 + a_2} \tag{6.1}$$

where a_1 = amplitude of lifetime 1

τ_1 = lifetime 1

a_2 = amplitude of lifetime 2

τ_2 = lifetime 2

Table 6.2: Concentrations of samples and slit widths used in determining fluorescence decay curves. For compound **63**, a slit width of 1 nm was used for the calcium complex. For compound **64**, a slit width of 1 nm was used for the Zinc complex. For compound **62**, a slit width of 1 nm was used for the Barium and Zinc complex.

Compound	**Concentration** (μM)	**Slit widths** (nm)	**Solvent**
52	3	2	1% H_2O/MeCN
62	3	2	1% H_2O/MeCN
63	5	2	1% H_2O/MeCN
64	5	2	1% H_2O/MeCN
65	5	3	1% H_2O/MeCN

6.3.9 Quantum Yield Measurements

Absolute PhotoLuminescent Quantum Yield (PLQY) was set on a Fluorolog-QM (HORIBA) spectrofluorometer system at 25°C equipped with a QuantaPhi Integrating Sphere using 4-curve acquisition. The absorbance spectrum of the receptor was obtained, and a concentration in which $Abs_{max} < 0.05$ was used. The exact concentrations of each receptor are found in Table 6.3. The receptor was made to this concentration with the indicated solvent. Optically matched 4 mL cuvettes were used, and a sample volume of 3 mL and a solvent volume of 3 mL were used.

The emission spectrum of the sample (E_c) was first obtained at the optimal excitation wavelength and Neutral Density (ND) filters were equipped to control the amount of light reaching the detector with a maximum photon count of 10^6. Following this, the emission spectrum of the blank (E_a) was also obtained with the instrumental parameters kept unchanged. Following this, an emission spectrum was obtained of the blank, where the emission range included the excitation peak (Rayleigh peak, L_c) only. The blank was replaced with the sample and emission spectrum of the Rayleigh peak (L_a) for the sample obtained.For each determination, the slit widths were adjusted according to Table 6.3. Absolute PLQY was calculated using equation 6.2:

$$\phi_f = \frac{E_c - E_a}{L_a - L_c} \tag{6.2}$$

where E_c = Integrated luminescence of the sample

E_a = Integrated luminescence of solvent

L_c = Integrated excitation profile of the sample

L_a = Integrated excitation profile of solvent

Table 6.3: Concentrations of samples, slit widths and solvent system used in determining Quantum Yields.

Compound	**Concentration** (μM)	**Slit widths** (nm)	**Solvent**
52	3	2	1% H_2O/MeCN
62	3	2	1% H_2O/MeCN
63	10	2	1% H_2O/MeCN
64	10	2	1% H_2O/MeCN
65	5	4	1% H_2O/MeCN
66	2	3	1% H_2O/MeCN
86	4	2	1:1 H_2O/MeCN
88	4	3	1:1 H_2O/MeCN
68	4	3	1:1 H_2O/MeCN
81	2	2	H_2O
67	2	2	H_2O
79	2	3	1:1 H_2O/MeCN

6.3.10 Temperature Dependency Studies

Temperature dependent emission studies were performed on the Horiba Fluoro-Max. The receptor was dissolved in glycerol at a concentration of 5 μM and the emission spectrum was measured at 10°C, 20°C, 30°C, 40°C, 60°C and 70°C. Slit widths were maintained at 3 nm. Following this, Gaussian peak deconvolution was performed using Origin 2021b software to extract both emission peaks.

6.3.11 pH Spectrofluorometric Titrations

63 was made to a 5 μM concentration (for fluorescence studies) and 40 μM (for UV-Vis studies) in a solution of 1% HCl/MeCN, and in 1% aq. TBAOH/MeCN and 0.8 mL added to a one dimensional 1 mL cuvette. Following this, the emission or absorbance was recorded. Aliquots of the receptor in basic solution were added,

with the pH measured and the emission or absorbance recorded after stirring for 30 seconds. This was repeated for a range of pH values.

A solution of the **67** was dissolved in the required solvent to a concentration of 60 μM. Following this, a 2.5 mL aliquot was added to a 21 mL vial, and acidified to pH 1.4 using 100 μL of 1 M perchloric acid. The UV-Visible absorbance spectrum was recorded. Following this, aliquots of an aqueous solution of 0.2 M NaOH were added to the sample with stirring until the pH stabilised at the desired pH, and the absorbance spectrum was collected once more. This process was repeated until pH 12. Fluorescence pH titrations were performed in the same manner, however the probe concentration was maintained at 10 μM.

To calculate the pK_a of the receptor, the maximum peak intensities were plotted against pH. This data was then fit to the Sigmoidal Boltzmann curve shown in equation 6.3 using the Origin 2021b software.

$$y = \frac{A_1 - A_2}{1 + e^{(x-x_0)/dx}} + A_2 \tag{6.3}$$

A.1 Equations

$$[HG] = \frac{1}{2}\left(G_0 + H_0 + \frac{1}{K_a}\right) - \sqrt{\left(G_0 + H_0 + \frac{1}{K_a}\right)^2 + 4[H_0][G_0]} \tag{A.11}$$

$$[G]^3(A) + [G]^2(B) + [G](C) - [G_0] = 0 \tag{A.12}$$

Where:

$$A = K_1K_2$$

$$B = K_1\left(2K_2[H]_0 - K_2[G]_0 + 1\right)$$

$$C = K_1\left([H]_0 - [G]_0\right) + 1$$

$$SE = \sqrt{\frac{\sum\left(y_{data} - y_{calc}\right)^2}{N-k}}, \quad \chi^2 = \sqrt{\frac{\sum\left(y_{data} - y_{calc}\right)^2}{N-k-1}} \tag{A.13}$$

$$\Delta A_{obs} = \varepsilon_{HG}([HG]) \tag{A.14}$$

$$\Delta F_{obs} = k_{HG}([HG]) \tag{A.15}$$

where k = rate constant.

$$\Delta F_{obs} = k_H[H] + k_{HG}([HG]) \tag{A.16}$$

where k = rate constant.

A.2 NMR Data

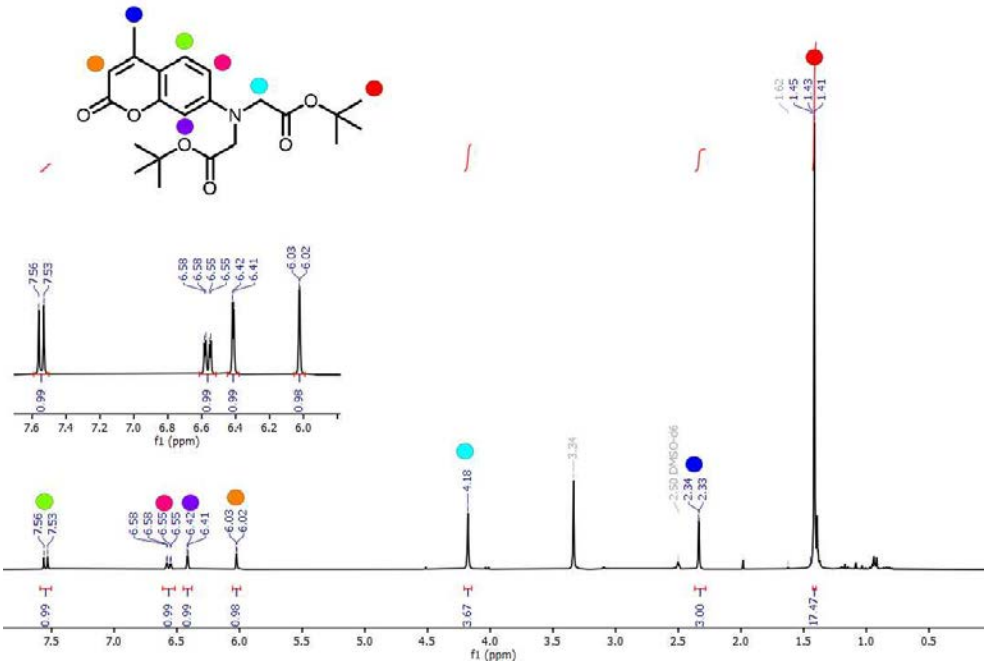

Figure A.2.1: Annotated NMR of **79** in DMSO-d_6.

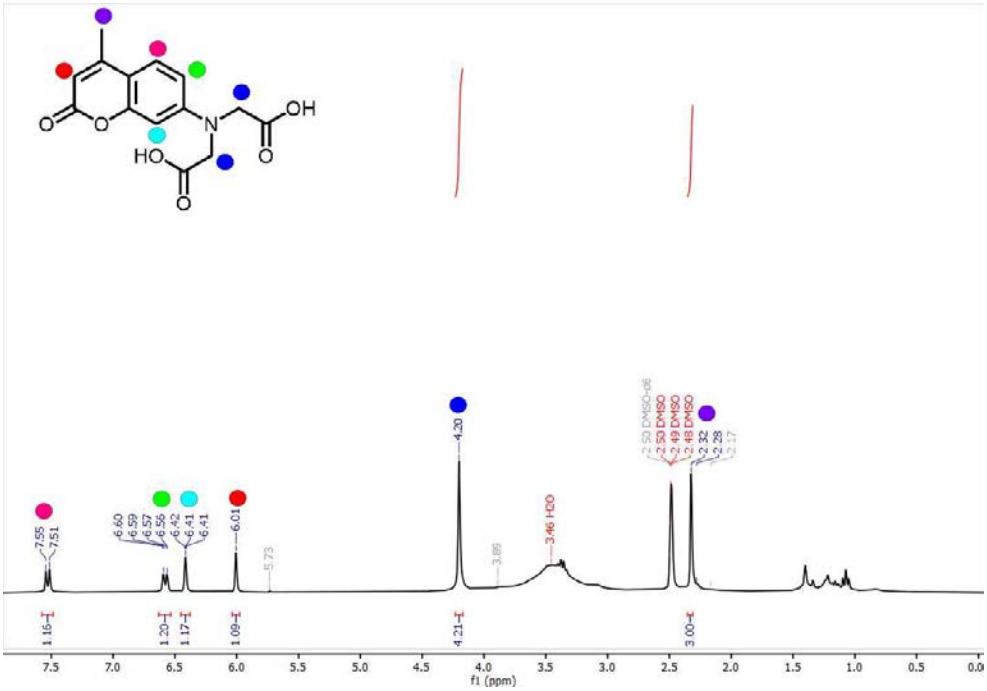

Figure A.2.2: Annotated NMR of **81** in DMSO-d_6.

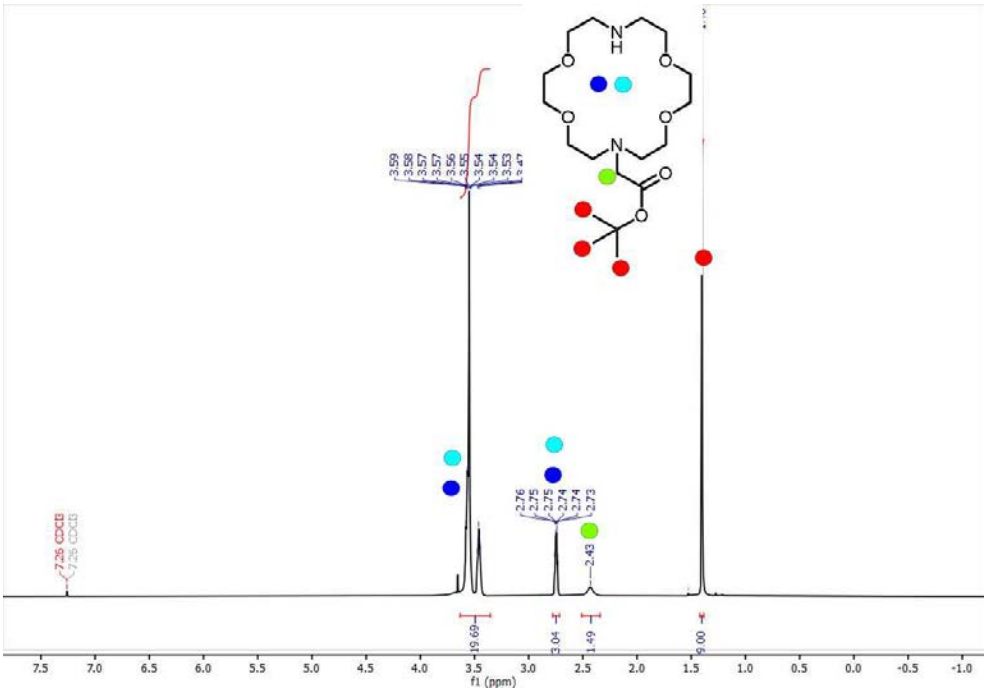

Figure A.2.3: Annotated ^{1}H NMR of **75** in $CDCl_3$.

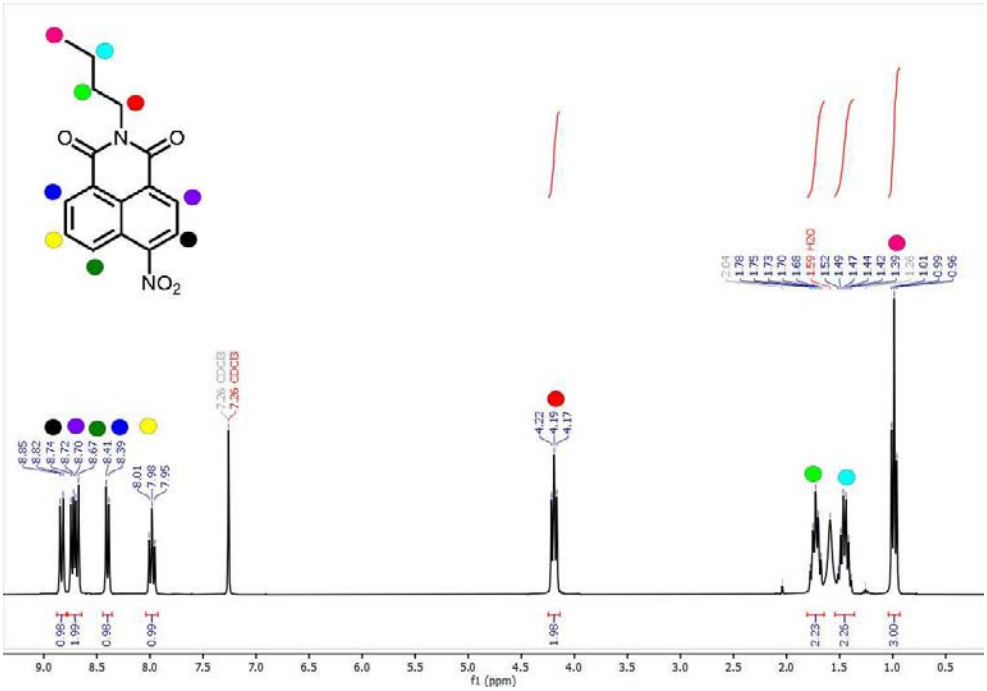

Figure A.2.4: Annotated NMR of **84** in $CDCl_3$.

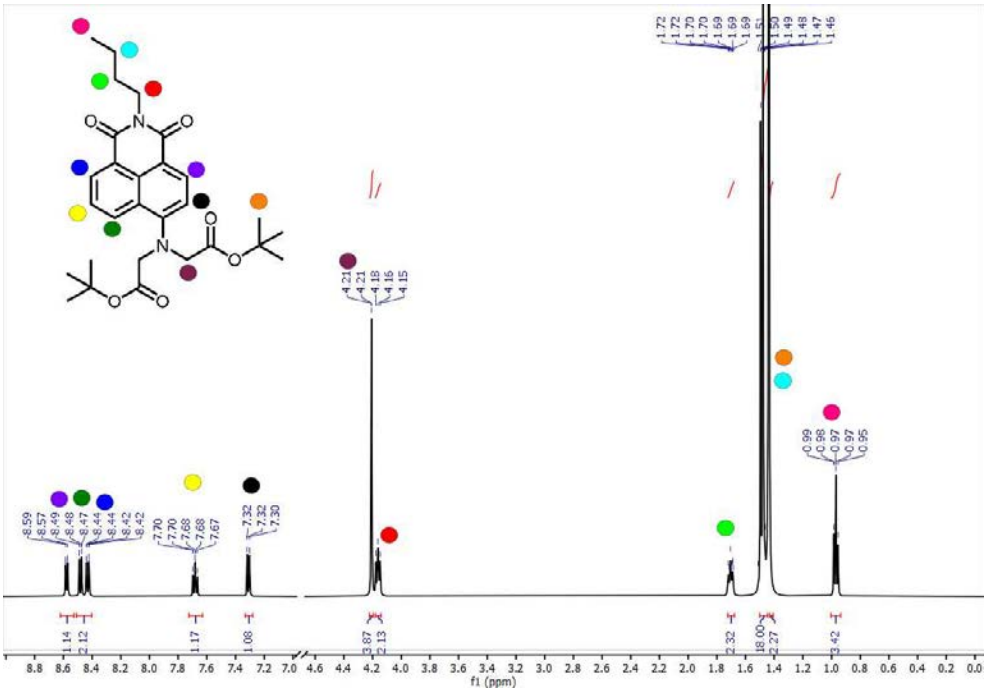

Figure A.2.5: Annotated NMR of **86** in $CDCl_3$.

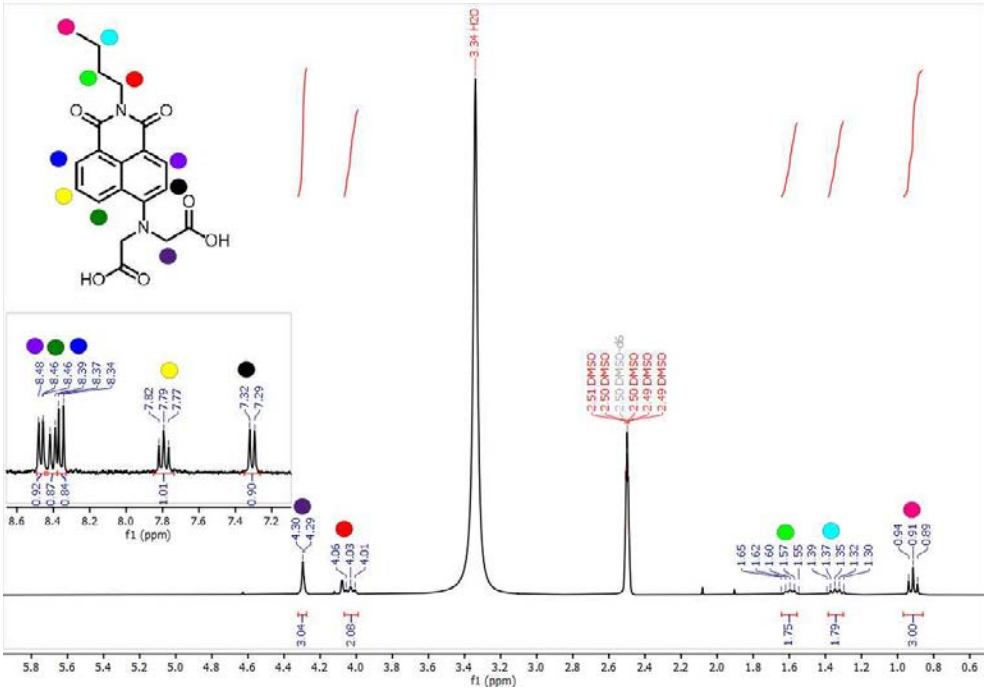

Figure A.2.6: Annotated NMR of **88** in DMSO-d_6.

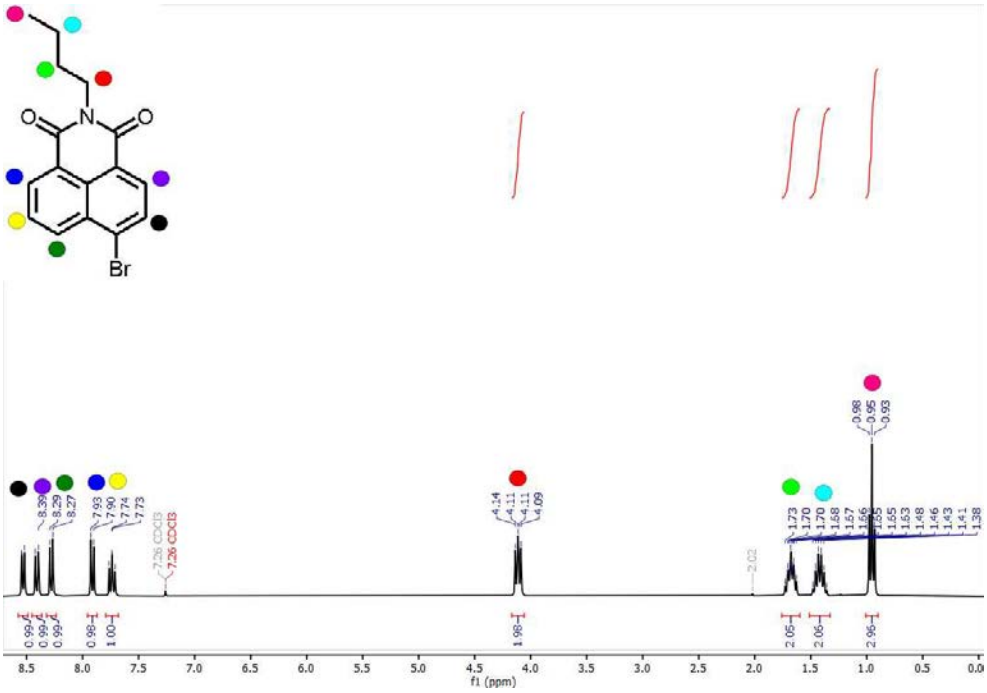

Figure A.2.7: Annotated ^{1}H NMR of **74** in $CDCl_3$.

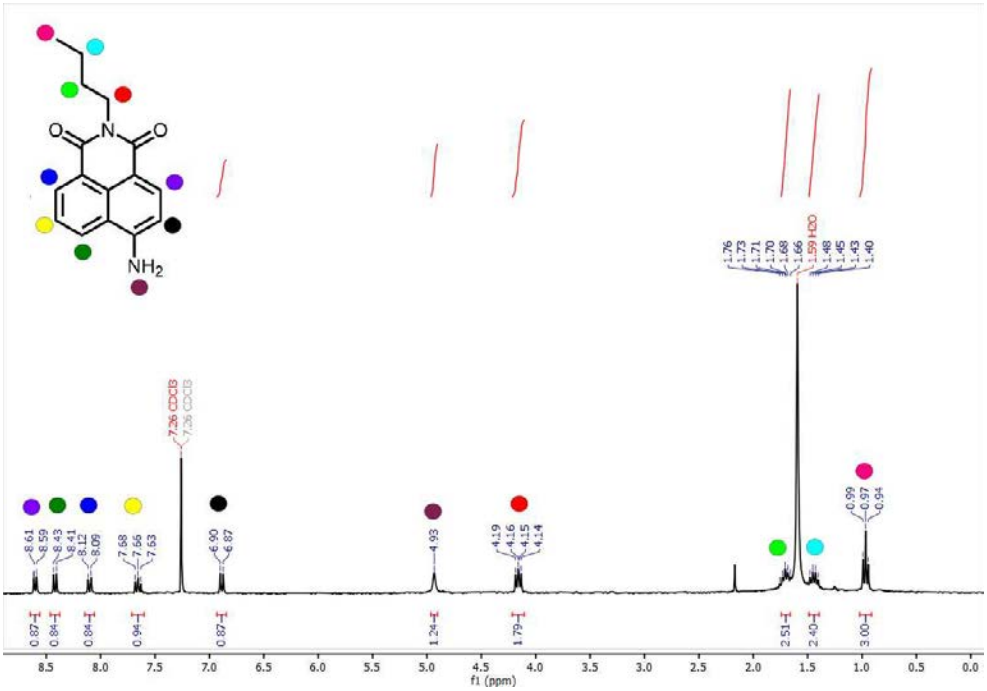

Figure A.2.8: Annotated ^{1}H NMR of **85** in $CDCl_3$.

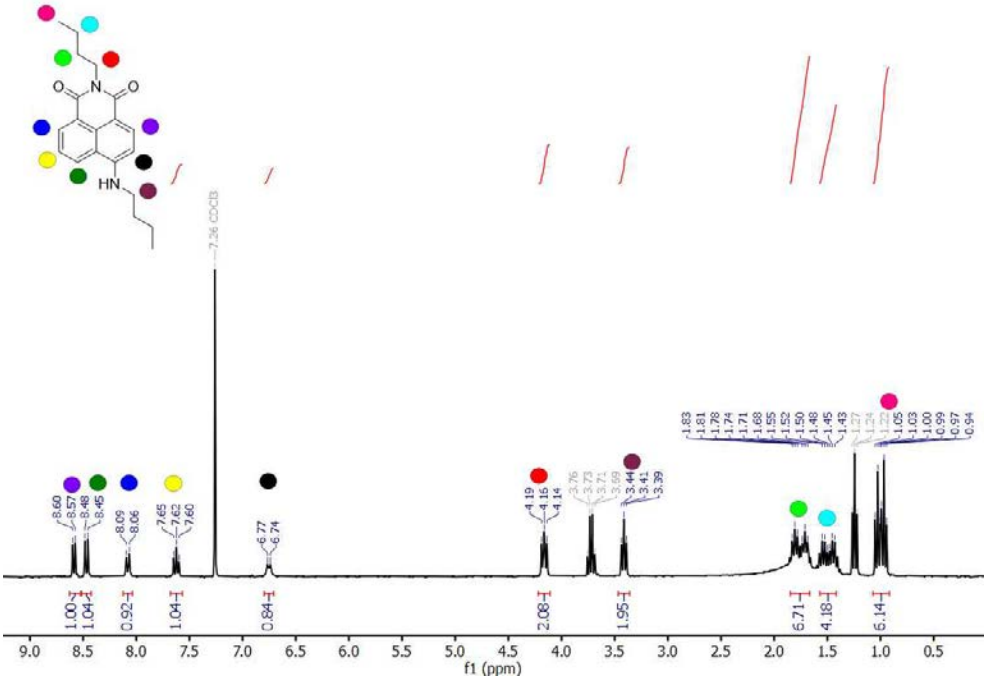

Figure A.2.9: ^{1}H NMR of **82** in $CDCl_3$.

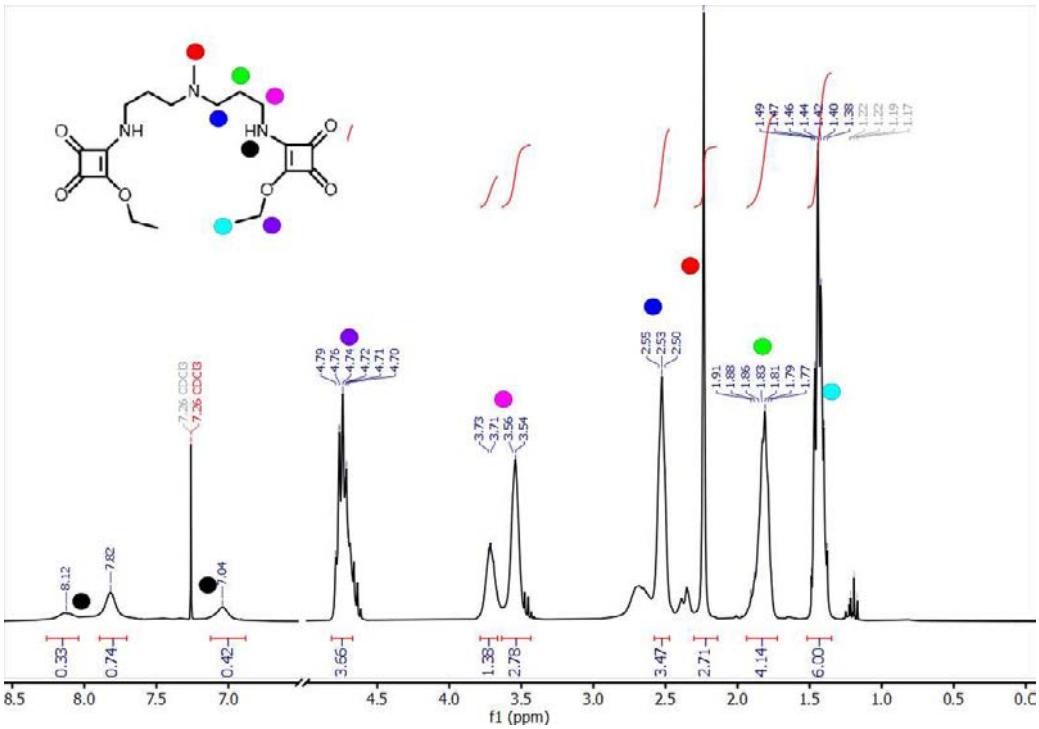

Figure A.2.10: NMR spectrum of **99** in $CDCl_3$.

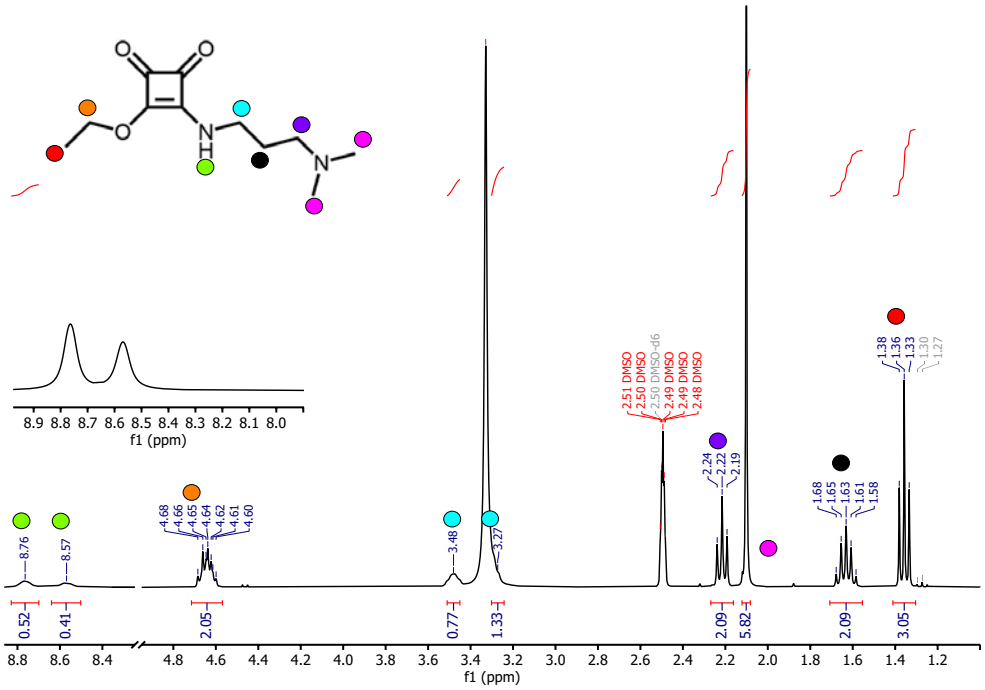

Figure A.2.11: NMR spectrum of **103** in DMSO-d_6.

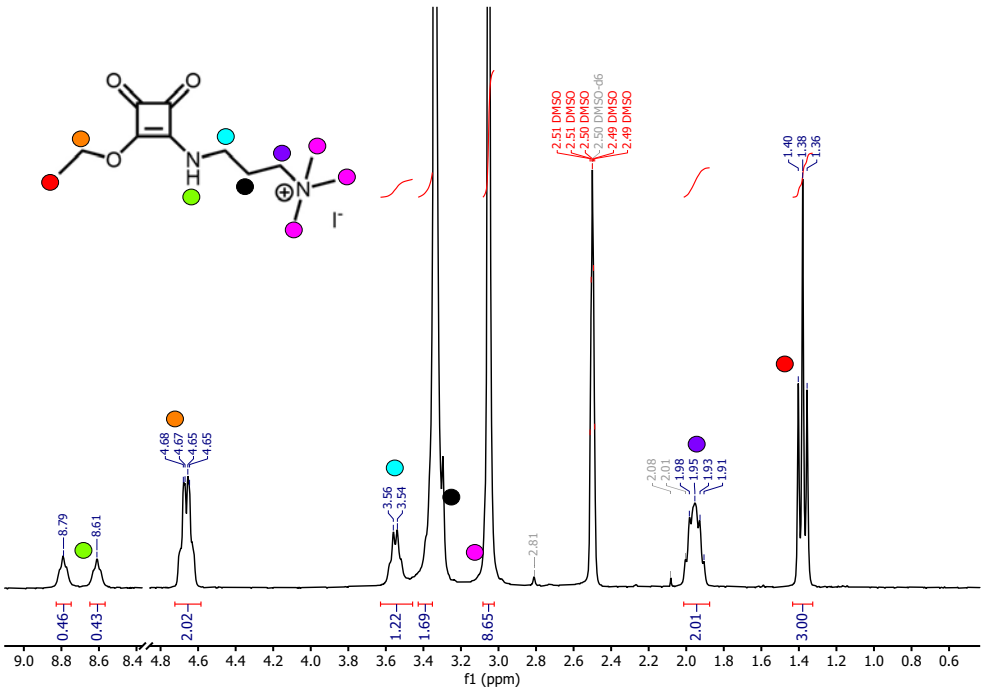

Figure A.2.12: NMR spectrum of **104** in DMSO-d_6.

A.3 Spectroscopic Data

A.3.1 Compound 52

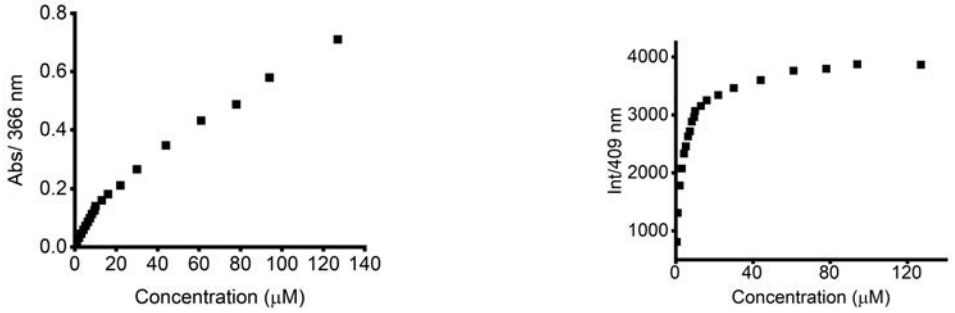

(a) UV-vis. **(b)** Fluorescence.

Figure A.3.1: Dilution study isotherms of **52** in 1% Water/MeCN presenting a graph of concentration vs change at λ_{max}.

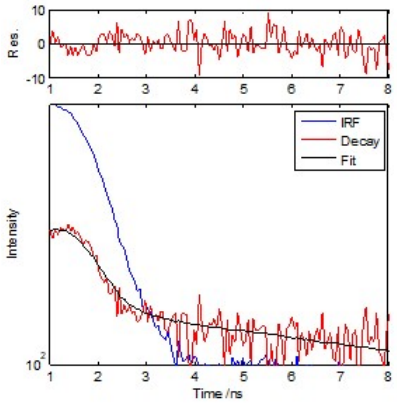

Figure A.3.2: Biexponential decay fit for **52** in 1% Water/MeCN.

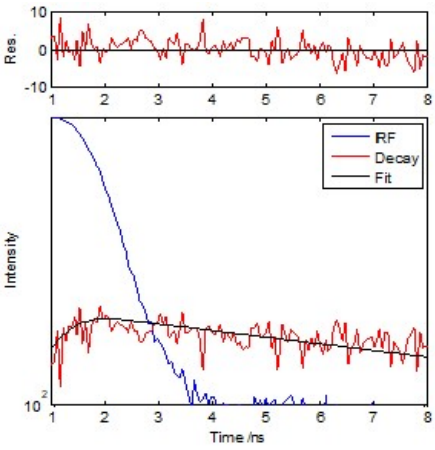

Zn(II)

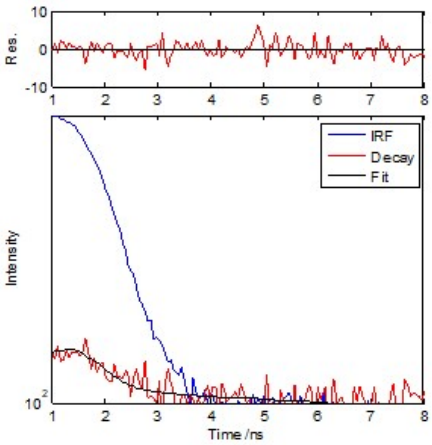

K(I)

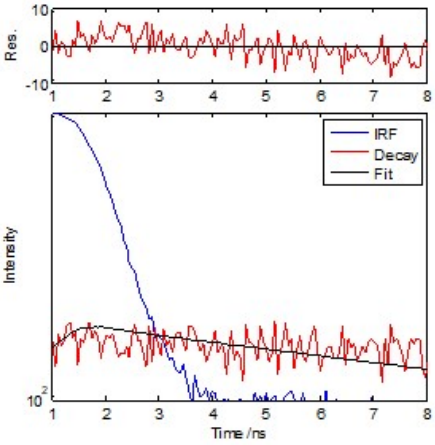

Mg(II)

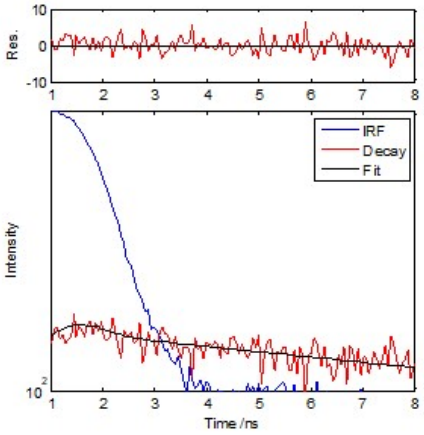

Li(I)

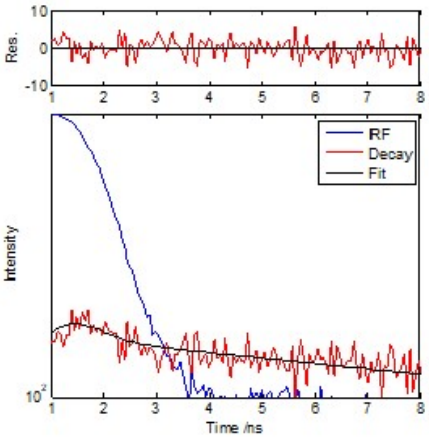

Ca(II)

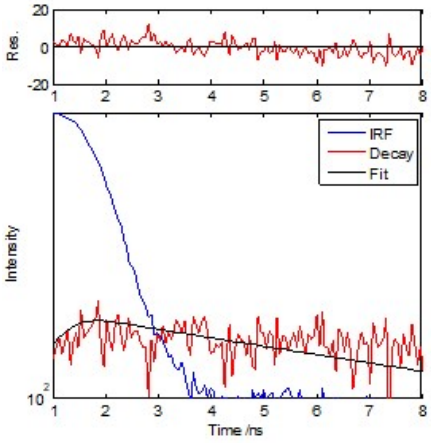

Ba(II)

Figure A.3.3: Biexponential decay fits generated by DecayFit for **52** complexes in 1% Water/MeCN.

Table 4: Bi-exponential lifetime amplitudes for **52**.

Metal Complex	a_1	a_2	τ_1 (ns)	τ_2 (ns)
52	0.94	0.06	0.00048	19.24
52-Ba(II)	0.84	0.12	0.0014	7.24
52-Ca(II)	0.95	0.05	0.00022	10.85
52-Li(I)	0.92	0.08	0.000098	10.99
52-Mg(II)	0.86	0.14	0.0000027	8.98
52-K(I)	0.97	0.03	0.00048	19.24
52-Zn(II)	0.59	0.31	0.0018	9.12

A.3.2 Compound 62

Table 5: Errors for **52** and **62** LogK_a values. Error calculated by combining standard deviation from both HypSpec and BindFit with n = 3.

Receptor	**Metal**	**LogK_a**	$\pm$
52	Li(I)	3.51	1.29
	K(I)	5.71	
	Mg(II)	4.69	1.50
62	K(I)	4.08	0.45
	Mg(II)	4.09	1.00
	Ba(II)	5.14	2.27

Table 6: Bi-exponential lifetime amplitudes for compound **62**.

Metal Complex	a_1	a_2	τ_1 (ns)	τ_2 (ns)
62	0.9	0.01	0.00051	5.87
62-Ba(II)	0.97	0.03	0.00019	8.15
62-Ca(II)	0.99	0.01	0.00075	6.60
62-Mg(II)	0.98	0.02	0.000077	8.77
62-K(I)	0.99	0.01	0.000013	6.86
62-Sr(II)	0.99	0.01	0.00034	8.13
62-Zn(II)	0.96	0.04	0.000045	10.27

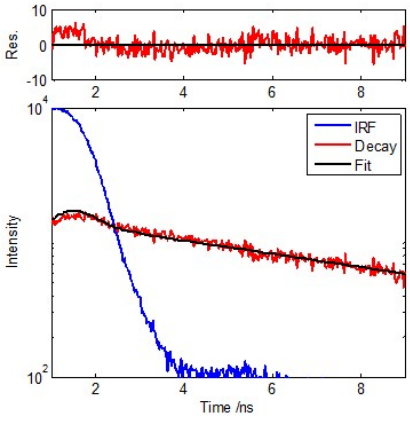

Ba(II)

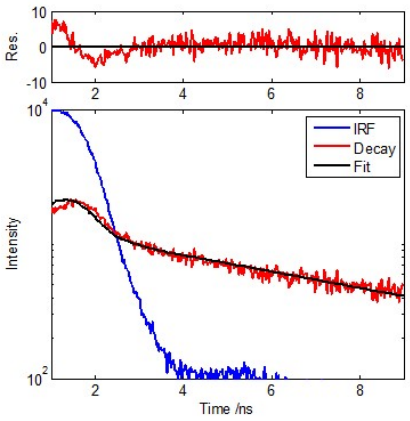

Ca(II)

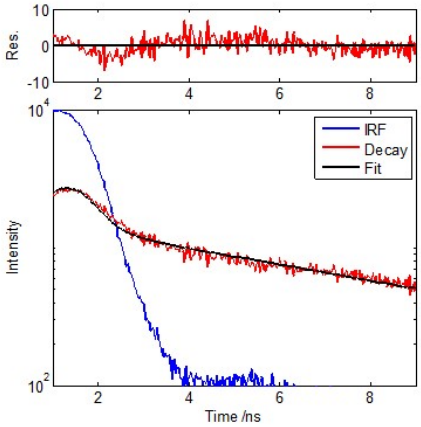

K(I)

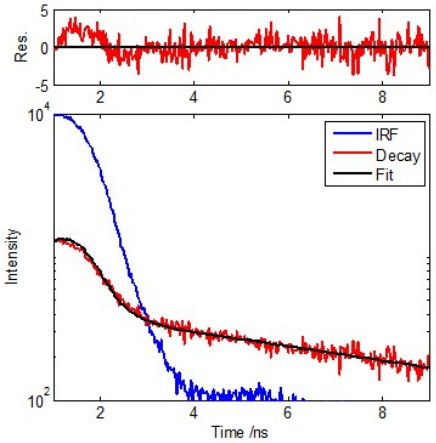

Sr(II)

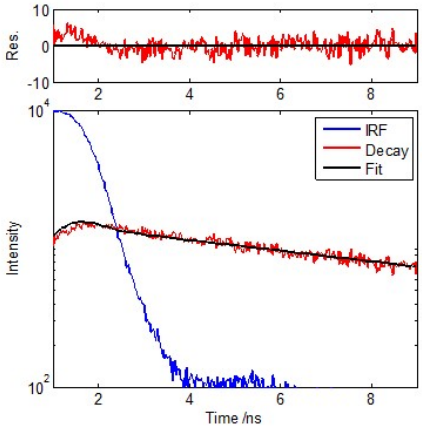

Zn(II)

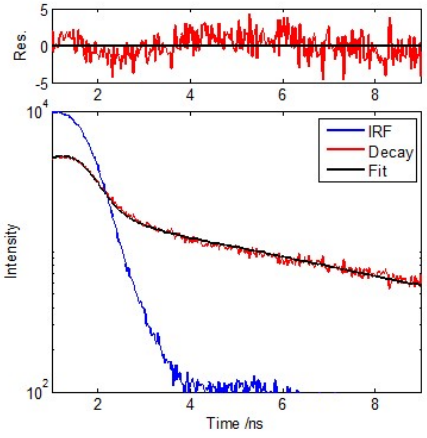

Probe

Figure A.3.4: Biexponential decay fits generated by DecayFit for **62** complexes in 1% Water/MeCN.

A.3.3 Compound 63

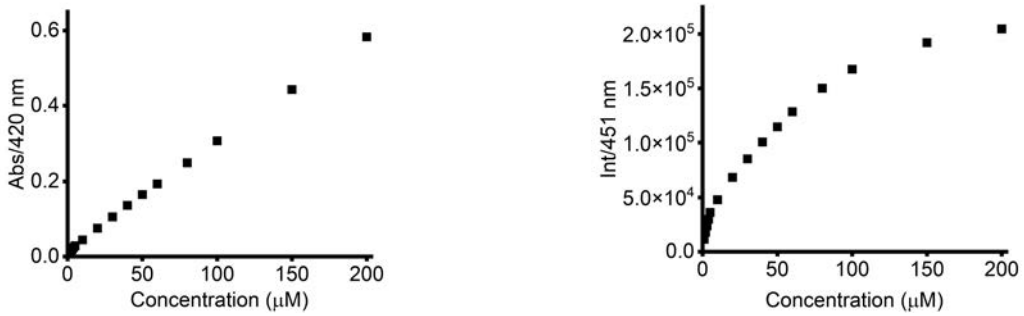

(a) UV-vis. **(b)** Fluorescence.

Figure A.3.5: Dilution study isotherms of **63** in 1% Water/MeCN presenting a graph of concentration vs change at λ_{max}.

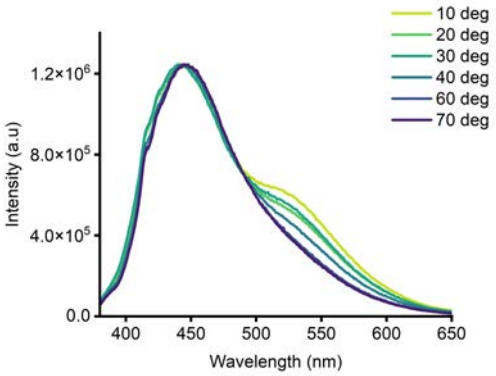

Figure A.3.6: Normalised emission data indicating the response of **63** in glycerol as temperature changes. The receptor was used at a concentration of 5 μM and an excitation wavelength of λ_{ex} = 370 nm was used.

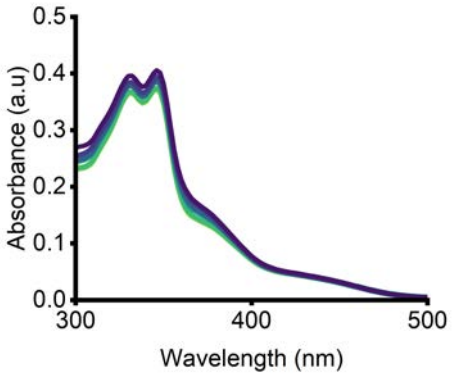

Figure A.3.7: Sulfate titration of the 1:1 complex **63**-Ba(II) in 1% Water/MeCN through UV-vis. Receptor concentration was 40 μM. Containing 140 mM $NaBF_4$, 2 mM KPF_6, 2.5 mM $Ca(ClO_4)_2$ and 120 mM $MgCl_2$.

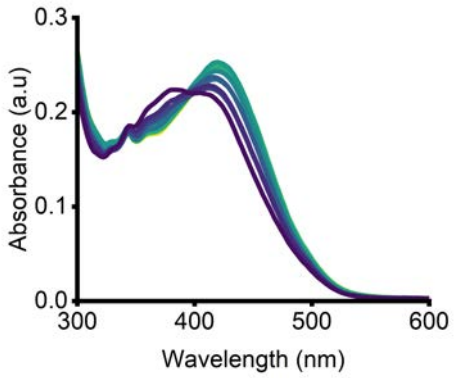

Figure A.3.8: SO_4^{2-} titration of the 1:1 complex compound **63**-Ba(II) in 1% Water:MeCN through UV-Vis. Receptor concentration was 40 μM. Containing 4 mM NaCl, 7 μM KCl, 9 μM $CaCl_2$ and 0.4 mM $MgCl_2$ with new sample preparation.

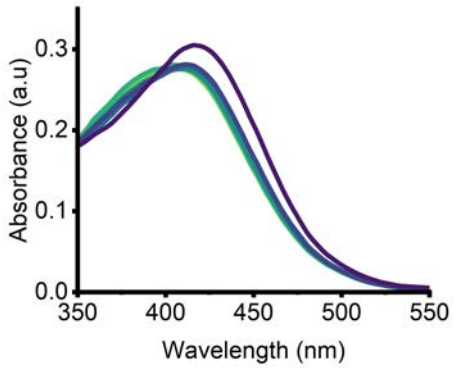

Figure A.3.9: Sulfate titration of the 1:1 complex compound **63**-Ba^{2+} in 1% Water/MeCN through UV-vis. Receptor concentration was 40 μM. Containing 5 mM NaCl, 9 μM KCl, 12 μM $CaCl_2$ and 0.5 mM $MgCl_2$.

Table 7: Bi-exponential lifetime amplitudes for compound **63**.

Metal Complex	a_1	a_2	τ_1 (ns)	τ_2 (ns)
63	0.69	0.31	1.39	9.39
63-Ba(II)	0.64	0.36	2.67	10.5
63-Ca(II)	0.69	0.31	4.08	8.31
63-Sr(II)	0.60	0.40	1.14	9.67
63-Mg(II)	0.68	0.32	1.68	9.14
63-Na(I)	0.86	0.14	2.48	10.5
63-K(I)	0.72	0.28	1.95	10.5
63-Li(I)	0.77	0.23	1.57	9.97
63-Cs(I)	0.68	0.32	0.92	9.97

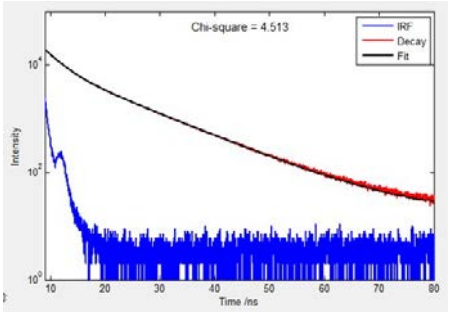

Ba(II)

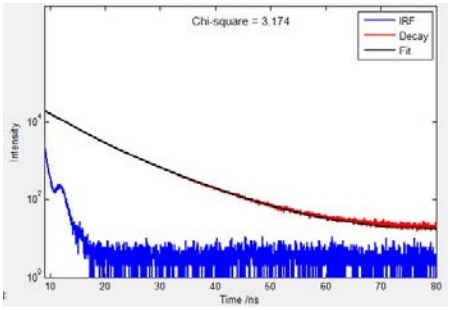

Ca(II)

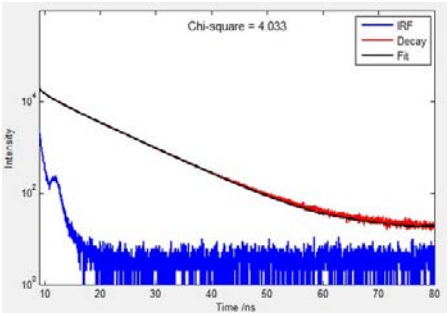

Zn(II)

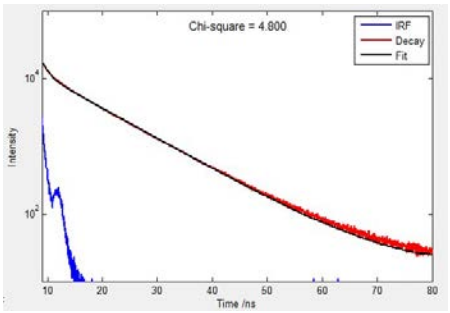

Sr(II)

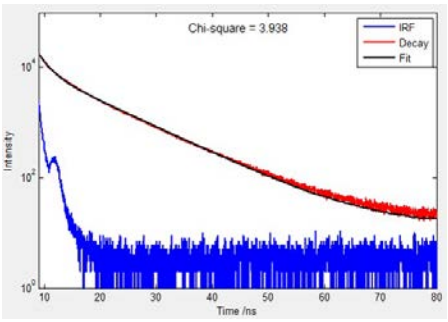

Mg(II)

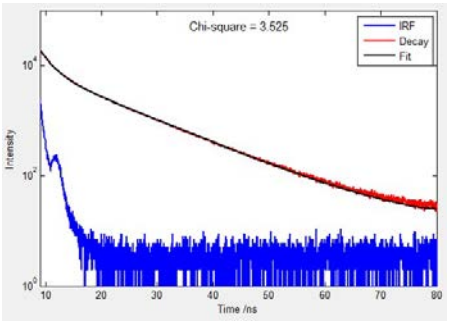

K(I)

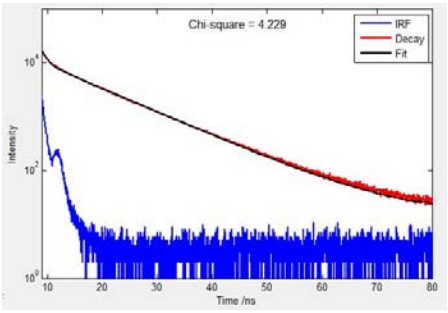

Cs(I)

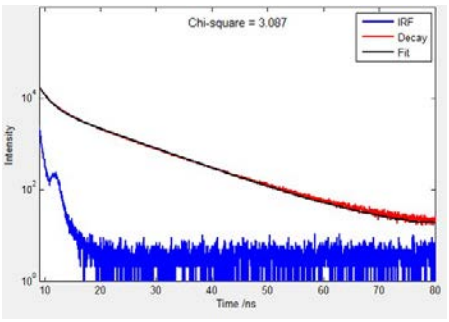

Li(I)

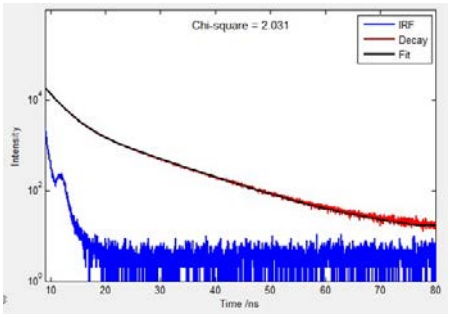

Na(I)

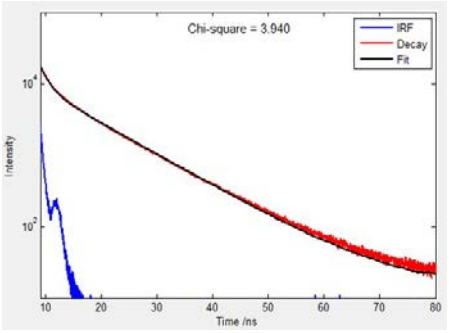

Probe

Figure A.3.10: Biexponential decay fits generated by DecayFit for **63** complexes in 1% Water/MeCN.

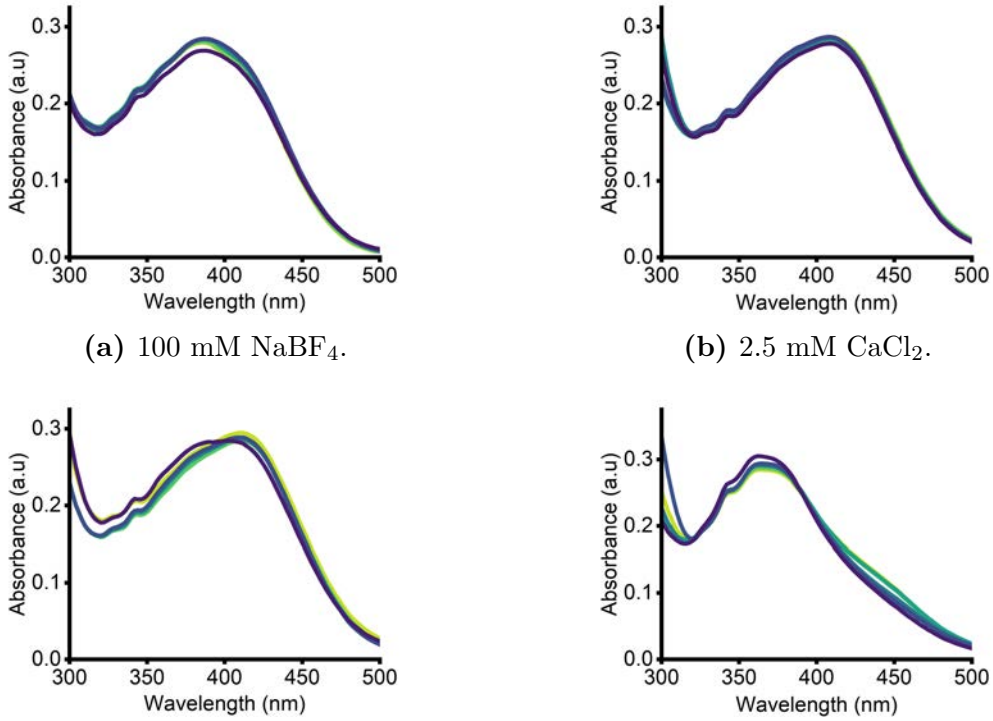

(a) 100 mM $NaBF_4$.

(b) 2.5 mM $CaCl_2$.

(c) 120 mM $MgCl_2$.

(d) 2 mM KPF_6.

Figure A.3.11: UV-vis spectroscopic titration of **63**-Ba(II) with increasing equivalents of TBA_2SO_4 in 1% water/MeCN ([probe] = 40 μM) containing the mentioned salts (concentration indicative of final salt concentration).

A.3.4 Compound 64

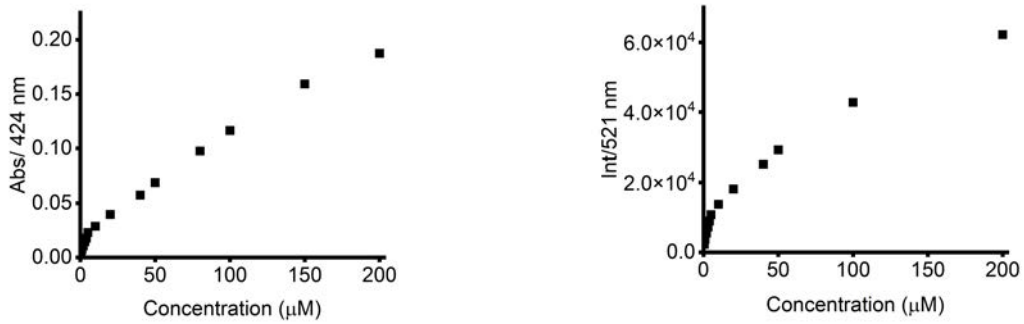

(a) UV-vis **(b)** Fluorescence

Figure A.3.12: Dilution study isotherms of **64** in 1% Water/MeCN presenting a graph of concentration vs change at λ_{max}.

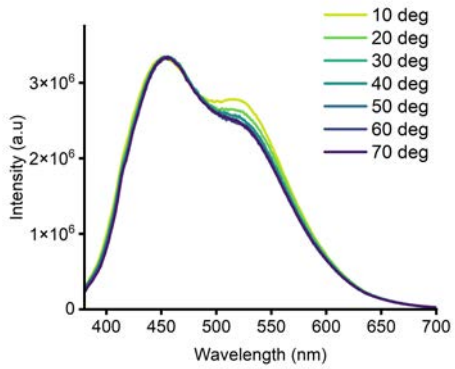

Figure A.3.13: Normalised emission data indicating the response of **64** in glycerol as temperature changes. The receptor was used at a concentration of 5 μM and an excitation wavelength of λ_{ex} = 370 nm was used.

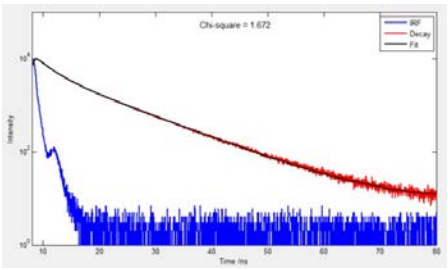

Ba(II)

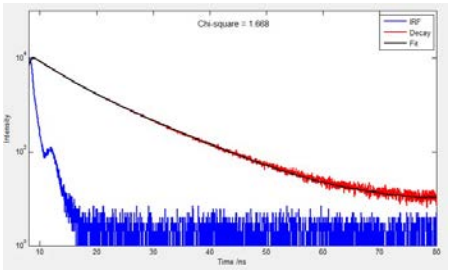

Ca(II)

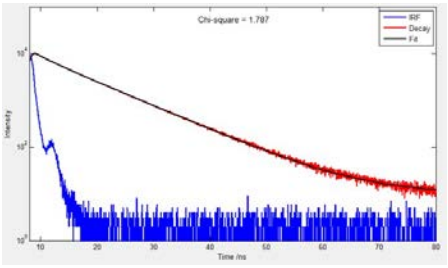

Zn(II)

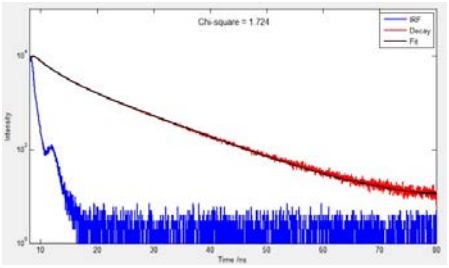

Sr(II)

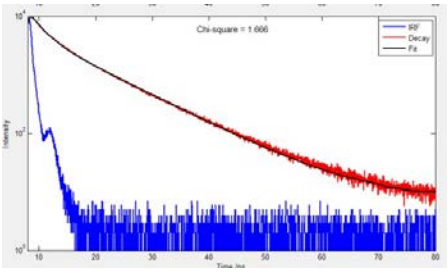

Mg(II)

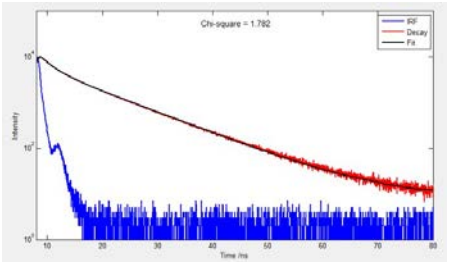

K(I)

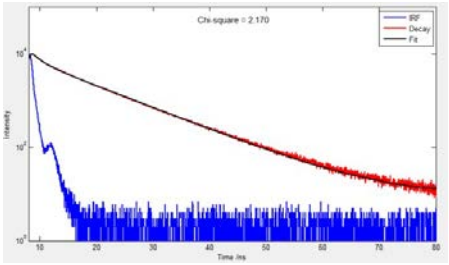

Cs(I)

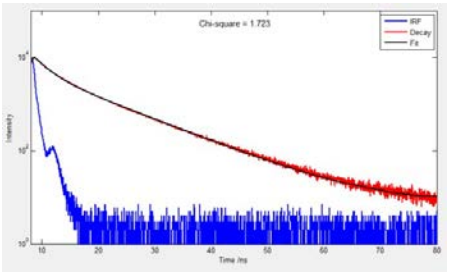

Li(I)

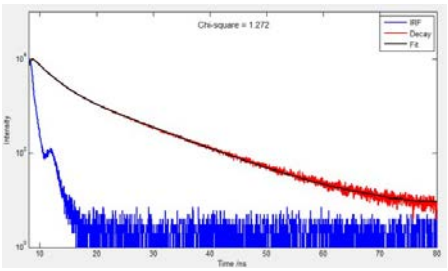

Na(I)

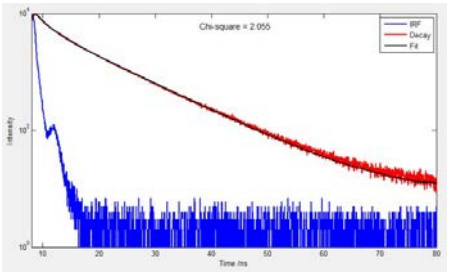

Probe

Figure A.3.14: Biexponential decay fits generated by DecayFit for **64** complexes in 1% Water/MeCN.

Table 8: Bi-exponential lifetime amplitudes for compound **64**.

Metal Complex	a_1	a_2	τ_1 (ns)	τ_2 (ns)
64	0.52	0.48	1.91	9.39
64-Ba(II)	0.58	0.42	2.46	9.55
64-Ca(II)	0.55	0.45	3.57	8.51
64-K(I)	0.56	0.44	1.85	9.40
64-Li(I)	0.32	0.68	2.12	9.21
64-Sr(II)	0.60	0.40	2.52	9.44
64-Mg(II)	0.62	0.38	2.01	9.00
64-Cs(I)	0.47	0.53	1.35	9.26
64-Na(I)	0.75	0.25	2.45	9.42

A.3.5 Compound 65

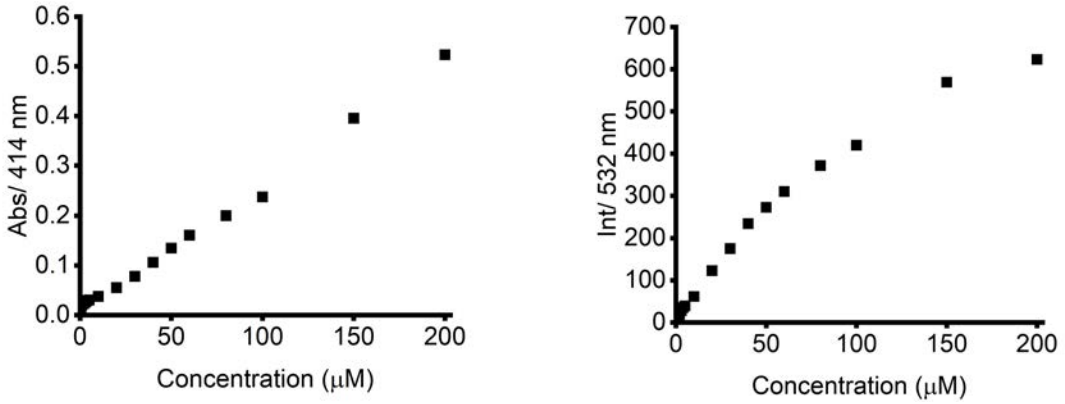

(a) UV-vis. **(b)** Fluorescence.

Figure A.3.15: Dilution study isotherms of **65** in 1% Water/MeCN presenting a graph of concentration vs change at λ_{max}.

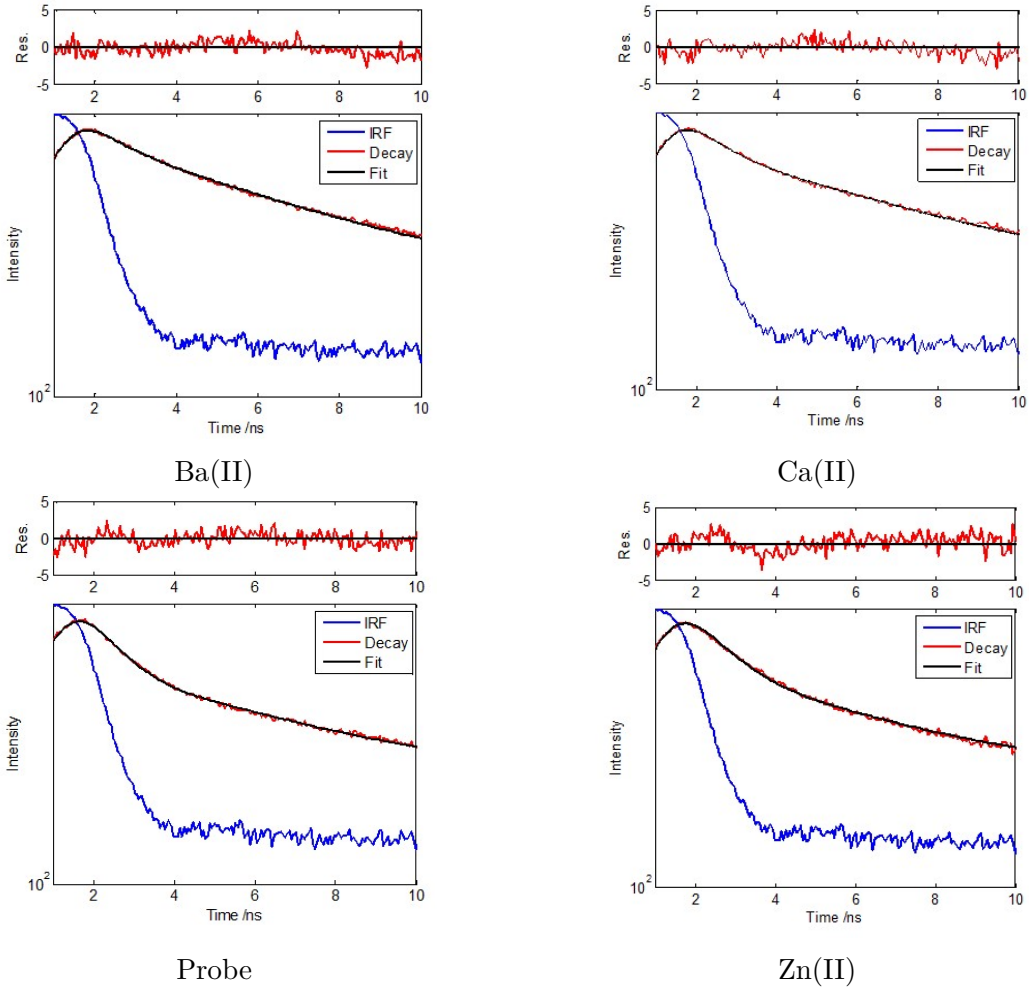

Figure A.3.16: Biexponential decay fits generated by DecayFit for **65** complexes in 1% Water/MeCN.

Table 9: Bi-exponential lifetime amplitudes for compound **65**.

Metal Complex	a_1	a_2	τ_1 (ns)	τ_2 (ns)
65	0.20	0.80	4.87	0.55
65-Ba(II)	0.52	0.48	0.48	4.11
65-Ca(II)	0.61	0.39	0.51	4.48
65-Zn(II)	0.25	0.75	4.82	0.78

Table 10: Errors for **63**, **64** and **65** $LogK_a$ values. Error calculated by combining standard deviation from both HypSpec and BindFit with n = 3.

Receptor	Metal	$LogK_a$	±
63	Na(I)	3.37	1.08
	K(I)	3.40	0.69
	Mg(II)	3.83	1.53
	Ca(II)	3.43	0.70
	Ba(II)	4.87	1.37
64	Na(I)	3.36	0.99
	K(I)	3.42	0.75
	Ca(II)	3.70	1.01
	Ba(II)	4.98	0.74
65	Li(I)	2.44	0.98
	K(I)	2.21	2.21
	Ca(II)	3.63	1.20
	Ba(II)	4.70	1.31

A.3.6 Compound 66

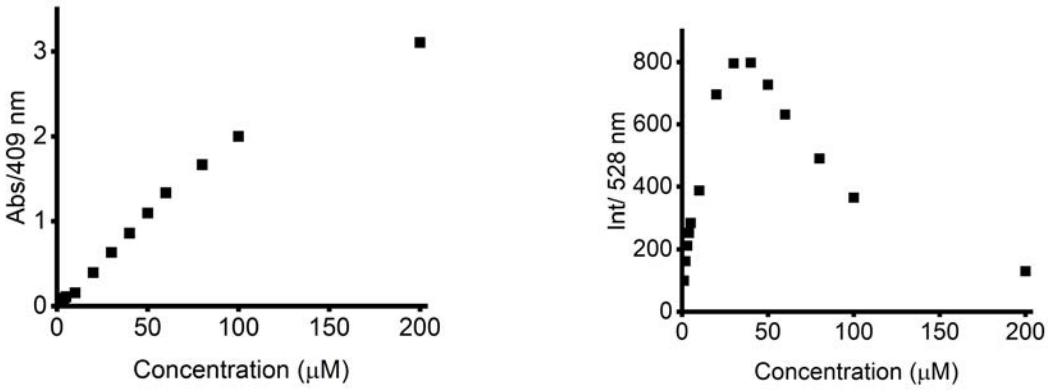

(a) UV-vis **(b)** Fluorescence

Figure A.3.17: Dilution study isotherms of **66** in 1% Water/MeCN presenting a graph of concentration vs change at λ_{max}.

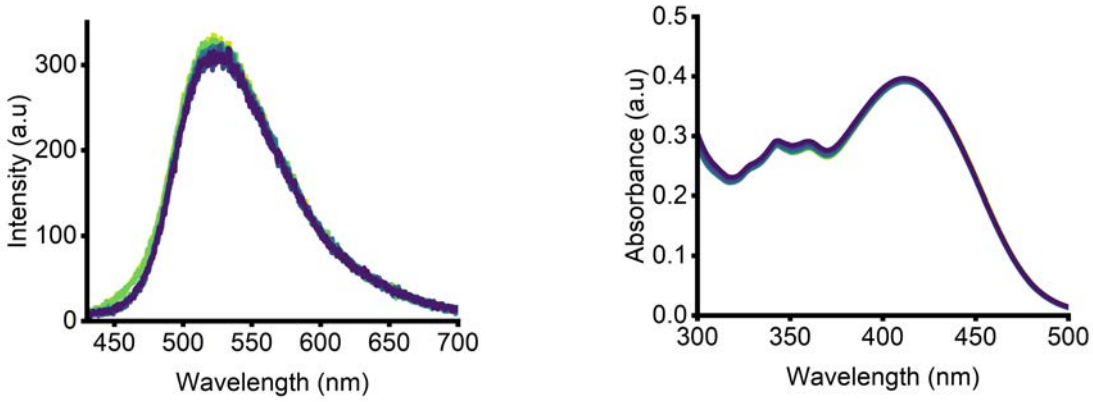

(a) Fluorescence **(b)** UV-vis

Figure A.3.18: Response of **66** to increasing concentrations of $Ba(ClO_4)_2.6H_2O$. The excitation band-pass was set to 5 nm and the emission band-pass was set to 10 nm. An excitation wavelength of $\lambda_{ex} = 410$ nm was used.The receptor was used at a concentration of 5 μM for Fluorescence studies and 40 μM for UV-Vis.

A.3.7 Compound 88

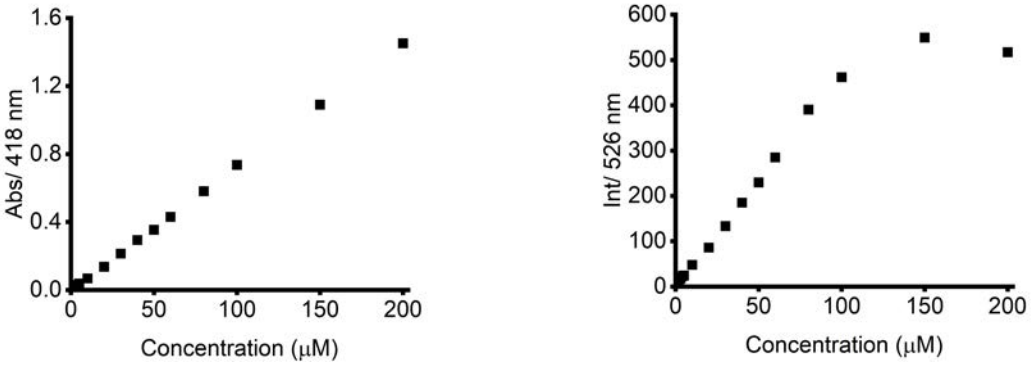

(a) UV-vis **(b)** Fluorescence

Figure A.3.19: Dilution study isotherms of **88** in 50% Water/MeCN presenting a graph of concentration vs change at λ_{max}.

A.3.8 Compound 67

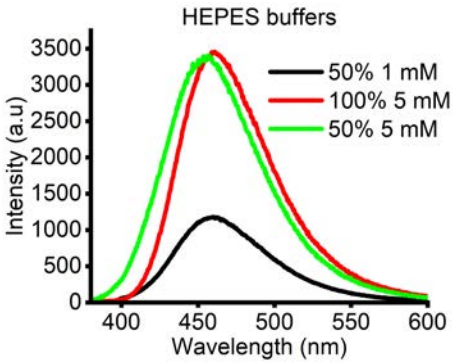

(a) pH 7.4 HEPES/MeCN

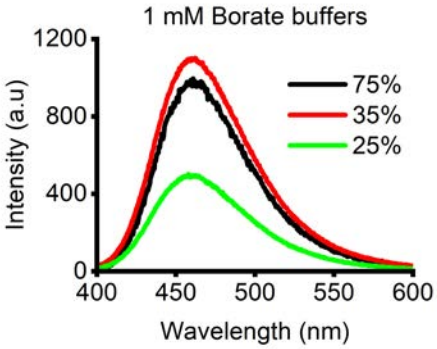

(b) pH 8.5 Borate/MeCN

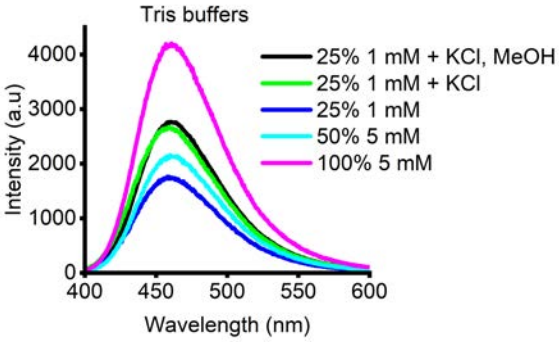

(c) pH 10 Tris

Figure A.3.20: Excitation and emission spectra of receptor **67** in a variety of buffer mixtures ([probe] = 60 μM, λ_{ex} = 390 nm). The excitation bandpass was 5 nm and the emission bandpass was 5 nm. For the Tris systems, MeCN was used as organic solvent, except where indicated with MeOH. KCl was added at a final concentration of 0.1 M where indicated.

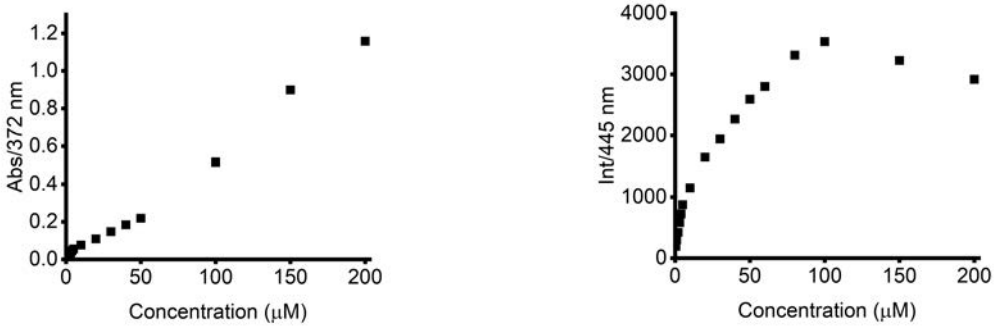

(a) UV-vis **(b)** Fluorescence

Figure A.3.21: Dilution study isotherms of **67** in 50% Water/MeCN presenting a graph of concentration vs change at λ_{max}.

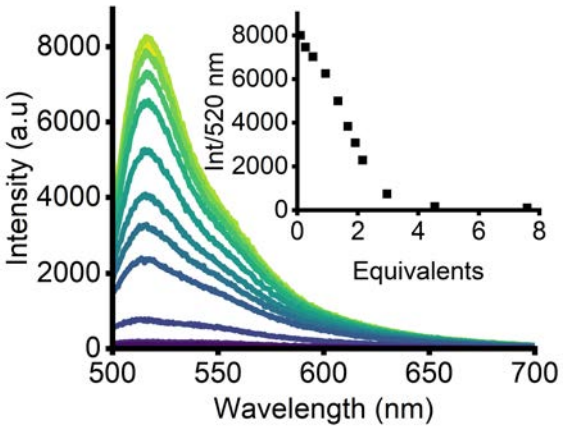

Figure A.3.22: Fluorescence titration of FNa_2 with increasing equivalents of $SO_4{}^{2-}$ performed in 10% H_2O:MeOH ([Indicator] = 14 μM, λ_{ex} = 490 nm). The excitation bandpass was 3 nm and the emission bandpass was 10 nm. Inset graph presents emission intensity as a function of guest equivalents.

Bibliography

1. Dawson, P., Petersen, S., Rodwell, R., Johnson, P., Gibbons, K., McWhinney, A., Bowling, F. & McIntyre, H. Reference intervals for plasma sulfate and urinary sulfate excretion in pregnancy. *BMC Pregnancy and Childbirth* **15.** 96 (2015).
2. Dordevic, D., Capikova, J., Dordevic, S., Tremlová, B., Gajdács, M. & Kushkevych, I. Sulfur content in foods and beverages and its role in human and animal metabolism: A scoping review of recent studies. *Heliyon* **9,** e15452 (2023).
3. Patrick, S., Beer, P. & Davis, J. Solvent effects in anion recognition. *Nature Reviews Chemistry* (2024).
4. Markovich, D. Physiological Roles and Regulation of Mammalian Sulfate Transporters. *Physiological Reviews* **81,** 1499–1533 (2001).
5. Bradley, H., Gough, A., Sokhi, R. S., Hassell, A., Waring, R. & Emery, P. Sulfate metabolism is abnormal in patients with rheumatoid arthritis. Confirmation by in vivo biochemical findings. *The Journal of Rheumatology* **21,** 1192–1196 (1994).
6. Wang, H. & Zhang, Q. Research advances in identifying sulfate contamination sources of water environment by using stable isotopes. *International Journal of Environmental Research and Public Health* **16,** 1914 (2019).
7. Cagno, V., Tseligka, E., Jones, S. & Tapparel, C. Heparan sulfate proteoglycans and viral attachment: True receptors or adaptation bias? *Viruses* **11,** 596 (2019).

8. Marcus, Y. Ionic radii in aqueous solutions. *Chemical Reviews* **88,** 1475–1498 (1988).
9. Arranz, P., Bencini, A., Bianchi, A., Diaz, P., García-España, E., Giorgi, C., Luis, S. V., Querol, M. & Valtancoli, B. Thermodynamics of sulfate anion binding by macrocyclic polyammonium receptors. *Journal of the Chemical Society, Perkin Transactions 2,* 1765–1770 (9 2001).
10. Hunter, T. Why nature chose phosphate to modify proteins. *Philosophical Transactions of the Royal Society B, Biological Sciences* **367,** 2513–2516 (2012).
11. Thordarson, P. Determining association constants from titration experiments in supramolecular chemistry. *Chemical Society Reviews* **40,** 1305–1323 (2011).
12. Robinson-Duggon, J., Pérez-Mora, F., Dibona-Villanueva, L. & Fuentealba, D. Potential Applications of Cucurbit[n]urils Inclusion Complexes in Photodynamic Therapy. *Israel Journal of Chemistry* **58,** 199–214 (2018).
13. Schneider, H. & Yatsimirsky, A. K. Selectivity in supramolecular hostguest complexes. *Chemical Society Reviews* **37,** 263–277 (2008).
14. Pereira, C., Roesler, C., Faria, J., Fessel, M. & Balan, A. Sulfate-Binding Protein (Sbp) from Xanthomonas citri: Structure and Functional Insights. *Molecular Plant-Microbe Interactions* **30,** 578–588 (2017).
15. Pflugrath, J. W. & Quiocho, F. A. The 2 Å resolution structure of the sulfate-binding protein involved in active transport in Salmonella typhimurium. *Journal of Molecular Biology* **200,** 163–180 (1988).
16. Ravikumar, I. & Ghosh, P. Recognition and separation of sulfate anions. *Chemical Society Reviews* **41,** 3077–3098 (2012).
17. Gale, P. & Caltagirone, C. Fluorescent and colorimetric sensors for anionic species. *Coordination Chemistry Reviews* **354,** 2–27 (2018).

18. Zhou, H., Zhao, Y., Gao, G., Li, S., Lan, J. & You, J. Highly Selective Fluorescent Recognition of Sulfate in Water by Two Rigid Tetrakisimidazolium Macrocycles with Peripheral Chains. *Journal of the American Chemical Society* **135,** 14908–14911 (2013).

19. Charles A. Seipp Neil J. Williams, V. S. B. & Moyer, B. A. Simple guanidinium motif for the selective binding and extraction of sulfate. *Separation Science and Technology* **53,** 1864–1873 (2018).

20. Elmes, R. B. P., K.Y.Yuen, K. & Jolliffe, K. A. Sulfate-Selective Recognition by Using Neutral Dipeptide Anion Receptors in Aqueous Solution. *Chemistry A European Journal* **20,** 7373–7380 (2014).

21. Lane, J. D. E., Shiels, G., Ramamurthi, P., Müllner, M. & Jolliffe, K. A. Water-Soluble Squaramide-Functionalized Copolymers for Anion Recognition. *Macromolecular Rapid Communications,* 2300406 (2023).

22. Al Sheakh, L., Niemann, T., Villinger, A., Stange, P., Zaitsau, D. H., Strate, A. & Ludwig, R. Three in One: The Versatility of Hydrogen Bonding Interaction in Halide Salts with Hydroxy-Functionalized Pyridinium Cations. *ChemPhysChem* **22,** 1850–1856 (2021).

23. Jing, L., Deplazes, E., Clegg, J. K. & Wu, X. A charge-neutral organic cage selectively binds strongly hydrated sulfate anions in water. *Nature Chemistry* **16,** 335–342 (2024).

24. Ni, X., Li, X., Wang, Z. & Cheng, J.-P. Squaramide Equilibrium Acidities in DMSO. *Organic Letters* **16,** 1786–1789 (2014).

25. Manna, U., Portis, B., Egboluche, T. K., Nafis, M. & Hossain, M. A. Anion binding studies of urea and thiourea functionalized molecular clefts. *Frontiers in Chemistry* **8,** 575701 (2020).

26. Picci, G., Kubicki, M., Garau, A., Lippolis, V., Mocci, R., Porcheddu, A., Quesada, R., Ricci, P. C., Scorciapino, M. A. & Caltagirone, C. Simple squaramide receptors for highly efficient anion binding in aqueous media

and transmembrane transport. *Chemical Communications* **56,** 11066–11069 (2020).

27. Jia, C., Wu, B., Li, S., Huang, X., Zhao, Q., Li, Q.-S. & Yang, X.-J. Highly Efficient Extraction of Sulfate Ions with a Tripodal Hexaurea Receptor. *Angewandte Chemie International Edition* **50,** 486–490 (2011).
28. Kaur, S., Day, V. W. & Bowman-James, K. Urea-Based Macrocycle Selective for Sulfate and Structurally Sensitive to Water. *Crystal Growth & Design* **20,** 4212–4216 (2020).
29. Qin, L., Hartley, A., Turner, P., Elmes, R. B. P. & Jolliffe, K. A. Macrocyclic squaramides: anion receptors with high sulfate binding affinity and selectivity in aqueous media. *Chemical Science* **7,** 4563–4572 (2016).
30. Custelcean, R., Bosano, J., Bonnesen, P. V., Kertesz, V. & Hay, B. P. Computer-Aided Design of a Sulfate-Encapsulating Receptor. *Angewandte Chemie International Edition* **48,** 4025–4029 (2009).
31. Zaleskaya, M., Karbarz, M., Wilczek, M., Dobrzycki,. & Romaski, J. Cooperative Transport and Selective Extraction of Sulfates by a Squaramide-Based Ion Pair Receptor: A Case of Adaptable Selectivity. *Inorganic Chemistry* **59,** 13749–13759 (2020).
32. Bak, K. M., Trzaskowski, B. & Chmielewski, M. J. Anion-templated synthesis of a switchable fluorescent [2]catenane with sulfate sensing capability. *Chemical Science* **15,** 1796–1809 (2024).
33. Brown, A. & Beer, P. D. Halogen bonding anion recognition. *Chemical Communications* **52,** 8645–8658 (2016).
34. Robinson, S. W., Mustoe, C. L., White, N. G., Brown, A., Thompson, A. L., Kennepohl, P. & Beer, P. D. Evidence for Halogen Bond Covalency in Acyclic and Interlocked Halogen-Bonding Receptor Anion Recognition. *Journal of the American Chemical Society* **137,** 499–507 (2015).

35. Tepper, R., Schulze, B., Jäger, M., Friebe, C., Scharf, D. H., Görls, H. & Schubert, U. S. Anion Receptors Based on Halogen Bonding with Halo-1,2,3-triazoliums. *The Journal of Organic Chemistry* **80,** 3139–3150 (2015).

36. Mullaney, B. R., Partridge, B. E. & Beer, P. D. A Halogen-Bonding Bis-triazolium Rotaxane for Halide-Selective Anion Recognition. *Chemistry A European Journal* **21,** 1660–1665 (2015).

37. González, L., Zapata, F., Caballero, A., Molina, P., Ramírez de Arellano, C., Alkorta, I. & Elguero, J. HostGuest Chemistry: Oxoanion Recognition Based on Combined Charge-Assisted CH or Halogen-Bonding Interactions and AnionAnion Interactions Mediated by Hydrogen Bonds. *Chemistry A European Journal* **22,** 7533–7544 (2016).

38. Turner, G., Docker, A. & Beer, P. D. Anion recognition by halogen bonding and hydrogen bonding bis(triazole)-imidazolium [2]rotaxanes. *Dalton Transactions* **50,** 12800–12805 (2021).

39. Ho, T.-L. Hard soft acids bases (HSAB) principle and organic chemistry. *Chemical Reviews* **75,** 1–20 (1975).

40. Lee, S., Yuen, K. K. Y., Jolliffe, K. A. & Yoon, J. Fluorescent and colorimetric chemosensors for pyrophosphate. *Chemical Society Reviews* **44,** 1749–1762 (7 2015).

41. Ngo, H. T., Liu, X. & Jolliffe, K. A. Anion recognition and sensing with Zn(ii)dipicolylamine complexes. *Chemical Society Reviews* **41,** 4928–4965 (14 2012).

42. Naveen, R., Niaz, A., Iqbal Zaman, M., Khan, S., Rahim, A., Zulfiqar, A., Tariq, M., Saleh, T. A., M. F. Santos, D. & Alsaiari, M. Colorimetric detection of phosphate-based on iron complexing catechol-displacement assay in eutrophicated water bodies. *Environmental Nanotechnology, Monitoring and Management* **20,** 100792 (2023).

43. Rhaman, M. M., Hasan, M. H., Alamgir, A., Xu, L., Powell, D. R., Wong, B. M., Tandon, R. & Hossain, M. A. Highly selective and sensitive macrocycle-based dinuclear foldamer for fluorometric and colorimetric sensing of citrate in water. *Scientific Reports* **8** (2018).

44. Esteves, C. V., Costa, J., Esteban-Gómez, D., Lamosa, P., Bernard, H., Platas-Iglesias, C., Tripier, R. & Delgado, R. Phosphate and polyphosphate anion recognition by a dinuclear copper(II) complex of an unsymmetrical squaramide. *Dalton Transactions* **48,** 10104–10115 (2019).

45. Formica, M., Fusi, V., Paderni, D., Ambrosi, G., Inclán, M., Clares, M. P., Verdejo, B. & García-España, E. A Metal-Based Receptor for Selective Coordination and Fluorescent Sensing of Chloride. *Molecules* **26** (2021).

46. Zhou, H., Zhao, Y., Gao, G., Li, S., Lan, J. & You, J. Highly Selective Fluorescent Recognition of Sulfate in Water by Two Rigid Tetrakisimidazolium Macrocycles with Peripheral Chains. *Journal of the American Chemical Society* **135,** 14908–14911 (2013).

47. He, Y.-C., Yan, Y.-M., Tong, H.-B., Ren, Z.-X., Wang, J.-H., Zhang, Y.-B., Chao, J.-B. & Wang, M.-L. Benzenebistriazole-strapped calix[4]pyrrole: a neutral anion receptor with CH and NH donor groups that exhibits high sulfate binding affinity and selectivity in aqueous solutions. *Chemical Communications* **56,** 9364–9367 (2020).

48. Chen, S.-Q., Yu, S.-N., Zhao, W., Liang, L., Gong, Y., Yuan, L., Tang, J., Yang, X.-J. & Wu, B. Recognition-guided sulfate extraction and transport using tripodal hexaurea receptors. *Inorganic Chemistry Frontiers* **9,** 6091–6101 (2022).

49. Piña, M. N., Soberats, B., Rotger, C., Ballester, P., Deyà, P. M. & Costa, A. Selective sensing of competitive anions by non-selective hosts: the case of sulfate and phosphate in water. *New Journal of Chemistry* **32,** 1919–1923 (2008).

50. Prohens, R., Martorell, G., Ballester, P. & Costa, A. A squaramide fluorescent ensemble for monitoring sulfate in water. *Chemical Communications,* 1456–1457 (2001).

51. Hickey, B. L., Raz, A. A. P., Chen, J., Moreno, J. L., Hartman, J. D., Zhong, W. & Hooley, R. J. Selective anion sensing in high salt water via a remote indicator displacement assay. *Chemical Communications* **59,** 7819–7822 (2023).

52. Hanshaw, R. G., Hilkert, S. M., Jiang, H. & Smith, B. D. An indicator displacement system for fluorescent detection of phosphate oxyanions under physiological conditions. *Tetrahedron Letters* **45,** 8721–8724 (2004).

53. Moffat, C. D., Weiss, D. J., Shivalingam, A., White, A. J. P., Salaün, P. & Vilar, R. Molecular Recognition and Scavenging of Arsenate from Aqueous Solution Using Dimetallic Receptors. *Chemistry A European Journal* **20,** 17168–17177 (2014).

54. Minami, T., Liu, Y., Akdeniz, A., Koutnik, P., Esipenko, N. A., Nishiyabu, R., Kubo, Y. & Anzenbacher, P. J. Intramolecular Indicator Displacement Assay for Anions: Supramolecular Sensor for Glyphosate. *Journal of the American Chemical Society* **136,** 11396–11401 (2014).

55. Zwicker, V. E., Oliveira, B. L., Yeo, J. H., Fraser, S. T., Bernardes, G. J. L., New, E. J. & Jolliffe, K. A. A Fluorogenic Probe for Cell Surface Phosphatidylserine Using an Intramolecular Indicator Displacement Sensing Mechanism. *Angewandte Chemie International Edition* **58,** 3087–3091 (2019).

56. Das, R., Mondal, M., Paul, S., Pan, A. & Banerjee, P. An easy-to-use phosphate triggered zinc-azophenine complex assisted metal extrusion assay: A diagnostic approach for chronic kidney disease and in silico docking studies. *Inorganica Chimica Acta* **548,** 121364 (2023).

57. Wang, J. & Ha, C.-S. Azobenzene-based system for fluorimetric sensing of $H_2PO_4^-$ (Pi) that works as a molecular keypad lock. *Analyst* **135,** 1214–1218 (2010).

58. Goh, H., Ko, Y. G., Nam, T. K., Singh, A., Singh, N. & Jang, D. O. A benzimidazole-based fluorescent chemosensor for Cu^{2+} recognition and its complex for sensing $H_2PO_4^-$ by a Cu^{2+} displacement approach in aqueous media. *Tetrahedron Letters* **57,** 4435–4439 (2016).

59. Hatai, J., Pal, S. & Bandyopadhyay, S. An inorganic phosphate (Pi) sensor triggers turn-on fluorescence response by removal of a Cu^{2+} ion from a Cu^{2+}-ligand sensor: determination of Pi in biological samples. *Tetrahedron Letters* **53,** 4357–4360 (2012).

60. Shao, N., Jin, J., Wang, G., Zhang, Y., Yang, R. & Yuan, J. Europium(III) complex-based luminescent sensing probes for multi-phosphate anions: modulating selectivity by ligand choice. *Chemical Communications,* 1127–1129 (2008).

61. Banerjee, T., Suresh, M., Ghosh, H. N. & Das, A. Competitive binding of Ba^{2+} and Sr^{2+} to 18-Crown-6 in a Receptor with a 1-Methoxyanthraquinone Analogue as the Other Binding Site. *European Journal of Inorganic Chemistry* **2011,** 4680–4690 (2011).

62. Steinberg, J., Bauer, D., Reissig, F., Köckerling, M., Pietzsch, H.-J. & Mamat, C. Modified Calix[4]crowns as Molecular Receptors for Barium. *ChemistryOpen* **7,** 432–438 (2018).

63. Grey, C. P. & Hall, D. S. Prospects for lithium-ion batteries and beyond-a 2030 vision. *Nature Communications* **11,** 6279 (2020).

64. Deshpande, S., Durdagi, S. & Noskov, S. Y. in *Encyclopedia of Metalloproteins* 1799–1804 (Springer New York, 2013).

65. Gokel, G. W., Leevy, W. M. & Weber, M. E. Crown Ethers: Sensors for Ions and Molecular Scaffolds for Materials and Biological Models. *Chemical Reviews* **104,** 2723–2750 (2004).

66. Izatt, R. M., Bradshaw, J. S., Nielsen, S. A., Lamb, J. D., Christensen, J. J. & Sen, D. Thermodynamic and kinetic data for cation-macrocycle interaction. *Chemical Reviews* **85,** 271–339 (1985).

67. Steed, J. W. First- and second-sphere coordination chemistry of alkali metal crown ether complexes. *Coordination Chemistry Reviews* **215,** 171–221 (2001).

68. Krakowiak, K. E., Bradshaw, J. S. & Zamecka-Krakowiak, D. J. Synthesis of aza-crown ethers. *Chemical Reviews* **89,** 929–972 (1989).

69. Buschmann, H. The macrocyclic and cryptate effects. Complexation of alkali ions by monocyclic and bicyclic ligands in methanol. *Inorganica Chimica Acta* **125,** 31–35 (1986).

70. Hamdiani, S., Savalas, L. R. T., Purwoko, A. A. & Hadisaputra, S. Theoretical study on the binding selectivity of 18-membered azacrown ethers with alkaline earth metal species. *Acta Chimica Asiana* **1,** 17–23 (2018).

71. Poonia, N. S. & Bajaj, A. V. Coordination chemistry of alkali and alkaline earth cations. *Chemical Reviews* **79,** 389–445 (1979).

72. Austin, C. & Rodgers, M. Intrinsic affinities of alkali metal cations for diaza-18-crown-6: Effects of alkali metal cation size and donor atoms on the binding energies. *International Journal of Mass Spectrometry* **377,** 64–72 (2015).

73. Haymore, B. L., Lamb, J. D., Izatt, R. M. & Christensen, J. J. Thermodynamic origin of the macrocyclic effect in crown ether complexes of Na^+, K^+, and Ba^{2+}. *Inorganic Chemistry* **21,** 1598–1602 (1982).

74. Solov'ev, V. P., Strakhova, N. N., Kazachenko, V. P., Solotnov, A. F., Baulin, V. E., Raevsky, O. A., Rüdiger, V., Eblinger, F. & Schneider, H.-J. Steric and Stereoelectronic Effects in Aza Crown Ether Complexes. *European Journal of Organic Chemistry* **1998,** 1379–1389 (1998).

75. Thapa, P., Byrnes, N. K., Denisenko, A. A., Mao, J. X., McDonald, A. D., Newhouse, C. A., Vuong, T. T., Woodruff, K., Nam, K., Nygren, D. R., Jones, B. J. P. & Foss, F. W. J. Demonstration of Selective Single-Barium Ion Detection with Dry Diazacrown Ether Naphthalimide Turn-on Chemosensors. *ACS Sensors* **6,** 192–202 (2021).

76. Choi, S.-A., Park, C. S., Kwon, O. S., Giong, H.-K., Lee, J.-S., Ha, T. H. & Lee, C.-S. Structural effects of naphthalimide-based fluorescent sensor for hydrogen sulfide and imaging in live zebrafish. *Scientific Reports* **6** (2016).

77. Jiao, C., Liu, Y., Lu, W., Zhang, P., Ma, X. & Wang, Y. A simple sensor based on 1,8-naphthalimide with large Stokes shift for detection of hypochlorous acid in living cells. *RSC Advances* **9,** 31196–31201 (54 2019).

78. Coman, A. G., Stavarache, C., Paun, A., Popescu, C. C., Hdade, N. D., Ionita, P. & Matache, M. A novel profluorescent paramagnetic diaza-crown ether: synthesis, characterization and alkaline metal-ion complexation. *RSC Advances* **9,** 6078–6083 (2019).

79. Boubekeur-Lecaque, L., Souffrin, C., Gontard, G., Boubekeur, K. & Amatore, C. Water soluble diaza crown ether derivative: Synthesis and barium complexation studies. *Polyhedron* **68,** 191–198 (2014).

80. Basa, P. N., Bhowmick, A., Schulz, M. M. & Sykes, A. G. Site-Selective Imination of an Anthracenone Sensor: Selective Fluorescence Detection of Barium(II). *The Journal of Organic Chemistry* **76,** 7866–7871 (2011).

81. Wu, Y. X., Cao, J., Deng, H. Y. & Feng, J. X. Synthesis, complexation, and fluorescence behavior of 3,4-dimethylthieno[2,3-b]thiophene carrying two monoaza-15-crown-5 ether groups. *Spectrochimica Acta Part A: Molecular and Biomolecular Spectroscopy* **82,** 340–344 (2011).

82. Nakahara, Y., Kida, T., Nakatsuji, Y. & Akashi, M. A novel fluorescent indicator for Ba^{2+} in aqueous micellar solutions. *Chemical Communications,* 224–225 (2004).

83. Zhang, Q. & Duan, K. Fluorescence chemosensor containing 4-methyl-7-coumarinyloxy, acetylhydrazono and N-phenylaza-15-crown-5 moieties for K^+ and Ba^{2+} ions. *Heterocyclic Communications* **24,** 141–145 (2018).

84. Blakemore, J. D., Chitta, R. & DSouza, F. Synthesis and study of crown ether-appended boron dipyrrin chemosensors for cation detection. *Tetrahedron Letters* **48,** 1977–1982 (2007).

85. Kondo, S.-i., Takahashi, T., Takiguchi, Y. & Unno, M. Synthesis and photophysical properties of a 2,2-bianthracene-based receptor bearing two aza-15-crown-5 ethers for naked-eye detection of barium ion. *Tetrahedron Letters* **52,** 453–457 (2011).

86. Guo, H. & Kuwabara, T. Colorimetric Chemosensor for Barium Metal Ions Using Tris(bipyridiniumcrown ether) Conjugate. *Chemistry Letters* **42,** 194–196 (2013).

87. Cox, R. P., Sandanayake, S., Scarborough, D. L. A., Izgorodina, E. I., Langford, S. J. & Bell, T. D. M. Investigation of cation binding and sensing by new crown ether core substituted naphthalene diimide systems. *New Journal of Chemistry* **43,** 2011–2018 (2019).

88. Thapa, P., Arnquist, I., Byrnes, N., Denisenko, A. A., Foss, F. W., Jones, B. J. P., McDonald, A. D., Nygren, D. R. & Woodruff, K. Barium Chemosensors with Dry-Phase Fluorescence for Neutrinoless Double Beta Decay. *Scientific Reports* **9,** 15097 (2019).

89. Witulski, B., Weber, M., Bergsträsser, U., Desvergne, J.-P., Bassani, D. M. & Bouas-Laurent, H. Novel Alkali Cation Chemosensors Based on N-9-Anthrylaza-crown Ethers. *Organic Letters* **3,** 1467–1470 (2001).

90. Xu, H., Xu, X., Dabestani, R., Brown, G. M., Fan, L., Patton, S. & Ji, H.-F. Supramolecular fluorescent probes for the detection of mixed alkali metal ions that mimic the function of integrated logic gates. *Journal of the Chemical Society, Perkin Transactions 2,* 636–643 (2002).

91. Fedorov, Y. V., Fedorova, O. A., Andryukhina, E. N., Shepel, N. E., Mashura, M. M., Gromov, S. P., Kuzmina, L. G., Churakov, A. V., Howard, J. A. K., Marmois, E., Oberlé, J., Jonusauskas, G. & Alfimov, M. V. Supramolecular assemblies of crown-containing 4-styrylpyridine in the presence of metal cations. *Journal of Physical Organic Chemistry* **18,** 1032–1041 (2005).

92. Brandel, J., Sairenji, M., Ichikawa, K. & Nabeshima, T. Remarkable Mg^{2+}-selective emission of an azacrown receptor based on Ir(III) complex. *Chemical Communications* **46,** 3958–3960 (2010).

93. Benco, J. S., Nienaber, H. A., Dennen, K. & McGimpsey, W. A fluoroionophore for detection of potassium ions: 9-anthryl-substituted azacrown ether covalently linked to a 1,3-alternate calix[4]arene. *Journal of Photochemistry and Photobiology A: Chemistry* **152,** 33–40 (2002).

94. Yan, L.-Q., Xie, M.-S., Peng, M.-S. & Liu, W. A Coumarin Fluorescent Probe for Ca^{2+} Containing Aza-Crown Ether Unit. *Australian Journal of Chemistry* **66,** 1584–1586 (2013).

95. Hama, H., Morozumi, T. & Nakamura, H. Novel Mg^{2+}-responsive fluorescent chemosensor based on benzo-15-crown-5 possessing 1-naphthaleneacetamide moiety. *Tetrahedron Letters* **48,** 1859–1861 (2007).

96. Amit, K., Udita, T., Mulayam, S. & Rajeev, K. Assessment of malathion and its effects on leukocytes in human blood samples. *Journal of Biomedical Research* **30,** 52 (2016).

97. Uyuklu, M., Canpolat, M., Meiselman, H. J. & Baskurt, O. K. Wavelength selection in measuring red blood cell aggregation based on light transmittance. *Journal of Biomedical Optics* **16,** 117006 (2011).

98. Lakowicz, J. R. *Principles of fluorescence spectroscopy* 3rd ed. (Springer, New York, NY, 2006).

99. Bell, T. W. & Hext, N. M. Supramolecular optical chemosensors for organic analytes. *Chemical Society Reviews* **33,** 589–598 (2004).

100. Czarnik, A. W. in *ACS Symposium Series* 1–9 (American Chemical Society, 1993).

101. Meng, Q., Cheng, S., Lan, M. & Wei, G. A Novel and Simple Molecular Probe Sensing Hg(II) in Living Cells by Chelation-enhanced Fluorescence. *Chinese Journal of Chemistry* **30,** 249–253 (2012).

102. Gill, J. K. & Shaw, G. S. Using Förster Resonance Energy Transfer (FRET) to Understand the Ubiquitination Landscape. *ChemBioChem* **25,** e202400193 (2024).

103. Aich, K., Goswami, S., Das, S., Mukhopadhyay, C. D., Quah, C. K. & Fun, H.-K. Cd^{2+} Triggered the FRET ON: A New Molecular Switch for the Ratiometric Detection of Cd^{2+} with Live-Cell Imaging and Bound X-ray Structure. *Inorganic Chemistry* **54,** 7309–7315 (2015).

104. Niu, H., Liu, J., OConnor, H. M., Gunnlaugsson, T., James, T. D. & Zhang, H. Photoinduced electron transfer (PeT) based fluorescent probes for cellular imaging and disease therapy. *Chemical Society Reviews* **52,** 2322–2357 (2023).

105. Hu, M., Fan, J., Cao, J., Song, K., Zhang, H., Sun, S. & Peng, X. Enhanced fluorescent chemosensor for Ag^{+} in absolute aqueous solution and living cells: An experimental and theoretical study. *Analyst* **137,** 2107–2111 (2012).

106. Rettig, W. Charge Separation in Excited States of Decoupled Systems–TICT Compounds and Implications Regarding the Development

of New Laser Dyes and the Primary Process of Vision and Photosynthesis. *Angewandte Chemie International Edition in English* **25,** 971–988 (1986).

107. Sasaki, S., Drummen, G. P. C. & Konishi, G. Recent advances in twisted intramolecular charge transfer (TICT) fluorescence and related phenomena in materials chemistry. *Journal of Materials Chemistry C* **4,** 2731–2743 (2016).

108. Dash, N., Malakar, A., Kumar, M., Mandal, B. B. & Krishnamoorthy, G. Metal ion dependent ON intramolecular charge transfer (ICT) and OFF normal switching of the fluorescence: Sensing of Zn^{2+} by ICT emission in living cells. *Sensors and Actuators B: Chemical* **202,** 1154–1163 (2014).

109. Xu, Q., Qin, W., Qin, Y., Hu, G., Xing, Z. & Liu, Y. A ratiometric fluorescence probe for visualized detection of heavy metal cadmium and application in water samples and living cells. *Molecules* **29** (2024).

110. Köksoy, B., Özdemir, M., Altnk, S., Zorlu, Y., Yalçn, B., Durmu, M. & Koyuncu, S. Electron-Donating and Electron-Withdrawing Subunit Effects on Coumarin-BODIPY Dyads: Optical and Electrochemical Properties and Molecular Interactions. *ChemPhotoChem* **7,** e202300043 (2023).

111. Würth, C., Grabolle, M., Pauli, J., Spieles, M. & Resch-Genger, U. Relative and absolute determination of fluorescence quantum yields of transparent samples. *Nature Protocols* **8,** 1535–1550 (2013).

112. *Comparing Hole Extraction Efficiencies in Perovskite Solar Cells using Photoluminescence Quantum Yield - Edinburgh Instruments — edinst.com* `https://www.edinst.com/resource/application-note-comparing-hole-extraction-efficiencies-in-perovskite-solar-cells-using-photoluminescence-quantum-yield/`. [Accessed 09-02-2025]. 2021.

113. Mei, J., Leung, N. L. C., Kwok, R. T. K., Lam, J. W. Y. & Tang, B. Z. Aggregation-Induced Emission: Together We Shine, United We Soar! *Chemical Reviews* **115,** 11718–11940 (2015).

114. Chaichana, K., Phutlaprungrueang, N., Chaicharoenwimolkul, L., Promkatkaew, M. & Kongsriprapan, S. A selective fluorescence probe based on naphthalene for the detection of barium(II). *Spectrochimica Acta Part A: Molecular and Biomolecular Spectroscopy* **207,** 118–122 (2019).

115. Hall, A. C., Suarez, C., Hom-Choudhury, A., Manu, A. N. A., Hall, C. D., Kirkovits, G. J. & Ghiriviga, I. Cation transport by a redox-active synthetic ion channel. *Organic and Biomolecular Chemistry* **1,** 2973–2982 (2003).

116. Hamlin, T. A., Swart, M. & Bickelhaupt, F. M. Nucleophilic Substitution (S_N2): Dependence on Nucleophile, Leaving Group, Central Atom, Substituents, and Solvent. *ChemPhysChem* **19,** 1315–1330 (2018).

117. Zhang, X., Liu, X., Taddei, M., Bussotti, L., Kurganskii, I., Li, M., Jiang, X., Xing, L., Ji, S., Huo, Y., Zhao, J., Di Donato, M., Wan, Y., Zhao, Z. & Fedin, M. V. Red Light-Emitting Thermally-Activated Delayed Fluorescence of Naphthalimide-Phenoxazine Electron Donor-Acceptor Dyad: Time-Resolved Optical and Magnetic Spectroscopic Studies. *Chemistry – A European Journal* **28,** e202200510 (2022).

118. Thibon, A. & Pierre, V. C. A Highly Selective Luminescent Sensor for the Time-Gated Detection of Potassium. *Journal of the American Chemical Society* **131,** 434–435 (2009).

119. Hagen, V., Dekowski, B., Nache, V., Schmidt, R., Geissler, D., Lorenz, D., Eichhorst, J., Keller, S., Kaneko, H., Benndorf, K. & Wiesner, B. Coumarinylmethyl Esters for Ultrafast Release of High Concentrations of Cyclic Nucleotides upon One- and Two-Photon Photolysis. *Angewandte Chemie International Edition* **44,** 7887–7891 (2005).

120. Wang, C., Zheng, X., Huang, R., Yan, S., Xie, X., Tian, T., Huang, S., Weng, X. & Zhou, X. A 4-Amino-1,8-Naphthalimide Derivative for Selective Fluorescent Detection of Palladium(II) Ions. *Asian Journal of Organic Chemistry* **1,** 259–263 (2012).

121. Janosi, T. Z., Korppi-Tommola, J., Csok, Z., Kollar, L., Myllyperkio, P. & Erostyak, J. Anthracene Fluorescence Quenching by a Tetrakis (Ketocarboxamide) Cavitand. *Journal of Spectroscopy* **2014,** 708739 (2014).

122. Nakajima, A. Fluorescence spectra of anthracene and pyrene in water and in aqueous surfactant solution. *Journal of Luminescence* **15,** 277–282 (1977).

123. Schwarz, F. P. & Wasik, S. P. Fluorescence measurements of benzene, naphthalene, anthracene, pyrene, fluoranthene, and benzo[e]pyrene in water. *Analytical Chemistry* **48,** 524–528 (1976).

124. Momiji, I., Yoza, C. & Matsui, K. Fluorescence Spectra of 9-Anthracenecarboxylic Acid in Heterogeneous Environments. *The Journal of Physical Chemistry B* **104,** 1552–1555 (2000).

125. Wang, L., Fujii, M., Yamaji, M. & Okamoto, H. Fluorescence behaviour of 2-, 3- and 4-amino-1,8-naphthalimides: effects of the substitution positions of the amino functionality on the photophysical properties. *Photochemical and Photobiological Sciences* **17,** 1319–1328 (10 2018).

126. Prasannan, D. & Arunkumar, C. A turn-on-and-off pH sensitive BODIPY fluorescent probe for imaging E. coli cells. *New Journal of Chemistry* **42,** 3473–3482 (5 2018).

127. Szakács, Z., Rousseva, S., Bojtár, M., Hessz, D., Bitter, I., Kállay, M., Hilbers, M., Zhang, H. & Kubinyi, M. Experimental evidence of TICT state in 4-piperidinyl-1,8-naphthalimide a kinetic and mechanistic study. *Physical Chemistry Chemical Physics* **20,** 10155–10164 (2018).

128. Qin, W., Baruah, M., Sliwa, M., Van der Auweraer, M., De Borggraeve, W. M., Beljonne, D., Van Averbeke, B. & Boens, N. Ratiometric, Fluorescent BODIPY Dye with Aza Crown Ether Functionality: Synthesis, Solvatochromism, and Metal Ion Complex Formation. *The Journal of Physical Chemistry A* **112,** 6104–6114 (2008).

129. Nhu, Q. P. N., Abbas Abedi, S. A., Chanmungkalakul, S., Sukwattanasinitt, M., Chang, Y.-T. & Rashatasakhon, P. Solvatochromic fluorescent ethynyl naphthalimide derivatives for detection of water in organic solvents. *Dyes and Pigments* **227,** 112188 (2024).

130. Wang, K.-P., Lei, Y., Chen, J.-P., Ge, Z.-H., Liu, W., Zhang, Q., Chen, S. & Hu, Z.-Q. The coumarin conjugate: synthesis, photophysical properties and the ratiometric fluorescence response to water content of organic solvent. *Dyes and Pigments* **151,** 233–237 (2018).

131. Martell, A. E. & Hancock, R. D. *Metal Complexes in Aqueous Solutions* (Springer, 1996).

132. Panchenko, P. A., Fedorov, Y. V., Perevalov, V. P., Jonusauskas, G. & Fedorova, O. A. Cation-Dependent Fluorescent Properties of Naphthalimide Derivatives with N-Benzocrown Ether Fragment. *The Journal of Physical Chemistry A* **114,** 4118–4122 (2010).

133. Baruah, M., Qin, W., Vallée, R. A. L., Beljonne, D., Rohand, T., Dehaen, W. & Boens, N. A Highly Potassium-Selective Ratiometric Fluorescent Indicator Based on BODIPY Azacrown Ether Excitable with Visible Light. *Organic Letters* **7,** 4377–4380 (2005).

134. Cosnard, F. & Wintgens, V. A new fluoroionophore derived from 4-amino-N-methyl-1,8-naphthalimide. *Tetrahedron Letters* **39,** 2751–2754 (1998).

135. Rusalov, M. V., Uzhinov, B. M., Alfimov, M. V. & Gromov, S. P. Photoinduced recoordination of metal cations in complexes with chromogenic crown ethers. *Russian Chemical Reviews* **79,** 1099 (2010).

136. Cho, U. & Chen, J. K. Lanthanide-based optical probes of biological systems. *Cell Chemical Biology.* **27,** 921–936 (2020).

137. Panchenko, P. A., Fedorov, Y. V., Fedorova, O. A. & Jonusauskas, G. Comparative analysis of the PET and ICT sensor properties of 1,8-naphthalimides containing aza-15-crown-5 ether moiety. *Dyes and Pigments* **98,** 347–357 (2013).

138. Yang, J.-S., Hwang, C.-Y. & Chen, M.-Y. Bimodal fluorescence signaling based on control of the excited-state conformational twisting and the ground-state protonation processes. *Tetrahedron Letters* **48,** 3097–3102 (2007).

139. Gans, P., Sabatini, A. & Vacca, A. Investigation of equilibria in solution. Determination of equilibrium constants with the HYPERQUAD suite of programs. *Talanta* **43,** 1739–1753 (1996).

140. Novikov, E., Stobiecka, A. & Boens, N. Analysis of Fluorometric Titration Curves. *The Journal of Physical Chemistry A* **104,** 5388–5395 (2000).

141. *Ion Exchange Chromatography — shimadzu.com.au* `https://www.shimadzu.com.au/service-support/technical-support/analysis-basics/basic/ion_exchange_chromatography.html`.

142. Bak, F., Scheff, G. & Jansen, K.-H. A rapid and sensitive ion chromatographic technique for the determination of sulfate and sulfate reduction rates in freshwater lake sediments. *FEMS Microbiology Letters* **85,** 23–30 (1991).

143. Jun, X., Lima, J. L. F. C. & Montenegro, M. C. B. S. M. Fast determination of sulfate by ion chromatography based on a permanently coated column. *Analyst* **120,** 2469–2473 (1995).

144. Rozman, P., Kim, H., Madhu, C. & Klaassen, C. Tissue sulfate determination by ion chromatography. *Journal of Chromatography B: Biomedical Sciences and Applications* **574,** 146–149 (1992).

145. Wang, S. H., Raptis, E. & Yeh, J. Ion chromatography for the determination of sulfate in STEALTH liposomes. *Journal of Chromatography A* **1039,** 51–58 (2004).

146. Wang, R., Wang, N., Ye, M. & Zhu, Y. Determination of low-level anions in seawater by ion chromatography with cycling-column-switching. *Journal of Chromatography A* **1265,** 186–190 (2012).

147. Piña, M. N., Rotger, C., Soberats, B., Ballester, P., Deyà, P. M. & Costa, A. Evidence of anion-induced dimerization of a squaramide-based host in protic solvents. *Chemical Communications,* 963–965 (2007).

148. Vijayakumar, P. & Dawson, P. A. Analytical methods for quantitating sulfate in plasma and serum. *Essays in Biochemistry* **68,** 383–389 (2024).

149. Gros, N., Camões, M., Oliveira, C. & Silva, M. Ionic composition of seawaters and derived saline solutions determined by ion chromatography and its relation to other water quality parameters. *Journal of Chromatography A* **1210,** 92–98 (2008).

150. Bissell, R. A., Calle, E., de Silva, A. P., de Silva, S. A., Gunaratne, H. Q. N., Habib-Jiwan, J.-L., Peiris, S. L. A., Rupasinghe, R. A. D. D., Shantha, T. K., Samarasinghe, D., Sandanayake, K. R. A. S. & Soumillion, J.-P. Luminescence and charge transfer. Part 2. Aminomethyl anthracene derivatives as fluorescent PET (photoinduced electron transfer) sensors for protons. *Journal of the Chemical Society, Perkin Transactions 2,* 1559–1564 (1992).

151. Luo, H., Dai, S. & Bonnesen, P. V. Solvent Extraction of Sr^{2+} and Cs^{+} Based on Room-Temperature Ionic Liquids Containing Monoaza-Substituted Crown Ethers. *Analytical Chemistry* **76,** 2773–2779 (2004).

152. Yang, R.-Y., Bao, C.-Y., Lin, Q.-N. & Zhu, L.-Y. A light-regulated synthetic ion channel constructed by an azobenzene modified hydraphile. *Chinese Chemical Letters* **26,** 851–856 (2015).

153. Ao, X., Bright, S. A., Taylor, N. C. & Elmes, R. B. P. 2-Nitroimidazole based fluorescent probes for nitroreductase; monitoring reductive stress in cellulo. *Organic and Biomolecular Chemistry* **15,** 6104–6108 (2017).

154. Shao, Z., Zhang, C., Zhu, X., Wang, Y., Xu, W., Chen, Y., Wang, X., Zhu, H. & Liang, Y. Design of a 1,8-naphthalimide-based OFF-ON type bioorthogonal reagent for fluorescent imaging in live cells. *Chinese Chemical Letters* **30,** 2169–2172 (2019).

155. Rotger, M. C., Piña, M. N., Frontera, A., Martorell, G., Ballester, P., Deyà, P. M. & Costa, A. Conformational Preferences and Self-Template Macrocyclization of Squaramide-Based Foldable Modules. *The Journal of Organic Chemistry* **69,** 2302–2308 (2004).

156. Fierová, E. & Kubala, M. Mean fluorescence lifetime and its error. *Journal of Luminescence* **132,** 2059–2064 (2012).